Systematic Structure Investigation of YBCO Thin Films with Direct Methods and Surface X-ray Diffraction

---

Dissertation
zur
Erlangung der naturwissenschaftlichen Doktorwürde
(Dr. sc. nat.)
vorgelegt der
Mathematisch-naturwissenschaftlichen Fakultät
der
Universität Zürich
von

Christian M. Schlepütz
aus
Deutschland

Promotionskomitee
Prof. Dr. Jürg Osterwalder (Vorsitz)
Prof. Dr. Philip R. Willmott (Leitung der Dissertation)
Prof. Dr. Hugo Keller
Prof. Dr. Joël Mesot
Prof. Dr. Bruce D. Patterson

Zürich, 2009

To my family

This document was prepared using $\LaTeX2_\varepsilon$ using Philip R. Willmott's customized version of the document class file `book.cls`, named `coolhab.cls`, and a customized bibliography style created using the `custom-bib` package.

Printed in Switzerland

Acknowledgments

Synchrotron-based structural investigations may hardly be carried out by one person alone, but rather require a concerted team effort. I want to thank the many people who have been part of this team, supporting me throughout my entire project.

First, I thank Philip Willmott for his guidance and support during this project, and the opportunity to work very independently in such a stimulating atmosphere, while always being sure of his trust in my judgment and my decisions and his honest appreciation for my work in our team. His willingness to share his scientific insight and his talent to explain seemingly complex things in a simple manner have greatly influenced this work. I also want to thank him for his personal friendship.

I am especially indebted to Jürg Osterwalder from the University of Zürich for taking me on as his PhD student. In spite of the geographical distance and the correspondingly infrequent meetings, I was always assured of his backing and support for my work, and his interest in the project. I also want to thank the other members of my PhD committee, Hugo Keller, Joël Mesot, and Bruce Patterson for their support, input, and valuable suggestions.

A great deal of the structural analyses in this work could only be done thanks to Matts Björck. Not only did he provide us with the astonishing DCAF direct method and his genetic algorithms "work-horse" GenX, but his expertise and many new ideas were of invaluable help. Also my co-graduates Roger Herger, Domenico Martoccia, Stephan Pauli have always been intimately involved in this project. All of them, I want to thank for many lively and instructive discussions, the long nights spent jointly at the beamline, the joy of discovering and understanding new things together, their helping hands whenever most needed, and last but not least, their personal friendships.

These studies would not have been possible without the high-quality samples produced for us by film growth experts. I am thankful to Milan Radovic and Fabio Miletto Granozio from the Università di Napoli, Italy, and to Edmond Koller and Øystein Fischer, Université de Genève,

Switzerland, for their efforts to grow the best possible films in the shortest possible time.

A special word of thanks belongs to Yizhak Yacoby from the Hebrew University of Jerusalem for inviting me to Israel and introducing me to his COBRA method. I am equally thankful to Roy Clarke, Divine Kumah, Codrin Cionca, and Naji Husseini at the University of Michigan, USA, for a great collaboration and the chance to expand my COBRA experience.

I wish to extend my thanks to Oliver Bunk for many helpful and lively discussions, for offering and sharing his expertise during the development of the most crucial parts of the beamline controls software, and for showing me how to use his SXRD fitting program FIT.

A good detector makes a world of difference, and thanks to our dedicated detector group and the DECTRIS team, we were given the unique chance to be at the forefront to explore this new world with the spectacular PILATUS 100k pixel detector. I am grateful to Christian Brönnimann, Bernd Schmitt, Philipp Kraft, Beat Henrich, Markus Näf, Petr Salficky, and Eric Eikenberry for this opportunity and for their continued support of my project.

Without the help of our team technicians, Michael Lange and Dominik Meister, this work would certainly not have been possible and I appreciate their reliable support and helpful hands during many beamtimes. Also, I want to thank all other present, former, and affiliated members of the beamline, Fabia Gozzo, Marco Stampanoni, Antonio Cervellino, David Maden, and Xiaoqiang Wang, for the pleasant and motivating working environment and a very warm welcome in their team.

Many other people at the PSI have been of great help during the project in sample characterization, preparation, evaluation and for invaluable discussions: Yasmine Sassa, Luc Patthey, Stephane Pailhes, Virgina Perez-Dieste, Ekaterina Pomjakishina, Kasimierz Conder, Krunoslav Prsa, Michael Schneider, Rolf Schelldorfer, Hans Grimmer, Hans Sigg, Philippe Lerch, and many more. Finally, I want express my gratitude especially to those people not directly involved in this thesis project, but whose dependable assistance is so vital for an inspiring and efficient working atmosphere. Their help usually goes without saying, and one inevitably starts to take it for granted. I want to thank our virtually invisible cleaning personnel, the excellent Oase team and friendly cafeteria staff, the competent people from IT support, the speedy administration and logistics departments, our knowledgeable librarians, our excellent secretaries, and everyone else whose support has helped me during my work.

Last, but definitely not least, I thank Sarah and my family for sharing this enormously enriching time with me, and showing great interest in my work, while reassuring me with their continuous encouragement and support, their trust and belief in me, and their love.

Abstract

Complex transition metal oxides and strongly correlated electron systems (SCES) exhibit an extraordinary wealth of physical phenomena and properties, ranging from features as diverse as ferroelectricity and colossal magnetoresistance to mulitferroicity and high-temperature superconductivity. The combination of several such materials into artificial heterostructures has led to new and entirely unexpected phenomena at their interfaces, for example the formation of a high-mobility two-dimensional electron-gas at the heterointerface of the two bandgap insulators $SrTiO_3$ and $LaAlO_3$.

These systems are both interesting from a fundamental point of view as well as for their large potential in technological applications. The complex interactions between the spin, charge, lattice, and orbital degrees of freedom in SCES are strongly affected by small atomic displacements. The exact knowledge of the atomic structure down to well below the sub-Angstrom length scale is therefore of paramount significance both for the understanding and theoretical modeling of the physical effects, as well as for the design of nano-scaled technical devices.

Surface x-ray diffraction (SXRD) offers unique capabilities for the investigation of two-dimensional systems such as surfaces, interfaces, and thin films or heterostructures. The high spatial resolution of a few thousandths of an Angstrom, in combination with the high penetration power of the x-rays, allows for the three-dimensional reconstruction of the atomic structure for surfaces and even for buried interfaces.

One of the main challenges for SXRD lies in the structural complexity of such systems, which often involve simultaneous atomic rearrangements over a region comprising several unit cells in depth, containing typically several dozens of individual atoms. Traditional model refinement techniques are bound to fail for such complex systems. Recent developments in direct methods for SXRD, in conjunction with the enhanced data quality and quantity provided by fast, single-photon counting area pixel detectors, can help to overcome this limitation. By iteratively reconstructing the experimentally unaccessible phases, based only on the measured diffraction

intensities and other *a priori* knowledge of the system, the recorded diffraction pattern can be inverted directly to yield a three-dimensional electron-density map of the investigated structure, which can be interpreted directly in terms of an atomic structure or used as a starting point for further refinement steps.

In this thesis, we present SXRD studies of thin $YBa_2Cu_3O_{7\text{-x}}$ (YBCO) films grown by pulsed laser deposition on $SrTiO_3$ (STO), $(La_xSr_{1\text{-x}})(Al_yTa_{1\text{-y}})O_3$ (LSAT), and $NdGaO_3$ (NGO). With a thickness of approximately 4 unit cells, the c-axis oriented YBCO films represent one of the most complex systems investigated with direct methods and SXRD to date. This makes it an ideal testbed to evaluate different combinations of direct method and refinement approaches in terms of their relative merits and limitations. The level of consistency between the different methods and for random restarts of individual algorithms gives a direct feedback about the credibility of the final structure solutions.

Using this approach, the atomic structure of YBCO both on STO and on LSAT was found to be exceedingly bulk-like in terms of the interatomic distances and bond angles, but heteroepitaxially strained to match the in-plane lattice constants of each substrate. This results in (a) a very slight contraction of the YBCO *c*-axis constant of less than 1%, in response to the tensile in-plane strain, and (b) the formation of a tetragonal YBCO unit cell due to the equal lengths of the substrate *a*- and *b*-axes. This change in symmetry may have important consequences for the physical properties of the films, especially regarding the effects on the CuO chain layers of YBCO, which show a strong anisotropy in the *a*- and *b*-directions of the orthorhombic YBCO bulk unit cell.

This detailed structural information is of eminent importance for the interpretation of surface-sensitive measurements, for example of the electronic structure using angle-resolved photoelectron spectroscopy, and as a starting point for theoretical calculations. Finally, the fact that the film structures are very bulk-like may allow for a direct correlation between bulk properties and results obtained from surface-sensitive measurements, making high-quality thin films viable substitutes for bulk samples, where they are unavailable in sufficient quality.

Zusammenfassung

Bei komplexen Übergangsmetalloxiden und stark korrelierten Elektronensystemen lassen sich eine überwältigende Anzahl verschiedener physikalischer Effekte und Eigenschaften beobachten, die von der Ferroelektrizität über den kolossalen Magnetoresistiven Effekt (CMR-Effekt) und Multiferroizität bis hin zur Supraleitung reichen. Bringt man verschiedene solcher Materialien in Kontakt miteinander, so können unerwartet neue Effekte an deren Grenzflächen auftreten. Ein prominentes Beispiel hierfür ist die Entstehung eines zweidimensionalen Elektronengases hoher Leitfähigkeit an der Grenzfläche zwischen den beiden Bandisolatoren $SrTiO_3$ und $LaAlO_3$.

Die Untersuchung solch künstlicher Strukturen mit neuartigen Eigenschaften ist sowohl für die Grundlagenforschung als auch für deren technische Anwendung wichtig. Kleinste Veränderungen in der atomaren Struktur haben oft drastische Auswirkungen auf das komplexe Zusammenspiel der verschiedenen Freiheitsgrade im System. Die Kenntnis der genauen Atompositionen bildet daher eine grundlegende Voraussetzung sowohl für das theoretische Verständnis und die Präzisierung von theoretischen Modellen als auch für die Entwicklung neuer Komponenten in der Nanotechnologie.

Dank der hohen räumlichen Auflösung von wenigen Tausendstel Ångström und der grossen Eindringtiefe von Röntgenstrahlen kann man mittels Oberfächenröntgenbeugung die dreidimensionale atomare Struktur von Grenz- und Oberflächen sowie von dünnen Beschichtungen sehr genau bestimmen. Die Komplexität der hier betrachteten Systeme stellt jedoch eine grosse Herausforderung für die Methode dar, da typischerweise die Positionen dutzender Atome über einen Bereich von mehreren Einheitszellen gleichzeitig bestimmt werden müssen. Unter diesen Bedingungen ist eine verlässliche Strukturbestimmung mittels traditioneller Datenanalysemethoden, welche auf der Optimierung von Strukturmodellen beruhen, fast aussichtslos.

Der Einsatz neuartiger Pixeldetektoren hat jedoch zu einer markanten Beschleunigung der Datennahme und Steigerung der Datenqualität geführt, einer wichtigen Voraussetzung zur

Anwendung von direkten Methoden. Dabei wird in einem iterativen Prozess die fehlende Phaseninformation der Beugungsdaten rekonstruiert, was es einem schliesslich erlaubt, die dreidimensionale Elektronendichte der untersuchten Struktur zu berechnen. Diese kann direkt als atomare Struktur interpretiert werden oder als Startpunkt für weitere Modelloptimierungen dienen.

Im Rahmen dieser Arbeit haben wir dünne $YBa_2Cu_3O_{7-x}$-Beschichtungen (YBCO) untersucht, die mittels gepulster Laserablation auf $SrTiO_3$ (STO), $(La_xSr_{1-x})(Al_yTa_{1-y})O_3$ (LSAT) und $NdGaO_3$ (NGO) Substraten gewachsen wurden. Mit einer Dicke von ungefähr 4 Einheitszellen entlang der c-Achse stellen diese Filme eines der komplexesten Systeme dar die bislang mit direkten Methoden und Oberflächenröntgenbeugung analysiert wurden. Damit eignen sie sich hervorragend um verschiedene Kombinationen von direkten Methoden und Strukturanalysemethoden zu testen, und deren jeweilige Vor- und Nachteile und allfällige Einschränkungen zu ermitteln. Der Grad der Übereinstimmung zwischen den verschiedenen Analysemethoden gibt zudem klare Hinweise zur Glaubwürdigkeit der individuell bestimmten Strukturen.

Die mit dieser Methode bestimmten Strukturen von YBCO auf STO und LSAT weisen eine grosse Änlichkeit mit der Festkörperstruktur von YBCO auf, vor allem was die interatomaren Abstände und Bindungswinkel betrifft. Der Einfluss der Substratstrukturen beschränkt sich fast ausschliesslich auf eine Dehnung der YBCO Einheitszelle in der Grenzflächenebene, so dass die Gitterparameter a und b denen des jeweiligen Substrates entsprechen. Diese heteroepitaktische Dehnung hat zwei wichtige Konsequenzen: (a) die YBCO Einheitszelle im Dünnfilm zeigt eine leichte Kontraktion entlang der c-Achse um knapp 1% im Vergleich zum ungedehnten Festkörper, und (b) eine Änderung der Symmetrie von orthorhombisch zu tetragonal, da die Gitterparameter a und b in beiden Substraten jeweils gleich sind. Diese Symmetrieänderung könnte weitreichende Folgen für die physikalischen Eigenschaften des Films haben, vor allem in Bezug auf die CuO Schichten, welche in der orthorhombischen Struktur eine starke Anisotropie aufweisen, da sich die Sauerstoffatome vorwiegend entlang der b-Achse anordnen und die sogenannten Kupferoxid-Ketten formen.

Die genaue Kenntnis der Filmstruktur ist von grosser Wichtigkeit für die Interpretation von oberflächensensitiven Messungen, zum Beispiel bei der winkelaufgelösten Photoemissionsspektroskopie, oder als Startpunkt für theoretische Berechnungen. Die Tatsache, dass die Filmstruktur derjenigen des Volumenkristalls von YBCO so ähnlich ist, lässt zudem hoffen, dass Messresultate der Filmeigenschaften direkt auf den Festkörper übertragbar sind.

Contents

Appendix

List of Figures

List of Tables

Chapter 1

Introduction

Complex transition metal oxides (TMOs) exhibit an astonishing wealth of physical phenomena and properties, making them both interesting from a fundamental point of view as well as for their technical applications. These compounds include ferroelectric, ferromagnetic, magnetoresistive, and multiferroic materials, and they can assume any conduction state from Mott or bandgap insulators, via semiconductors and semi-metals to high-temperature superconductors [1–6]. The quality and crystal perfection of today's state-of-the-art TMO materials are comparable, if not superior in some cases, to what can be achieved with semiconductors. This is demonstrated in an impressive manner in Figure 1.1, comparing the HRTEM images of a GaAs/AlAs and $PbTiO_3$/$SrTiO_3$ multilayer. Over and above that, the excellent chemical compatibility between many TMO materials not only allows for the specific tailoring of single properties via a controlled change of doping or of the stoichiometry, but opens up the opportunity to combine materials with either complementary, competing or even mutually incompatible characteristics into artificially assembled heterostructures. This has led to many surprising discoveries, as for example in the formation of a conducting layer at the interface between the two band-gap insulators $SrTiO_3$ (STO) and $LaAlO_3$ (LAO) [7], and the formation of the so-called improper ferroelectricity in multilayers of STO and $PbTiO_3$ [8].

The unusual effects observable in most TMOs are caused by a complex interplay between the many degrees of freedom in the form of spin, orbit, charge, and lattice interactions. The electronic interactions are very localized, usually involving strong correlations between the electrons on a few nearest-neighbor sites. For this reason, the theoretical description in terms of a free electron within an average field generated by the surrounding charges, as used in

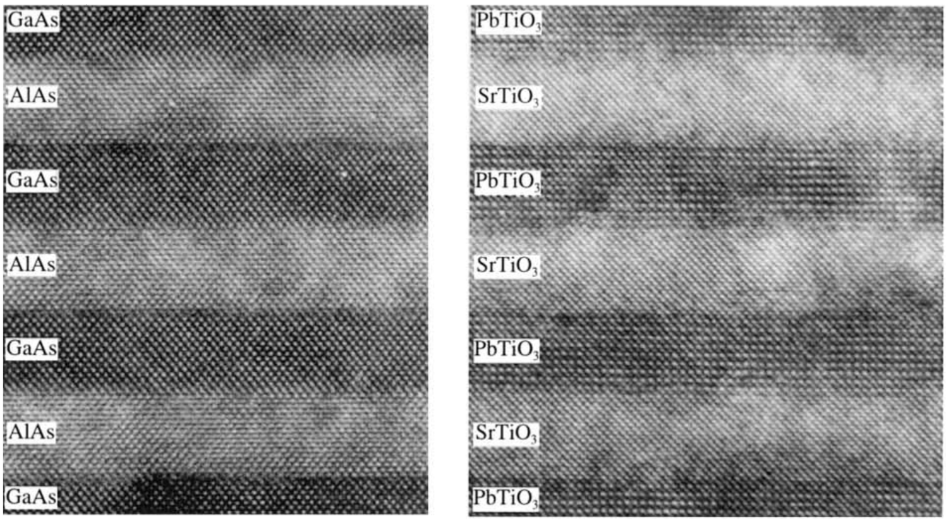

Figure 1.1: Comparison of high-resolution transmission electron microscopy (HRTEM) images of state-of-the-art GaAs/AlAs multilayers [9] (left) and a complex metal oxide $PbTiO_3/SrTiO_3$ multilayer [10] (right). From Ref. [11]. (Reprinted with permissions from [9], copyright 1995, Wiley-VCH Verlag GmbH & Co. KGaA, and from [10], copyright 1999, American Institute of Physics, and from [11], copyright 2008, IOP Publishing.)

mean field theories, breaks down for these *strongly correlated electron systems* (SCESs). More complicated models, such as the *Hubbard-Model*, aim to take both the electron mobility within the average field as well as the correlations with its nearest neighbors into account. Because of the strong interactions between electrons, subtle structural changes of the crystal lattice can cause large changes in the physical properties of SCESs [12]. Due to the many competing interaction between different degrees of freedom, however, a prediction of these changes from theory still fairly unreliable, and any information based on experiments is invaluable for the further development and improvement of the theoretical models.

The resolution required to detect the subtle structural changes in TMOs is certainly of the order of 0.01 Å, and naturally includes all three spatial directions. Due to the strong ionic bonding in TMOs, the distortions induced by, for example, the presence of defects, a surface, or an interface, propagate over significant distances of several unit cells. In many cases, this implies that the positions of up to a few hundred atoms need to be determined accurately.

To date, only surface x-ray diffraction (SXRD) is capable of fulfilling all of these demands simultaneously. Scanning probe techniques, like scanning tunneling microscopy (STM) and atomic force microscopy (AFM), provide very localized information, but lack a sufficient resolution as well as the ability to see below the surface layer. Transmission electron microscopy (TEM), on the other hand, does provide depth sensitive information, but also lacks the required resolution. Furthermore, it requires a mechanical thinning of the sample, thus destroying the specimen and precluding any in-situ experiments or other subsequent investigations. Low-energy electron-diffraction (LEED) has proved to be an invaluable tool in many structure determinations, and the achievable resolution comes close to what is required. The strong interactions of the electrons with the sample are a blessing in terms of the high scattering efficiency, but at the same time represent a major drawback of the technique, since dynamical scattering theory needs to be used to quantitatively analyze the diffraction patterns. In addition, the penetration depth into the sample is very small, and the investigation of buried layers more than a few atomic spacings from the surface becomes impossible. X-rays, on the other hand, interact very weakly with matter. This means that they can penetrate deeply into a sample, providing depth-sensitive information for thin films with thicknesses of several nanometers, and even reaching buried interfaces. Also, the much simpler kinematical diffraction theory can be applied for quantitative data analysis, and the ultimate resolution far exceeds that obtained with other diffraction techniques. The tradeoff lies in the exceedingly weak scattered intensities, requiring the use of synchrotron light for the measurements.

Probably, the most severe drawback of all scattering techniques is the fact that the investigated structures are not measured directly, but only through the diffraction pattern they generate. In the process of measuring the diffracted intensities, the information about the scattering phases are lost in the experiment, and a direct inversion of the diffraction pattern to yield the atomic structure is impossible. This is the well-known *phase problem* in crystallography.

Traditionally, this problem is circumvented by using model-refinement procedures, where the parameters of a structural starting model are adjusted such as to minimize the discrepancies, measured in terms of a so-called *figure of merit*, between the measured and calculated intensities. For increasingly large and complex systems, this approach is bound to fail, since the correct starting model may not be known *a priori*, and the simultaneous determination of hundreds of parameters represents a non-trivial computational problem. As an example, although the final structure of a five unit cell LAO film grown on top of an STO substrate “looks” bulk-like, if one begins the refinement procedure with the atoms placed at their bulk positions, the refinement procedure failed to find a physically reasonable solution [13].

There is, therefore, a strong need for an alternative to model-based refinement techniques as the first steps in structure solution. Ideally, the full information contained in the diffraction pattern should be used directly to produce the most complete possible structure representation without the need to include any detailed knowledge about the atomic arrangements. This step can be achieved by the use of *direct methods*, which have been successfully applied to SXRD [14–17] over the past few years. Based only on generic *a priori* knowledge of the system (for example, the fact that the electron density should be positive) and the measured diffraction intensities, the corresponding phases can be reconstructed using iterative procedures, allowing for a direct reconstruction of the electron density in real space. This electron density map may either be interpreted directly or can be used as a starting model for a subsequent model refinement. In the LAO-STO example discussed above, only by using the atomic positions extracted from the electron density map generated by the COBRA direct method, model-fitting led to a successful structure solution [13].

The exact prerequisites for a successful structure determination, both with regards to refinement procedures and direct methods, are an open question. Indisputably, the quality of the diffraction data plays a crucial role. Of almost equal importance, at least for the direct methods, may be the number of independent structure factor measurements, as each data point adds to the overall information available about the system. The advent of the PILATUS x-ray pixel detectors [18], offering single-photon counting technology with a high dynamic range, short readout times and zero readout-noise, has revolutionized SXRD data acquisition, both in terms of speed and reliability [19]. In order to exploit the full potential of the PILATUS detectors, developing a detailed understanding of how the measurement processes need to be adapted to this new technology is absolutely essential. Only under those circumstances can the acquisition procedures be optimized, and any differences with regard to the traditionally used detection schemes may be evaluated judiciously.

Relying purely on *a priori* information and the measured diffraction data, direct methods greatly benefit from every available experimental piece of information. This is especially true for the absolute scaling of the measured diffraction intensities, as it directly contains the knowledge about the number of electrons involved in the scattering process, and thereby the correct scaling of the electron density to be retrieved. Furthermore, it determines the contribution of the scattering from the unknown structure at the surface or interface with respect to that from the known bulk structure of the sample. However, obtaining the proper normalization of the measured reflections is difficult experimentally. For this reason, the vast majority of SXRD studies to date has relied on measuring relative intensities, and fitting a corresponding scale factor to the data set. Thanks to the high-quality diffraction data recorded with the PILATUS pixel detector, the appropriate normalization may be more readily obtained, and first attempts have been made to achieve this.

In order to investigate, for a given data set, the best way of retrieving a structural solution and the reliability thereof, it is necessary to perform systematic tests involving different combinations of techniques. From the range of emerging solutions, the stable and reproducible structural features may be inferred by comparison and a measure of error may be deduced. This may help to establish a better understanding of the capabilities of the technique as a whole, and of its sensitivity to certain features of interest for a particular system under investigation.

The structure of $YBa_2Cu_3O_{7\text{-x}}$ (YBCO) films with thicknesses of a few unit cells is interesting both from a fundamental point of view as well as for the material's use in technical applications. Heteroepitaxial growth of YBCO on various substrate materials might induce different structural distortions, possibly leading to new and unexpected physical properties. For example, it has been shown that the superconducting transition temperature of thin films can be drastically enhanced due to strain effects [20]. Several other interesting questions concern the minimum thickness required to observe superconductivity (is it possible to have a single superconducting layer?), the effects of the tetragonal distortion of the nominally orthorhombic YBCO unit cell, induced by cubic and tetragonal substrates, on the preferential ordering of the oxygens in the Cu-O chains, the possibility of oxygen vacancy ordering, and so on. For other surface-sensitive techniques, in particular for angle-resolved photoemission spectroscopy (ARPES), the arrangements in the topmost atomic layers are of special importance, in order to decide whether the observed effects can be attributed to the relevant bulk properties of the materials, or whether one is in fact observing a surface-specific phenomenon.

The growth substrates selected for this study are $SrTiO_3$ (STO), $NdGaO_3$ (NGO), and $(La_xSr_{1\text{-x}})(Al_yTa_{1\text{-y}})O_3$ (LSAT), each of them having a different lattice match, and thus a different interfacial strain, with YBCO, and a particular symmetry of their surface unit cell.

Owing to the relatively large unit cell of YBCO, the number of atoms involved in a structure determination is large and can easily reach 100 individual atoms. The solution of such a system, therefore, represents a major challenge for direct methods and a nearly impossible task for the use of traditional refinement procedures without the availability of complementary information. This makes it an ideal testbed for investigating the current capabilities and limitations of these techniques in a "real case" scenario rather than in comparison to generated test data.

The outline of this thesis is as follows: We begin with a qualitative introduction about the principles of surface x-ray diffraction and a description of the experimental setup in Chapter 2, followed by a general discussion of *direct methods*, including their specific adaptation to SXRD and two examples of the particular algorithms used in this work in Chapter 3. The preparation and initial characterization of YBCO thin films grown on different substrate materials is detailed in Chapter 4. This is followed by a very detailed account of the attempted structure solutions, using different combinations of direct methods and refinement algorithms in order to combine their strengths and to evaluate their relative merits for two test systems of YBCO on STO (Chapter 5) and YBCO on LSAT (Chapter 6). Finally, we turn to a critical discussion of the achieved results, in terms of their present limitations and their implications for the improvements necessary for future projects in Chapter 8. Most of the technical details concerning the measurement of accurate SXRD data using the novel PILATUS 100k pixel detectors, the precise procedures for data treatment and corrections, and the necessary angle calculations for controlling the diffractometer are deferred to the appendices, along with a more rigorous and quantitative derivation of the scattered intensities measured in a diffraction experiment. Although very technical in nature, the content of these appendices represents a major part of the work performed in this thesis, and is a prerequisite for turning to the fascinating physical questions and phenomena that can be investigated with the unique qualities of surface x-ray diffraction.

Bibliography

[1] J. G. Bednorz and K. A. Müller: "Possible high T$_c$ superconductivity in the Ba-La-Cu-O system." *Z. Phys. B: Condens. Matter.* **64**(2), 189–193 (1986), doi:10.1007/BF01303701.

[2] S. Jin, T. Tiefel, M. McCormack, R. Fastnacht, R. Ramesh, and L. Chen: "Thousandfold Change in Resistivity in Magnetoresistive La-Ca-Mn-O Films." *Science* **264**(5157), 413 (1994), doi:10.1126/science.264.5157.413.

[3] M. B. Salamon and M. Jaime: "The physics of manganites: Structure and transport." *Rev. Mod. Phys.* **73**(3), 583–628 (2001), doi:10.1103/RevModPhys.73.583.

[4] C. Ahn, K. Rabe, and J.-M. Triscone: "Ferroelectricity at the Nanoscale: Local Polarization in Oxide Thin Films and Heterostructures." *Science* **303**(5657), 488 (2004), doi:10.1126/science.1092508.

[5] D. Fong, G. Stephenson, S. Streiffer, J. Eastman, O. Auciello, P. Fuoss, and C. Thompson: “Ferroelectricity in Ultrathin Perovskite Films.” *Science* **304**(5677), 1650 (2004), doi: 10.1126/science.1098252.

[6] M. Dawber, K. M. Rabe, and J. F. Scott: “Physics of thin-film ferroelectric oxides.” *Rev. Mod. Phys.* **77**(4), 1083–1130 (2005), doi:10.1103/RevModPhys.77.1083.

[7] A. Ohtomo and H. Y. Hwang: “A high-mobility electron gas at the $LaAlO_3/SrTiO_3$ heterointerface.” *Nature* **427**(6973), 423 (2004), doi:10.1038/nature02308.

[8] E. Bousquet, M. Dawber, N. Stucki, C. Lichtensteiger, P. Hermet, S. Gariglio, J.-M. Triscone, and P. Ghosez: “Improper ferroelectricity in perovskite oxide artificial superlattices.” *Nature* **452**(7188), 732–736 (2008), doi:10.1038/nature06817.

[9] A. K. Gutakovskii, L. I. Fedina, and A. L. Aseev: “High resolution electron microscopy of semiconductor interfaces.” *Phys. Status Solidi A* **150**(1), 127–140 (1995), doi:10.1002/pssa.2211500111.

[10] J. C. Jiang, X. Q. Pan, W. Tian, C. D. Theis, and D. G. Schlom: “Abrupt $PbTiO_3/SrTiO_3$ superlattices grown by reactive molecular beam epitaxy.” *Appl. Phys. Lett.* **74**(19), 2851 (1999), doi:10.1063/1.124035.

[11] S. A. Pauli and P. R. Willmott: “Conducting interfaces between polar and non-polar insulating perovskites.” *J. Phys.: Condens. Matter* **20**(26), 264012 (2008), doi:10.1088/0953-8984/20/26/264012.

[12] Y. Tokura: “Correlated-Electron Physics in Transition-Metal Oxides.” *Phys. Today* **56**(7), 50–55 (2003), doi:10.1063/1.1603080.

[13] P. R. Willmott, S. A. Pauli, R. Herger, C. M. Schlepütz, D. Martoccia, B. D. Patterson, B. Delley, R. Clarke, D. P. Kumah, C. N. Cionca, and Y. Yacoby: “Structural basis for the conducting interface between $LaAlO_3$ and $SrTiO_3$.” *Phys. Rev. Lett.* **99**, 155502 (2007), doi: 10.1103/PhysRevLett.99.155502.

[14] Y. Yacoby, R. Pindak, R. MacHarrie, L. Pfeiffer, L. E. Berman, and R. Clarke: “Direct structure determination of systems with two-dimensional periodicity.” *J. Phys.: Condens. Matter* **12**(17), 3929–3938 (2000), doi:10.1088/0953-8984/12/17/301.

[15] D. K. Saldin, R. J. Harder, V. L. Shneerson, and W. Moritz: “Phase retrieval methods for surface x-ray diffraction.” *J. Phys.: Condens. Matter* **13**(47), 10689–10707 (2001), doi:10.1088/0953-8984/13/47/311.

[16] L. D. Marks, N. Erdman, and A. Subramanian: “Crystallographic direct methods for surfaces.” *J. Phys.: Condens. Matter* **13**, 10677 (2001), doi:10.1088/0953-8984/13/47/310.

[17] M. Björck, C. M. Schlepütz, S. A. Pauli, D. Martoccia, R. Herger, and P. R. Willmott: "Atomic imaging of thin films with surface x-ray diffraction: introducing DCAF." *J. Phys.: Condens. Matter* **20**(44), 445006 (2008), doi:10.1088/0953-8984/20/44/445006.

[18] A. Bergamaschi, Ch. Brönnimann, E. F. Eikenberry, B. Henrich, M. Kobas, P. Kraft, and B. Schmitt: "Experience and Results from the 6 Megapixel PILATUS System." *PoS* **057**, 049 (2007).

[19] C. M. Schlepütz, R. Herger, P. R. Willmott, B. D. Patterson, O. Bunk, Ch. Brönnimann, B. Henrich, G. Hülsen, and E. F. Eikenberry: "Improved data acquisition in grazing-incidence X-ray scattering experiments using a pixel detector." *Acta Crystallogr. A* **61**, 418–425 (2005), doi: 10.1107/S0108767305014790.

[20] J.-P. Locquet, J. Perret, J. Fompeyrine, E. Mächler, J. W. Seo, and G. V. Tendeloo: "Doubling the critical temperature of $La_{1.9}Sr_{0.1}CuO_4$ using epitaxial strain." *Nature* **394**(6692), 453 (1998), doi:10.1038/28810.

Chapter 2

Surface X-ray Diffraction

2.1 Introduction

Though initially often regarded a curiosity, the discovery of x-rays by Wilhelm Conrad Röntgen [1] in 1895 marked the arrival of a new research tool that would revolutionize our understanding of matter and its internal structure. Quickly, the "new rays" became a topic of huge interest and one of the most important experimental probes. Their application in medical diagnosis was swift. It was not until a few years later, though, that von Laue had the insight to use them as a probe for the internal structure of crystals. Together with Friedrich and Knipping, he published the first crystal x-ray diffraction images of a zinkblende (ZnS) crystal [2]. This initiated a rapid development of the technique. One of the most important contributions to explain the observed diffraction patterns was that of the father-and-son team William Henry Bragg and William Lawrence Bragg, who connected the scattered signals with reflections from evenly spaced planes of atoms in a crystal to formulate the well-known Bragg law [3, 4]. These events laid the foundation for a new and powerful technique for the structure determination on an atomic scale: x-ray diffraction (XRD).

Today, state-of-the-art single-crystal or powder XRD measurements on small molecules can determine the interatomic distances with a precision down to a few thousandths of an Angstrom, and a few tenths of degrees for the bond angles. In macromolecular crystallography, even the structure of viruses, containing hundreds of thousands of atoms, has been solved, albeit at a reduced spatial resolution.

The applicability of x-rays to study the atomic structures of surfaces has been hampered by the very low signal intensities obtained from an essentially 2-dimensional diffraction volume. It was not until the advent of dedicated synchrotron sources, providing well collimated x-ray beams of high intensities, that the investigation of surface structures became feasible. Low-energy electron-diffraction (LEED), on the other hand, had long ago established itself as a routine method to investigate surfaces, primarily due to the very strong interactions of electrons with matter making them exceedingly surface sensitive. But at the same time, the surface sensitivity of LEED proved to be also one of its most severe drawbacks: due to the strong interactions, multiple scattering effects severely complicate a quantitative interpretation of the scattering data. Not so for the very weakly scattering x-rays: Once the problem of the weak intensities is overcome, data analysis in the *kinematical approximation* is fairly straightforward from a theoretical point of view.

The potential of x-rays to provide valuable information about surfaces was first demonstrated by two pioneering experiments by Marra, Eisenberger and Cho [5] in 1979, and Eisenberger and Marra [6] in 1981. In 1983, Robinson was able to resolve a long-standing controversy regarding the (1×2) reconstruction of the Au(110) surface [7], for which several models existed. These experiments paved the way for a new branch of x-ray crystallography, namely that of *surface x-ray diffraction* (SXRD) [8–11].

Apart from the simplicity of their theoretical treatment, the use of x-rays to study surfaces has several other advantages. Firstly, x-rays can easily pass through appropriate sample containers and are largely unaffected by the presence of gases. This eliminates the need for UHV conditions commonly encountered for other probes such as electrons, and makes studies at ambient or even high pressure conditions feasible[1]. Secondly, the high penetration power of x-rays allows for the investigation of buried layers of material or interfaces deep within a sample.

First, we will give a brief and pictorial description of some scattering fundamentals, both for the case of single crystals and crystal surfaces, before we turn to the somewhat more practical aspects of measuring SXRD data in the second part of this chapter.

---

[1] It should be noted, however, that the surface itself might be affected by ambient gases, and also that radiation damage of the surface can be exacerbated by, e.g., oxygen radicals formed by absorption of x-rays by surface adsorbates.

2.2 SXRD theory

In this section we shall review some basic principles of x-ray diffraction in general, and surface x-ray diffraction in particular, in a rather qualitative manner. It is by no means intended to be a comprehensive account of these techniques. The objective is, rather, to provide the reader with some essential concepts needed to follow the arguments made in this thesis. A somewhat more comprehensive and formal treatment of selected elements of scattering theory is deferred to Appendix A. There, a list of helpful literature and further references can also be found.

The arguments in this chapter are centered around the fact that the diffraction pattern of a given crystal structure is proportional to the square modulus of the Fourier transform of its electron density distribution. With the aid of the convolution theorem, it is then possible to deduce some qualitative aspects of the diffraction pattern obtained from bulk crystals and crystal surfaces.

2.2.1 The convolution theorem

The *convolution* of two functions $f(x)$ and $g(x)$ is denoted by the operator symbol $\otimes$ and defined as

$$(f \otimes g)(x) \equiv \int_{-\infty}^{\infty} f(x') \cdot g(x - x')\, dx'. \tag{2.1}$$

Figure 2.1 (a) gives a graphical example of the operation. In simple terms, the convolution (sometimes also called “folding”) operation “slides” the function $g(x')$ over the “stationary” $f(x')$, taking on the value of the integrated area of the product of both functions for each sliding position x. If one of the functions, say $f(x')$, is a δ-function, the convolution has the shape of $g(x')$ centered at the position of $f(x')$, as shown in Figure 2.1 (b).

The *convolution theorem* now states that the Fourier transform of the product of two functions f and g is equal to the convolution of the Fourier transforms of the individual functions:

$$\mathcal{F}(f \cdot g) = \mathcal{F}(f) \otimes \mathcal{F}(g). \tag{2.2}$$

Using this theorem, we will try to explain some qualitative aspects of diffraction theory in the following paragraphs.

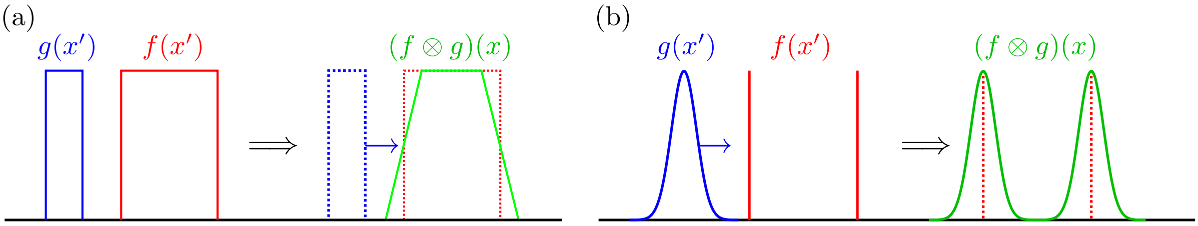

Figure 2.1: The convolution of two functions f and g. (a) The convolution operation "slides" $g(x')$ across $f(x')$, plotting the integral of their product for each sliding position x. (b) If $f(x')$ is a set of δ-functions and $g(x')$ some shape function, the convolution results in a set of shape functions at the positions given by the δ-functions.

2.2.2 Scattering from a bulk crystal

An ideal bulk crystal consists of an infinite and periodic repetition of identical building blocks, the crystal's *unit cell*. The crystal structure can be described in terms of a *basis*, which is everything the unit cell contains, and a *crystal lattice* or *Bravais lattice*, which is a mathematical construct defining all the points in space to which such a basis is attached (sometimes called a "comb" function). For the sake of simplicity, let us assume for now that we are looking at a basis which contains just one single atom.

X-rays with energies in the keV range only interact very weakly with matter. This is in stark contrast to the scattering of electrons, for example, and allows for a much simpler description of the scattering processes. In the *kinematical approximation*, it is assumed that the incoming x-rays are scattered only once, that their scattering is elastic, and that no interaction between the incoming and scattered beams occurs. Within this approximation, the scattering of x-rays from a crystal can be essentially described in terms of the Huygens principle. Each electron (or atom) represents a scattering center which emits a secondary spherical wave when excited by the incoming plane wave field. Only if the secondary waves of all emitters are in phase do their amplitudes add up constructively to produce a total outgoing wave with a high intensity. This is the origin of the Bragg peaks, and the set of all wavevectors corresponding to such Bragg peaks makes up a discrete regular grid in momentum space, called the *reciprocal lattice* of the crystal. Very importantly, this grid is equal to the Fourier transform of the real space crystal lattice[2]. In fact, the distribution of the (complex) scattering amplitudes in momentum

---

[2] In the case of several atoms per unit cell, the points of constructive interference can also be present only on a subset of the reciprocal lattice, as so-called "extinction rules", due to internal symmetries of the unit cell, can

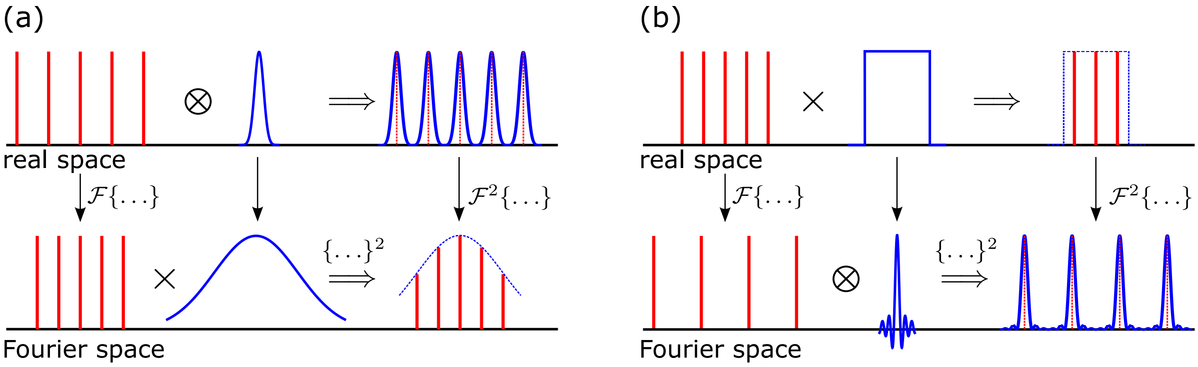

Figure 2.2: Application of the convolution theorem to visualize the correlations between real space structure and the corresponding diffraction pattern. (a) An atomic charge distribution of finite width around each atom position causes the diffraction pattern to fall off in intensity. (b) Peak broadening and intensity fringes on the Bragg peaks are caused by a finite crystal size.

or reciprocal space is equal to the Fourier transform of the entire electron distribution inside the crystal. This point will now allow us to use the convolution theorem to illustrate some properties of the diffraction pattern of a crystal. It is important to keep in mind, however, that the (real) intensities measured in a diffraction experiment are proportional to the squared moduli of the scattered amplitudes.

We can think of the electronic distribution inside the crystal as a convolution of the crystal lattice with the electron density of the basis. This is shown graphically for a 1-dimensional case in Figure 2.2 (a). Using the convolution theorem, the diffraction pattern must therefore be equal to the product of the Fourier transforms of the crystal lattice and of the electron distribution inside the unit cell. The former is just the reciprocal lattice (a set of δ-functions), while the latter is some continuous function in momentum space which falls off towards higher momentum values. The result is that the scattered intensities (which are proportional to the square of this product) must on average fall off with increasing momentum transfer.

The effect of a finite crystal size can also be examined easily using this principle. Starting from an infinite lattice in real space, we construct a finite crystal by multiplying the lattice with a window function having the size of the crystal, again shown for a 1-dimensional case in Figure 2.2 (b). The diffraction pattern is now given by the square of the convolution of the reciprocal space lattice with the Fourier transform of the window function. The result is that

---

result in a complete destructive interference on the rest of the points. Also in this case, the reciprocal lattice is still the Fourier transform of the real space lattice, though.

each Bragg peak in reciprocal space is broadened and decorated with intensity oscillations to both sides, which are sometimes called finite size fringes. The widths of a Bragg peak and the spacing of the fringes can therefore give direct information about the size of the diffracting structure. For any crystal larger than only a few unit cells in each direction, however, the Bragg peaks become very narrow, and no signal intensity between the peaks can normally be measured (ignoring any background for now). This situation will change drastically, however, for crystals with well-defined and sharp surfaces, as we shall see in the next section.

2.2.3 Scattering from surfaces

When considering a crystal with a surface, the idealized model of an infinite repetition of unit cell building blocks in all three directions of space breaks down. In a direction perpendicular to the surface, which we will call the z-direction, the structure of the crystal is no longer periodic, and the symmetry is broken. Simply considering the fact that we are now dealing with a non-periodic structure in the out-of-plane direction z means that its Fourier transform along this direction cannot be discrete any longer, and hence its diffraction pattern must be continuous. The qualitative shape of the intensity distribution can again be visualized through the convolution theorem. Look at Figure 2.3. In real space, the crystal's surface is produced through a truncation of the infinite and ideal crystal lattice by multiplying it with the step function along the z-direction. The Fourier transform of this abrupt step is a shape function with a $1/q_z$-dependence. The diffraction pattern is therefore equal to the square of the convolution of the ideal diffraction pattern, consisting of sharp Bragg peaks, with the shape function. The result is a "smearing" of the Bragg peaks into streaks of intensity perpendicular to the surface. If the streaks happen to fall directly onto a line of Bragg peaks (as is normally the case for a surface which is cut along one of the crystal planes), they overlap to form continuous rods, the so-called crystal truncation rods (CTRs).

The intensity variation along the CTR close to the Bragg peak, where there is no significant overlap between the streaks from neighboring peaks, is given by the $1/q_z$ shape function and therefore goes with $1/(\Delta q_z)^2$ where Δq_z is the reciprocal space distance away from the Bragg peak.

So far, we have assumed an absolutely perfect and infinitely sharp truncation at the surface, mathematically expressed as a step function. This is, of course, an idealized picture, and usually there is a broader transition due to surface roughness, some of the outermost electrons

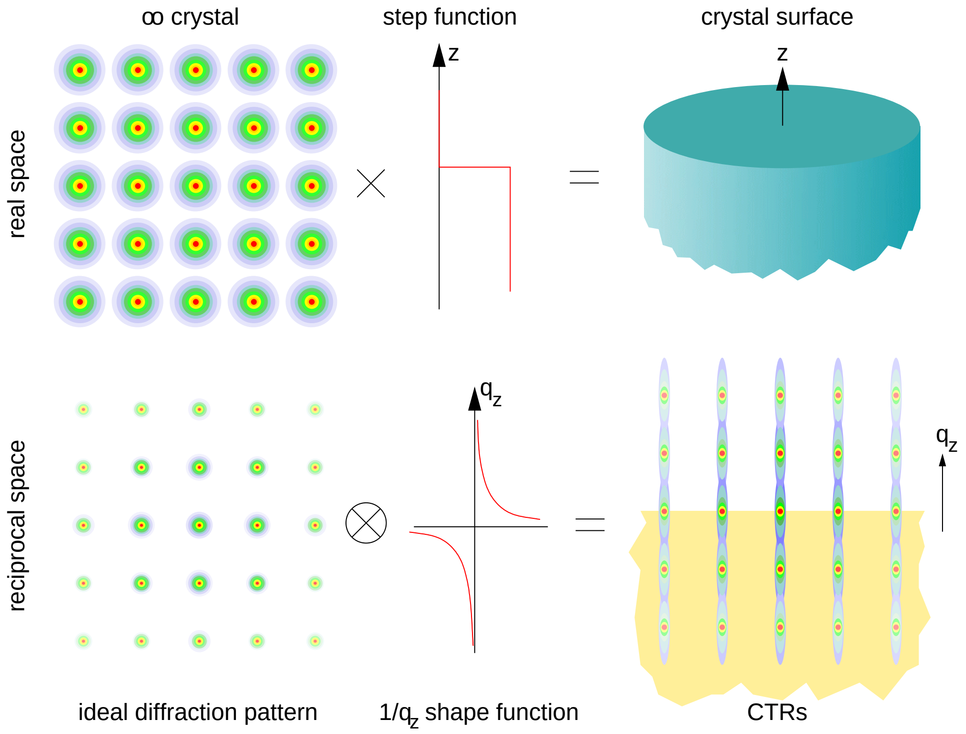

Figure 2.3: The origin of the crystal truncation rods (CTRs), as explained by the convolution theorem.

in dangling bonds extending further into the vacuum, or other similar effects. This means that we have to multiply the perfect crystal by a broadened truncation function in real space, which will result in a narrower shape function in reciprocal space and causes the intensity on the CTRs to fall off more rapidly around the Bragg peaks. A comparison between an ideal CTR and one for a broadened crystal truncation function is shown in Figure 2.4.

Up to this point, our crystal surface is a more or less abrupt truncation of a bulk crystal. We have not allowed any atoms to move in response to the loss of their neighbors on the vacuum side in any way. Physically, such an unperturbed behaviour seems very improbable. A much more likely scenario would be the formation of a thin surface layer, where the atomic structure is different from deep within the bulk. In fact, the whole purpose of SXRD it is exactly the determination of these changes with regard to the usually known crystal structure.

Trying to visualize the changes to the shapes of the CTRs when atoms are displaced from their bulk positions by using the convolution theorem is no longer straightforward. But simply by considering Huygens principle, it is obvious that a change is to be expected. Due to the now

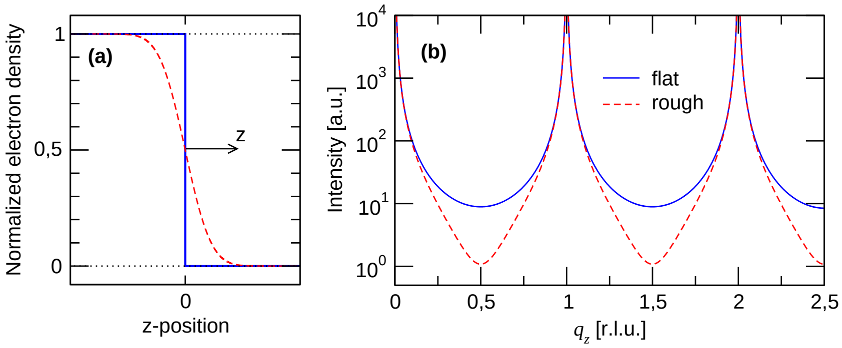

Figure 2.4: Influence of surface roughness on the shape of CTRs. (a) Normalized electron density profiles along the out-of-plane z-direction for a perfectly flat crystal surface (blue solid line) and a broadened truncation function (red dashed line). (b) The corresponding CTR profiles show that the intensity falls off more rapidly for the rough surface and has a much reduced intensity between the Bragg peaks compared to an ideally flat surface.

different orientation of a displaced atom with respect to all the others, a shift in the relative phase of its scattered secondary wave occurs and changes the overall interference pattern of the structure. The corresponding calculations are detailed in Appendix A. It remains to be demonstrated that such a shift produces any significant and measurable effect on the CTRs. Figure 2.5 (a) shows simulated CTR data for a structure where just the topmost atomic layer is allowed to relax along the out-of-plane direction by up to ±10% of a unit cell spacing. The resulting changes are dramatic, and the reason for that is simple: In between the Bragg peaks, the contributions from all bulk atoms interfere destructively, and it is the small deviations away from the complete destructive interference which dominate the diffraction signal.

2.2.4 Adding a thin film on top of the substrate

Many fundamentally and technologically interesting systems consist of very thin films of functional materials deposited on top of a suitable growth substrate. Also in this case, SXRD is ideally suited to determine the atomic structure of the entire system across the film-substrate interface, as long as the film maintains a well-defined epitaxial relationship with the substrate, meaning that the film unit cell fits exactly onto a substrate unit cell in the in-plane directions[3].

---

[3] In principle, any combination of n film unit cells on m substrate unit cells is allowed, where n and m are integer numbers. However, in order to solve such superstructures, n and m should be small numbers.

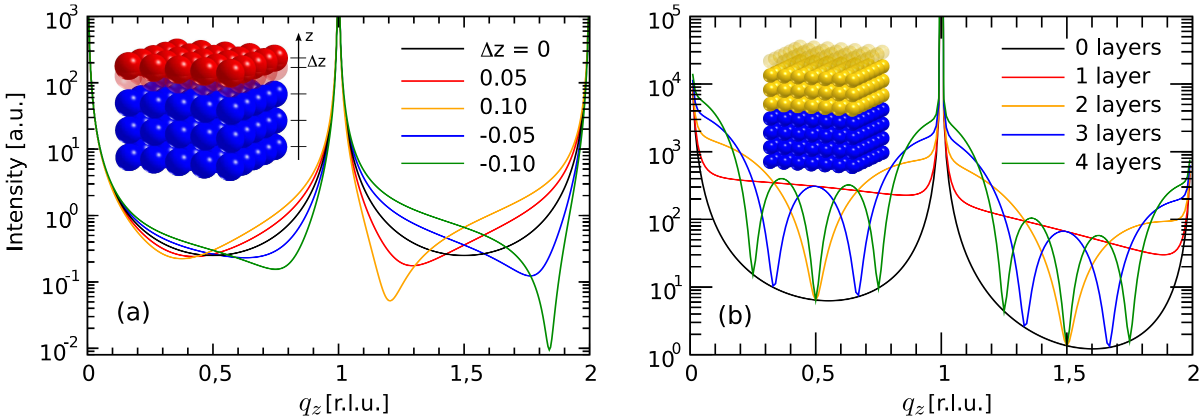

Figure 2.5: Examples for the sensitivity of a CTR intensity profile to structural changes. (a) A displacement of the topmost atomic layer along the *z*-direction results in a distinct skewness of the intensity profile in between Bragg peaks. (b) Adding atomic layers of a different material on top of a bulk crystal causes the characteristic thickness fringes to appear on the CTRs. In the case shown here, the density of the film layer has been chosen to be larger than that of the substrate, $\rho_{\text{film}} > \rho_{\text{subs}}$.

A striking effect occurs if the film layer has a different average electron density than the substrate. The vacuum–film and film–substrate interfaces represent two boundaries between media of differing optical densities. At each interface, one observes reflection and refraction of the incoming wave, which can again interfere with each other. The phase difference between the interfering waves is a function of the scattering vector, and changes continuously between constructive and destructive interference, which results is a distinct beating pattern on the CTRs. The fringe spacing depends on the thickness d of the film layer and decreases inverse proportionally with increasing d. An example of this is shown in Figure 2.5 (b), where a CTR has been simulated for a thin gold film with a varying number of atomic layers on top of a Cu-crystal. Obviously, one can obtain direct information on the film thickness from the spacing of these so-called finite-size fringes or Laue oscillations.

In conclusion, we have explained the origin of CTRs based on a simple argument involving the convolution theorem, and demonstrated their sensitivity to structural changes in the surface region or the presence of thin films on top of a substrate. In the following, we shall briefly discuss the experimental aspects of SXRD and show how CTRs can be measured.

2.3 SXRD experiments

SXRD experiments have been carried out at the Surface Diffraction Station of the Materials Science Beamline X04SA at the Swiss Light Source (SLS), Paul Scherrer Institut, Villigen, Switzerland. The beamline design has been described in detail elsewhere [12, 13]. In brief, x-rays between 5 and 40 keV are produced by a small-gap (8 mm) wiggler. The optics consist of a mirror – monochromator – mirror setup. The first mirror is used to collimate the x-ray beam in the vertical plane, and to adjust the vertical beam position going into the Si(111) double crystal monochromator ($\Delta E/E \sim 1.5 \times 10^{-4}$), whose first crystal must be cooled to absorb the heat load. A variable horizontal focussing of the beam can be achieved through a sagittal bending of the second crystal. Finally, the second mirror can be both tilted to adjust the outgoing beam height and bent to control the vertical focus of the x-ray beam.

2.3.1 The Surface Diffraction station

Although suited for a wide variety of diffraction experiments, the Surface Diffraction station has been designed and optimized specifically for SXRD measurements at grazing incidence angles. At the heart of the station, a large (2+3)-type diffractometer [14] (Newport Microcontrols) provides the possibility to mount a large variety of different sample environments and heavy sample chambers [15, 16]. Two configurations of the diffractometer allow for the sample surface to be oriented either horizontally ("horizontal" geometry, sample surface normal in vertical direction) or vertically ("vertical" geometry, sample surface normal is oriented in the horizontal plane). Two sample and three detector circles can be moved independently and give access to a large range of reciprocal space, both for parallel and perpendicular scattering vectors with respect to the sample surface.

The use of a PILATUS 100k pixel detector has revolutionized the way to record diffraction data and greatly improved the reliability and speed of SXRD experiments [17]. For this reason, we shall discuss detector issues in more detail in the following section.

2.3.2 Detectors

Detector requirements for SXRD experiments are predominantly dictated by the large variations in intensities to be recorded. In order to deal with the signals spanning several orders of magnitude in intensity, a large detector dynamic range is needed, in conjunction with excellent linearity. For strong signals, the maximum count rate, which is essentially given by the detector's dead time, should be high. On the other hand, low signal intensities between the strong Bragg peaks usually require long exposure periods, which strongly limit the acceptable amount of readout noise in the data and require a good detector stability. Unless one is interested in time-resolved experiments, the readout time of the detector does not play an important role, as long as it remains comparable to the overall dead time between exposures given by diffractometer movements and other control issues. Since the elastic scattering from a monochromatic source is measured, there is no need for any energy resolution in principle, even though a simple energy discrimination can be very advantageous, as will be shown later. Finally, the spatial or angular resolution requirements are modest for standard scans, and can be improved by using additional optical components like Soller slits or crystal analyzers, if necessary.

Traditionally, most SXRD setups employ point detectors. Apart from providing the aforementioned features, they are simple to operate, require only minimal cabling and are very light weight, thus reducing the load on the diffractometers and facilitating high-precision movements. Collimating slits provide the means to adjust the detectors angular acceptance or the active scattering source size, thereby controlling the reciprocal space resolution. Obviously, each measurement provides one single intensity measurement, so it is necessary to scan either the detector position or the sample orientation for a given set of detector angles, in order to record meaningful diffraction features, including the background signal in so-called *rocking scans*.

Doubtlessly, an extended “peripheral” vision as granted by area detectors will greatly enhance the amount of information to be gained from a single measurement. Despite this obvious realization, it was not until recently that 2D-detectors have been routinely used in SXRD experiments [17].

The use of CCD area detectors in SXRD has been limited due to the difficulty of obtaining high-quality data. Firstly, their relatively small dynamic range compared to a point detector renders it difficult to simultaneously record strong and weak diffraction features in a single frame. Secondly, dark currents and readout noise hamper the detection of the typically very weak SXRD signals. Long exposures cannot remedy this problem, since the noise build-up continues in parallel to the acquisition of the true diffraction signal. Moreover, the relatively large point-spread functions of CCD detectors smear out sharp diffraction features. Another inconvenience is caused by the indirect detection of x-rays via the conversion to electrons whose charge is integrated in each pixel. The measured intensity values must thus be converted back to the number of x-rays, introducing another statistical uncertainty and making careful calibrations necessary. Finally, the relatively long readout times prohibit fast and efficient measurements of sufficiently strong signals or, indeed, time-resolved experiments of processes in the sub-second time-domain, an example of which could be the evolution of diffraction signals during the growth of thin films. Today's state-of-the-art CCDs have made considerable advances in dealing with these issues, but still their use in SXRD is rare as other alternative technologies have in the meantime become available.

The PILATUS pixel detectors have been developed at the Paul Scherrer Institut specifically to meet the stringent requirements of high-resolution protein crystallography [18, 19]. The basic entities of the PILATUS detectors are modules with an active area of 83.8×33.5 mm^2, consisting of a single monolithic silicon sensor bump-bonded to an array of 8×2 CMOS readout chips, comprising a total of $487\times195 = 94\,965$ pixels with 172×172 μm^2 pitch. Large-area detectors can be assembled by combining several modules, leading to a great flexibility of the achievable geometries, which can, in principle, be tailored to the particular need of an experiment. Single-photon counting technology results in a direct conversion from x-rays to counts and is absolutely noise-free (no leakage currents, readout noise, etc.). Each individual pixel is connected to a 20-bit counter, yielding a dynamic range of $2^{20} \approx 10^6$. Depending on the particular choice of gain setting, counter dead times ranging from 100 to 400 ns allow for maximum count rates of up to 2×10^6 photons/second/pixel. The readout time for the entire module is approximately 3.6 ms and frame rates up to 200 Hz can be achieved for single module detectors. The quantum efficiency of the 320 μm thick silicon sensors is optimal for experiments in the energy range from 3 to 15 keV, however the detector can be used up to energies of 40 keV with reasonable efficiencies for many experiments.

X-rays impinging on the silicon sensor are absorbed inside the material, thereby creating a charge cloud, which can be collected in the read out electronics by applying an electric field across the sensor. The amplitude of the collected charge pulse is related to the energy of the absorbed photon. The counter is incremented only for charge pulses exceeding a given threshold, while pulses remaining below this limit are not counted. This can be used to a great advantage in many experiments. By adjusting the threshold level carefully, it is possible to discriminate between elastically and inelastically scattered x-rays, providing an efficient filter

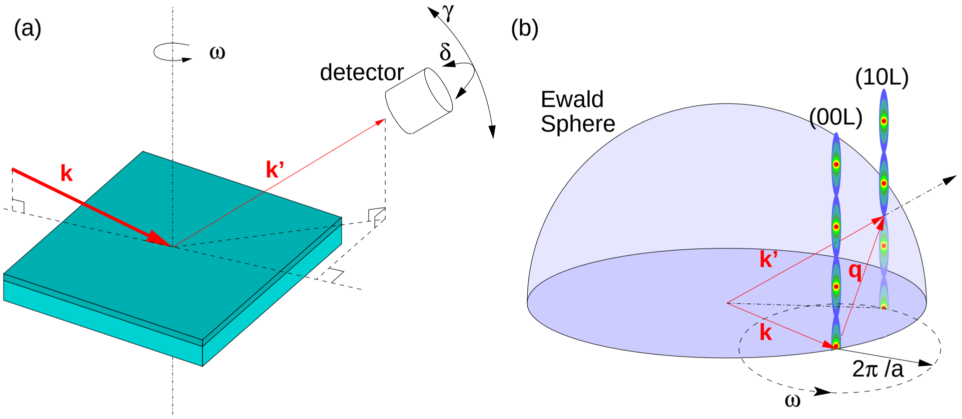

Figure 2.6: Principle and geometry of an SXRD measurement (a) in real space, and (b) in reciprocal space.

to suppress fluorescence background signals.

All experiments in the framework of this thesis have been performed using a PILATUS 100k single module detector. Further details and information about the PILATUS detectors can be found in Appendix D or in the literature [18–21].

Despite the obvious advantages of using area detectors, it should be kept in mind that some of their benefits may become unavailable under certain circumstances. Whenever high-resolution scans are required, for example, the use of secondary optical components such as slits or crystal analyzers will limit the applicability of the peripheral vision.

2.3.3 Measurements

Typically, surface sensitive diffraction measurements are carried out at very small incident beam angles with respect to the sample surface, either just below the critical angle (α_c) for total external reflection or slightly above it. This limits the amount of diffuse scattering from the bulk of the sample, since the x-rays penetration depth is small at grazing angles. When studying buried interfaces, on the other hand, care has to taken that the x-ray can actually penetrate far enough into the sample.

To record intensities on the crystal truncation rods, the detector and sample need to be positioned such that the diffraction condition for the particular point in reciprocal space to be measured is fulfilled. The challenge lies in correlating the reciprocal space coordinates with the corresponding diffractometer positions, the calculation of which is detailed in Appendix A. Here we shall limit ourselves to an illustration of the basic principle. Figure 2.6 shows a graphical representation of the situation in real (left) and reciprocal space (right). The elastic diffraction condition for a particular point (hkl) is fulfilled when that point lies on the Ewald sphere, which is fixed in space by the direction and magnitude of the incoming beam wavevector $\mathbf{k}$. For non-specular CTRs, this can be achieved by rotating the sample around its surface normal (i.e., around ω), which corresponds to a rotation around the $(00l)$ direction in reciprocal space[4]. The angle of rotation determines the point where the CTR crosses the Ewald sphere, which defines the scattering triangle of $\mathbf{q} = \mathbf{k}' - \mathbf{k}$. For a given rod, the maximum measurable l-value is reached when the scattering triangle is perpendicular to the surface plane.

Traditionally, when using point detectors, the intensity of each point along a CTR has to be recorded with a rocking scan. Keeping the detector position, and hence the diffraction condition, fixed and selecting a small range Δl of l-values with the detector slits, the sample is rotated around ω. This effectively produces an in-plane cut through the rod, collecting the intensity within a slice of thickness Δl. After the proper background subtraction, the rocking scan can be integrated to give the intensity for this particular l-range. This procedure is greatly simplified when using an area detector. Here, the entire diffraction signal can be collected at once in a single exposure in the so-called “stationary mode” [22]. The image also contains the background around the diffraction feature, which can then easily be subtracted. Furthermore, any possible artifacts, such as Debye-Scherrer rings originating from the sample environment, can be clearly identified. This has led to a remarkable increase in speed and reliability [17]. A more detailed discussion of these scans and the limitations to their applicability is given in Appendix B.

Bibliography

[1] W. C. Röntgen: “On a New Kind of Rays.” *Nature* **53**(1369), 274–276 (1896), doi: 10.1038/053274b0.

[2] W. Friedrich, P. Knipping, and M. Laue: “Interferenzerscheinungen bei Röntgenstrahlen.” *Ann. Phys.* **346**(10), 971–988 (1913), doi:10.1002/andp.19133461004.

---

[4] Note how the incoming wave vector $\mathbf{k}$ ends in the origin (000) of reciprocal space, as this is where the scattering vector $\mathbf{q}$ is zero and no momentum transfer takes place. The l-direction is usually chosen to be normal to the physical sample surface, such that it represents the direction of perpendicular momentum transfer, $\mathbf{q}_\perp$.

[3] W. L. Bragg: "The Specular Reflection of X-rays." *Nature* **90**(2250), 410–410 (1912), doi: 10.1038/090410b0.

[4] W. L. Bragg: "The Structure of Some Crystals as Indicated by Their Diffraction of X-rays." *Proc. Roy. Soc. Lond.: Math. Phys. Sci.* **89**(610), 248–277 (1913).

[5] W. C. Marra, P. Eisenberger, and A. Y. Cho: "X-ray total-external-reflection–Bragg diffraction: A structural study of the GaAs-Al interface." *J. Appl. Phys.* **50**(11), 6927 (1979), doi: 10.1063/1.325845.

[6] P. Eisenberger and W. C. Marra: "X-Ray Diffraction Study of the Ge(001) Reconstructed Surface." *Phys. Rev. Lett.* **46**(16), 1081–1084 (1981), doi:10.1103/PhysRevLett.46.1081.

[7] I. K. Robinson: "Direct Determination of the Au (110) Reconstructed Surface by X-Ray Diffraction." *Phys. Rev. Lett.* **50**, 1145 – 1148 (1983), doi:10.1103/PhysRevLett.50.1145.

[8] M. Nielsen: "Single crystal surface structure by bragg scattering." *Z. Phys. B: Condens. Matter.* **61**(4), 415–420 (1985), doi:10.1007/BF01303546.

[9] R. Feidenhans'l: "Surface structure determination by X-ray diffraction." *Surf. Sci. Rep.* **10**(3), 105–188 (1989), doi:10.1016/0167-5729(89)90002-2.

[10] I. K. Robinson: "Surface Crystallography." In *Handbook on Synchrotron Radiation*, Edited by G. Brown and D. E. Moncton, chapter 7, 221–266, Elsevier Science Publishers, third edition (1991).

[11] I. K. Robinson and D. J. Tweet: "Surface X-ray diffraction." *Rep. Progr. Phys.* **55**, 599–651 (1992), doi:10.1088/0034-4885/55/5/002.

[12] B. D. Patterson, Ch. Brönnimann, D. Maden, F. Gozzo, A. Groso, B. Schmitt, M. Stampanoni, and P. R. Willmott: "The materials science beamline at the Swiss Light Source." *Nucl. Instrum. Meth. B* **238**, 224–228 (2005), doi:10.1016/j.nimb.2005.06.194.

[13] B. D. Patterson, R. Abela, H. Auderset, Q. Chen, F. Fauth, F. Gozzo, G. Ingold, H. Kühne, M. Lange, D. Maden, D. Meister, P. Pattison, T. Schmidt, B. Schmitt, C. Schulze-Briese, M. Shi, M. Stampanoni, and P. R. Willmott: "The materials science beamline at the Swiss Light Source: design and realization." *Nucl. Instrum. Meth. A* **540**(1), 42–67 (2005), doi: 10.1016/j.nima.2004.11.018.

[14] E. Vlieg: "A (2+3)-Type Surface Diffractometer: Mergence of the z-Axis and (2+2)-Type Geometries." *J. Appl. Crystallogr.* **31**(2), 198–203 (1998), doi:10.1107/S0021889897009990.

[15] P. R. Willmott, C. M. Schlepütz, B. D. Patterson, R. Herger, A. Lange, D. Meister, D. Maden, Ch. Brönnimann, E. F. Eikenberry, G. Hülsen, and A. Al-Adwan: "In situ studies of complex

PLD-grown films using hard X-ray surface diffraction." *Appl. Surf. Sci.* **247**, 188–196 (2005), doi: 10.1016/j.apsusc.2005.01.133.

[16] P. R. Willmott, R. Herger, C. M. Schlepütz, D. Martoccia, and B. D. Patterson: "Technical Reports: Pulsed Laser Deposition and in situ Surface X-ray Diffraction at the Materials Science Beamline at the Swiss Light Source." *Synch. Rad. News* **18**(4), 37–42 (2005), doi:10.1080/08940880500457230.

[17] C. M. Schlepütz, R. Herger, P. R. Willmott, B. D. Patterson, O. Bunk, Ch. Brönnimann, B. Henrich, G. Hülsen, and E. F. Eikenberry: "Improved data acquisition in grazing-incidence X-ray scattering experiments using a pixel detector." *Acta Crystallogr. A* **61**, 418–425 (2005), doi: 10.1107/S0108767305014790.

[18] Ch. Brönnimann, E. F. Eikenberry, B. Henrich, R. Horisberger, G. Huelsen, E. Pohl, B. Schmitt, C. Schulze-Briese, M. Suzuki, T. Tomizaki, H. Toyokawa, and A. Wagner: "The PILATUS 1M detector." *Journal of Synchrotron Radiation* **13**(2), 120–130 (2006), doi:10.1107/S0909049505038665.

[19] A. Bergamaschi, Ch. Brönnimann, E. F. Eikenberry, B. Henrich, M. Kobas, P. Kraft, and B. Schmitt: "Experience and Results from the 6 Megapixel PILATUS System." *PoS* **057**, 049 (2007).

[20] P. Kraft, A. Bergamaschi, Ch. Brönnimann, R. Dinapoli, E. F. Eikenberry, H. Graafsma, B. Henrich, I. Johnson, M. Kobas, A. Mozzanica, C. M. Schlepütz, and B. Schmitt: "Characterization and Calibration of PILATUS Detectors." *IEEE Trans Nucl Sci* (2009). Accepted.

[21] P. Kraft, A. Bergamaschi, Ch. Brönnimann, R. Dinapoli, E. F. Eikenberry, B. Henrich, I. Johnson, M. Kobas, C. M. Schlepütz, P. R. Willmott, and B. Schmitt: "Performance of single photon counting pixel detector modules." *J. Synch. Rad.* **16**(3), 368–375 (2009), doi: 10.1107/S0909049509009911.

[22] E. Vlieg: "Integrated Intensities Using a Six-Circle Surface X-ray Diffractometer." *J. Appl. Crystallogr.* **30**(5), 532 – 543 (1997), doi:10.1107/S0021889897002537.

Chapter 3

Direct Methods

In the previous chapter, we have discussed the fundamental working principle of X-ray diffraction and how a regular distribution of electrons, atoms, or groups of atoms, gives rise to a diffraction pattern of scattered intensity. Given an electron density distribution in real-space, the calculation of the resulting diffraction pattern is routine. The daily work of a crystallographer consists of the reverse process, however, i.e., finding the electron density which causes a measured diffraction pattern. It turns out that this step is much less straightforward and poses a fundamental challenge to crystal structure determination. In this chapter we shall concern ourselves with ways to solve this dilemma and take a close look at a class of algorithms designed to overcome this barrier, the so-called *direct methods*.

First, a general introduction and motivation for the use of direct methods will be given, followed by a description of the basic concepts of iterative phase retrieval algorithms and the use of *a priori* information.

In the second part of this chapter, we will focus on the specific problem of direct methods in SXRD and how the procedures described earlier can be adapted to efficiently deal with this specialized case. The two specialized algorithms developed for the structure determination of thin films which have been employed in the framework of this thesis will be discussed in detail.

3.1 The phase problem

The complex structure factors (CSFs) of a periodic structure in real-space are equal to points in the Fourier transform of the electron density (ED) in a single unit cell. By measuring these CSFs of an unknown structure, one should therefore be able to reconstruct the real-space ED simply through the corresponding inverse Fourier transform. Unfortunately, there is no way of measuring the CSFs directly, as they are complex quantities. The easily accessible scattering intensities in a diffraction pattern are proportional only to their squared magnitudes, but the phases are lost in such a measurement. This is the well-known and ubiquitous *phase problem*.

3.2 The limitations of model fitting

The classical way to work around the phase problem in SXRD is to resort to model fitting. An initial guess for the structure is parameterized and used to calculate the expected diffraction pattern. The parameters are then varied such as to minimize the discrepancies, measured in terms of a so-called *figure of merit* (FOM), between the measured data and the intensities predicted by the model. This method has been successfully applied to solve many surface structures, but suffers from some severe limitations.

When dealing with surface structures comprising more than a few atoms, for example in larger surface reconstructions, or in several atomic layers, as in thin films, the number of parameters needed to describe the system rapidly increases. In such cases, standard model fitting and refinement procedures quickly run into problems, primarily due to the following reasons:

1. The number of different structures, or starting guesses, to be tested increases swiftly with increasing complexity of the system.
2. The space of possible refinement solutions directly depends on the parameterization of each structural model. However, the correct parameterization is not known *a priori*. A wrong parameterization will always give a solution out of the available solution space, but the true solution might not be inside this solution space.
3. Different choices for the FOM (e.g. R-factor, χ^2, etc.) to be optimized can lead to very

different solutions, due to entirely different topologies of the corresponding search spaces.

4. Strong correlations between the fit parameters result in the optimized FOM having a complex topology with possibly many local minima. An unequivocal determination of the true global minimum is therefore severely hampered, if not rendered essentially impossible.
5. For standard "downhill" optimization routines, the search result is usually confined to the closest (local) minimum to the chosen starting point. Naturally, the correct starting guess to reach the right solution is not known *a priori*.
6. The computational effort increases dramatically with the number of free parameters, resulting in a marked decrease in the convergence speed.
7. The number of data points required to describe the system in an overdetermined way also increases at least linearly with the number of free parameters. Their processing in larger numbers further reduces the convergence speed of the fitting process.

While the last two aspects are of purely technical nature, and can be overcome to a certain extent by efficient and parallelized computing strategies, points 4 and 5 pose a more serious challenge. There are a few "clever" global search techniques, either based on statistical or thermodynamical concepts (e.g., simulated annealing or direct Monte-Carlo sampling) or heuristic arguments (e.g., genetic algorithms, differential evolution, or particle swarm optimization), designed to escape from local minima in search of a global solution. However, this comes at a great cost of speed and computing time. And, naturally, there is no guarantee for success, as all of these techniques are based on random search processes. In turn, they allow for reproducibility checks of a solution by comparing several runs of the random search process.

The first three items in the list, on the other hand, pose a fundamental problem without any immediate solution. The choice of parameterization and FOM is relegated to the researcher's intuition. Obviously, any complementary information about the system is of tremendous help in choosing the appropriate model. However, there will always be an element of subjectivity, and the danger that those conditions leading to the correct solution are not discovered. Ideally, one would therefore like to have a well-defined and objective method to aid in the determination of the correct parameterization and starting guess to be used in the refinement process. This can be achieved, at least partially, through the use of *direct methods*.

3.3 Introducing direct methods

Crystallographic direct methods aim to solve the phase problem by estimating the phases of complex structure factors of the scattering electron density from the corresponding measured magnitudes. In addition to this direct experimental information, they make use of the fact that some fundamental *a priori* properties of the system are known. As an example, the so-called *positivity constraint* requires that the electron density, as the source of the scattered x-ray intensity, has to be non-negative. Other typical properties may be *atomicity* – the knowledge that most of the electrons are concentrated in a small volume close to the core of the atoms – or a finite *support*, limiting the extent of the structure to be recovered.

In this work, we will focus on the so-called *iterative phase retrieval algorithms* to solve the phase problem. The basic idea is to start from an arbitrary, usually random, guess for the unknown phases. The algorithm alternates back and forth between real and reciprocal space through the proper Fourier transformations. In each iteration, it consecutively applies the known constraints, i.e., the measured structure factor amplitudes in reciprocal space and the *a priori* constraints in real-space, to the current estimate of the structure factors and corresponding real-space structure, resulting in a new phase estimate to initialize the next iteration. The intention is to iteratively reach a state of self-consistency where the structure factor magnitudes predicted by the obtained real-space structure, which is compatible with all *a priori* constraints, agree with the measured intensities.

One of the first examples of a working phase retrieval algorithm was presented by Gerchberg and Saxton [1, 2]. It was developed for the phase determination in electron microscopy experiments, where one can measure the amplitudes of the investigated object both in real-space (absorption contrast image in transmission mode, measured in the near contact regime) and in Fourier space (the corresponding diffraction pattern recorded in the far-field, or Fraunhofer regime). The iterative numerical algorithm improves the phase estimates progressively by alternating between those two Fourier-related domains.

Fienup modified and extended the Gerchberg-Saxton algorithm to the case of an object for which no real-space image is available, but which can be described by a (unmeasured) function that is required to be positive and real and possibly of limited extent [3, 4]. This step laid the foundation for x-ray diffraction phase-retrieval experiments and opened up the applicability to systems where direct real-space information cannot be obtained.

A second important breakthrough came with the theoretical insight that the constraints applied during the iterations could be mathematically described as projections in Hilbert space [5]. This has enabled theoreticians to formulate the algorithms in a more rigorous manner, carefully analyze their behavior, and generalize the concepts of the basic Fienup algorithm to a new class of so-called *iterative projection algorithms* [6–10].

3.3.1 Oversampling

The theory of x-ray diffraction has been discussed in detail in Chapter 2. Remember that the diffraction intensities are equal to the squared modulus of the Fourier transform (FT) of the scattering electron density $\rho(\mathbf{r})$:

$$I(\mathbf{q}) = |\,\mathrm{FT}[\rho(\mathbf{r})]\,|^2 = \mathrm{FT}[\rho(\mathbf{r})]^\dagger \cdot \mathrm{FT}[\rho(\mathbf{r})]. \tag{3.1}$$

The inverse FT of the intensity is not equal to $\rho(\mathbf{r})$ itself, but to the autocorrelation function of $\rho(\mathbf{r})$:

$$\mathrm{IFT}\,[I(\mathbf{q})] = \rho(-\mathbf{r}) * \rho(\mathbf{r}). \tag{3.2}$$

The phase retrieval problem therefore consists of solving equation 3.2 for $\rho(\mathbf{r})$, given the measured intensities $I(\mathbf{q})$ and using the known constraints about the system.

But what requirements are there for the data set $I(\mathbf{q})$ to render a successful phase retrieval run feasible? Let us consider an isolated (non-periodic) object with density $\rho(\mathbf{r})$, where $\mathbf{r}$ is the coordinate inside the object (real-space), and which has a known size. In other words, $\rho(\mathbf{r}) = 0$ for all $\mathbf{r}$ outside the object. The density $\rho(\mathbf{r})$ is sampled on a discrete and equidistant voxel grid. $\mathrm{FT}[\rho(\mathbf{r})]$ can then be calculated using a discrete Fourier transform, resulting in a likewise equidistant set of points in reciprocal space. The set of voxels inside the object (where $\rho(\mathbf{r}) \geqslant 0$) is called its *support*.

The autocorrelation function $\rho(-\mathbf{r}) * \rho(\mathbf{r})$ in equation 3.2 has twice the linear size of the object's support. Since the extent of an object in real-space translates to a sampling density in Fourier space, we need to sample the diffraction pattern at least twice as finely as expected from the extent of the object itself in order to be able to solve equation 3.2 (this lower limit is called *critical sampling*). Measuring with even finer sampling rates adds a border of zero-padding around the the recovered autocorrelation function and in principle contains no extra information about the system (Shannon theorem)[1]. Less than critical sampling can lead to multiple recovery solutions of an object. Intuitively, the required oversampling factor of 2 seems right, since for each (real-valued) density voxel, both the complex phase and amplitude need to be determined.

This method of oversampling is only possible for non-periodic structures, since they result in a continuous diffraction pattern which can in principle be measured at arbitrary sampling frequencies. In crystal structure determination, however, one usually deals with periodic structures, resulting in the strongly enhanced but discrete intensity distribution in the form of Bragg peaks. The consequent loss of information in reciprocal space has to be compensated for by other means, e.g. through the knowledge of parts of the real-space object, the presence of heavy atoms, anomalous diffraction experiments, etc.

Similar arguments are applicable to determine the achievable real-space resolution of the recovered density $\rho(\mathbf{r})$. Again, the sampling in real-space translates to an extent in reciprocal space. The higher the $\mathbf{q}$-values of the measured intensities, the finer is the real-space resolution. This is not to say that measuring only the highest momentum transfers is sufficient, as the low frequency Fourier components are equally important to recover the object. Ideally, the available diffraction data should fill the entire reciprocal space grid up to the highest necessary scattering vectors[2].

In summary, the objects size determines the required reciprocal space sampling, and the measured range of the diffraction sets an upper limit to the achievable real-space resolution. Both of these factors need to be considered carefully in order to obtain a data set suitable for direct methods.

3.3.2 The concept of projections

As mentioned above, the central concept in direct methods is that of constraints, describing an *a priori* property of the system to be fulfilled by a valid solution. In x-ray diffraction, the system is described by an electron density. The set of those electron densities compatible with a given constraint forms a subset of the entire search space of possible electron densities. Mathematically, the application of a constraint can be formulated in terms of a projection

---

[1] In practice, a larger oversampling seems to help the convergence of many algorithms.

[2] Symmetry considerations about the object and its diffraction pattern can, however, drastically reduce the portion of reciprocal space that needs to be sampled.

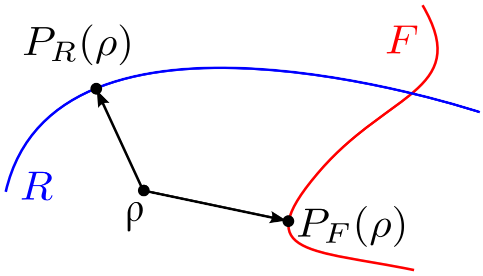

Figure 3.1: Schematic representation of projections. $\mathbf{P_F}$ and $\mathbf{P_R}$ are the distance minimizing projections mapping the starting point ρ onto the nearest point of their corresponding constraint sets $\mathbf{F}$ and $\mathbf{R}$.

operator [11], which assigns to an arbitrary point in the search space the nearest point of the corresponding constraint subset.

This situation is illustrated schematically in Figure 3.1. Two constraint sets, $\mathbf{F}$ and $\mathbf{R}$, in a two-dimensional Hilbert space are represented by sets of points on a line. A point ρ outside the constraint sets is mapped onto the respective set through the projections $\mathbf{P_F}$ and $\mathbf{P_R}$. $\mathbf{P_F}(\rho)$ and $\mathbf{P_R}(\rho)$ are defined as those points on the constraint sets which are closest to the original point ρ. For this reason, one also speaks of distance-minimizing projections.

As a more realistic example of one such constraint in diffraction experiments, *positivity* requires that the electron density has to be non-negative. Its distance minimizing projection operator $\mathbf{P_p}$, acting on the electron density ρ, is written as

$$\mathbf{P_p}(\rho) = \begin{cases} \rho, & \rho \geq 0 \\ 0, & \rho < 0. \end{cases} \tag{3.3}$$

Another important constraint is the magnitude projection $\mathbf{P_M}$ in Fourier space, enforcing the amplitudes of the complex structure factors to be equal to the square root of the measured intensities. The distance-minimizing projection leaves the phases unchanged:

$$\mathbf{P_M}(\rho) = \mathrm{IFT}\left[\sqrt{I_{\mathrm{meas}}} \cdot \frac{\mathrm{FT}(\rho)}{|\mathrm{FT}(\rho)|}\right]. \tag{3.4}$$

Direct method algorithms use a combination of such projection operators (henceforth referred to as projections) to find those points of the search space which satisfy all corresponding constraints simultaneously. In other words, the intersection of all constraint subsets forms the set of valid solutions. Depending on the particular choice of constraints and their mutual compatibility, the solution subset may contain exactly one solution in the ideal case, several (multiple) solutions, or no solutions at all. It is therefore the applicability and effectiveness of the employed projections which determines the success of the direct method in solving a particular problem.

3.3.3 Iteration schemes

With these projections at hand, we now need an iterative algorithm which will perform the search for a solution. Many such algorithms are available, each having its own characteristic benefits and drawbacks. A nice overview of their definitions and a comparison of the characteristics in their search behavior has been written by Marchesini [11]. Here, we will focus on the most relevant developments with regard to this thesis.

Fienup type algorithms

The Fienup type algorithms [4] are based on a generalization of the Gerchberg-Saxton algorithm to a wider range of applications. The basic concept can be described in four simple steps: (1) Fourier transform an estimate of the object to be recovered (in the case of diffraction experiments this is an estimate of the electron density); (2) replace the calculated modulus of the Fourier Transform by the square root of the measured intensities to yield a new estimate of the Fourier transform compatible with the experimental data; (3) inverse Fourier transform this estimate to yield an updated object function; and (4) apply the real-space constraints to the object function in order to create a new estimate of the object. The original block diagram of this algorithm as published by Fienup is shown in Figure 3.2 (a). Steps (1) through (4) constitute one iteration of the algorithm and are repeated until both the real-space estimate of the object and its Fourier transform cease to change. In other words, one simply transforms back and forth between the two domains, satisfying all the constraints in one before returning to the other, until a state of self-consistency is reached.

Fienup realized that the right hand side of the block diagram could be written as a nonlinear operator with an input g and an output g', as shown in Figure 3.2 (b), and termed this the *input-output concept*. In modern words, it is identical to the magnitude projection discussed in Section 3.3.2, equation 3.4. Containing no object-domain operations, it provides full flexibility in the choice of modification which is applied to the output g' in order to create the next input

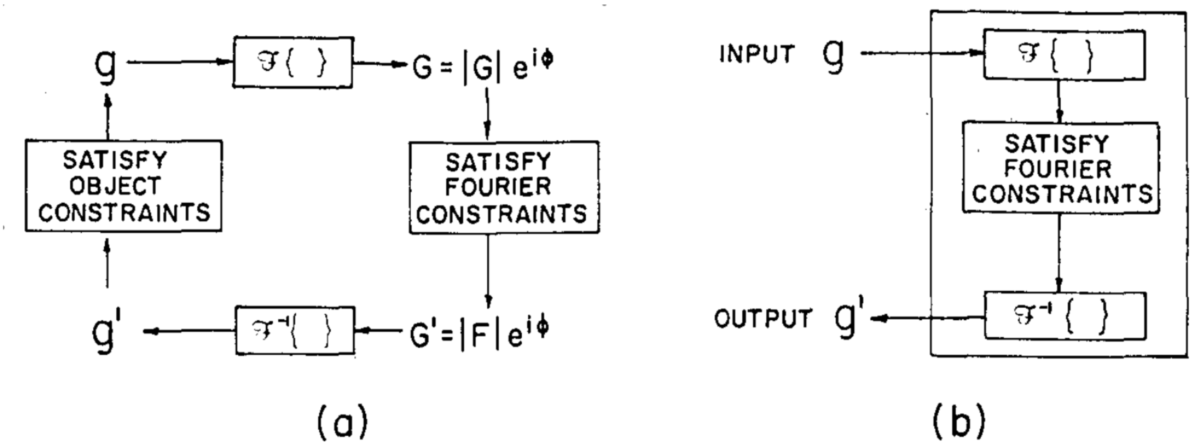

Figure 3.2: (a) Iteration scheme of the error-reduction (Gerchberg-Saxton) algorithm. (b) Block diagram of the generalized input-output scheme. (Original drawing by Fienup, Ref. [3]. Reprinted with permission of the Optical Society of America).

g. Since in the case of diffraction experiments, the object is the electron density, we will call these operations *density modifications*.

Using the original terminology by Fienup, where g_k represents the object estimate of the k^{th} iteration and g'_k is the subsequent result of the input-output operation, the density modification for the *error-reduction algorithm* (ER) can be written as

$$g_{k+1}(\mathbf{r}) = \begin{cases} g'(\mathbf{r}), & \text{if } \mathbf{r} \in \gamma \\ 0, & \text{if } \mathbf{r} \notin \gamma, \end{cases} \tag{3.5}$$

where γ is the set of all density points in agreement with the chosen real-space constraints, e.g., where $g'(\mathbf{r})$ is positive and optionally inside a given support region of the object.

Crucially, Fienup recognized that the input g does not necessarily need to comply with the object-domain constraints (the output, on the other hand, will always conform with the Fourier constraints). Rather, one could attempt to counteract the known shortcomings of $g'_k(\mathbf{r})$ in terms of its compatibility with the constraints by modifying $g_{k+1}(\mathbf{r})$ in the appropriate manner. This concept is based on nonlinear feedback control theory. To illustrate the idea further, consider the case of $g'_k(\mathbf{r})$ having a negative value at a certain position $\mathbf{r}_0$. Assuming we initially started from $g_k(\mathbf{r}_0) \geq 0$, the input-output operation obviously results in an excessive reduction of that value. By setting $g_{k+1}(\mathbf{r}_0)$ to a value more positive than $g_k(\mathbf{r}_0)$ by some fraction β of $g'_k(\mathbf{r}_0)$, the reduction effect in iteration $k+1$ should result in a value $g'_{k+1}(\mathbf{r}_0)$ which is closer to fulfilling the positivity constraint. Therefore, the desired change of the output to counteract the constraint violations is

$$\Delta g_k(\mathbf{r}) = \begin{cases} 0, & \text{if } \mathbf{r} \in \gamma \\ -g'_k(\mathbf{r}), & \text{if } \mathbf{r} \notin \gamma. \end{cases} \tag{3.6}$$

This leads to a few simple new choices for the next input. The *basic input-output algorithm* (IO) uses

$$\begin{aligned} g_{k+1}(\mathbf{r}) &= g_k(\mathbf{r}) + \beta \Delta g_k(\mathbf{r}) \\ &= \begin{cases} g_k(\mathbf{r}), & \text{if } \mathbf{r} \in \gamma \\ g_k(\mathbf{r}) - \beta g'_k(\mathbf{r}), & \text{if } \mathbf{r} \notin \gamma. \end{cases} \end{aligned} \tag{3.7}$$

Instead of applying the compensation to the former input $g_k(\mathbf{r})$, one can also modify $g_k(\mathbf{r})$ directly, leading to the *output-output algorithm* (OO):

$$\begin{aligned} g_{k+1}(\mathbf{r}) &= g'_k(\mathbf{r}) + \beta \Delta g_k(\mathbf{r}) \\ &= \begin{cases} g'_k(\mathbf{r}), & \text{if } \mathbf{r} \in \gamma \\ g'_k(\mathbf{r}) - \beta g'_k(\mathbf{r}), & \text{if } \mathbf{r} \notin \gamma. \end{cases} \end{aligned} \tag{3.8}$$

A combination of the latter two methods finally leads to the *hybrid input-output algorithm* (HIO):

$$g_{k+1}(\mathbf{r}) = \begin{cases} g'_k(\mathbf{r}), & \text{if } \mathbf{r} \in \gamma \\ g_k(\mathbf{r}) - \beta g'_k(\mathbf{r}), & \text{if } \mathbf{r} \notin \gamma. \end{cases} \tag{3.9}$$

The difference map

Elser and co-workers have developed a generalized hybrid input-output type algorithm, with a very efficient search method, which avoids getting trapped in local minima on its search for a global solution [9]. This so-called *difference map algorithm* is formulated entirely using the language of projections, and can be used in principle to find the intersection, or simultaneous solution, between any two independent constraint sets (e.g., the two lines shown in Figure 3.1). Anticipating the usual choice of real and Fourier space constraints, we denote the two projections with $\mathbf{P_R}$ and $\mathbf{P_F}$. Using the same notation as Fienup, where g_k represents the object estimate[3], the difference map can be written as [8–10]

$$\begin{aligned} g_{k+1} &= g_k + \beta\left[T_1(g_k) - T_2(g_k)\right], \\ T_1(g_k) &= \mathbf{P_R}\left[(1+\beta^{-1})\mathbf{P_F} - \beta^{-1}\right] g_k, \\ T_2(g_k) &= \mathbf{P_F}\left[(1-\beta^{-1})\mathbf{P_R} + \beta^{-1}\right] g_k, \end{aligned} \tag{3.10}$$

where β is a control parameter in the interval $(0,1]$. Studies have indicated that the optimal value for β should be in the range $0.4 \leq \beta \leq 0.8$ [9]. Tests performed in our group [12] show no clear correlations between the number of iterations and β, a trend which other studies [13] have also observed. Consequently, all analysis runs presented in this work use $\beta = 1$, which simplifies the difference map to:

$$\begin{aligned} g_{k+1} &= g_k + \mathbf{P_R}(2\mathbf{P_F} - 1)g_k - \mathbf{P_F}g_k \\ &= g_k + 2\mathbf{P_R}\mathbf{P_F}g_k - \mathbf{P_R}g_k - \mathbf{P_F}g_k. \end{aligned} \tag{3.11}$$

This leads to an algorithm very similar to the hybrid input-output algorithm [4]. Additionally, it reduces the number of projections to be applied in one iteration from 4 to 2, as a comparison of equations 3.10 and 3.11 shows, resulting in a corresponding speed-up of the iteration scheme.

To monitor the progress of the algorithm we use the difference map error [9], defined as

$$\epsilon_{DM,k+1} = \left\| T_1(g_k) - T_2(g_k) \right\|, \tag{3.12}$$

which is equal to the distance between the two projections taken for the current object estimate. For $\beta = 1$, it simplifies to

$$\epsilon_{DM,k+1} = \left\| 2\mathbf{P_R}\mathbf{P_F}g_k - \mathbf{P_R}g_k - \mathbf{P_F}g_k \right\|. \tag{3.13}$$

3.3.4 Starting point

All of the discussed iterative projection algorithms need to be initialized with a starting guess for the object estimate g. Choosing a random starting point renders it possible to verify the

---

[3] As always, for crystallographic structure determination experiments, g_k represents the electron density and can be directly thought of as ρ_k.

uniqueness of the solution by repeating the search several times. For diffraction experiments, the obvious option is to initialize the electron density ρ_0 in each voxel to a random value. Alternatively, one can assign random phases to the measured structure factor amplitudes:

$$\rho_0 = \mathrm{IFT}\left(|F_{\mathrm{meas}}|\, e^{\mathrm{rand}(0,\,2\pi)i}\right). \tag{3.14}$$

It is also possible to use a simple model of the structure as the starting point. This can facilitate the search for a solution, but may compromise the verification of its uniqueness.

3.4 Direct methods in SXRD

The aim of SXRD experiments is to solve the atomic structure of a single crystal surface, the interface between two epitaxial materials, or of a thin film deposited on some substrate. For simplicity, we will use the term *surface* in the following discussion synonymously for any surface, interface or thin film system, as all the following arguments are equally valid for any of those cases.

The measured diffraction intensities contain contributions from the surface structure under investigation as well as from the supporting bulk crystal. Usually, the latter is known with great precision or can be determined with complementary methods such as powder or single crystal bulk diffraction. This provides an important advantage for the solution of the surface structure as the knowledge of the underlying bulk can be used as a reference, much like the reference wave in a holographic analysis or a known building block in structure completion methods in macromolecular crystallography. Furthermore, the symmetry-breaking due to the truncation of the crystal results in a non-periodic structure in the direction perpendicular to the surface and gives rise to the continuous diffraction signal of the crystal truncation rods (see Section 2.2.3). This continuous signal provides the required oversampling of the data in the out-of-plane direction needed to solve equation 3.2.

Using the known bulk structure factor F_{bulk} as a reference, the total measured structure factor can be expressed in terms of the unknown surface electron density ρ_{surf}, which gives rise to the surface structure factor F_{surf}, in the following manner:

$$F_{tot}(\rho_{\mathrm{surf}}) = F_{surf}(\rho_{\mathrm{surf}}) + F_{bulk} = \mathrm{FT}[\rho_{\mathrm{surf}}] + F_{bulk}. \tag{3.15}$$

The quantity ρ_{surf} is non-zero only for a finite region, given by the thickness of the unknown surface structure, and thus defines a support constraint. This fact, in conjunction with the ability to oversample, provides the necessary ingredients to apply direct methods to surface systems.

Based on these general concepts, Marks and co-workers were the first to formulate a direct method algorithm for SXRD in the late 1990s [14–17]. The method is rather complex and involves many statistical arguments such as maximum entropy considerations, etc. A much simpler approach has been developed by Saldin *et al.* [18–20], combining Fienup's error-reduction algorithm with the elementary support and positivity constraints. Their algorithm, named PARADIGM (**P**hase and **A**mplitude **R**ecovery **A**nd **D**iffraction **I**mage **G**eneration **M**ethod), has successfully been applied to solve the previously unknown surface structures of Au(110)-(2×1) [21] and two reconstructions in the Sb/Au(110) system [22, 23]. A somewhat different route has been taken by Yacoby and co-workers [24–26], resulting in a method called COBRA (**CO**herent **BR**agg **R**od **A**nalysis), which will be discussed extensively at the end of this chapter. In an attempt to combine the strengths of those various pioneering approaches, Björck and colleges [12] have begun developing a method especially suited for the application to thin film systems, called DCAF (**D**ifference map using the **C**onstraints of **A**tomicity and **F**ilm shift). Again, a detailed account of the algorithms will be given later on in this chapter.

3.4.1 Projections for SXRD

Fourier space

For an electron density to be a valid solution, the most important constraint is that its Fourier transform agrees with the measured structure factor magnitudes. Due to the phase problem, the respective phases cannot be constrained and are thus left unchanged. For SXRD, the *magnitude projection* is written as

$$\mathbf{P_M}(\rho_{\text{surf}}) = \text{IFT}\left[|F_{\text{meas}}| \cdot \frac{F_{\text{tot}}(\rho_{\text{surf}})}{|F_{\text{tot}}(\rho_{\text{surf}})|} - F_{\text{bulk}}\right], \tag{3.16}$$

where the bulk contribution has been subtracted such that only the structure factors of the unknown part remain. This step has one very important consequence, however: the value of $|F_{\text{meas}}|$ must be known on an absolute scale, given by the definition of F_{bulk}, for the subtraction to yield a correct result.

It is worth noting that the magnitude projection implicitly applies a second constraint on the electron density. Since the diffraction pattern is assumed to be centro-symmetric[4], its Fourier transform results in a real-valued electron density, even though the structure factors are complex numbers.

One problem is how to treat missing data points in the diffraction pattern, since the corresponding structure factors cannot be constrained directly. The approach used in this work is to simply leave those structure factors unchanged. However, it is also possible to include a projection that enforces an upper limit on F_{surf}, given by the expected total number of electrons in the system. This improves the convergence speed of the difference map algorithm, but requires additional chemical information about the system.

Real space

The selection of real-space constraints is usually more flexible than for the Fourier constraint and depends naturally on the system under investigation and the actual demand for strong additional *a priori* information. Typical properties are the following: (1) the electron density is non-negative (positivity); (2) the unknown part has a certain maximal extension in the out-of-plane direction (support); and (3) the electrons in the unknown part are concentrated around the cores of atoms (atomicity). The *positivity projection* has been discussed earlier in Section 3.3.2 and is defined through equation (3.3). The projection enforcing the *support constraint* $\mathcal{S}$ is simple:

$$\mathbf{P}_{\mathbf{s}}\left(\rho(\mathbf{r})\right) = \begin{cases} \rho(\mathbf{r}), & \rho(\mathbf{r}) \in \mathcal{S} \\ 0, & \rho(\mathbf{r}) \notin \mathcal{S}. \end{cases} \tag{3.17}$$

Note that $\mathcal{S}$ only limits the out-of-plane extension of the unknown electron density, since the in-plane size is confined to one unit cell through the periodicity of the system in any case.

A clear-cut algorithm for identifying atoms has been described by Elser [9], where each atom is assumed to occupy $n_1 \times n_2 \times n_3$ voxels (typically, $n_1 = n_2 = n_3 = 3$) in the ED map. The different steps of the projection are illustrated in Figure 3.3. The search for atoms is conducted only inside a certain region given by the thickness of the unknown part (which

---

[4] In SXRD, only diffraction signals above the surface, i.e. with $l > 0$, can be measured and the diffraction pattern is completed for negative l-values by a point reflection of the data with respect to the reciprocal space origin.

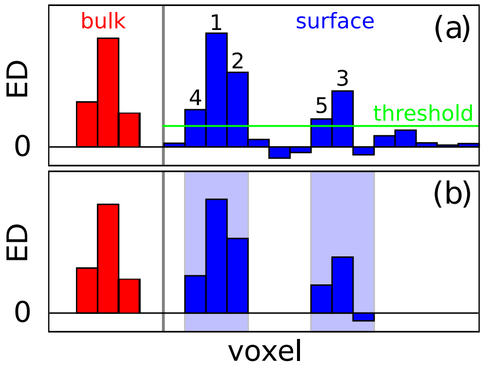

Figure 3.3: Working principle of the atomicity projection: (a) Situation before applying the projection. The pixel ranking is indicated by the numbers above the voxels exceeding the threshold level given by the green line. (b) Result of the projection: all electron density outside the identified atoms is set to zero.

should probably coincide with the support constraint), and is the range denoted as “surface” in Figure 3.3 (a). The voxels in this 3D volume are ranked according to their electron density values, as indicated by the indices shown above the bars. Starting from the highest ranked pixel and successively working down the ranking list one by one, it is checked whether placing a new atom at the indexed position will cause any overlapping with previously placed atoms. If the current position is still available, a new atom is placed there; otherwise the algorithm proceeds immediately to the next voxel in the list. There are two common criteria to stop the search for all atoms: Either a previously fixed number of atoms has been found, or the electron density at the current position in the pixel ranking drops below a certain threshold.

In the example given in Figure 3.3, the threshold criterion is used, marked by the green line in panel (a). A first atom is placed at position 1. The voxel marked with 2 has the second highest ranking, but is rejected because it would result in an overlap with the first atom. The next available position is marked with 3. All the remaining rankings would either cause an overlap with an existing atom or lie below the threshold. The last step of the projection sets the values in all voxels outside any atoms to zero. The result can be seen in Figure 3.3 (b). Put into a formula, the *atomicity projection* becomes

$$\mathbf{P}_{\mathbf{a}}\left(\rho(\mathbf{r})\right) = \begin{cases} \rho(\mathbf{r}), & \rho(\mathbf{r}) \in \mathcal{A} \\ 0, & \rho(\mathbf{r}) \notin \mathcal{A} \end{cases}, \tag{3.18}$$

where $\mathcal{A}$ is a voxel mask containing the atomic volumes determined by the procedure above.

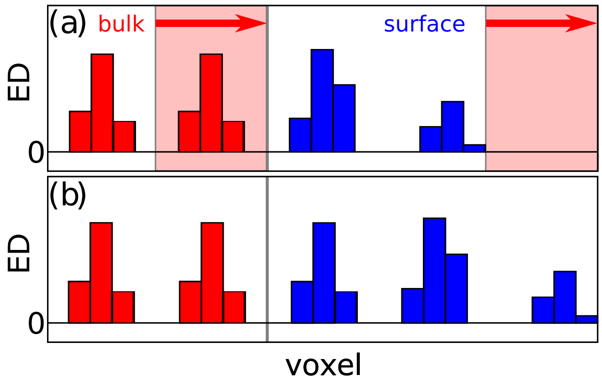

Figure 3.4: Film shift projection employed by DCAF: To ensure a maximum filling of the unknown region (labeled "surface", blue), the *film shift projection* shifts the entire electron density towards the upper boundary of the unknown region by one substrate unit cell (red shaded area) if this volume is unfilled at the top.

3.4.2 DCAF

Recently, Björck *et al.* [12] have developed a new implementation of direct methods for SXRD, addressing the particular issue of dealing with thin film systems. The method, called DCAF (**D**ifference map using the **C**onstraints of **A**tomicity and **F**ilm shift), combines the proven strengths of already available algorithms and extends this with a powerful modification of the support constraint especially suited for the application to thin films grown on bulk substrates. It is the first direct method for SXRD based on the difference map iteration scheme and uses, apart from the traditional constraints of atomicity and positivity, a novel constraint, coined the *film shift*. The difference map has been chosen as the iteration scheme for its robustness and very efficient search behavior.

A problem that one frequently encounters when looking at a thin film on top of a semi-infinite substrate is the ambiguity as to where the film, or the unknown part of the structure, meets the substrate, or the reference structure. This may be especially true if one or more substrates unit cells are significantly distorted from their bulk structure by the presence of the film or surface, and hence must be treated as part of the unknown. Shifting the boundary between the reference and unknown region by exactly one unit cell results in an identical overall structure, but changes the contents of the unknown electron density, producing two equally valid solutions.

The approach to circumvent this type of multiple solution is inspired by the dynamical threshold support [27] and is illustrated in Figure 3.4. First, an upper limit to the extent of the unknown region in the out-of-plane direction is defined (gray vertical line). The film shift projection then forces a maximum filling of this entire unknown part (labeled "surface"): Once the atomicity projection has been performed, it is checked whether the distance between the topmost atom and the upper boundary of the unknown region is larger than a bulk unit cell (red shaded area). If this is the case, the entire structure is shifted up by one unit cell and a substrate unit cell is inserted at the bottom, the result of which is seen in panel (b). This always ensures a maximum filling with atoms, keeping the surface of the unknown close to the top of the defined unknown region. First test have demonstrated that this procedure provides a strong support constraint despite of the ambiguity of the actual extent of the region to be chosen [12].

As usually the case for the difference map iteration scheme, DCAF can be initialized with a random starting guess, providing the means to verify the uniqueness of a solution.

For complex structures involving severals dozens of atoms, DCAF typically requires a few thousand iterations to find a stable solution, a process which takes of the order of one to several hours on a standard PC. Figure 3.5 displays the difference map error ϵ_{DM} (defined in Section 3.3.3) as a function of iteration for a typical phase retrieval run of a four-monolayer thick $YBa_2Cu_3O_{7\text{-x}}$ film on top of $SrTiO_3(001)$. The final solution is taken to be the electron density of the iteration with the lowest difference map error (marked by a red dot in Figure 3.5).

The atomicity constraint employed by DCAF is very sensitive to a sufficient real-space resolution of the ED map. For its proper operation, all atoms within the structure need to be resolved as separate entities, meaning that they cannot overlap within a volume of typically $3 \times 3 \times 3$ voxels (see Section 3.4.1). While this might be well fulfilled for the bulk structure of the system under investigation, any potential atomic movements due to reconstructions or relaxations could violate this criterion, and hence become incompatible with the phase retrieval method even if physically perfectly reasonable. Furthermore, the use of the atomicity constraint rules out the detection of discrete atomic displacements, such as in a ferroelectric distortion, causing a domain structure. In the case of an averaging of such domains, this should become visible as overlapping atoms, causing a double peak feature. However, the atomicity constraint prohibits overlapping of several peaks and may only provide evidence of such a case through an enhanced width of the corresponding atomic peak.

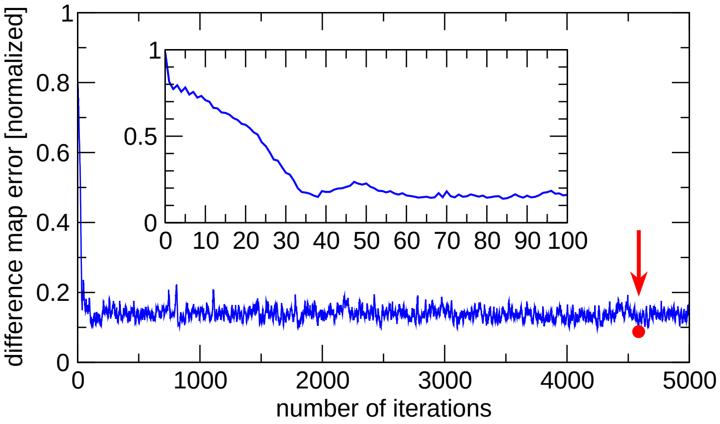

Figure 3.5: Convergence behavior of the difference map used by DCAF. For a well-constrained problem, the algorithm converges quickly, here after about 100 iterations. From there on, it fluctuates randomly about some average level, caused by the experimental noise. The best solution reached during the entire runs is marked by the red dot.

3.4.3 COBRA

A somewhat different *ansatz* to solving the phase problem in surface x-ray diffraction has been developed by Yacoby and coworkers [26]. Their method, called **CO**herent **BR**agg **R**od **A**nalysis (COBRA), differs from other implementations mainly through a new type of Fourier constraint. In addition to the standard magnitude projection, it also includes a direct phasing of the structure factors with respect to a known reference. The simultaneous recovery of both phase and amplitude results in a marked increase of the convergence speed.

The fundamental working principle of COBRA is based on the fact that the complex structure factor (CSF) is a continuously varying function along a crystal truncation rod, or Bragg rod. This implies that also its phase must change in a continuous manner.

The electron density in real-space, ρ, is represented as the sum of a known reference ED, ρ_{ref}, and an unknown difference ED, ρ_{diff}, which contains the deviations of the real ED from the reference. Since the Fourier transform is a linear transformation, the same is true in reciprocal space: the CSF of the real structure (T) is equal to the sum of CSFs from the reference structure (S) and the unknown difference structure (U):

$$T(\mathbf{q}) = S(\mathbf{q}) + U(\mathbf{q}). \tag{3.19}$$

For two adjacent points along the CTR, separated by $\mathbf{\Delta q}$ we can therefore write

$$\begin{aligned} T\left(\mathbf{q}-\frac{\Delta\mathbf{q}}{2}\right) &= S\left(\mathbf{q}-\frac{\Delta\mathbf{q}}{2}\right)+U\left(\mathbf{q}-\frac{\Delta\mathbf{q}}{2}\right), \\ T\left(\mathbf{q}+\frac{\Delta\mathbf{q}}{2}\right) &= S\left(\mathbf{q}+\frac{\Delta\mathbf{q}}{2}\right)+U\left(\mathbf{q}+\frac{\Delta\mathbf{q}}{2}\right). \end{aligned} \tag{3.20}$$

Using the fact that the CSF is a continuous function, we make the following approximation:

$$U\left(\mathbf{q}-\frac{\Delta\mathbf{q}}{2}\right) \cong U\left(\mathbf{q}+\frac{\Delta\mathbf{q}}{2}\right) \equiv U_a\left(\mathbf{q}\right). \tag{3.21}$$

Inserting this into equation (3.20) and taking the absolute values leads to

$$\begin{aligned} |T_1| &\equiv \left|T\left(\mathbf{q}-\frac{\Delta\mathbf{q}}{2}\right)\right| &= \left|S\left(\mathbf{q}-\frac{\Delta\mathbf{q}}{2}\right)+U_a\left(\mathbf{q}\right)\right| &\equiv |S_1+U_a|, \\ |T_2| &\equiv \left|T\left(\mathbf{q}+\frac{\Delta\mathbf{q}}{2}\right)\right| &= \left|S\left(\mathbf{q}+\frac{\Delta\mathbf{q}}{2}\right)+U_a\left(\mathbf{q}\right)\right| &\equiv |S_2+U_a|. \end{aligned} \tag{3.22}$$

The approximation in equation (3.21) is valid only if the rate of change in U is significantly smaller than that in S. According to Yacoby *et al.* [26], this can be guaranteed by the following means:

1. The origin of the real-space coordinate system is chosen close to the middle of the unknown structure[5].
2. The reference electron density is chosen to resemble the physical system as closely as possible such that their scattering factors are of similar magnitude.

While the first point is easily achieved without any loss of generality, it seems that the second is somewhat contradictory to the notion of direct methods. Its consequences will be discussed in detail later on.

The absolute values on the left hand side of equations 3.22 are proportional to the square root of the experimentally measured diffraction intensities. These two real-valued equations can be solved for one complex unknown, the unknown part of the structure factor U_a. The graphical representation of this set of equations, shown in Figure 3.6 (a), reveals the fact that, in general, they have two solutions (U_a, U_b). The orientations of the arrows, drawn in the

---

[5] While this origin shift by $\mathbf{R_0}$ leaves the magnitudes of the CSFs unchanged, it introduces an additional phase factor of $e^{i\mathbf{q}\cdot\mathbf{R_0}}$. The total phase factor $e^{i\mathbf{q}\cdot(\mathbf{R_0}-\mathbf{r})}$ for atoms at positions $\mathbf{r}$ close to the new origin $\mathbf{R_0}$ will then vary slowly compared to atoms further away.

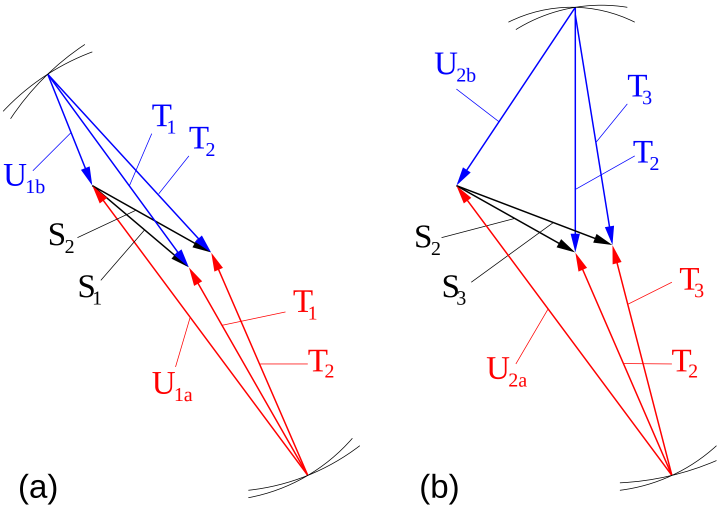

Figure 3.6: Graphical representation of the COBRA ansatz: (a) The relation between T_1 and T_2. (b) The same construction for T_2 and T_3.

complex plane, represent the phase of the CSFs, while the lengths are proportional to the magnitudes. The reference CSFs S_1 and S_2 are fixed both in phase and magnitude, while only the magnitude is known for the total CSFs T_1 and T_2, as determined from experiment. Using the approximation that U is identical for the two adjacent pairs, both T_1 and T_2 must originate at the same point. This point is determined by drawing circles with a radius equal to $|T_1|$ and $|T_2|$ around the end points of S_1 and S_2, respectively. The intersection points of those circles yield the two possible solutions U_{1a} and U_{1b} for the unknown CSF.

In order to identify the correct solution, two consecutive pairs of points along the rod need to be considered. So we compare T_2 from above with

$$|T_3| \equiv \left| T\left(\mathbf{q} + \frac{3\Delta\mathbf{q}}{2}\right) \right| = \left| S\left(\mathbf{q} + \frac{3\Delta\mathbf{q}}{2}\right) + U_a\left(\mathbf{q}\right) \right| \equiv |S_3 + U_a| \,. \tag{3.23}$$

This situation is depicted in Figure 3.6 (b). Again, two solutions U_{2a} and U_{2b} are obtained. Using the assumption that U varies slowly, the pair with the smallest difference between U_1 and U_2 must be the right solution. In the figure, these are U_{1a} and U_{2a}.

With this procedure, we determine a first approximation for the unknown CSFs, and can therefore calculate the phase for the total CSFs. The inverse Fourier transform yields an updated estimate of the total electron density of the system.

The real-space constraints employed in COBRA are positivity, applied to the total ED

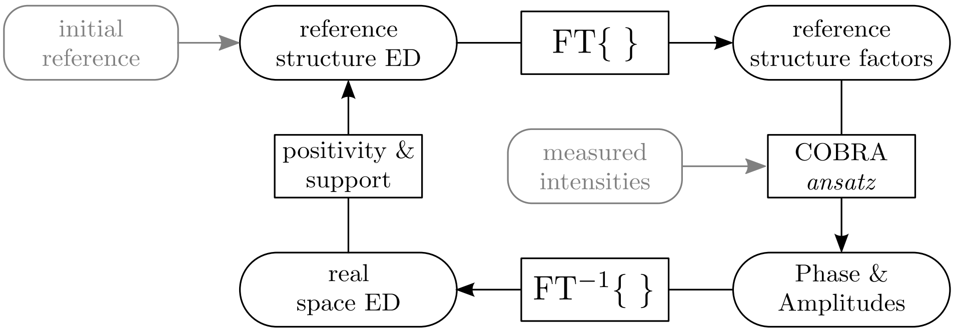

Figure 3.7: Iteration scheme of the COBRA method.

$\rho_{\text{ref}} + \rho_{\text{diff}}$, and a fixed support constraint limiting the extent where the difference ED, ρ_{diff}, is allowed to be nonzero (both positive and negative values are allowed for the difference).

The iteration scheme that COBRA uses looks very similar to Fienup's error reduction algorithm [4]. A diagram of a so-called *small iteration* is shown in Figure 3.7. The process is initialized with the chosen reference structure, based on which the phasing step described above is carried out. This yields an improved estimate for the total electron density, which is used as the new reference after applying the real-space positivity and support constraints. As the updated reference converges towards the real structure, the unknown part U of the structure factor should tend towards zero.

Figure 3.8 (a), where the average of all unknown structure factor magnitudes, $\mathcal{U} = \overline{|U|}$, is shown, demonstrates that this is generally only the case for the first few iterations. We observe a rapid initial decrease of $\mathcal{U}$, followed by seemingly random fluctuations. Supposedly, these are caused by an increasing noise level with the number of iterations [28]. The same behavior can be seen in Figure 3.8 (b) when monitoring the evolution of any other type of figure of merit (FOM), for example the crystallographic R-factor [29], the sum of squared deviations between data and simulation, or the amount of negative electron density produced by the phasing step. Concomitant with the fluctuations in the FOM is a degradation of the ED map, as clearly seen by comparing Figures 3.8 (c) and (d). The fit must therefore be stopped before the noise contributions start to dominate the result.

The most remarkable feature of COBRA over other direct methods for SXRD is certainly its extraordinary speed, owing to the direct phasing step. Typically, as few as three to a maximum of ten small iterations are required to yield impressive agreements between measured structure

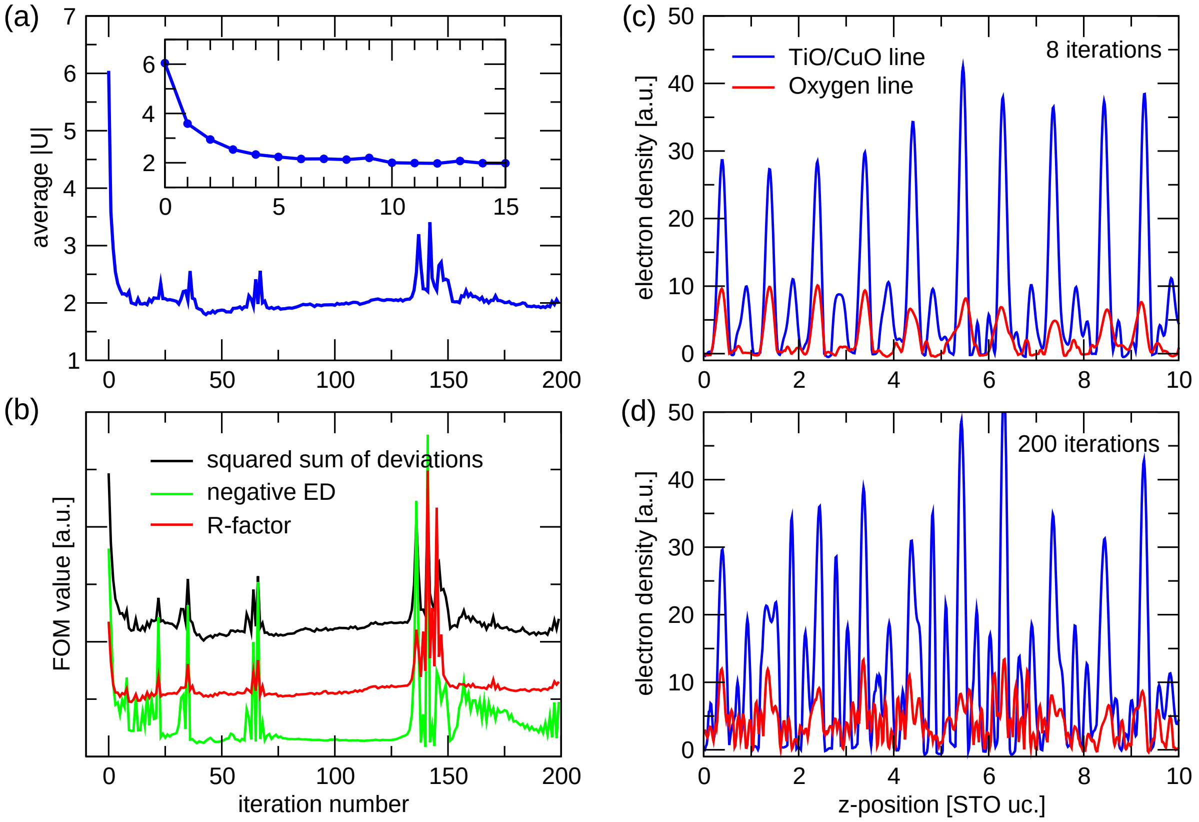

Figure 3.8: Convergence of COBRA. (a) Mean value of the unknown structure factor magnitudes $|U|$ as a function of iteration number, showing a seemingly chaotic behavior after a steep decrease in the first few iterations (expanded in the inset). (b) Alternative figures of merit as a function of the number of iterations, displaying the same chaotic behavior. (c) Electron-density plots along the out-of-plane direction through the TiO/CuO and oxygen lines of YBCO on STO(001) after 8 iterations and (d) 200 iterations.

factors and those calculated based on the resulting ED. Also, the obtained ED seems to be directly interpretable in terms of atom positions and movements, occupancies, intermixing, broadening caused by site-specific static disorder, etc. However, the results are to be handled with care and may not necessarily lead to the correct solution.

Most importantly, the requirement mentioned before, that the reference electron density needs to be chosen to resemble the physical system as closely as possible, seems to be problematic. In fact, it is exactly because of the difficulty in determining a sufficiently good starting guess that the need for direct methods arises. COBRA provides the means to improve the reference structure when the deviations from the result become unreasonably large. In a so-called *large iteration*, the changes in the ED map obtained from a series of small iterations are used as input to produce a better parameterization of the reference itself. Then the process is reinitiated with this updated reference structure. Although this step generally improves the quality of the fit, tests have shown that the correct starting guess is unlikely to be recovered if it differs significantly from the initially used reference structure. As a result, the algorithm can become trapped in local minima.

In contrast to most other direct methods, COBRA is initialized with a fixed starting point, which is the chosen reference structure. Since the algorithm itself is deterministic in nature, this precludes the possibility of random restarts to test the reproducibility of a solution.

Despite these limitations, COBRA has been proven to be an invaluable tool for solving many surface structures [24, 28, 30–35].

Bibliography

[1] R. W. Gerchberg and W. O. Saxton: "A Practical Algorithm for the Determination of Phase from Image and Diffraction Plane Pictures." *Optik* **35**(2), 237–246 (1972).

[2] R. W. Gerchberg and W. O. Saxton: "Phase Determination from Image and Diffraction Plane Pictures in the Electron Microscope." *Optik* **34**(3), 275–284 (1971).

[3] J. R. Fienup: "Reconstruction of an object from the modulus of its Fourier transform." *Optic. Lett.* **3**(1), 27–29 (1978), doi:10.1364/OL.3.000027.

[4] J. R. Fienup: "Phase retrieval algorithms: a comparison." *Appl. Optic* **21**(15), 2758–2769 (1982).

[5] A. Levi and H. Stark: "Image restoration by the method of generalized projections with application to restoration from magnitude." *J. Opt. Soc. Am. A* **1**(9), 932 (1984), doi:10.1364/JOSAA.1.000932.

[6] H. H. Bauschke, P. L. Combettes, and D. R. Luke: "Hybrid projection–reflection method for phase retrieval." *J. Opt. Soc. Am. A* **20**(6), 1025–1034 (2003), doi:10.1364/JOSAA.20.001025.

[7] H. H. Bauschke, P. L. Combettes, and D. R. Luke: "Phase retrieval, error reduction algorithm, and Fienup variants: a view from convex optimization." *J. Opt. Soc. Am. A* **19**(7), 1334 (2002), doi:10.1364/JOSAA.19.001334.

[8] V. Elser: "Random projections and the optimization of an algorithm for phase retrieval." *J. Phys. Math. Gen.* **36**(12), 2995–3007 (2003), doi:10.1088/0305-4470/36/12/309.

[9] V. Elser: "Solution of the crystallographic phase problem by iterated projections." *Acta Crystallogr. A* **59**, 201–209 (2003), doi:10.1107/S0108767303002812.

[10] V. Elser: "Phase retrieval by iterated projections." *J. Opt. Soc. Am. A* **20**(1), 40–55 (2003), doi: 10.1364/JOSAA.20.000040.

[11] S. Marchesini: "A unified evaluation of iterative projection algorithms for phase retrieval." *Rev. Sci. Instrum.* **78**(1), 011301 (2007), doi:10.1063/1.2403783.

[12] M. Björck, C. M. Schlepütz, S. A. Pauli, D. Martoccia, R. Herger, and P. R. Willmott: "Atomic imaging of thin films with surface x-ray diffraction: introducing DCAF." *J. Phys.: Condens. Matter* **20**(44), 445006 (2008), doi:10.1088/0953-8984/20/44/445006.

[13] P. Thibault, V. Elser, C. Jacobsen, D. A. Shapiro, and D. Sayre: "Reconstruction of a yeast cell from X-ray diffraction data." *Acta Crystallogr. A* **62**(4), 248–261 (2006), doi: 10.1107/S0108767306016515.

[14] L. D. Marks, W. Sinkler, and E. Landree: "A feasible set approach to the crystallographic phase problem." *Acta Crystallogr. A* **55**(4), 601–612 (1999), doi:10.1107/S0108767398014408.

[15] L. D. Marks, N. Erdman, and A. Subramanian: "Crystallographic direct methods for surfaces." *J. Phys.: Condens. Matter* **13**, 10677 (2001), doi:10.1088/0953-8984/13/47/310.

[16] L. D. Marks, E. Bengu, C. Collazo-Davila, D. Grozea, E. Landree, C. Leslie, and W. Sinkler: "Direct Methods for Surfaces." *Surf. Rev. Lett.* **5**(5), 1087–1106 (1998), doi:10.1142/S0218625X98001444.

[17] L. D. Marks: "General solution for three-dimensional surface structures using direct methods." *Phys. Rev. B* **60**(4), 2771–2780 (1999), doi:10.1103/PhysRevB.60.2771.

[18] D. K. Saldin, R. J. Harder, H. Vogler, W. Moritz, and I. K. Robinson: "Solving the structure completion problem in surface crystallography." *Comput. Phys. Comm.* **137**(1), 12–24 (2001), doi: 10.1016/S0010-4655(01)00169-2.

[19] D. K. Saldin, R. J. Harder, V. L. Shneerson, and W. Moritz: "Phase retrieval methods for surface x-ray diffraction." *J. Phys.: Condens. Matter* **13**(47), 10689–10707 (2001), doi:10.1088/0953-8984/13/47/311.

[20] D. K. Saldin, R. J. Harder, V. L. Shneerson, and W. Moritz: "Surface x-ray crystallography with alternating constraints in real and reciprocal space." *J. Phys.: Condens. Matter* **14**(16), 4087 (2002), doi:10.1088/0953-8984/14/16/303.

[21] P. F. Lyman, V. L. Shneerson, R. Fung, R. J. Harder, E. D. Lu, S. S. Parihar, and D. K. Saldin: "Atomic-scale visualization of surfaces with x rays." *Phys. Rev. B* **71**(8), 081402 (2005), doi: 10.1103/PhysRevB.71.081402.

[22] R. Fung, V. L. Shneerson, P. F. Lyman, S. S. Parihar, H. T. Johnson-Steigelman, and D. K. Saldin: "Phase and amplitude recovery and diffraction image generation method: structure of Sb/Au(110)–$\sqrt{3} \times \sqrt{3}$R54.7 ° from surface X-ray diffraction." *Acta Crystallogr. A* **63**(3), 239–250 (2007), doi:10.1107/S0108767307002930.

[23] P. F. Lyman, V. L. Shneerson, R. Fung, S. S. Parihar, H. T. Johnson-Steigelman, E. Lu, and D. K. Saldin: "Structure and stability of Sb/Au(110)-c(2×2) surface phase." *Surf. Sci.* **600**(2), 424–435 (2006), doi:10.1016/j.susc.2005.11.019.

[24] M. Sowwan, Y. Yacoby, J. Pitney, R. MacHarrie, M. Hong, J. O. Cross, D. A. Walko, R. Clarke, R. Pindak, and E. A. Stern: "Direct atomic structure determination of epitaxially grown films: Gd_2O_3 on GaAs (100)." *Phys. Rev. B* **66**(20), 205311 (2002), doi:10.1103/PhysRevB.66.205311.

[25] Y. Yacoby, R. Pindak, R. MacHarrie, L. Pfeiffer, L. E. Berman, and R. Clarke: "Direct structure determination of systems with two-dimensional periodicity." *J. Phys.: Condens. Matter* **12**(17), 3929–3938 (2000), doi:10.1088/0953-8984/12/17/301.

[26] Y. Yacoby, M. Sowwan, E. A. Stern, J. O. Cross, D. Brewe, R. Pindak, J. Pitney, E. B. Dufresne, and R. Clarke: "Direct determination of epitaxial film and interface structure: Gd_2O_3 on GaAs (100)." *Phys. B: Condens. Matter.* **336**(1-2), 39–45 (2003), doi:10.1016/S0921-4526(03)00267-9.

[27] S. Marchesini, H. He, H. N. Chapman, S. P. Hau-Riege, A. Noy, M. R. Howells, U. Weierstall, and J. C. H. Spence: "X-ray image reconstruction from a diffraction pattern alone." *Phys. Rev. B* **68**(14), 140101 (2003), doi:10.1103/PhysRevB.68.140101.

[28] C. N. Cionca: *Imaging Interfaces in Epitaxial Heterostructures.* Ph.D. thesis, University of Michigan (2005).
URL `http://www.aps.anl.gov/Sectors/Sector7/Science/Publications/theses/CCioncaThesis.pdf`

[29] W. C. Hamilton: "Significance tests on the crystallographic R factor." *Acta Crystalogr.* **18**(3), 502–510 (1965), doi:10.1107/S0365110X65001081.

[30] D. P. Kumah, A. Riposan, C. N. Cionca, N. S. Husseini, R. Clarke, J. Y. Lee, J. M. Millunchick, Y. Yacoby, C. M. Schlepütz, M. Björck, and P. R. Willmott: "Resonant coherent Bragg rod analysis of strained epitaxial heterostructures." *Appl. Phys. Lett.* **93**(8), 081910 (2008), doi: 10.1063/1.2975835.

[31] Y. Yacoby, M. Sowwan, E. A. Stern, J. O. Cross, D. Brewe, R. Pindak, J. Pitney, E. M. Dufresne, and R. Clarke: "Direct determination of epitaxial interface structure in Gd_2O_3 passivation of GaAs." *Nat. Mater.* **1**(2), 99–101 (2002), doi:10.1038/nmat735.

[32] C. N. Cionca, D. A. Walko, Y. Yacoby, C. Dorin, J. M. Millunchick, and R. Clarke: "Interfacial

structure, bonding and composition of InAs and GaSb thin films determined using coherent Bragg rod analysis." *Phys. Rev. B* **75**, 115306 (2007), doi:10.1103/PhysRevB.75.115306.

[33] Y. Yacoby, J. O. Cross, D. A. Walko, C. N. Cionca, N. S. Husseini, A. Riposan, and R. Clarke: "Structural changes induced by metal electrode layers on ultrathin $BaTiO_3$ films." *Phys. Rev. B* **77**(19), 195426 (2008), doi:10.1103/PhysRevB.77.195426.

[34] R. Herger, P. R. Willmott, C. M. Schlepütz, M. Björck, S. A. Pauli, D. Martoccia, B. D. Patterson, D. P. Kumah, R. Clarke, Y. Yacoby, and M. Döbeli: "Structure determination of monolayer-by-monolayer grown $La_{1-x}Sr_xMnO_3$ thin films and the onset of magnetoresistance." *Phys. Rev. B* **77**, 085401 (2008), doi:10.1103/PhysRevB.77.085401.

[35] P. R. Willmott, S. A. Pauli, R. Herger, C. M. Schlepütz, D. Martoccia, B. D. Patterson, B. Delley, R. Clarke, D. P. Kumah, C. N. Cionca, and Y. Yacoby: "Structural basis for the conducting interface between $LaAlO_3$ and $SrTiO_3$." *Phys. Rev. Lett.* **99**, 155502 (2007), doi: 10.1103/PhysRevLett.99.155502.

Chapter 4

Growth of Thin $YBa_2Cu_3O_{7\text{-}x}$ Films

4.1 Introduction

The first superconducting cuprate thin films, albeit with a reduced critical temperature, were grown using sputter deposition of $YBa_2Cu_3O_{7\text{-}x}$ by Somekh *et al.* in April 1987 [1], only weeks after the discovery of superconductivity above liquid nitrogen temperatures in the Y-Ba-Cu-O compound system [2], and just one year after the epochal manifestation of high-temperature superconductivity in the La-Ba-Cu-O system [3]. What followed resembled a gold rush in materials synthesis and superconductivity research, spurring an unprecedented effort to discover even better materials, investigate the fundamental mechanisms of superconductivity and explore the exciting prospects for new technological devices. Common to all activities was the demand for well-characterized, high-quality samples. Especially with regard to device fabrication, but also in order to probe fundamental size and dimensionality effects, the successful growth of thin superconducting films represented a crucial step, and countless groups devoted their research to prepare those samples using various techniques. Within three months of Somekh's first results, Enomoto *et al.* [4] produced YBCO films with high T_c and critical current density J_c.

Pulsed laser deposition was to become one of the most powerful and versatile methods to grow superconducting thin films [5, 6], and the first results with YBCO presented by Dijkkamp *et al.* in August 1987 [7] reported transition temperatures close to the optimal bulk values of $T_c = 93K$.

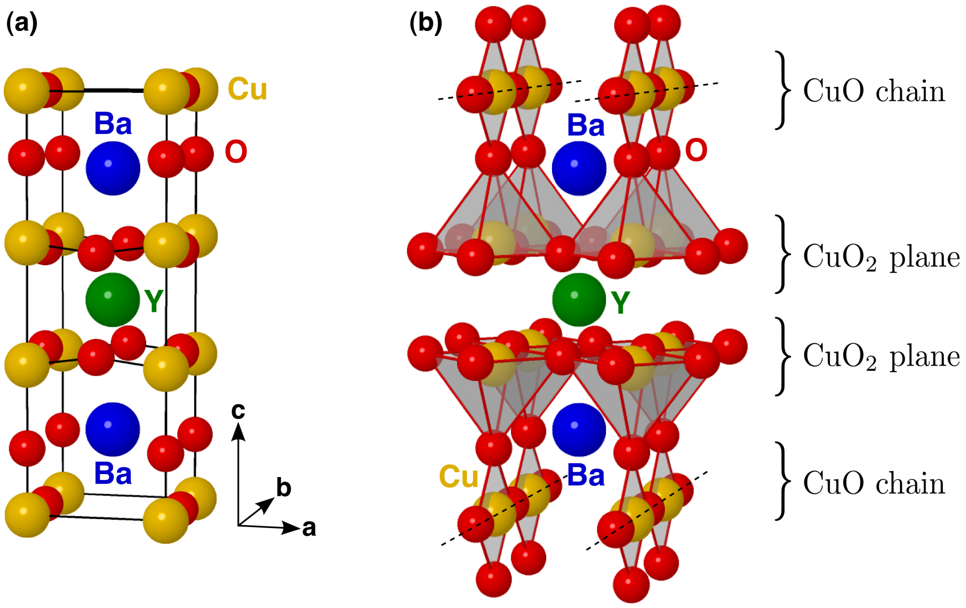

Figure 4.1: Atomic structure of $YBa_2Cu_3O_{7-x}$: (a) The orthorhombic unit cell of YBCO with the heavy atoms at the center positions. (b) Highlighting the structural features of YBCO: Y is surrounded by the two CuO_2 planes, while the two BaO layers are separated by CuO chains, running along the crystallographic b-direction.

4.2 The atomic structure of YBCO

The atomic structure of $YBa_2Cu_3O_{7-x}$ depends critically on the oxygen deficiency [8]. For values of $x \gtrsim 0.5$, the unit cell is tetragonal and YBCO is non-superconducting. At around $x = 0.5$, there is a structural phase transition from tetragonal to orthorhombic with increasing oxygen content (decreasing x). The orthorhombic structure, shown in Figure 4.1, is characterized by an ordering of the oxygen vacancies in the base plane between the Ba atoms, with oxygen atoms preferentially occupying the site in the bc-plane, resulting in the formation of CuO chains along the crystallographic b-direction [9].

The second prominent structural feature of YBCO are the two CuO_2 planes surrounding the Y layer, the former being responsible for the superconducting properties. The structure is obviously highly anisotropic with well-separated conduction layers along the c-direction, resulting in a much larger conductivity along the a and b-directions. For thin film applications, it is therefore important to obtain layers with their c-axis out-of-plane and the conducting layers running along the film plane.

4.3 Growth substrates

Thin films are grown on some sort of support or substrate onto which the material deposited. The chemical and crystallographic properties of the substrate will influence the formation of the thin film, at least in its initial phase, and consequently might affect its properties. While this may be seen as a serious handicap for studying the material in its unperturbed state, very importantly, it also allows one to purposefully tailor the properties of the thin films through the interactions with the substrate. In any case, whether it be to minimize its impact, or to achieve a certain response, the careful choice of an appropriate substrate material is crucial, and assuring a good and well-defined surface quality can only benefit the growth.

The ideal substrate should be lattice and thermal expansion matched and chemically compatible with the film material, and undergo no structural phase transitions between the film fabrication and device usage temperature. In view of possible microwave applications in HTSCs, the material should also have either a relatively low or high (and preferably isotropic) dielectric constant, plus a very low loss tangent [10]. In practice, each substrate will exert a different influence on the film characteristics. Since specific applications require certain properties, a good compromise for the particular purpose at hand has to be found. This explains why a wide variety of substrates has been used to grow YBCO thin films [5] (for example: Al_2O_3, yttria stabilized zirconia (YSZ), $SrTiO_3$, $NdGaO_3$, $(La_xSr_{1\text{-}x})(Al_yTa_{1\text{-}y})O_3$, $LaAlO_3$, $YAlO_3$, MgO, or CeO_2, to name but a few).

4.3.1 Choice of substrate materials

When the goal is heteroepitaxial growth of thin films with very smooth surfaces, as required for SXRD, the two most important aspects for choosing a substrate are (a) its lattice match to the film material to minimize the residual strain across the interface, and (b) an atomically flat surface to start with. Furthermore, the substrate should approximately match the film's thermal expansion coefficient γ and not undergo any structural phase transitions, in order to avoid crack or defect formation during heating and cooling. Because of their close structural similarity to YBCO, perovskite materials are ideal candidates. The cationic ordering of alternating A- and B-site layers is expected to prevail through the substrate-film interface, resulting in a well-defined stacking sequence. We will now briefly describe the three particular substrates chosen for this study. An overview of their most important physical properties compared to

YBCO is given in Table 4.1.

STO

$SrTiO_3$ (STO) in the (001) orientation is the prototypical substrate for YBCO growth. It is readily available in good twin-free crystal quality, has a good lattice match to YBCO (∼1.29%), and its surface can be prepared to be single terminated on the B-site layer (TiO_2) and made to be atomically flat (see Section 4.3.2). Its crystal structure is simple cubic with space group $Pm\bar{3}m$ and a lattice constant of $a = 3.9045$ Å, a model of which is shown in Figure 4.2(a). Below 105 K, however, it undergoes a structural phase transition and becomes orthorhombic. This is approximately 14 K above the critical temperature of YBCO.

LSAT

So-called mixed perovskites have been specifically developed for the growth of HTSC films [11]. They consist of perovskite structures where both the cationic A- and B-sites are randomly occupied by two or more different atomic species. $(La_xSr_{1-x})(Al_yTa_{1-y})O_3$ (LSAT) is a prominent member of this class of perovskite materials. It is particularly well suited for the growth of YBCO due to its excellent lattice match and outstanding microwave properties [12]. LSAT was first described by Mateika *et al.* [11] and Shimamura *et al.* [13]. Its standard composition is produced from a 30/70 mole % solid solution of $LaAlO_3$ (LAO) and Sr_2AlTaO_6 (SAT).

Despite the increasingly important role of LSAT as a HTSC substrate, there remains a considerable uncertainty regarding its crystal structure [14]. Most publications report a face-centered cubic structure (fcc, $Pn\bar{3}m$ symmetry) with a lattice constant of $a \simeq 7.73$Å [11–13, 15–20], while others treat it as a simple cubic structure (sc, $Pm\bar{3}m$ symmetry) with $a \simeq 3.87$ Å [21, 22]. Li *et al.* [14] and Runka *et al.* [23] found that both of the above structures can be present, depending on the degree of disorder of the Al/Ta cations, whereby a larger disorder results in the simple cubic case, and the higher order causes a superstructure and hence a doubling of the unit cell. Chakoumakos *et al.*, who have measured the simple cubic structure at elevated temperatures, claim that a slight structural distortion occurs upon cooling at around 150 K, lowering the symmetry of the structure to either tetragonal ($I4/mcm$) or orthorhombic ($Imma$) [21]. Finally, Xiao *et al.* obtained a tetragonal LSAT crystal at room temperature when using a $LaAlO_3$ rod as a growth seed [24], and also Steins *et al.* have measured a tetragonal structure ($I\bar{4}$) [25].

In spite of these discrepancies, all reports agree on the fact that the structural deviations from simple cubic are small, as can be seen in Figure 4.2(b). The structure of LSAT is closely related to its two mother compounds, SAT and LAO. By adjusting the relative concentration of the two mother compounds in the solid solution, and hence changing x and y, the lattice parameter can actually be continuously varied between that of LAO (7.585 Å, doubled unit cell) and that of SAT (7.797 Å). In our studies, we have used substrates with the standard composition of $(La_{0.27}Sr_{0.73})(Al_{0.65}Ta_{0.35})O_3$. Suitable preparation of the surface results in an almost complete single termination on the B-site layer (AlO_2/TaO_2) [26].

NGO

The third substrate type employed in this work is the (110) surface of $NdGaO_3$ (NGO). In contrast to LSAT(001) and STO(001), its surface unit cell is rectangular with an orthorhombicity of $\epsilon = (a - b)/(a + b) = 1.04 \times 10^{-3}$. For thin epitaxial films, it is hoped that this property will cause the YBCO unit cell, whose unperturbed (001) surface unit cell is also rectangular, to lock in with the substrate, and lift the orientational degeneracy it has on LSAT and STO due to their quadratic surface unit cells. Further features which make NGO very attractive as a HTSC growth substrate are its exceedingly good crystalline quality and the fact that its surface, in contrast to those of LSAT and STO, is naturally terminated on the A-site layer (NdO) [26], as will be discussed in Section 4.3.2.

NGO has an orthorhombic unit cell with lattice parameters $a = 5.426$ Å, $b = 5.496$ Å, and $c = 7.707$ Å. It consists of four heavily distorted perovskite units in the true crystallographic unit cell. The oxygen octahedra are tilted significantly, and even the Nd^{3+} ions are substantially displaced from their cubic high-symmetry positions. A structural model of the NGO unit cell is shown in Figure 4.2(c) and (d).

The symmetry of the bulk crystal structure of NGO has been a subject of debate. Early crystallographic studies by Geller [27] on rare earth gallates report on NGO belonging to the *Pbnm* space group[1]. The first dedicated structure determination with x-ray diffraction by

---

[1] Note that the *Pbnm* space group does not appear in the International Tables for Crystallography, since it is based on a non-standard notation of the unit cell axes. However, it seems to be the most common description

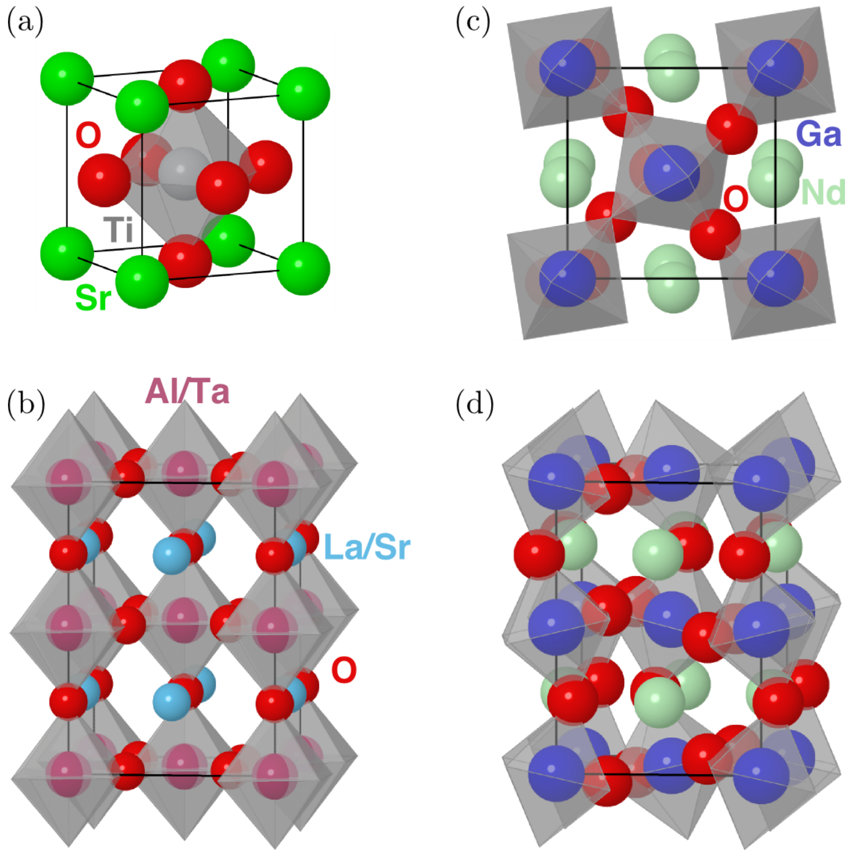

Figure 4.2: Atomic structure of the growth substrates: (a) The simple cubic unit cell of $SrTiO_3$. (b) The tetragonal unit cell of $(La_xSr_{1-x})(Al_yTa_{1-y})O_3$ [25]. No significant distortions away from a simple cubic lattice can be observed. (c) $NdGaO_3$ has an orthorhombic unit cell which is composed of four heavily distorted perovskite units, here seen from the top. Note the large rotations of the oxygen octahedra and the displacements of the Nd atoms from their high-symmetry positions. (d) The same $NdGaO_3$ unit cell seen in perspective, highlighting the significant octahedral tilts.

Brusset *et al.* [28] assigned NGO to the non-centro-symmetric $Pbn2_1$ space group, a fact which was confirmed by neutron powder diffraction by Marti *et al.* [29]. Other studies using x-ray powder diffraction [30] and Raman and IR spectroscopy [31] re-established the presence of an inversion center, correspondingly reverting to the centro-symmetric *Pbnm* space group. Also Marti *et al.* [32] revised their structural model using x-ray single crystal diffraction and thereby

---

for orthorhombic perovskite systems in the literature. The standard notation can be regained by a cyclic permutation of the unit cell axes assignments: $abc \rightarrow bca$. This transforms *Pbnm* into the tabulated standard space group *Pnma*.

confirmed the existence of centro-symmetry. Other recent studies by Vasylechko *et al.* [33, 34] further refined the structural parameters within this now firmly established model.

Material	Bulk crystal system	Surface unit cell a [Å]	b [Å]	symmetry	Orthorhombicity $\epsilon = \frac{a-b}{a+b}$	YBCO misfit [%] (a/b)	γ [10^{-6}/K]	Surface termination
STO(001)	cubic	3.905	3.905	$p4mm$	0	+0.45 / +2.13	9.4	B: TiO_2
LSAT(001)	cubic	3.866	3.866	$p4mm$	0	−0.54 / +1.12	8.2	B: $(Al/Ta)O_2$
NGO(110)	orthorhombic	7.723	7.707	pm	1.04×10^{-3}	−0.66 / +0.80	9.0	A: NdO
YBCO(001)	orthorhombic	3.887	3.823	$p2mm$	8.37×10^{-3}	–	10–13	?

Table 4.1: Structure and properties of the three used growth substrates, STO(001), LSAT(001), and NGO(110), in comparison with YBCO(001). (γ denotes the thermal expansion coefficient. The YBCO misfit is calculated as a/a_{YBCO} and b/b_{YBCO}. "+" denotes tensile strain on YBCO, "−" stands for compressive strain. For LSAT, the simple cubic structure is used, as described in the text.)

4.3.2 Substrate preparation

When striving for atomically controlled epitaxial thin film growth, a well-defined substrate surface to start with is a prerequisite for success.

Perovskite materials with a primitive composition of ABO_3 can be terminated either on their AO or their BO_2 plane, when cut perpendicular to one of their principle cubic or quasi-cubic axes, e.g., (100) or (001). Which termination is actually realized in nature depends on the subtle balance of chemical bond strengths and the feasibility of the system reaching its ground state of minimum energy. As a result, some materials are naturally A- or B-site terminated, while for others, the differences in surface energies are small enough to allow for a metastable coexistence of both terminations. In many cases, a careful annealing procedure can help the material to reach its single terminated ground state, while for other systems, chemically selective processes like etching must be employed.

NGO(001) has been shown to have an A-site terminated surface as its ground state [26]. The reported procedure to achieve this termination is a simple annealing step in air at 1000°C for two hours. Since the (110) NGO surface is chemically very similar to (001) and exhibits the same stacking of NdO and GaO_2 layers, it seems reasonable to assume that a similar annealing procedure would result in a single termination also for this orientation.

Mechano-chemically polished NGO(110) substrates (Crystec GmbH, Berlin) with miscut angles below 0.1° are annealed in a flow of pure oxygen (grade 5) at temperatures between 1100°C and 1200°C for 10 to 20 hours. And indeed, the AFM images recorded after the annealing display large uniform terraces with step edges of approximately 4 Å height [c.f. Figure 4.3 (a)], equal to the separation of two consecutive NdO or GaO_2 planes, respectively. This fact confirms a single termination. However, it cannot give any information as to which is the topmost atomic layer. Complementary techniques like low energy ion scattering (LEIS) or depth sensitive XPS would be required to clarify this. Externally conducted LEIS measurements (Calipso B.V., Technical University of Eindhoven, the Netherlands; not shown here) tend to support an NdO terminating layer, but lack sufficient accuracy for a quantitative analysis. Recent studies of heteroepitaxial STO growth on the prepared NGO substrates reported a SrO termination for the film, another circumstantial piece of evidence that the substrate is most likely NdO terminated [35].

The procedure to produce single terminated STO(001) is more intricate than for NGO, because it involves both chemical and thermal treatments, and has been the subject of intense research [36, 37]. The resulting surfaces are atomically flat and agreed to be 100% terminated on TiO_2, although the atomic structure at the surface is still the subject of debate and includes, besides a whole variety of surface reconstructions [38–52], the extensively discussed scenario of a TiO_2 double layer [44, 47, 48, 50–53] instead of a single layer. As to the consequences this might have for the growth of thin films remains to be investigated.

Briefly, the preparation itself consists of the four followings steps: Native mechano-chemically polished STO substrates are ultrasonically cleaned in Millipore grade water for 30 minutes. Thereby, the surface Sr reacts to form strontium-hydroxide complexes while Ti remains chemically inert. Wet etching in a buffered HF solution ($HF/NH_4F = 1/7$, pH ≈ 5.5) for one minute efficiently removes the hydroxide complexes while preserving the TiO_2 layers. After rinsing the substrates in Millipore water to remove any residual wet etch solution, they are dried in a stream of high-purity (grade 5) nitrogen gas. At this stage, the single termination is achieved, but the surfaces are generally rough on the unit cell scale and exhibit many small islands or etch pits. An annealing step at 950°C for 10 hours in a pure oxygen flow results in very smooth terrace steps and assures full oxidation of the STO surface. Figure 4.3 (b) shows an AFM image of the single terminated STO samples, and again, the measured terrace steps are equal to the height of a single unit cell.

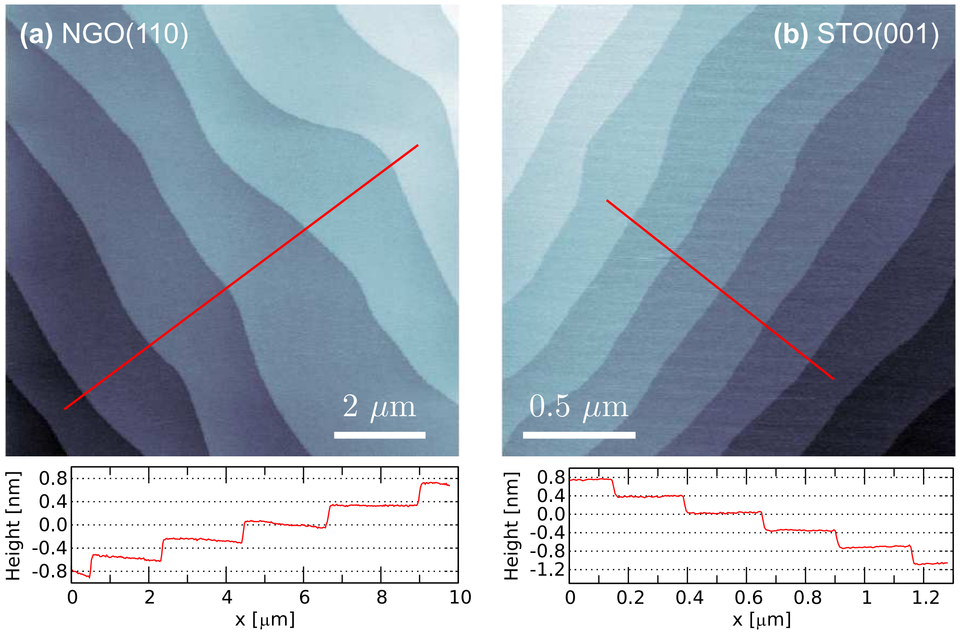

Figure 4.3: AFM images of prepared substrates: (a) NGO(110), (b) STO(001). The measured height profiles, evaluated along the red lines, are plotted below the images. Those profiles prove that the crystals are single terminated, since all terrace steps are one unit cell (≈ 4 Å) high.

4.4 Sample growth and characterization

4.4.1 In-house pulsed laser deposition growth

The initial objective of this thesis was the careful *in-situ* characterization of the initial YBCO thin films growth modes under reliably controlled conditions, and their resulting atomic structure with regard to film thickness measured on various technologically relevant substrates. A dedicated UHV chamber for *in-situ* pulsed laser deposition (PLD) experiments at the Surface Diffraction Station of the Materials Science Beamline, Swiss Light Source allows for simultaneous x-ray diffraction measurements during film growth [54, 55]. Furthermore, sample surfaces are kept clean for hours and even days under UHV conditions with a base pressure $< 10^{-9}$ mbar, opening up the possibility to interrupt the growth process at any desired point, carry out the necessary measurements to perform a full structure determination, and then continue to grow. The ultimate goal of achieving a full understanding of the growth process as a function of layer thickness and underlying substrate type thus becomes viable.

In order to perform such ambitious experiments, the routine production of reproducible high-quality superconducting YBCO thin films is an absolute prerequisite. Establishing the optimal conditions to grow excellent YBCO layers with PLD has been the subject of intense research, in particular for STO [7, 56–69] and NGO [70–80] substrates, and a general and consistent growth-“recipe” may be extracted from the reported findings.

Generally, near UV and visible lasers (190 nm $\lesssim \lambda \lesssim$ 532 nm) seem to be ideal for the ablation of complex oxide materials, as they are able to generate a congruent material transfer from the ablation target to the substrate, thereby ensuring the correct stoichiometry of the growing film. Typical laser pulse repetition rates range from 1 Hz to 10 Hz, and the laser energy and focus spot is adjusted to yield a laser fluence of 1.0–4.0 J cm^{-2}.

The substrate is placed three to eight cm away from the target in the direct propagation direction of the ablation plume, and held at temperatures ranging from approximately 670°C to 800°C. During the deposition process, a moderate background pressure of oxygen is necessary to ensure a sufficient oxygenation as the film grows and to supply the necessary equilibrium pressure to avoid oxygen loss in the film. The spread of employed pressures is very large, from 10^{-4} to several mbar, but many studies seem to have established that background pressures of approximately 0.1–0.2 mbar are ideal.

In most cases, as-grown films are oxygen deficient and need to be annealed in higher pressures to develop their best superconducting properties. Here, the reported procedures differ even more than for the growth process itself. The general consensus seems to be that oxygen pressures up to 1 bar should be introduced as soon as possible after growth while the substrate is slowly cooling down. During the cool down, the temperature is often fixed at certain values for prolonged periods.

Unfortunately, this fairly consistent understanding of the film growth does not define a sufficiently accurate procedure to achieve reliable results. Due to the very rich phase diagram of YBCO, its growth is very sensitive to small changes in the deposition conditions. Furthermore, each PLD apparatus has its unique characteristics, and growth parameters may not easily be transferred from one system to another. Therefore, the precise control and careful calibration of all parameters is necessary for each system, and finding the correct conditions is often a very time-consuming and painstaking procedure.

A critical point which requires careful attention is to ensure that growth proceeds within the

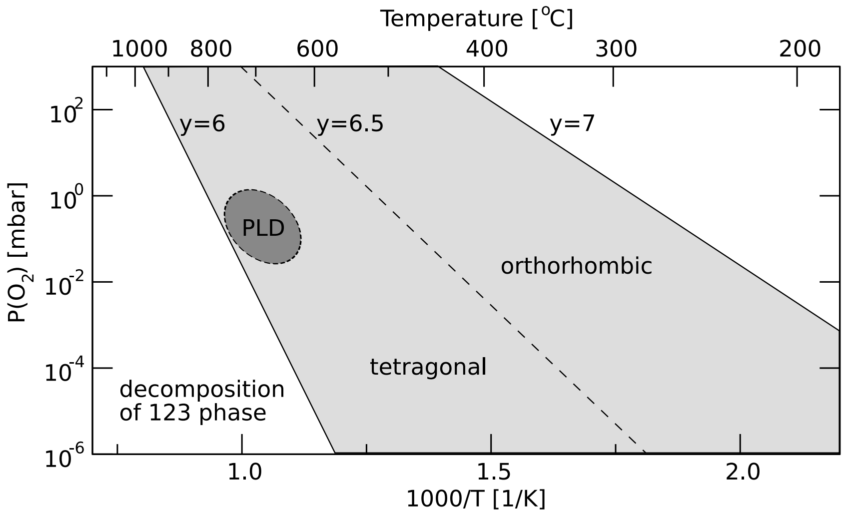

Figure 4.4: Temperature vs. partial oxygen pressure phase diagram for YBCO according to Bormann and Nölting [81] and Hammond and Bormann [82]. The decomposition line is indicated by y=6, above which the 123-phase is stable. The stability regime is divided up into a tetragonal and an orthorhombic crystallographic phase. PLD, as most film growth techniques, apparently works optimally in the tetragonal phase close to the decomposition line. (adapted from Ref. [6])

thermodynamic stability boundaries of the desired $YBa_2Cu_3O_{7\text{-}x}$ phase (the so-called "123"-phase). The applicable stability criteria have been investigated by Bormann and Nölting [81] and Hammond and Bormann [82][2]. If the partial oxygen pressure during growth is lower than a certain critical pressure, the perovskite structure decomposes into various other phases like Y_2BaCuO_5, $BaCuO_2$ and Cu_2O. This temperature-dependent phase boundary is located at the point where the oxygen content in the 123-phase drops below $y = 6.0$, i.e. where $x > 1$, as shown in Figure 4.4, which is an adaptation of Hammond and Bormann's original diagram [82] inspired by Wördenweber [6]. The phase transition from the tetragonal to the desired high-T_c orthorhombic 123-phase occurs for an oxygen content of at least 6.5 ($x \leqslant 0.50$). Apparently, the best growth normally proceeds in the tetragonal phase close to the decomposition line, where the temperature, and hence the surface mobility, is high, and partial oxygen pressures, and therefore the oxygen reactivity, relatively low. A transition to the orthorhombic phase and an ideal oxygenation of $7-x \approx 6.9$ of the compound is then achieved by an *in-situ* post-annealing step.

---

[2] Note, however, that the measured stability criteria apply to the bulk phase of YBCO and might be subject to significant changes for heteroepitaxial films, because of substrate-induced strain effects.

To aid the oxygenation during growth and to avoid falling into the decomposition regime for the relatively high substrate temperatures necessary to ensure a good surface mobility for the desired two-dimensional growth of the films, we have used two proven methods to enhance the oxygen pressure during the deposition: (a) A pulsed oxygen gas valve, synchronized to the laser frequency, increases the oxygen pressures during the arrival of the deposited material on the substrate, while maintaining a low average pressure inside the chamber in between laser shots [61, 67]. By crossing this gas pulse with the ablation plume, the gas species become highly activated and their reactivity is amplified [83]. This is hoped to ensure that sufficient oxygen is present during the very short times of extremely high deposition rates occurring for each laser pulse. (b) A bleed gas capillary can be pointed onto the sample surface to enhance the oxygen pressure even further during growth and help to maintain the equilibrium pressure locally without the need for a high overall background pressure inside the chamber [62, 84, 85].

Despite these efforts, we have not been able to reliably produce high-quality films. Good characteristics were obtained on a few occasions, but the growth conditions were not sufficiently stable to reproduce these properties from film to film. The best results obtained are shown in Figure 4.5. Panel (a) shows a θ-2θ-scan of an approximately 15 monolayer (ML) thick YBCO film grown on NGO(110). The Bragg peaks originating from the film prove that the YBCO is oriented with its c-axis out of the substrate plane, i.e., parallel to the NGO(110) direction. Between the Bragg peaks, the clear presence of Laue oscillations, caused by the finite layer thickness, proves that the film is exceedingly flat and of good crystalline quality. Unfortunately, the film is also insulating. The opposite phenomenon can be seen in panel (b), where the resistivity curve for a 70 nm thick superconducting film is shown. The transition is fairly broad, but has an onset at about 91 K. However, the film is very rough and far too thick for SXRD measurements.

The major stumbling block, we believe, is the substrate heating. The heating mechanism consists of clamping the growth substrate onto a Si-wafer of the same size, which can be heated by passing a current through it. This can be problematic since the Si oxidizes quickly at the typical oxygen pressures used for YBCO growth – a process which potentially deteriorates the electrical contact to the holder. If parts of the contact area start to conduct less efficiently, the current distribution through the wafer becomes non-uniform and those areas with a larger current begin to heat up more rapidly. Since Si is a semiconductor, the resistance in the hotter regions becomes smaller, causing even greater currents to flow there. The result is a classical runaway effect which cannot be sufficiently damped by thermal conduction processes. This

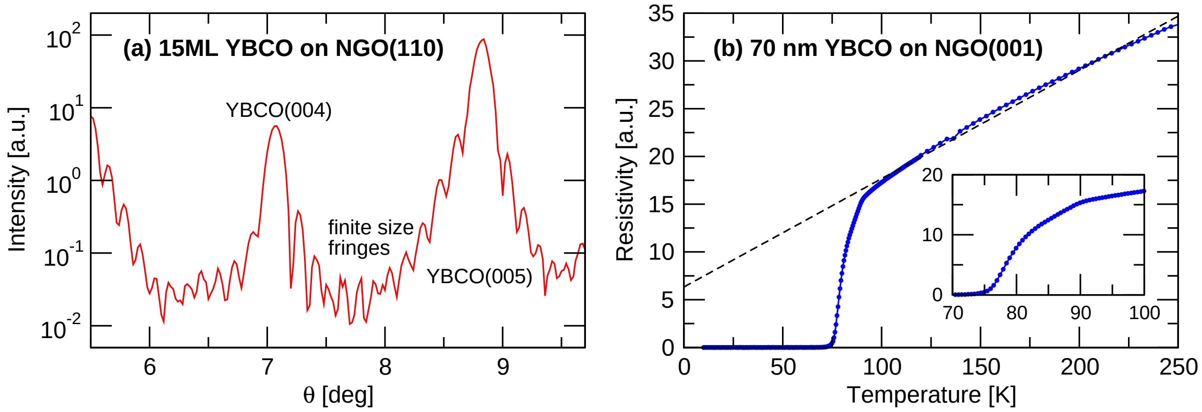

Figure 4.5: In-house results for the growth of YBCO films on NGO(110) (a) θ-2θ-scan for a 15 ML thick YBCO film, revealing clear finite size fringes. The sample was found to be insulating, however. (b) Resistivity curve for an approximately 70 nm thick YBCO film, showing a broadened superconducting transition (inset), centered around 82 K with an onset slightly above 90 K.

causes an inhomogeneous heating of the growth substrate where temperature differences can reach up to over a hundred degrees over the entire substrate area. In view of the complicated YBCO phase diagram, it seems very plausible that the reliability and reproducibility of film growth is severely hampered under these conditions.

A few alternative heating solutions have been tested, but assuring a reliable thermal contact to the substrates has remained elusive. Furthermore, most of these alternatives were not compatible with the requirements for *in-situ* x-ray measurements in grazing incidence geometry.

4.4.2 External pulsed laser deposition (Napoli)

Thin YBCO films of much better quality grown by PLD were produced by M. Radovic and F. Miletto Granozio at the University of Napoli, Italy. NGO(110) substrates were prepared at PSI according to the procedure described above (Section 4.3.2) and then sent to Italy. A KrF Excimer laser (λ = 248 nm) at a repetition rate of 1–2 Hz and a laser fluence of 2–3 J cm^{-2} was used for deposition in a background pressure of 0.25 mbar oxygen at a substrate temperature of approximately 800°C. After growth, the films were annealed in 200 mbar of oxygen at 450°C for 1 hour. The growth oscillations were monitored *in-situ* with RHEED and the clearly streaked diffraction patterns indicated good two-dimensional growth of the films.

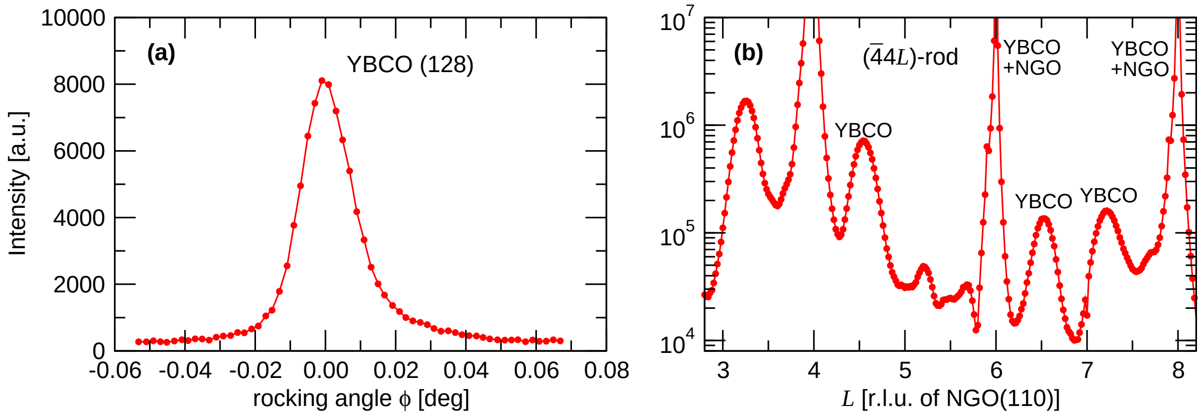

Figure 4.6: SXRD measurements on an approximately 4-5 ML thick YBCO film grown by the group in Napoli. (a) Rocking scan around the (128) YBCO Bragg peak (units of bulk YBCO). The presence of one single peak centered at the nominal in-plane position of the NGO reciprocal lattice proves that the film is fully strained (and therefore untwinned). (b) The $\bar{4}$4L CTR of YBCO on NGO(110). The YBCO Bragg peaks are clearly visible, but there are not finite size Laue oscillations in between those peaks – a clear indication for a non-uniform YBCO layer thickness.

LEED patterns measured on the same films corroborated the good surface quality and showed no evidence of any surface reconstructions.

The sample best suited for SXRD was the thinnest film, and approximately 4-5 monolayers thick (90 laser shots with PLD), as determined from the low-angle reflectivity and the widths of the YBCO Bragg peaks in a θ-2θ-scan. The crystalline properties of this film were further assessed with SXRD. Rocking scans around the (248) reflection show the presence of one single peak at an in-plane position, corresponding to the reciprocal lattice of the underlying NGO substrate, plotted in Figure 4.6 (a). This means that the film layer is fully heteroepitaxially strained. Twinning can only arise for relaxed films and is therefore not an issue here. Scans along the in-plane h- and k-axes reveal the absence of any extra peaks in between the integer substrate coordinates, so the YBCO unit cells must all be oriented with their c-axis out of the substrate surface plane. No reconstructions are present, as previously determined with LEED.

Crystal truncation rod scans show clear YBCO Bragg peaks with a separation of approximately 1/3 of a reciprocal substrate lattice unit, confirming the c-axis growth. An example of this is shown in Figure 4.6 (b), where the $\bar{4}$4L-rod (in units of the NGO surface unit cell) is plotted. In contrast to the scan shown in Figure 4.5 (a), however, there are no clear Laue oscillations between the YBCO Bragg peaks, indicating that the film does not have a well defined layer thickness, causing the oscillations to wash out. The same behavior could be seen on all other measured samples, though this was not unsurprising for the significantly larger YBCO thicknesses. Unfortunately, this non-uniformity in the film thickness poses a serious problem for direct methods and traditional fitting procedures when attempting to refine the structure. For the former, it results in a weakened support constraint and many atoms with partial occupation, which will be difficult to quantify, while for the latter case, the *a priori* unknown nature of the thickness variation needs to be modeled appropriately, introducing additional parameters.

The thickness variations are likely to be caused by the deposition process itself. The samples are relatively large (10×10 mm^2) and were held at a distance of only 3.5 cm from the ablation target. Firstly, the angular distribution of the ablated species inside the plume is not isotropic, but has a rather distinct forward direction, which is frequently modeled by a $\cos^n\theta$, with n ranging from 2 to over 20 [86]. Assuming a perfectly centered sample and an intermediate value of $n = 10$, $\cos(\arctan(5/35))^{10} \approx 0.9$ meaning that the edges of the grown film will be only 90% of the thickness at the center. The corners are even further away from the center, and there $\cos(\arctan(\sqrt{2}\cdot 5/35))^{10} \approx 0.82$. This situation rapidly worsens if the centering is non-perfect, so a thickness variation of 5±1 ML is not at all unsurprising.

In conclusion, the films are of excellent crystallinity, but their non-homogenous layer thickness is not ideal for SXRD experiments. This fact will be discussed in more detail in the later chapters concerned with the analysis and interpretation of the data.

4.4.3 Off-axis magnetron sputtering (Geneva)

Another set of high-quality samples was grown by Edmond Koller at the University of Geneva by rf magnetron sputtering in an off-axis geometry. The growth apparatus allows for the simultaneous deposition of several samples, assuring that they are subject to identical growth conditions, and thereby facilitating the direct comparison of their properties. Furthermore, the off-axis geometry results in a spatially much more homogeneous film growth than that achievable with PLD performed at very short target-to-sample distances.

Four different substrates of approximately $5\times5\times1$ mm^3 in size were used for the film growth: STO(001), LSAT(001), and two crystals of NGO(110). However, out of all four samples, only

Sample	Substrate	Treatment	T_c (5 nm)	T_c (30 nm)
SY107K13	$SrTiO_3$(001)	acetone cleaning	~ 43 K	~ 80 K
LY107K13	$(La_xSr_{1-x})(Al_yTa_{1-y})O_3$(001)	acetone cleaning	~ 68 K	~ 85 K
NY107K13	$NdGaO_3$(110)	acetone cleaning	~ 70/50 K	~ 86 K
NTY107K13	$NdGaO_3$(110)	O_2 annealing 1200°C	~ 65 K	~ 84 K

Table 4.2: Summary of samples grown by rf magnetron sputtering in Geneva by E. Koller: T_c (5 nm) gives the critical temperature for this particular film, and T_c (30 nm) refers to the transition temperature for the correspondingly prepared 30 nm thick film as detailed in the text.

one of two NGOs was treated with the previously discussed method to assure a single termination (see Section 4.3.2). The remaining substrates were simply cleaned with acetone as they were received. Table 4.2 gives a brief summary of the most important sample properties.

For the deposition process, the samples are glued to a substrate heater with silver paste to ensure a good thermal contact, and heated to the growth temperature of approximately 700 °C in vacuum. This rudimentary annealing step effectively removes any loosely bound contaminants on their surfaces. Once thermal equilibrium is reached, approximately 5 nm of $YBa_2Cu_3O_{7-x}$ are deposited in an atmosphere of 1.4×10^{-2} mbar of an O_2(20%)/Ar(80%) gas mixture using a stoichiometric densely pressed YBCO powder pellet as a sputtering target. After the deposition, the samples are slowly cooled to room temperature in 600 mbar of O_2 to achieve full oxidation of the film. Finally, a protective cap layer of 10 nm-thick amorphous $PrBa_2Cu_3O_{7-x}$ is deposited at room temperature on top of the YBCO to minimize oxygen out-diffusion from the YBCO layer and to minimize its degradation caused by exposure to ambient conditions.

SXRD experiments were carried out only a few days after film growth to further minimize the deterioration of the films with time. In order to preserve the best possible surface quality and cleanliness, all other characterizations were postponed until after the SXRD measurements had been completed, and could be performed only a few months later.

The presence of superconducting transitions in the thin YBCO films was assessed by inductance measurements, examples of which are shown in Figure 4.7 (a). Direct resistivity measurements could not be performed due to the difficulty in contacting the exceedingly thin and buried layers. From the graphs, it is immediately evident that all films exhibit a reduced critical temperature (T_c) compared to the bulk value for optimal doping of $T_c \simeq 91$ K. This is not unsurprising, as the structure of the thin films is indeed expected to be different from a

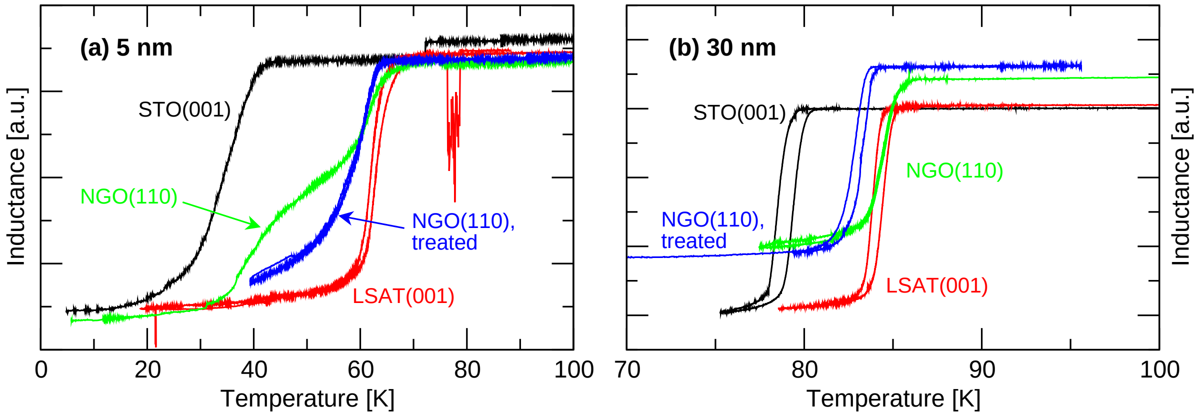

Figure 4.7: Inductance measurements of the magnetron sputtered YBCO films of (a) 5 nm, and (b) 30 nm thickness.

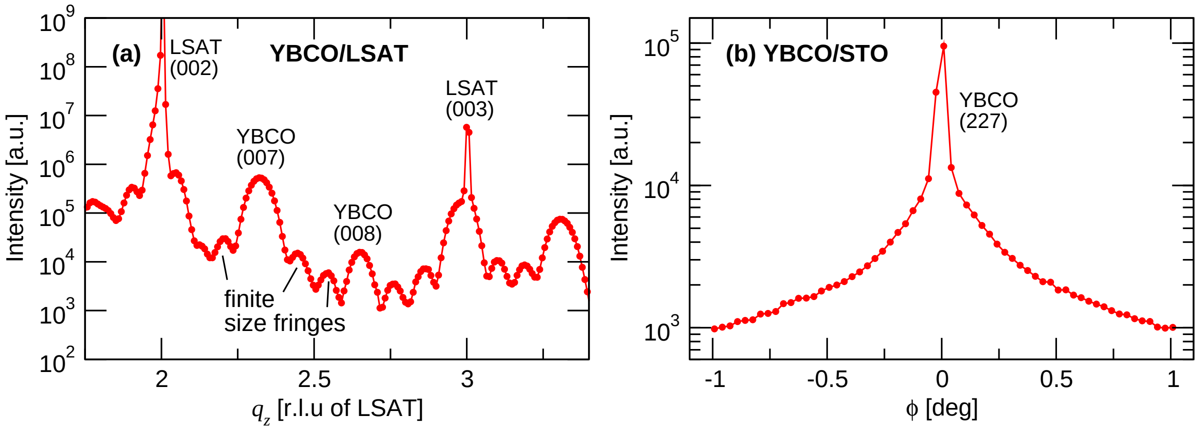

Figure 4.8: X-ray diffraction measurements on the magnetron sputtered YBCO films. (a) θ-2θ-scan (b) rocking scan (ϕ-scan) around the YBCO(227) Bragg peak.

bulk crystal, due to the strain induced by the heteroepitaxial growth on substrates with a slight lattice mismatch. To ascertain the suitability of the employed growth conditions, films with a thickness of 30 nm were deposited on a set of identical substrates and characterized carefully. The transitions are seen in Figure 4.7 (b) to be significantly closer to the optimal value, though the small difference still seems to suggest a finite size effect or a slight underdoping of the material.

The excellent crystalline quality of the thin films can be witnessed from the x-ray diffraction data in Figure 4.8. Panel (a) shows a θ-2θ-scan of the YBCO film grown on LSAT(001). The

YBCO Bragg peaks are clearly visible as well as the Laue fringes in between those Bragg peaks, caused by the finite and well-defined size of the film. The fact that two Laue fringes are present indicates that the film must be close to 4 ML of YBCO thick ($\approx$ 4.7 nm). An in-plane rocking scan across the (227) Bragg peak of YBCO is plotted in panel (b). The sharp peak shape and the absence of any side peaks show that the films are untwinned and epitaxially strained to match the substrate lattice parameters. Further in-plane scans (not shown) only yield signal at reciprocal lattice points corresponding to the LSAT bulk structure, proving that all YBCO unit cells are oriented with their c-axis out-of-plane.

Bibliography

[1] R. E. Somekh, M. G. Blamire, Z. H. Barber, K. Butler, J. H. James, G. W. Morris, E. J. Tomlinson, A. P. Schwarzenberger, W. M. Stobbs, and J. E. Evetts: "High superconducting transition temperatures in sputter-deposited YBaCuO thin films." *Nature* **326**(6116), 857–859 (1987), doi: 10.1038/326857a0.

[2] M. Wu, J. Ashburn, C. Torng, P. Hor, R. Meng, L. Gao, Z. Huang, Y. Wang, and C. Chu: "Superconductivity at 93 K in a new mixed-phase Y-Ba-Cu-O compound system at ambient pressure." *Phys. Rev. Lett.* **58**(9), 908–910 (1987), doi:10.1103/PhysRevLett.58.908.

[3] J. G. Bednorz and K. A. Müller: "Possible high T_c superconductivity in the Ba-La-Cu-O system." *Z. Phys. B: Condens. Matter.* **64**(2), 189–193 (1986), doi:10.1007/BF01303701.

[4] Y. Enomoto, T. Murakami, M. Suzuki, and K. Moriwaki: "Largely Anisotropic Superconducting Critical Current in Epitaxially Grown $Ba_2YCu_3O_{7-y}$ Thin Film." *Jpn. J. Appl. Phys.* **26**(Part 2, No. 7), L1248–L1250 (1987), doi:10.1143/JJAP.26.L1248.

[5] R. Singh and D. Kumar: "Pulsed laser deposition and characterization of high-T_c $YBa_2Cu_3O_{7-x}$ superconducting thin films." *Mater. Sci. Eng. R: Rep.* **22**(4), 113–185 (1998), doi:10.1016/S0927-796X(97)00019-3.

[6] R. Wördenweber: "Growth of high-T_c thin films." *Supercond. Sci. Tech.* **12**, R86–R102 (1999), doi:10.1088/0953-2048/12/6/202.

[7] D. Dijkkamp, T. Venkatesan, X. D. Wu, S. A. Shaheen, N. Jisrawi, Y. H. Min-Lee, W. L. McLean, and M. Croft: "Preparation of Y-Ba-Cu oxide superconductor thin films using pulsed laser evaporation from high T_c bulk material." *Appl. Phys. Lett.* **51**(8), 619 (1987), doi:10.1063/1.98366.

[8] K. Yvon and M. François: "Crystal structures of high-T_c oxides." *Z. Phys. B: Condens. Matter.* **76**(4), 413–444 (1989), doi:10.1007/BF01307892.

[9] R. J. Cava, B. Batlogg, C. H. Chen, E. A. Rietman, S. M. Zahurak, and D. Werder: "Single-phase 60-K bulk superconductor in annealed $Ba_2YCu_3O_{7-\delta}(0.3 < \delta < 0.4)$ with correlated oxygen vacancies in the Cu-O chains." *Phys. Rev. B* **36**(10), 5719–5722 (1987), doi:10.1103/PhysRevB.36.5719.

[10] J. M. Phillips: "Substrate selection for high-temperature superconducting thin films." *J. Appl. Phys.* **79**(4), 1829 (1996), doi:10.1063/1.362675.

[11] D. Mateika, H. Kohler, H. Laudan, and E. Völkel: "Mixed-perovskite substrates for high-T_c superconductors." *J. Cryst. Growth* **109**(1-4), 447–456 (1991), doi:10.1016/0022-0248(91)90215-Q.

[12] S. C. Tidrow, A. Tauber, W. D. Wilber, R. T. Lareau, C. D. Brandle, G. W. Berkstresser, A. J. V. Graitis, D. M. Potrepka, J. Budnick, and J. Z. Wu: "New substrates for HTSC microwave devices." *IEEE Trans. Appl. Supercond.* **7**(2), 1766–1768 (1997), doi:10.1109/77.620924.

[13] K. Shimamura, H. Tabata, H. Takeda, V. V. Kochurikhin, and T. Fukuda: "Growth and characterization of $(La,Sr)(Al,Ta)O_3$ single crystals as substrates for GaN epitaxial growth." *J. Cryst. Growth* **194**(2), 209–213 (1998), doi:10.1016/S0022-0248(98)00730-1.

[14] H. Li, L. Salamanca-Riba, R. Ramesh, and J. Scott: "Ordering in $(La,Sr)(Al,Ta)O_3$ substrates." *J. Mater. Res.* **18**(7), 1698–1704 (2003), doi:10.1557/JMR.2003.0233.

[15] H. Sakowska, M. Swirkowicz, K. Mazur, T. Łukasiewicz, and A. Witek: "Growth and Characterization of $(La,Sr)(Al,Ta)O_3$ Single Crystals: a Promising Substrate for GaN Epitaxial Growth." *Cryst. Res. Tech.* **36**(8-10), 851–858 (2001), doi:10.1002/1521-4079(200110)36:8/10¡851::AID-CRAT851¿3.0.CO;2-N.

[16] M. Ito, K. Shimamura, D. A. Pawlak, and T. Fukuda: "Growth of perovskite-type oxides $(RE,Sr)(Al,Ta)O_3$ as substrates for GaN epitaxial growth (RE=La,Nd)." *J. Cryst. Growth* **235**(1-4), 277–282 (2002), doi:10.1016/S0022-0248(01)01798-5.

[17] T. Łukasiewicz, M. Świrkowicz, H. Sakowska, A. Turos, M. Leszczyński, and R. Ratajczak: "New oxide crystal $(La,Sr)(Al,Ta)O_3$ as substrate for GaN epitaxy." *J. Cryst. Growth* **237-239**, 1118–1123 (2002), doi:10.1016/S0022-0248(01)02066-8.

[18] D. Tao, H. X. Wu, X. D. Xu, R. Yan, F. Y. Liu, A. P. B. Sinha, X. P. Jiang, and H. L. Hu: "Czochralski growth of $(La,Sr)(Al,Ta)O_3$ single crystal." *Opt. Mater.* **23**(1-2), 425–428 (2003), doi:10.1016/S0925-3467(02)00332-4.

[19] W. Wierzchowski, K. Wieteska, W. Graeff, H. Sakowska, T. Łukasiewicz, and M. Pawlowska: "Synchrotron X-ray investigation of $La_{0.3}Sr_{0.4}Al_{0.65}Ta_{0.35}O_3$ crystals." *Cryst. Res. Tech.* **40**(4-5), 517–522 (2005), doi:10.1002/crat.200410377.

[20] D. A. Pawlak, M. Ito, L. Dobrzycki, K. Wozniak, M. Oku, K. Shimamura, and T. Fukuda:

"Structure and spectroscopic properties of (AA')(BB')O_3 mixed-perovskite crystals." *J. Mater. Res.* **20**(12), 3329–3337 (2005), doi:10.1557/jmr.2005.0412.

[21] B. C. Chakoumakos, D. G. Schlom, M. Urbanik, and J. Luine: "Thermal expansion of $LaAlO_3$ and (La,Sr)(Al,Ta)O_3, substrate materials for superconducting thin-film device applications." *J. Appl. Phys.* **83**(4), 1979 (1998), doi:10.1063/1.366925.

[22] J. Kunert, M. Bäcker, M. Falter, and D. Schroeder-Obst: "Comparison of CSD-YBCO growth on different single crystal substrates." *J. Phys. Conf.* **97**, 012148 (2008), doi:10.1088/1742-6596/97/1/012148.

[23] T. Runka, K. Łapsa, A. Łapiński, R. Aleksiyko, M. Berkowski, and M. Drozdowski: "Spectroscopic study of mixed oxide SAT_{1-x}:LA_x perovskite crystals." *J. Mol. Struct.* **704**(1-3), 281–285 (2004), doi:10.1016/j.molstruc.2004.01.061.

[24] J. Xiao, M. Shao, Y. Tian, W. Huang, A. Wang, and S. Yin: "Czochralski growth and topographic study of tetragonal (La,Sr)(Al,Ta)O_3 single crystals." *J. Cryst. Growth* **236**(4), 671–675 (2002), doi:10.1016/S0022-0248(02)00853-9.

[25] M. Steins, J. Doerschel, and P. Reiche: "Crystal structure of aluminium lanthanum strontium tantalum oxide, $(La_{0.272}Sr_{0.728})(Al_{0.168}Ta_{0.352})O_3$." *Z. Kristallogr.: New Cryst. Struct.* **212**(2), 77 (1997).

[26] T. Ohnishi, K. Takahashi, M. Nakamura, M. Kawasaki, M. Yoshimoto, and H. Koinuma: "A-site layer terminated perovskite substrate: $NdGaO_3$." *Appl. Phys. Lett.* **74**(17), 2531 (1999), doi:10.1063/1.123888.

[27] S. Geller: "Crystallographic studies of perovskite-like compounds. IV. Rare earth scandates, vanadites, galliates, orthochromites." *Acta Crystalogr.* **10**(4), 243–248 (1957), doi:10.1107/S0365110X57000778.

[28] H. Brusset, H. Gillier-Pandraud, and J.-L. Berdot: "Structure cristalline du gallate de néodyme [$NdGaO_3$]." *Bull. Soc. Chim. Fr.* **8**, 2886 (1967).

[29] W. Marti, P. Fischer, F. Altorfer, H. J. Scheel, and M. Tadin: "Crystal structures and phase transitions of orthorhombic and rhombohedral $RGaO_3$ (R=La,Pr,Nd) investigated by neutron powder diffraction." *J. Phys.: Condens. Matter* **6**, 127 (1994), doi:10.1088/0953-8984/6/1/014.

[30] S. B. Ubizskii, L. O. Vasylechko, D. I. Savytskii, A. O. Matkovskii, and I. M. Syvorotka: "The crystal structure and twinning of neodymium gallium perovskite single crystals." *Supercond. Sci. Tech.* **7**, 766 (1994), doi:10.1088/0953-2048/7/10/012.

[31] D. I. Savytskii, D. Y. Sugak, A. Suchocki, I. V. Savytskii, V. I. Dzhala, and P. Kaczor:

"Optical spectroscopy and symmetry of $NdGaO_3$." *Proc. SPIE* **3178**, 283–286 (1997), doi: 10.1117/12.280753.

[32] W. Marti, P. Fischer, J. Schefer, and F. Kubel: "Structure characterization with neutron powder data of $LaGaO_3$ and $NdGaO_3$ based on X-ray single-crystal data: Evidence for an inversion center." *Z. Kristallogr.* **211**(12), 891–894 (1996).

[33] L. O. Vasylechko, A. O. Matkovskii, D. I. Savytskii, A. Suchocki, and F. Wallrafen: "Crystal structure of $GdFeO_3$-type rare earth gallates and aluminates." *J. Alloy Comp.* **291**(1-2), 57–65 (1999), doi:10.1016/S0925-8388(99)00247-9.

[34] L. O. Vasylechko, L. Akselrud, W. Morgenroth, U. Bismayer, A. O. Matkovskii, and D. I. Savytskii: "The crystal structure of $NdGaO_3$ at 100 K and 293 K based on synchrotron data." *J. Alloy Comp.* **297**(1-2), 46–52 (2000), doi:10.1016/S0925-8388(99)00603-9.

[35] M. Radovic, N. Lampis, F. M. Granozio, P. Perna, Z. Ristic, M. Salluzzo, C. M. Schlepütz, and U. Scotti di Uccio: "Growth and characterization of stable SrO-terminated $SrTiO_3$ surfaces." *Appl. Phys. Lett.* **94**(2), 022901 (2009), doi:10.1063/1.3052606.

[36] G. Koster, B. L. Kropman, G. J. H. M. Rijnders, D. H. A. Blank, and H. Rogalla: "Quasi-ideal strontium titanate crystal surfaces through formation of strontium hydroxide." *Appl. Phys. Lett.* **73**(20), 2920 (1998), doi:10.1063/1.122630.

[37] M. Kawasaki, K. Takahashi, T. Maeda, R. Tsuchiya, M. Shinohara, O. Ishiyama, T. Yonezawa, M. Yoshimoto, and H. Koinuma: "Atomic Control of the $SrTiO_3$ Crystal Surface." *Science* **266**(5190), 1540 (1994), doi:10.1126/science.266.5190.1540.

[38] J. E. T. Andersen and P. J. Moller: "Impurity-induced 900 °C (2×2) surface reconstruction of $SrTiO_3$(100)." *Appl. Phys. Lett.* **56**(19), 1847 (1990), doi:10.1063/1.103223.

[39] T. Matsumoto, H. Tanaka, T. Kawai, and S. Kawai: "STM-imaging of a $SrTiO_3$(100) surface with atomic-scale resolution." *Surf. Sci. Lett.* **278**(3), L153–L158 (1992), doi:10.1016/0167-2584(92)90249-5.

[40] M. Naito and H. Sato: "Reflection high-energy electron diffraction study on the $SrTiO_3$ surface structure." *Phys. C: Supercond.* **229**(1-2), 1–11 (1994), doi:10.1016/0921-4534(94)90805-2.

[41] Q. Jiang and J. Zegenhagen: "$SrTiO_3$(001) surfaces and growth of ultra-thin $GdBa_2Cu_3O_{7-x}$ films studied by LEED/AES and UHV-STM." *Surf. Sci.* **338**(1-3), L882–L888 (1995), doi:10.1016/0039-6028(95)00643-5.

[42] Q. Jiang and J. Zegenhagen: "c(6×2) and c(4×2) reconstruction of $SrTiO_3$(001)." *Surf. Sci.* **425**(2-3), 343–354 (1999), doi:10.1016/S0039-6028(99)00223-X.

[43] G. Charlton, S. Brennan, C. A. Muryn, R. McGrath, D. Norman, T. S. Turner, and G. Thornton: "Surface relaxation of $SrTiO_3$(001)." *Surf. Sci.* **457**(1-2), L376–L380 (2000), doi:10.1016/S0039-6028(00)00403-9.

[44] T. Kubo and H. Nozoye: "Surface Structure of $SrTiO_3$(100)-($\sqrt{5} \times \sqrt{5}$)-R26.6 °." *Phys. Rev. Lett.* **86**(9), 1801–1804 (2001), doi:10.1103/PhysRevLett.86.1801.

[45] A. Kazimirov, D. M. Goodner, M. J. Bedzyk, J. Bai, and C. R. Hubbard: "X-ray surface diffraction analysis of structural transformations on the (001) surface of oxidized $SrTiO_3$." *Surf. Sci.* **492**(1-2), L711–L716 (2001), doi:10.1016/S0039-6028(01)01442-X.

[46] N. Erdman, K. R. Poeppelmeier, M. Asta, O. Warschkow, D. E. Ellis, and L. D. Marks: "The structure and chemistry of the TiO_2-rich surface of $SrTiO_3$ (001)." *Nature* **419**(6902), 55–58 (2002), doi:10.1038/nature01010.

[47] M. R. Castell: "Nanostructures on the $SrTiO_3$(001) surface studied by STM." *Surf. Sci.* **516**(1-2), 33–42 (2002), doi:10.1016/S0039-6028(02)02053-8.

[48] K. Johnston, M. R. Castell, A. T. Paxton, and M. W. Finnis: "$SrTiO_3$(001)(2×1) reconstructions: First-principles calculations of surface energy and atomic structure compared with scanning tunneling microscopy images." *Phys. Rev. B* **70**(8), 085415 (2004), doi:10.1103/PhysRevB.70.085415.

[49] V. Vonk, S. Konings, G. van Hummel, S. Harkema, and H. Graafsma: "The atomic surface structure of $SrTiO_3$(001) in air studied with synchrotron X-rays." *Surf. Sci.* **595**(1-3), 183–193 (2005), doi:10.1016/j.susc.2005.08.010.

[50] F. Silly, D. Newell, and M. R. Castell: "$SrTiO_3$(001) reconstructions: the (2×2) to c(4×4) transition." *Surf. Sci.* **600**(17), 219–223 (2006), doi:10.1016/j.susc.2006.05.043.

[51] R. Herger, P. R. Willmott, O. Bunk, C. M. Schlepütz, B. D. Patterson, and B. Delley: "Surface of strontium titanate." *Phys. Rev. Lett.* **98**, 076102 (2007), doi:10.1103/PhysRevLett.98.076102.

[52] R. Herger, P. R. Willmott, O. Bunk, C. M. Schlepütz, B. D. Patterson, B. Delley, V. L. Shneerson, P. F. Lyman, and D. K. Saldin: "Surface structure of $SrTiO_3$(001)." *Phys. Rev. B* **76**, 195435 (2007), doi:10.1103/PhysRevB.76.195435.

[53] L. M. Liborio, C. G. Sánchez, A. T. Paxton, and M. W. Finnis: "Stability of Sr adatom model structures for $SrTiO_3$(001) surface reconstructions." *J. Phys.: Condens. Matter* **17**, L223–L230 (2005), doi:10.1088/0953-8984/17/23/L01.

[54] P. R. Willmott, R. Herger, C. M. Schlepütz, D. Martoccia, and B. D. Patterson: "Technical Reports: Pulsed Laser Deposition and in situ Surface X-ray Diffraction at the Materials Science Beamline at the Swiss Light Source." *Synch. Rad. News* **18**(4), 37–42 (2005), doi:10.1080/08940880500457230.

[55] P. R. Willmott, C. M. Schlepütz, B. D. Patterson, R. Herger, A. Lange, D. Meister, D. Maden, Ch. Brönnimann, E. F. Eikenberry, G. Hülsen, and A. Al-Adwan: "In situ studies of complex PLD-grown films using hard X-ray surface diffraction." *Appl. Surf. Sci.* **247**, 188–196 (2005), doi: 10.1016/j.apsusc.2005.01.133.

[56] G. Koren, A. Gupta, E. A. Giess, A. Segmüller, and R. B. Laibowitz: "Epitaxial films of $YBa_2Cu_3O_{7-\delta}$ on $NdGaO_3$, $LaGaO_3$, and $SrTiO_3$ substrates deposited by laser ablation." *Appl. Phys. Lett.* **54**(11), 1054 (1989), doi:10.1063/1.101559.

[57] G. Koren, A. Gupta, and R. J. Baseman: "Role of atomic oxygen in the low-temperature growth of $YBa_2Cu_3O_{7-\delta}$ thin films by laser ablation deposition." *Appl. Phys. Lett.* **54**(19), 1920 (1989), doi:10.1063/1.101496.

[58] M. Ohkubo, T. Kachi, T. Hioki, and J. Kawamoto: "Oxygen content control for as-deposited $YBa_2Cu_3O_x$ thin films by oxygen pressure during rapid cooling following laser deposition." *Appl. Phys. Lett.* **55**(9), 899 (1989), doi:10.1063/1.102449.

[59] T. Hase, H. Izumi, K. Ohata, K. Suzuki, T. Morishita, and S. Tanaka: "Partial oxygen pressure effects on the morphology of Y-Ba-Cu-O thin films in laser deposition process." *J. Appl. Phys.* **68**(1), 374 (1990), doi:10.1063/1.347149.

[60] M. Ohkubo, T. Kachi, and T. Hioki: "Epitaxial $YBa_2Cu_3O_x$ thin films with x=6–7 by oxygen in-diffusion following laser deposition." *J. Appl. Phys.* **68**(4), 1782 (1990), doi:10.1063/1.346609.

[61] A. Gupta and B. W. Hussey: "Laser deposition of $YBa_2Cu_3O_{7-\delta}$ films using a pulsed oxygen source." *Appl. Phys. Lett.* **58**(11), 1211 (1991), doi:10.1063/1.104367.

[62] K. H. Wu, J. Y. Juang, C. L. Lee, T. C. Lai, T. Uen, Y. S. Gou, S. L. Tu, S. J. Yang, and S. E. Hsu: "Optimization of depositing $Y_1Ba_2Cu_3O_{7-\delta}$ superconducting thin films by excimer laser ablation with CO_2 laser-heated substrates." *Phys. C: Supercond.* **195**(3-4), 241–257 (1992), doi:10.1016/0921-4534(92)90347-F.

[63] A. Gupta, M. Chern, and B. Hussey: "Layer-by-layer growth of cuprate thin films by pulsed laser deposition." *Phys. C: Supercond.* **209**(1-3), 175–178 (1993), doi:10.1016/0921-4534(93)90899-2.

[64] B. Dam, J. Rector, M. Chang, S. Kars, D. G. de Groot, and R. Griessen: "The laser ablation threshold of $YBa_2Cu_3O_{6+x}$ as revealed by using projection optics." *Appl. Surf. Sci.* **86**(1-4), 13–17 (1995), doi:10.1016/0169-4332(94)00372-6.

[65] B. Dam, C. Træholt, B. Stäuble-Pümpin, J. Rector, and D. G. de Groot: "The relation between the defect structure, the surface roughness and the growth conditions of $YBa_2Cu_3O_{7-\delta}$ films." *J. Alloy Comp.* **251**(1-2), 27–30 (1997), doi:10.1016/S0925-8388(96)02764-8.

[66] B. Dam, J. H. Rector, J. M. Huijbregtse, and R. Griessen: "The transition from 2D-nucleation

to spiral growth in pulsed laser deposited $YBa_2Cu_3O_{7-\delta}$ films." *Phys. C: Supercond.* **296**(3-4), 179–187 (1998), doi:10.1016/S0921-4534(97)01837-6.

[67] D. Marré, A. Diaspro, C. Ferdeghini, G. Grassano, I. Pallecchi, and A. S. Siri: "Two-dimensional growth of atomically smooth YBCO epitaxial films deposited by PLD in a pulsed oxygen flow." *Supercond. Sci. Tech.* **11**, 737–743 (1998), doi:10.1088/0953-2048/11/8/005.

[68] G. J. H. M. Rijnders, G. Koster, D. H. A. Blank, and H. Rogalla: "In-situ monitoring during PLD of $YBa_2Cu_3O_{7-\delta}$ using RHEED at high oxygen pressure." *IEEE Trans. Appl. Supercond.* **9**(2), 1547–1550 (1999), doi:10.1109/77.784689.

[69] J. Kim, D. B. Chrisey, C. M. Gilmore, and J. S. Horwitz: "Evidence of a critical film thickness for the early growth stage transition in $YBa_2Cu_3O_{7-\delta}$ thin films." *Supercond. Sci. Tech.* **13**, 417–420 (2000), doi:10.1088/0953-2048/13/4/314.

[70] M. Ece, E. G. Gonzalez, H.-U. Habermeier, and B. Oral: "Evolution of morphology, crystallinity, and growth modes of thin superconducting $YBa_2Cu_3O_{7-x}$ films on $SrTiO_3$ and $NdGaO_3$ substrates." *J. Appl. Phys.* **77**(4), 1646 (1995), doi:10.1063/1.358921.

[71] D. H. A. Blank, A. J. H. M. Rijnders, F. J. G. Roesthuis, G. den Ouden, and H. Rogalla: "Improved properties of Pulsed Laser Deposited YBaCuO on $NdGaO_3$ using CeO_2 template layers." *Appl. Surf. Sci.* **96-98**, 685–688 (1996), doi:10.1016/0169-4332(95)00544-7.

[72] D. Schweitzer, T. Bollmeier, B. Stritzker, and B. Rauschenbach: "Twinning of $YBa_2Cu_3O_7$ thin films on different substrates." *Thin Solid Films* **280**(1-2), 147–151 (1996), doi:10.1016/0040-6090(95)08210-7.

[73] C. Villard, G. Koren, D. Cohen, E. Polturak, B. Thrane, and D. Chateignier: "*ab*-Plane Anisotropy of Transport Properties in Unidirectionally Twinned $YBa_2Cu_3O_{7-\delta}$ Films." *Phys. Rev. Lett.* **77**(18), 3913–3916 (1996), doi:10.1103/PhysRevLett.77.3913.

[74] J. Rector, P. Koster, F. Peerdeman, D. G. de Groot, and B. Dam: "Twin-free $YBa_2Cu_3O_{7-\delta}$ films on (001) $NdGaO_3$ showing isotropic electrical behaviour." *J. Alloy Comp.* **251**(1-2), 114–117 (1997), doi:10.1016/S0925-8388(96)02781-8.

[75] K. H. Wu, S. P. Chen, J. Y. Juang, T. Uen, and Y. S. Gou: "Investigation of the evolution of $YBa_2Cu_3O_{7-\delta}$ films deposited by scanning pulsed laser deposition on different substrates." *Phys. C: Supercond.* **289**, 230 – 242 (1997).

[76] B. Dam, J. Rector, R. Surdeanu, R. J. Wijngaarden, G. Koster, F. Peerdeman, J. van Berkum, D. G. de Groot, and R. Griessen: "The ab-Anisotropy of Twinfree $YBa_2Cu_3O_{7-\delta}$ Films Above and Below T_c." *Phys. C: Supercond.* **282-287**(2), 665–666 (1997), doi:10.1016/S0921-4534(97)00482-6.

[77] B. Dam and B. Stäuble-Pümpin: "Growth mode issues in epitaxy of complex oxide thin films." *J. Mater. Sci.: Mater. Electron.* **9**(3), 217–226 (1998), doi:10.1023/A:1008882309295.

[78] L. Cao and J. Zegenhagen: "Elemental Substitution and Strain in $RBa_2Cu_3O_{7-\delta}$ Superconducting Thin Films." *Phys. Status Solidi B* **215**(1), 587–590 (1999), doi:10.1002/(SICI)1521-3951(199909)215:1¡587::AID-PSSB587¿3.0.CO;2-P.

[79] P. Gierłowski, E. Dynowska, A. Abaloshev, J. Pełka, W. Paszkowicz, D. Kostrzeska, C. Bähtz, and M. Knapp: "Structure of laser-modified $YBa_2Cu_3O_{7-x}$ thin films." *J. Alloy Comp.* **362**(1-2), 293–296 (2004), doi:10.1016/S0925-8388(03)00601-7.

[80] J. Nam, R. A. Hughes, J. P. Castellan, B. D. Gaulin, J. F. Britten, and J. S. Preston: "The origin of preferential twinning in $YBa_2Cu_3O_{7-\delta}$ thin films deposited on the (001) $NdGaO_3$ substrate." *J. Appl. Phys.* **97**(12), 123906 (2005), doi:10.1063/1.1926395.

[81] R. Bormann and J. Nölting: "Stability limits of the perovskite structure in the Y-Ba-Cu-O system." *Appl. Phys. Lett.* **54**(21), 2148 (1989), doi:10.1063/1.101513.

[82] R. Hammond and R. Bormann: "Correlation between the in situ growth conditions of YBCO thin films and the thermodynamic stability criteria." *Phys. C: Supercond.* **162-164**, 703–704 (1989), doi:10.1016/0921-4534(89)91218-5.

[83] P. R. Willmott: "Pulsed reactive crossed-beam laser ablation." *Appl. Phys. A: Mater. Sci. Process* **69**(7), S437–S440 (1999), doi:10.1007/s003390051433.

[84] R. K. Singh, L. Ganapathi, P. Tiwari, and J. Narayan: "Effect of processing geometry in oxygen incorporation and in situ formation of $YBa_2Cu_3O_7$ superconducting thin films by pulsed laser evaporation technique." *Appl. Phys. Lett.* **55**(22), 2351 (1989), doi:10.1063/1.102364.

[85] K. H. Wu, C. L. Lee, J. Y. Juang, T. M. Uen, and Y. S. Gou: "In situ growth of $Y_1Ba_2Cu_3O_{7-x}$ superconducting thin films using a pulsed neodymium:yttrium aluminum garnet laser with CO_2 laser heated substrates." *Appl. Phys. Lett.* **58**(10), 1089 (1991), doi:10.1063/1.104380.

[86] P. R. Willmott and J. R. Huber: "Pulsed laser vaporization and deposition." *Rev. Mod. Phys.* **72**(1), 315–328 (2000), doi:10.1103/RevModPhys.72.315.

Chapter 5

$YBa_2Cu_3O_{7\text{-}x}$ on $SrTiO_3$

5.1 Introduction

Despite an overwhelming number of studies about YBCO thin films grown on STO, there still remains a considerable deal of ambiguity regarding the epitaxial relationship between the substrate and the film layer, especially in terms of the arrangement of atomic layers at the interface, the effect of the substrate symmetry and lattice match on the crystallographic structure, and the surface termination of the film. With these global aspects still under debate, there has been little hope to investigate more subtle structural effects, for example slight distortions of the cationic lattice close to the interface in response to the abrupt change in composition or variations in the oxygen ordering and occupations as a result of strain and symmetry.

Most studies agree on the observation that the growth proceeds in a unit cell-by-unit cell manner [1, 2], even though the nucleation mechanism on the substrate surface has been reported to proceed in smaller sub-units for coverages below one monolayer (ML), which supposedly transform into the tetragonal or orthorhombic phases with the correct stoichiometry at coverages above one ML [3–5].

Among other aspects, there are certainly three important considerations to be made when analyzing the global features of the thin film structure: (i) the chemical matching at the substrate-film interface, (ii) the charge neutrality of the possible growth unit, and (iii) the formation of a thermodynamically stable surface. The first point (i) implies that the choice of substrate material and its termination are crucial for the resulting layer stacking across the interface, while (ii) then determines the set of possible growth units. A full unit cell of YBCO is always charge neutral, hence definitely constitutes a valid entity. Assuming a chemically fixed interface and growth unit, the terminating surface layer is in principle directly determined by factors (i) and (ii), but there is no guarantee that it represents a stable surface. Rather, the thermodynamical stability is, to a first approximation, governed by the cuprate structure itself, regardless of the underlying substrate. All other things being equal, a non-polar surface termination can be assumed to have a lower surface energy than a polar one, and is thus a more likely candidate.

The cleaving plane of YBCO perpendicular to its *c*-axis lies between the CuO-chain layer and one of the two neighboring BaO layers [6–8]. The vast majority of surface studies on thin films and bulk crystals confirm these two surfaces as terminating layers, either as a mixture of both [9], a pure BaO termination [10–12], or a pure CuO termination [3, 13–15]. However, a few reports about other terminations also exist, among them an SXRD study on single crystal YBCO surfaces, finding Y to be the final layer [16].

The situation at the interface with the substrate was also heavily debated, but presents a fairly consistent picture. All studies confirm the alternation of A- and B-type layers prevailing across the interface. This seems to be a sensible prerequisite for the chemical matching. Depending on the topmost STO substrate layer, the structure is either TiO_2–SrO|CuO_2–BaO or SrO–TiO_2|BaO–CuO_2 [4, 5, 11, 17–20]. The possibility of a SrO–TiO_2|Y–CuO_2 stacking has never been reported, but rather firmly excluded, based on experimental evidence, in one particular study [17].

Performing SXRD experiments on ultra-thin YBCO films gives one the opportunity to investigate the interface and surface of the structure simultaneously, in contrast to most other studies focussing predominantly on only one of these two aspects.

5.2 SXRD measurements and data reduction

The structural studies of YBCO films grown on STO presented here have been carried out on a high-quality sample grown by off-axis magnetron sputtering by E. Koller at the University of Geneva. Sample preparation and initial characterization have been detailed in Section 4.4.3. SXRD measurements on this system were performed at room temperature using 16.000(1) keV synchrotron radiation ($\lambda = 0.7749$ Å). The sample was kept under moderate vacuum conditions (estimated pressure between 10^{-5} and 10^{-2} mbar) inside a small spherical beryllium dome with a wall thickness of 0.5 mm. The cubic unit cell of $SrTiO_3$ (STO) has been used as the reference lattice during data acquisition and analysis. Its real space lattice parameter of $a = 3.9045$ Å results in a reciprocal lattice unit (r.l.u.) of $2\pi/a = 1.6092\text{Å}^{-1}$.

A large CTR data set has been acquired on this system. For the chosen x-ray energy, and requiring that all diffractometer angles should not exceed 90^o, only those rods with in-plane indices satisfying $h^2 + k^2 < 26$ could be reached, and were scanned in l-steps of 0.01 r.l.u. starting from $l = 0.2$ up to the highest reachable point on the CTR. All rods in the first quadrant ($h, k \geqslant 0$) of reciprocal space were recorded. Based on symmetry arguments (see later), which were confirmed by a comparison of all the CTRs belonging to the $(21l)$ family, this is sufficient to reconstruct the entire diffraction pattern. However, to investigate systematic effects, a large number of randomly selected rods in the remaining three quadrants were also recorded. Unfortunately, the specular $(00l)$ rod was acquired under different experimental conditions, and could not be merged into the final data set.

Several groups have observed surface superstructures on YBCO or on structurally very similar $R\text{Ba}_2\text{Cu}_3\text{O}_{7-x}$ (R = rare earth ion) films, in particular a (2×2), c(2×2), (2×1), and c(4×4) reconstruction [9, 10, 21, 22], which are commonly attributed to ordering of oxygen vacancies in the system. The diffraction pattern has therefore been extensively searched for signs of surface or interface reconstructions at non-integer reciprocal lattice positions, also for different types than those reported, but no indications for the formation of any superstructures could be found on the sample.

The recorded SXRD data were then analyzed according to the procedures described in Appendix C. A total of 16 472 structure factors on 43 different CTRs could be extracted from the data set and corrected appropriately. In general, the diffraction features were very clean and sharp. Around the Bragg peaks of the thin YBCO films, there were significant contributions of diffuse scattering arising from the film layer, the exact origin of which is unknown. Nevertheless, it was possible to reliably subtract this background and obtain the pure diffraction intensities from coherent bulk and film scattering.

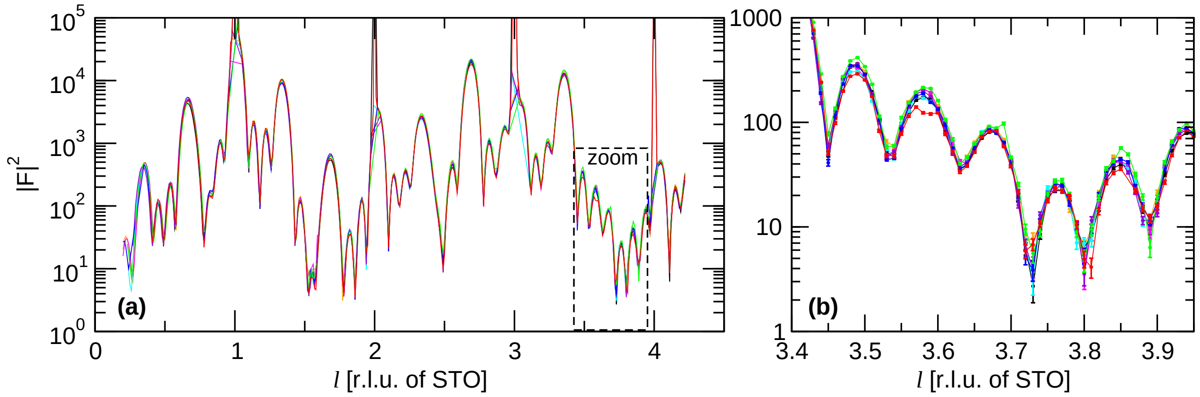

Figure 5.1: Plot of all eight $p4mm$-symmetric CTRs of the $(21l)$-family. (a) Overview of the entire CTRs. Significant deviations are visible at low l-values. (b) Enlargement of the zoom area marked in the left panel. The statistical error bars for all eight rods are also shown here, demonstrating that the systematic deviations between equivalent rods are the major source of errors in this set.

5.2.1 Symmetry considerations

The first very important question about the data set concerns its symmetry. STO(001) has a $p4mm$ surface symmetry, whereas that of the orthorhombic bulk-like YBCO(001) is only $p2mm$. For a combination of the two pure bulk structures, the total symmetry would correspond to the lower $p2mm$. There are two good reasons why the diffraction pattern we see should nevertheless be $p4mm$ symmetric. First, assuming a bulk-like YBCO structure grown on STO, we would expect there to be two domains in the film, due to the fact that there is no preferred in-plane orientation of the a and b-axes of YBCO with respect to the quadratic surface unit cell of STO. In the absence of terrace steps, which are very rare according to the low miscut of the substrates, or any other symmetry breaking features on the substrate surface, the population of both domains should be equal. In this case, the diffraction pattern represents the averaged domain structure of individual $p2mm$ domains rotated by 90^o with respect to each other, resulting in an overall apparent $p4mm$ symmetry.

Secondly, we are not dealing with a bulk-like film structure, but rather an epitaxially strained YBCO film which assumes the in-plane lattice parameters of the quadratic surface unit cell of STO, as was confirmed by scans across the YBCO Bragg peaks perpendicular to the l-direction. This lifts the a-b asymmetry of YBCO itself and results naturally in a $p4mm$ symmetric diffraction pattern.

Figure 5.1 shows a plot of the eight CTRs from the $(21l)$ and $(12l)$ families, indicating clearly that the diffraction pattern has in fact $p4mm$ symmetry. This is confirmed by the calculation of the systematic errors between nominally equivalent reflections (refer to Section C.9 for a definition), which give $\epsilon_{\mathrm{std}} = 0.1054$ for the mean total error between equivalents, $\epsilon_{\mathrm{stat}} = 0.0173$ for the statistical contribution alone, and $\epsilon_{\mathrm{syst}} = 0.1040$ for the systematic contribution. This has to be compared to the same values calculated for a $p2mm$ symmetry: $\epsilon_{\mathrm{std}} = 0.1042$, $\epsilon_{\mathrm{stat}} = 0.0146$, $\epsilon_{\mathrm{syst}} = 0.1032$. The latter are only insignificantly smaller, whereas one would expect a large effect if the $p2mm$ symmetry was in fact the real symmetry of the data set. We therefore conclude that the $p4mm$ is the correct symmetry of the diffraction pattern and hence the atomic structure.

The averaging procedure leads to a total of 5397 independent structure factors on 14 inequivalent rods, and an irreducible reciprocal space volume contained in one octant of the in-plane coordinate grid ($0 \leqslant h$ and $0 \leqslant k \leqslant h$ for all inequivalent reflections).

The forced increase in symmetry of the YBCO film has important consequences for its structure. A prominent feature of the YBCO structure in its bulk form are the CuO chains along the crystallographic b-direction, separated by oxygen voids in the a-direction. This in-plane directionality disappears with the straining of the film, however, and the effect on the structure of the Cu planes formerly containing the CuO chains needs to be investigated.

5.3 Solving the structure

Analysis of the fringe spacing of the finite-size Laue oscillations seen in Figure 5.1, immediately shows that the film thickness is of the order of four monolayers (ML) of YBCO, possibly containing a partially occupied fifth layer. The presence of strong Bragg peaks, spaced approximately $^1/_3$ of an STO l-unit apart from each other, proves that the film is composed of structural units equivalent to about three STO unit cells in height, or in other words, that it is made from entire unit cells of the correct YBCO crystal structure and not some random collection of structural sub-units.

Previous studies on the structure of perovskite substrate-film systems have shown that significant distortions in the substrate are possible down to a few unit cells [23–25]. This means that solving the structure of this particular system involves finding the positions of roughly 85 atoms. (Not all atoms are symmetry-independent, though. The $(^1/_2, 0, z)$ and

(0, $^1/_2$, z) positions are related through a 90 degree rotation, hence the 2 atoms must have identical z-movements to satisfy the symmetry.) Including intermixing effects at the interface, partial occupations, and global Debye-Waller factors for each atomic species, this leads to a refinement problem with at least 70 independent parameters, but more likely with more than 100 for the more detailed models. As discussed extensively in Chapter 3, this represents a huge challenge for traditional refinement procedures, and bears the inevitable risk of ending up in a local minimum rather than finding the true solution.

To complicate things further, the choice of a starting model is far from obvious. Especially the correct layer stacking at the interface is a moot point. Chemically, it seems reasonable that the alternating stacking of AO and BO_2 layers in perovskites should prevail across the interface, continuing the network of oxygen octahedra enclosing the small cations, although the formation of interfaces with stacking faults cannot be categorically excluded. Since a properly prepared STO substrate terminates on a TiO_2 layer, the first YBCO layer is expected to be either BaO or Y. This still allows for three different stacking models of the atomic layers (here, "B" denotes the B-site (TiO_2) termination of the substrate and "|" stands for the nominal interface position):

- B1: substrate–SrO–TiO_2 | BaO–CuO_2–Y–CuO_2–BaO–CuO–...
- B2: substrate–SrO–TiO_2 | BaO–CuO–BaO–CuO_2–Y–CuO_2–...
- B3: substrate–SrO–TiO_2 | Y–CuO_2–BaO–CuO–BaO–CuO_2–...

These items do not include the possibility of a TiO_2 double layer at the STO surface (see Section 4.3.2), which would produce an awkward stacking sequence of substrate–A–**B**–**B** | A'–B'–... Indeed, other studies of $(La_xSr_{1-x})MnO_3$ [25] or $LaAlO_3$ [24] thin films grown on single terminated STO clearly do not support the presence of such a double layer, which, in turn, raises the question what happens to that layer during the initial stages of the growth. The incorporation of the corresponding atoms into the growing film has been discussed as a possible scenario, opening up the possibility for yet another new set of possible structures.

In contrast to many other studies, the substrate used for growing the particular film under investigation here has not been prepared for a single termination, meaning that its surface most probably had a mixed termination of TiO_2 and SrO before starting the growth. Considering the case of an at least partially SrO terminated substrate leads to three more possible stacking sequences ("A" stands for the A-site (SrO) termination):

- A1: substrate–TiO_2–SrO | CuO–BaO–CuO_2–Y–CuO_2–BaO–...
- A2: substrate–TiO_2–SrO | CuO_2–BaO–CuO–BaO–CuO_2–Y–...
- A3: substrate–TiO_2–SrO | CuO_2–Y–CuO_2–BaO–CuO–BaO–...

If both terminations were present at the same time, the resulting structure could be made up from any combination of the individual possible scenarios, leading to another increase in the number of structures to be tested.

Similarly, the surface termination of the YBCO film is not known, and, in fact, should be determined through the structure solution. In principle, all 6 atomic layers of YBCO have to be considered possible candidates. Assuming that the growth of YBCO films proceeds in a unit cell-by-unit cell mode, the stacking sequence at the substrate–film interface should determine the topmost atomic layer. However, not all of the corresponding layers might represent stable surfaces. Also here, various different cases therefore need to be considered.

To cut a long argument short, the vast variety of possible starting models to be tested, in combination with the large number of free parameters for each model, renders the structure solution via traditional refinement procedures impracticable. On the other hand, a large and fairly complete diffraction data set[1] is available for this system, which lends itself to the application of direct methods. These should provide an unbiased, model-free structure determination directly from the diffraction data.

5.3.1 First attempts to retrieve the structure

COBRA

The first attempts to retrieve the atomic structure of the approximately 4 ML-thick film have been made with the COBRA algorithm. The method has been described in detail in Section 3.4.3. In contrast to other direct methods, COBRA is not entirely model-free for the surface or film structure, but relies on a rough starting guess. While this is somewhat contradictory to our aim of getting an independent initial model, it is hoped that the changes induced in the retrieved electron density which are generated from a wrong starting model will make apparent the necessary modifications to obtain the true structure.

---

[1] where complete means that all the measurable data points within a given resolution shell have been measured, or can be reconstructed from measured reflections through the application of symmetry operations.

To verify this last hypothesis, two different stacking sequences were used as reference structures, namely A1 and B1 from the above listings. B1 seems to be the favored model in the literature for a B-site terminated substrate, and A1 represents the corresponding stacking for an A-site termination.

Before starting the actual phase-retrieval step, a small number of global parameters describing the model need to be refined in order to guarantee a good approximate match between the data and the starting model structure factors. This includes a scale factor for the data set[2], average Debye-Waller (DW) factors for the substrate atoms and the film atoms, and usually a fit of the layer occupations in the film. For the film under investigation, we have fitted a global scale factor, DW factors for film and substrate atoms, the layer occupation of the fourth and fifth YBCO layers and an expansion coefficient for the strained YBCO unit cell with regard to its c-axis lattice parameter in bulk form. The fitted layer occupation of the 5th layer remained consistently below 5%, and gave between 60% and 80% for the fourth layer, while the c-axis lattice expansion of less than 1% was insignificant for the starting guess. As a result, the starting model used the bulk-like c-axis positions and a layer occupation of 75% for the fourth layer, and excluded the fifth layer completely.

The phase-retrieval support constraint was deliberately chosen to include a one ML-high empty region above the surface to allow for any indications for a fifth layer to reappear in the electron density. On the substrate side, 4 ML of STO have been included in the support to monitor structural changes induced by the presence of the film.

The results of the phase retrieval runs for the two starting models are compared in Figure 5.2. For clarity, the two graphs have been offset horizontally by approximately one half of an STO unit cell, such that the ionic lattice of the two YBCO films coincide vertically. It is immediately evident that the two structure solutions are not identical, i.e., that the choice of the starting model influences the final answers, which in these two cases are exceedingly similar to the starting models. The expectation that by using the wrong reference structure, significant changes would be induced in the electron density (ED) is not fulfilled. Rather, the opposite seems to be true here. Both ED maps, based on the same data set, look physically reasonable, even though they represent different structures. The biggest discrepancies (highlighted in

---

[2] The absolute scaling obtained through the careful corrections of the data, described in detail in Chapter C, is not valid here, because COBRA does not use the usual definition of atomic form factors but uses a Gaussian approximation, which results in a different scaling with respect to the measured data.

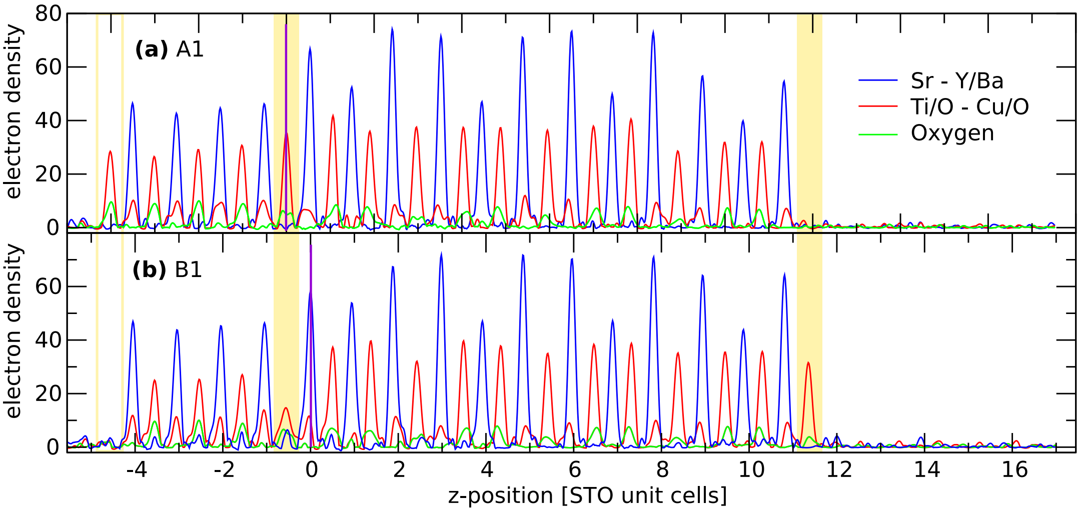

Figure 5.2: Comparison of the first two COBRA phase retrieval runs. Plotted is the retrieved electron density (in arbitrary units) along the out-of-plane direction for three lines going through the high-symmetry atomic positions of the starting models. In (a), the stacking sequence A1 with a SrO terminated STO was used as a reference, while (b) displays the result of starting from B1, having a TiO_2 termination of the substrate. The violet lines mark the nominally first atomic plane of the YBCO film. The two graphs have been offset horizontally by approximately half of an STO unit cell to highlight the structural changes with respect to the ionic network of the YBCO film itself. The regions highlighted in yellow contain the largest discrepancies.

yellow) are seen for the terminating substrate layer, which seems to become slightly disordered for model B1, and the film termination, which maintains those of the initial reference structures in both cases. It should also be noted that the comparison to the measured data yields very comparable R-factors of approximately 5% for both results.

Clearly, at least one of two ED maps (or possibly both) cannot represent the real structure. Neither of them, however, gives any conclusive indications what changes would be required to yield the true structure. In conclusion, COBRA does not seem to be able to unequivocally resolve the ambiguity regarding the correct stacking sequence and surface termination for this particular case. Therefore, the next step is to turn to a truly model-independent phase-retrieval method.

DCAF

The DCAF method, described in Section 3.4.2, is completely model-independent insofar that it does not require any atomic information about the film structure. Rather, the ED inside the chosen support region is initialized with random values, and the algorithm only uses the reference structure of the bulk and the measured structure factors to retrieve the ED map.

Although DCAF is model-free, there are a few parameters in the algorithm which need to be optimized for the problem at hand. As in the case for the COBRA analysis, the support constraint for DCAF was originally chosen to be large enough to accommodate five ML of YBCO on top of two ML of STO. However, no indications for the presence of a fifth layer were found in any of the runs. At this point, the support was reduced to four ML of YBCO plus two ML of STO, thereby strengthening the corresponding constraint, which in turn resulted in a much improved convergence stability of the algorithm. Another parameter which influences the reliability of the retrieved ED is the threshold value for the identification of atoms employed by the atomicity constraint. The algorithm becomes unstable when the threshold level approaches the noise level caused by the non-perfect structure-factor measurements. Choosing too high a threshold, on the other hand, prohibits the identification of lighter atoms inside the real structure, thereby also deteriorating the performance. During the identification of a proper threshold level, it was noticed that applying a slight scaling to the structure factors also improved the results. This is despite the fact that the structure factors were carefully corrected to yield absolute measurements. However, confirming the absolute scaling and obtaining an estimate of the uncertainty involved in the process is only possible through the comparison with a known structure, and has not yet been achieved. The scaling factor applied in DCAF was approximately 1.4, which may be well within the experimental uncertainty.

It should be made very clear that the optimization of the threshold, support and scaling parameters discussed here only affect the performance of the DCAF algorithm, but have never been observed to produce ambiguities in the actual structure solution. In other words, the use of non-ideal parameters usually causes the obtained solutions to be less accurate and more difficult to interpret, and in many cases obstructs a proper convergence, but does not produce structure solutions contradictory to those obtained with the ideal parameters. Rather, the optimization seems to be independent of the type of solution obtained and is therefore legitimate, preserving the *a priori* nature of the approach.

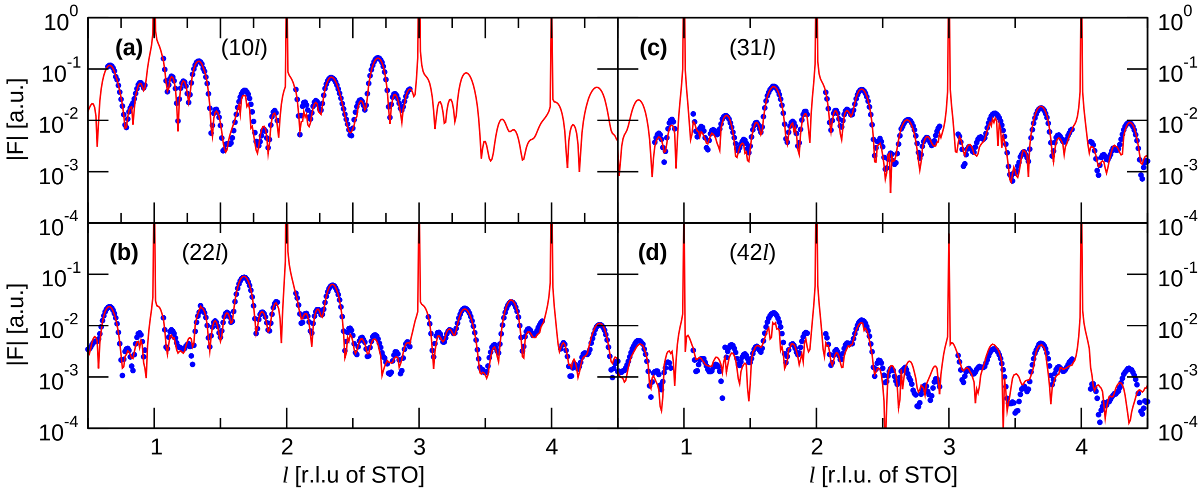

Figure 5.3: Measured CTRs (blue dots) in comparison to the results of a typical DCAF run(red lines). Shown are (a) the (10l) CTR, (b) the (22l) CTR, (c) the (31l) CTR, and (d) the (42l) CTR.

Figure 5.3 shows the result of a typical DCAF run in comparison to the measured structure factors. The crystallographic R-factor for this particular run was $R = 9.85\%$, whereby the typical range of values was between 9.5% and 11.3% for different runs under the most stable conditions. Some rods are seen to show significant discrepancies in various regions, but the overall agreement is good. The main cause for the relatively large differences may be the use of the atomicity constraint, which results in a non-optimal representation of those atoms centered close to the borders between two voxels. Nevertheless, we will see that the resulting ED map gives a very good initial guess for the structure.

Because of the random initialization of DCAF, it is possible to confirm the reproducibility of a solution by running the algorithm several times. Figure 5.4 shows the results of 10 DCAF runs under optimized conditions. The retrieved electron density along the atomic rows of Sr–Ba/Y (top) and Ti/O–Cu/O (bottom) is plotted as a function of the out-of-plane position. Very clearly, there are stable peaks at the predicted lattice spacing for an YBCO-like structure, also showing the expected ordering. It should be stressed that these peaks emerged from a random electron density distribution, only through enforcing a few real-space constraints and using the measured diffraction intensities. In no way were the expected positions and the ordering of these peaks included in the algorithm. In other words, DCAF does not know we are looking for YBCO!

The resolution of the presented ED-lines corresponds directly to the maximum resolution

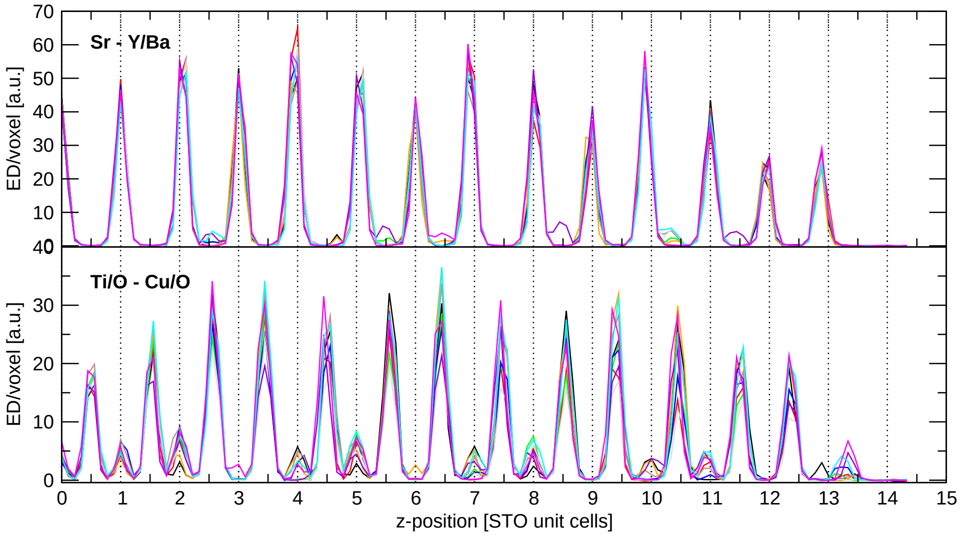

Figure 5.4: Comparison of the results obtained from ten DCAF runs. The two panels show the line plots of the retrieved electron density along the out-of-plane direction through atomic rows of Sr–Ba/Y (top) and Ti/O–Cu/O (bottom). The support regions, equal to 15 unit cells of STO in height, are large enough to contain the equivalent of four unit cells of YBCO and two of STO.

obtainable from the diffraction data, as given by the highest measured momentum transfer in reciprocal space. The reason that the plots shown earlier for the COBRA results look much smoother is that they are upsampled artificially by a factor of seven during the phase retrieval run. Note, however, that there is no diffraction data supporting this upsampling, and that the actual real space resolution is the same as that presented here (meaning that the very small oscillations on the ED lines are artifacts of the upsampling and do not represent any real features which are supported by the data). Obviously, the resolution is on the lower limit for a reliable distinction of atoms, but seems to be sufficient.

The scatter between the ten solutions gives an indication for the reliability of the retrieved structures. For example, the seven small peaks in the upper panel only appear in very few runs and are probably artifacts (in a bulk-like YBCO structure, there are no atoms at these positions). The opposite is true on the Ti/O–Cu/O lines (bottom). Here, the small peaks would correspond to oxygen atoms in the YBCO unit cell. Although they do not appear for some of the results, their occurrence is much higher than for the peaks in the upper panel. Note also that the small peaks in the lower panel occur with high probability in a regular periodic manner for two out of three positions. Their incidence in the third is much lower,

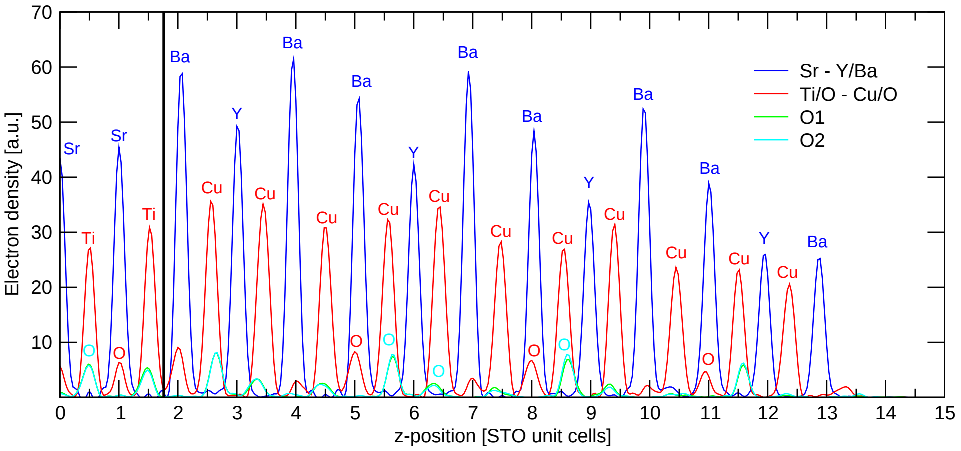

Figure 5.5: The averaged and artificially upsampled (×3) electron-density line-profiles from ten phase-retrieval runs. Four lines through the high-symmetry in-plane positions of the bulk STO reference structure are shown. The tentative assignment of atom types is indicated above the peaks (not all oxygens are labeled). The black vertical line marks one possible choice of the interface position. More details are given in the text.

corresponding to the absence of oxygen atoms in the Y-planes. The uncertainty in the ED map therefore seems to be on the level of these small peaks, meaning that the sensitivity limit is of the order of a few oxygens for the entire structure comprising over 75 atoms. This is confirmed by the fact that the presence and positions of the heavy ions are exceedingly stable in all ten runs.

To determine a first model of the atomic structure from the DCAF solutions, the average of all ten ED maps has been calculated. This will naturally cause a slight blurring of the features, but enhances the consistent peaks while suppressing spurious features. Visually, an artificial upsampling of the ED is very helpful, and does not produce any artifacts if performed only at the end of the analysis. A plot of the averaged and upsampled ED lines is displayed in Figure 5.5. Based on these plots, a first structural model can be proposed.

The identification of atom types based on the number of electrons they contain is fairly straightforward. Table 5.1 lists these, along with the real part of the corresponding atomic scattering factors[3] $f_1 \approx f_0 + f'$, calculated for 16 keV.

Clearly, Ba is the heaviest constituent of the structure and will almost definitely correspond

---

[3] The approximation neglects the nuclear scattering term and any relativistic effects.

Atom	Z	f_1	Atom	Z	f_1
Sr	38	33.54	Y	39	36.66
Ti	22	22.32	Ba	56	55.97
O	8	8.01	Cu	29	29.31

Table 5.1: Atomic number and real part of the scattering factor $f_1 \approx f_0 + f'$ at 16 keV for all atoms in the STO-YBCO system.

to the highest peaks in the ED map. Y lies in between the Ba atoms with a significantly lower number of electrons, comparable to that of Sr. We therefore conclude that the blue line in Figure 5.5 represents the Sr–Y/Ba lines of YBCO. The red line contains the Cu and Ti ions, separated by oxygens in most places. Finally, there are two lines containing only oxygen atoms, labeled "O1" and "O2". The Y planes of bulk-like YBCO do not contain any oxygens, which also agrees well with the obtained ED map, as there are no indications of oxygen peaks at the Y positions (e.g. at $z = 3, 6, 9, 12$). The registry of the assigned lines with the reference structure of the STO bulk in the substrate is also correct, meaning that the STO layers obtained in the ED map are a continuation of the bulk structure.

The layer stacking of the system can now be directly established. Obviously, there are four unit cells of YBCO. The surface terminates on a somewhat reduced Ba peak. The reduction is probably caused by the algorithm itself, producing a continuous drop off in the electron density towards the surface caused by the application of a window function to the measured structure factor (details of which can be found in [26]). The oxygen peak in this layer is not present, but this may also be due to the reduced value dropping below the atomicity threshold. Finally, there is a small red peak corresponding to a Cu site at the top, which could be interpreted as a low coverage with CuO_x on the surface, but which is suppressed in the ED map by the window function. The interface stacking clearly continues the alternation of A and B-type layers, without breaking the network of oxygen octahedra enclosing the B-site ions. The black vertical line in the figure marks the tentative interface between substrate and film, which would therefore correspond to a B1 stacking sequence (substrate–SrO–TiO_2 | BaO–CuO_2–Y–CuO_2–BaO–CuO–…). However, the peak just to the left of the black line cannot be clearly assigned to either Ti or Cu, and the interface could be shifted downwards by half a unit cell to yield an A1 stacking sequence (substrate–TiO_2–SrO | CuO–BaO–CuO_2–Y–CuO_2–BaO–…), which would explain better the termination of the YBCO film on the Ba layer. Yet another, and very likely, possibility is that the structure is represented by a mixture of both interfaces, caused by the mixed termination of the substrate before the growth. However, the layer stacking a few atomic planes above the interface clearly indicates the establishment of a well-defined order. Getting back to the questionable Cu peak on the surface, we see that, if a fraction of the nominal B-type STO terminates on SrO, the block-by-block growth would result in a surface termination of Ba or Y (probably Ba). For the proper termination on TiO_2, on the other hand, the last atom is, indeed, expected to be Cu.

5.3.2 Defining a refinement strategy

Based on the very positive results from the DCAF analysis, a more detailed structure determination can be initiated. The aim is to rely as much as possible on the information provided by the direct methods and to proceed according to a well-defined protocol. In this way, we hope to be able to systematically compare the results obtained with various combinations of direct method and refinement techniques.

In a first step, the direct methods runs will be optimized as far as possible, followed by a more quantitative analysis of the results in terms of precise atomic positions of the atoms. As seen in the last section, DCAF may not be able to identify with certainty each expected atom within the structure. The presence of an atom will be accepted as stable if the corresponding peak appears in at least 5 out of 10 retrieval runs. For those expected atoms which cannot be retrieved reliably, we will instead calculate a starting position by enforcing the average bulk-like bond length ratios to its next stably retrieved neighbors. In this manner, the structure can be completed according to a well-defined rule, yielding a full starting guess directly based on the DCAF or COBRA results.

These atomic positions, along with other predominant features of the ED maps, such as the layer occupations, layer stacking, terminating surface layer, etc. will form a “standard model” to initialize the actual refinement procedures. It is hoped that through the comparison of different combinations of direct method and refinement algorithms, a clear statement regarding the stability of the solutions can be made.

Based on the structural solutions emerging from the standard model, a further adaptation and optimization of the parameterization may be performed, leading the way to a consistent structure determination.

5.3.3 More detailed DCAF results

The ED map produced by DCAF contains much more quantitative information than that gleaned by the visual inspection discussed in Section 5.3.1. The position and width of each peak can be extracted to give hints about the accurate atomic positions and broadening effects caused by static or thermal atomic displacements from the average atomic positions. Furthermore, analyzing the deviations of the extracted values between multiple randomly initialized DCAF runs directly yields an estimate of the statistical uncertainty.

Since the ED resembles the bulk-like structure of YBCO on STO so closely, the peaks in the ED map were compared directly to the expected atomic positions. For each atom in the structure, the nearest peak in the ED map within a given maximum x, y, and z range of 0.2 STO unit cells was identified for each of the ten individual DCAF runs, and its position in all three directions was calculated as its center of mass. Several weaker peaks do not appear in all runs, but may still correspond to the correct atomic position in those occasions when they are present. Finally, the mean width and position are calculate, together with the standard deviation, averaged over then number of runs where a peak could be identified. The integrated ED within each peak should be indicative of the number of electrons of the atom, provided the correct scaling of the structure factors.

Table 5.2 shows a small excerpt of the analysis for the topmost substrate- and the first film-unit cells. The atomic occupation is calculated as the integrated ED divided by the expected real part of the structure factor, f_1. It should be noted, however, that the former is difficult to extract numerically and likely to be fairly inaccurate, mainly due to the relatively low spatial resolution of the ED map (remember that each peak consists of essentially three voxels in each direction when using the native resolution of the diffraction pattern, as shown in Figure 5.4).

The $p4mm$ symmetry of the structure prohibits any in-plane movements of atoms. Therefore, the observed shifts in the x and y-directions should be all zero. However, in DCAF, this symmetry constraint is not applied directly in real space to the retrieved ED, but only indirectly through the corresponding symmetrization of the diffraction pattern. The observed shifts can therefore give a direct estimate about the approximate accuracy of the calculated peak positions. For those values listed in the table, it can be seen that the z-shifts are hardly significantly larger than those in x and y, which means that they should be interpreted cautiously.

	Bulk reference				DCAF result								Shift				
Atom	x	y	z	f_1	$\bar{x}$	σ_x	$\bar{y}$	σ_y	$\bar{z}$	σ_z	Z	σ_Z	x	y	z	occ.	hits
⋮																	
Ti^{4+}	0.0	0.0	-1.000	22.32	0.003	0.014	0.009	0.012	-0.995	0.014	20.27	1.20	0.003	0.009	0.005	0.91	10
O^{2-}	0.5	0.0	-1.000	8.01	0.498	0.009	0.022	0.009	-1.021	0.027	4.93	1.73	-0.022	0.022	-0.021	0.62	10
O^{2-}	0.0	0.5	-1.000	8.01	-0.002	0.026	0.504	0.007	-1.020	0.030	4.67	1.47	-0.002	0.004	-0.020	0.58	10
Sr^{2+}	0.5	0.5	-0.500	33.54	0.500	0.005	0.503	0.004	-0.493	0.009	38.14	2.13	0.000	0.003	0.007	1.13	10
O^{2-}	0.0	0.0	-0.500	8.01	0.007	0.019	0.012	0.020	-0.490	0.012	4.53	1.20	0.007	0.012	0.010	0.56	10
Cu^{2+}	0.0	0.0	0.000	29.30	0.005	0.020	0.011	0.016	0.031	0.014	25.87	2.40	0.005	0.011	0.031	0.88	10
O^{2-}	0.0	0.5	0.000	4.01	-0.001	0.026	0.514	0.018	-0.028	0.020	5.20	1.20	-0.001	0.014	-0.028	1.28	9
O^{2-}	0.5	0.0	0.000	4.01	0.513	0.022	0.013	0.023	-0.035	0.023	5.467	1.33	0.013	0.013	-0.035	1.36	10
O^{2-}	0.0	0.0	0.472	8.01	0.012	0.020	0.006	0.031	0.493	0.022	8.00	1.86	0.012	0.006	0.021	0.99	10
Ba^{2+}	0.5	0.5	0.559	55.96	0.502	0.008	0.506	0.007	0.565	0.014	52.40	2.93	0.002	0.006	0.005	0.93	10
Cu^{2+}	0.0	0.0	1.067	29.30	0.003	0.020	0.012	0.017	1.076	0.006	32.27	2.00	0.003	0.012	0.008	1.10	10
O^{2-}	0.5	0.0	1.133	8.01	0.498	0.010	0.020	0.022	1.155	0.012	8.66	1.46	-0.003	0.020	0.021	1.08	10
O^{2-}	0.0	0.5	1.133	8.01	0.007	0.028	0.504	0.010	1.159	0.015	8.80	1.60	0.007	0.004	0.025	1.09	10
Y^{3+}	0.5	0.5	1.495	36.65	0.502	0.006	0.504	0.005	1.517	0.016	40.80	1.46	0.002	0.004	0.021	1.11	10
O^{2-}	0.5	0.0	1.863	8.01	0.504	0.017	0.039	0.019	1.825	0.014	6.80	3.33	0.004	0.039	-0.038	0.84	6
O^{2-}	0.0	0.5	1.863	8.01	0.004	0.036	0.517	0.040	1.802	0.038	6.00	2.53	0.004	0.017	-0.062	0.74	7
Cu^{2+}	0.0	0.0	1.929	29.30	0.004	0.023	0.014	0.018	1.943	0.007	34.40	2.93	0.004	0.014	0.013	1.17	10
Ba^{2+}	0.5	0.5	2.438	55.96	0.502	0.010	0.506	0.008	2.452	0.014	56.27	4.80	0.002	0.006	0.014	1.00	10
O^{2-}	0.0	0.0	2.524	8.01	0.012	0.027	0.015	0.020	2.533	0.026	4.00	1.33	0.012	0.015	0.008	0.49	6
⋮																	

Table 5.2: Excerpt from the quantitative DCAF analysis. Shown are the values for the topmost substrate unit cell and the first YBCO unit cell, the interface is marked by the dividing line. The averages are taken over ten DCAF runs, and "hits" gives the number of times the atom could be identified in the ED map. The occupation (occ.) is calculated as Z/f_1.

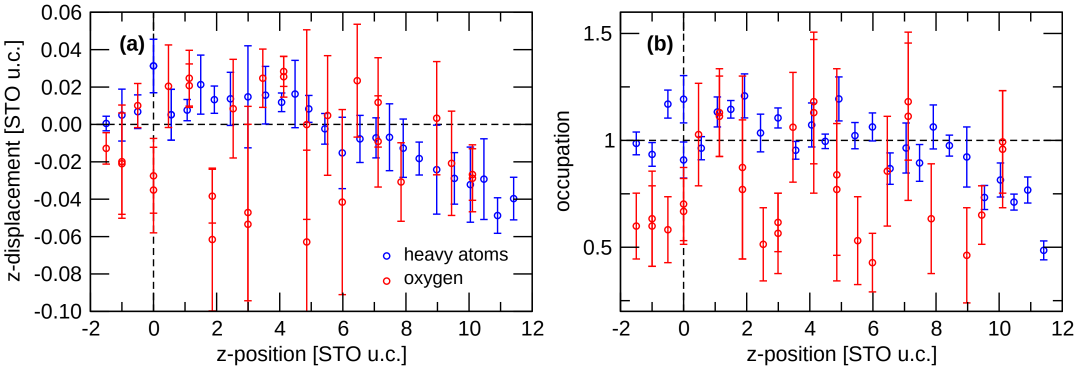

Figure 5.6: Quantitative DCAF results, shown for the very reliably identified heavy atoms (blue) and the more unstable oxygen atoms (red). The vertical dashed line marks the position of the nominally first YBCO layer above the interface. (a) Atomic displacements in the z-direction with respect to a bulk-like YBCO structure, measured in fractions of the STO unit cell. (b) Calculated occupation of the atomic sites as a function of depth (see text for details).

This result is summarized graphically in Figure 5.6 for the entire film, where both the atomic shifts in the z-direction and the calculated occupation for each site are plotted. Both should be interpreted with care, as mentioned above. The displacements along z are fairly small over the entire film thickness and confirm the close resemblance of the film structure with a bulk-like model. Moreover, there seems to be a consistent dilation of the heavy ion lattice in the first two YBCO unit cells, followed by a slight compression in the topmost layers towards the surface. The effect is very small, however, as the total displacement at the surface corresponds to approximately 0.16 Å over a film thickness of close to 45 Å.

The exceptional achievement of the DCAF algorithm in retrieving the electron density of this film from a completely random starting guess on the one hand, and the striking similarity between the result and a bulk-like model on the other hand, can perhaps be best appreciated by direct comparison. Figure 5.7 shows a plot of 3-dimensional ED isosurfaces from the DCAF solution averaged over the 10 runs (middle) next to a ball-and-stick model (left) and the simulated ED isosurfaces based on this model (right). All of the heavy ions are obviously present in the expected positions, and the majority of the oxygen atoms is also recovered.

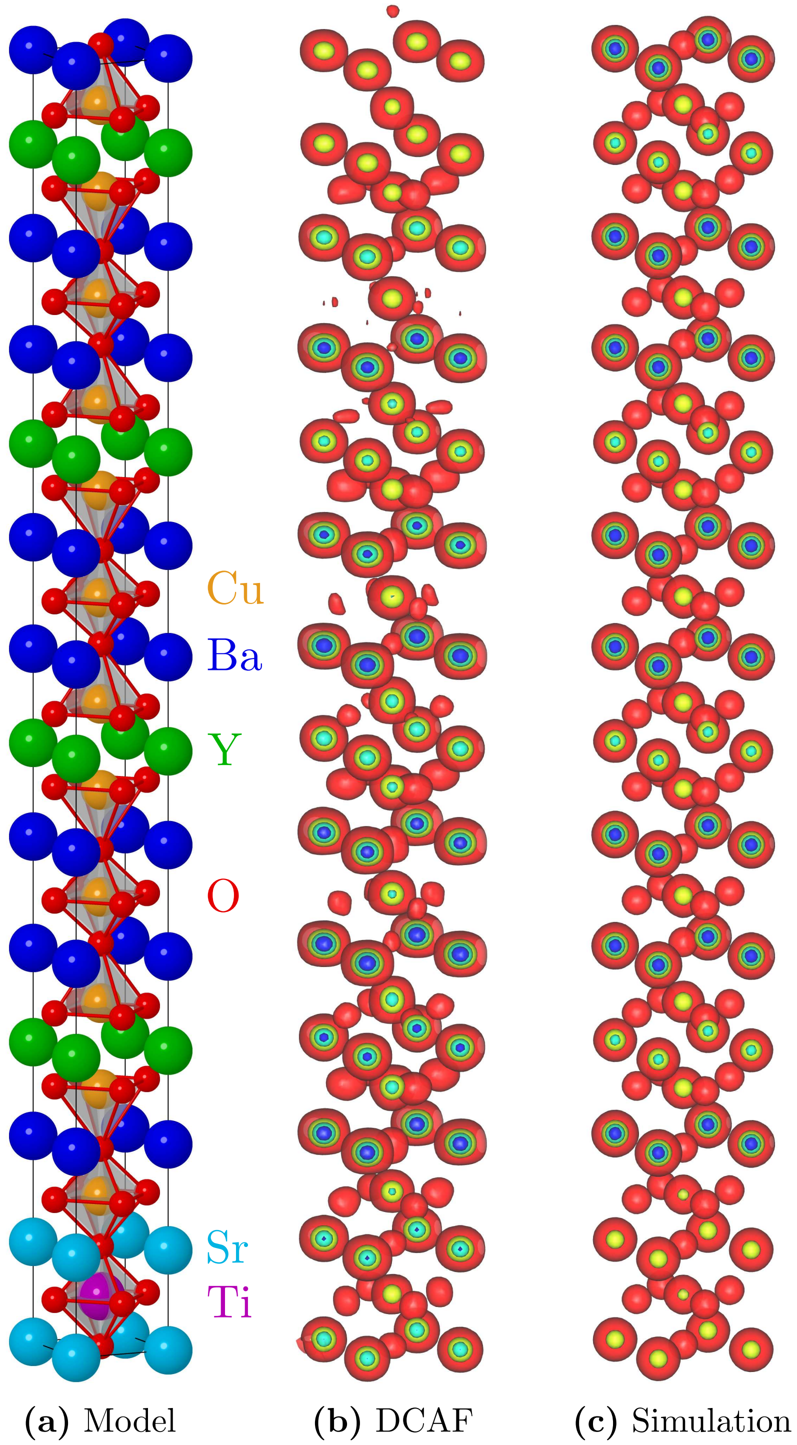

(a) Model **(b)** DCAF **(c)** Simulation

Figure 5.7: DCAF result compared to a bulk-like YBCO structure on STO: (a) ball-and-stick model, (b) isosurfaces of the DCAF retrieved ED map, and (c) isosurfaces of a simulated ED map based on (a).

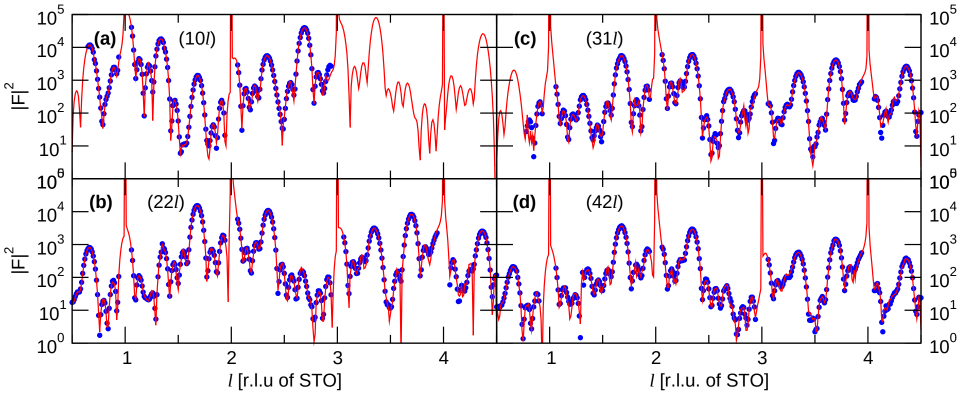

Figure 5.8: Measured data (blue dots) in comparison to the COBRA result (red lines) for the same four CTRs shown previously (see Figure 5.3) for DCAF. The agreement is clearly much better here, for reasons explained in the text.

5.3.4 COBRA results

With the most probable layer stacking determined by DCAF, this starting model can now be used as the initial reference structure for further COBRA analysis. This should remove the cause for the ambiguity found in the initial COBRA runs (see Section 5.3). Stacking sequence A1 automatically results in the observed BaO termination at the surface when stacking an integer number of unit cells. Since the atomic positions determined by DCAF are substantially the same as in the bulk model, we will take the latter as a reference. Also, the somewhat loose support constraint is tightened by excluding the possibility of a fifth YBCO layer, for which no indications could be found from DCAF and in the previous COBRA runs.

Since COBRA does not use atomicity, but only enforces the weaker positivity constraint, it has more flexibility to adapt the ED to the measured structure factors, and should, in general, achieve a better fit to the data. Figure 5.8 clearly supports this notion, displaying a stunning agreement with the measurement. The resulting crystallographic R-factor for this solution was $R(|F|^2) = 6.2\%$ [4].

A closer inspection of the resulting electron density, shown for the usual four line-profiles along the z-axis through the in-plane high-symmetry positions in Figure 5.9, reveals clean peaks

---

[4] Note, however, that the R-factor measure is heavily biased towards the high-intensity data points. For a better numerical confirmation of the visual appearance on a logarithmic scale, one should use a logarithmic R-factor to compare between different results.

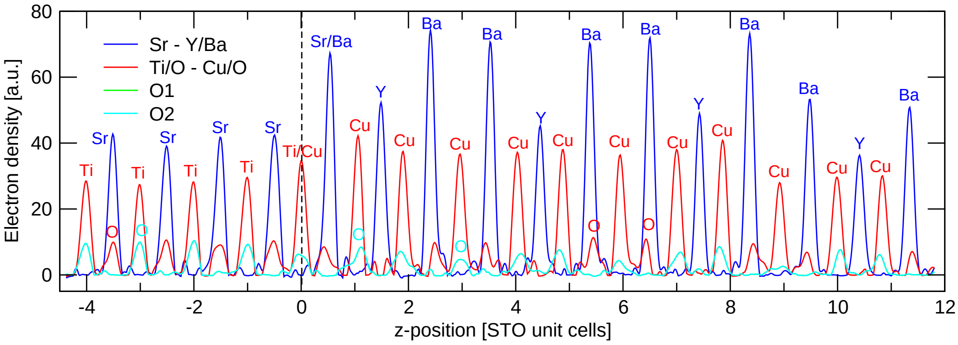

Figure 5.9: Line profiles through the high-symmetry positions of the ED map produced by COBRA along the z-direction. The nominal interface of the reference structure is indicated by the dashed vertical line. Tentative atom labels are shown, but the assignments, particularly in the vicinity of the interface, are not obvious. Rather, the gradual change in peak heights may suggest intermixing at the interface.

for the heavy atoms. Most oxygen peaks are clearly visible, but exhibit dubious distortions, which are difficult to interpret physically. They could represent shifts of the atoms and a splitting of the average positions, but more likely they are indicative of the noise level introduced in the COBRA analysis (which dominates the ED map after a larger number of iterations, as discussed in detail in Section 3.4.3). The extraction of the positions and especially the integrated number of electrons within the peaks is therefore more unstable than for the heavier atoms. The smooth transitions from Ti to Cu and Sr to Ba in the interface region could be indicative of a slight intermixing of these layers at the interface. On the surface side, the fourth YBCO unit cell has a consistently reduced peak height, while maintaining the same peak widths.

The results of a quantitative analysis of the ED map, similar to that described for DCAF, are summarized in Figure 5.10. The observed z-shifts are very small, but show a consistent compression of the unit cell in the out-of-plane direction, in good agreement with the DCAF results. However, there are no signs for the dilation of the first two unit cells, but rather the contraction seems to be very similar in all four unit cells, amounting to less than -0.16 Å (≈ -0.04 u.c. of STO) over the entire film thickness, or approximately 0.35%. The occupation parameter calculated for each atomic site fluctuates around unity for the first three monolayers, while being consistently lower for the fourth unit cell, suggesting an occupation of 70–80%.

A last note concerns the uncertainties to be expected for the extracted quantities. Since

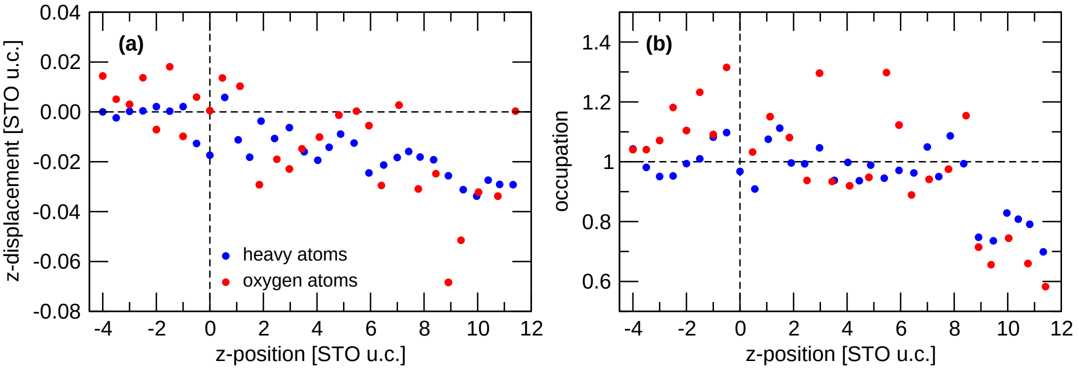

Figure 5.10: Quantitative results from the COBRA analysis for heavy atoms (blue) and oxygen (red). (a) z-displacements of the peak centers with respect to the bulk-like starting reference. (b) Calculated occupation of the atomic sites from the integration of a Gaussian fit to the ED peaks.

COBRA is a deterministic algorithm initialized with a given starting guess, the reproducibility of the result cannot be assessed through multiple analysis runs. The estimation of errors is therefore more involved and not as easily obtained as in the previous DCAF analysis. Here, we thus dispense with a more detailed error evaluation and turn to the problem of parametrizing a sensible physical model of the system based on the information obtained from DCAF and COBRA.

5.3.5 The "standard model"

Following our strategy for the structure determination, we now need to build up an parametrized atomic model for the YBCO/STO structure, based on the insights obtained from the direct methods analysis. We will therefore define the following parameterization as our "standard model" for the further analysis.

Atom	x	y	z	occ.
Sr^{2+}	$^1/_2$	$^1/_2$	$^1/_2$	1
Ti^{4+}	0	0	0	1
O^{2-}	$^1/_2$	0	0	1
O^{2-}	0	$^1/_2$	0	1
O^{2-}	0	0	$^1/_2$	1

Table 5.3: Atomic positions and occupations for the cubic SrTiO$_3$ substrate unit cell with $a = 3.9045$Å.

The model consists of four ML of SrO-terminated STO and four ML of YBCO, with BaO

Atom	x	y	z	occ.	Atom	x	y	z	occ.
Y^{3+}	$^1/_2$	$^1/_2$	0.5000	1	O^{2-}	0	$^1/_2$	0.0000	$^1/_2$
Ba^{2+}	$^1/_2$	$^1/_2$	0.1864	1	O^{2-}	$^1/_2$	0	0.0000	$^1/_2$
Ba^{2+}	$^1/_2$	$^1/_2$	0.8136	1	O^{2-}	0	0	0.1575	1
Cu^{2+}	0	0	0.0000	1	O^{2-}	$^1/_2$	0	0.3784	1
Cu^{2+}	0	0	0.3561	1	O^{2-}	0	$^1/_2$	0.3784	1
Cu^{2+}	0	0	0.6439	1	O^{2-}	$^1/_2$	0	0.6216	1
O^{2-}	0	0	0.8425	1	O^{2-}	0	$^1/_2$	0.6216	1

Table 5.4: Atomic positions and occupations for a $p4mm$ symmetrized unit cell of $YBa_2Cu_3O_{7\text{-x}}$. The symmetrization results in two half-occupied oxygen atoms in the former CuO chain planes. The unit cell is stretched to match the in-plane dimensions of the STO substrate, while retaining its bulk-like out-of-plane dimension: $a = b = 3.9045$ Å, $c = 11.68$ Å.

constituting the topmost layer, as observed in the direct methods ED maps. Tables 5.3 and 5.4 list the corresponding bulk-like atomic positions for STO and YBCO, respectively. Although the experimental data has in principle been normalized to yield absolute values of the structure factor, it is necessary to introduce a general scale factor — if for no other reason than to prove the validity of the applied normalization. Further, the elements inside the substrate are attributed an atom-specific Debye-Waller (DW) factor. No significant evidence can be found to justify individual or even anisotropic DW factors for the film atoms, so also here we will assign only one global parameter for each type of atom (The oxygen atoms of the substrate are treated separately from those in the film).

Based on the established growth mode in blocks of entire unit cells, each unit cell layer is assigned a separate occupation parameter. For the lower three layers, this occupation is fixed at unity in the standard model, while the fourth layer is initialized with a partial occupation of 75%.

Because of the $p4mm$ symmetrization of the unit cell structure, the two now symmetry-equivalent oxygen sites in the nominal CuO-chain layers of the bulk YBCO unit cell will now be randomly occupied by oxygen, with an average occupation of $^1/_2$, assuming the same composition as for the bulk. When considering a partially occupied unit cell layer, the occupation of these oxygen sites should therefore be set to $^1/_2$ of the corresponding layer occupation, in order to preserve the nominal stoichiometry of the unit cell. This is enforced for all CuO layers, apart from the one at the interface, where the intermixing might occur[5].

---

[5] The assumption of a preserved oxygen stoichiometry might not actually be correct for this strained system,

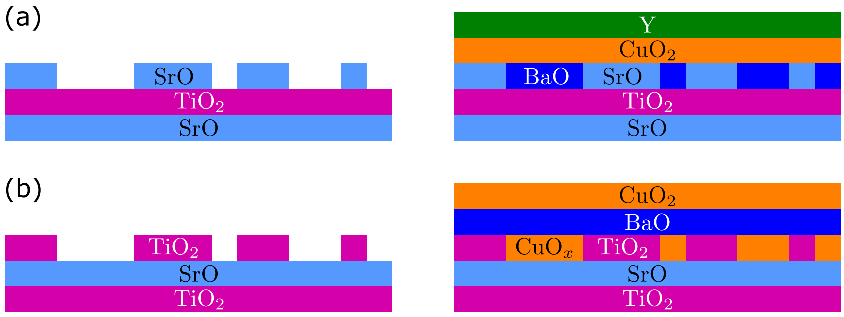

Figure 5.11: On the possible origin of interface intermixing caused by a double termination of the substrate surface. (a) An only partially occupied SrO top layer may lead to a Sr/Ba intermixing (b) The same for a partial coverage with TiO_2, causing a Ti and Cu to mix. Note that for unit cell-by-unit cell growth, the topmost film layer should mirror the interface, and will hence be of mixed termination if intermixing occurs at the interface.

The particular choice of the substrate termination on SrO is arbitrary, since no definitive statement about the stacking of the atomic layers could be extracted from direct methods. For this reason, we allow for the intermixing of substrate and film atoms of the A- and B-sites, respectively, within the two atomic layers at the interface, describing the two possible substrate terminations. To avoid the formation of vacancies, the sum of partial occupations of the atoms at one particular site is restricted to unity. The physical origin of the intermixing can be explained as a result of a mixed substrate termination, which is likely to be present in this sample, as no measures were taken to guarantee a single STO termination. The most plausible scenario is that the STO surface consists of SrO islands on top of a fully covered and thermodynamically more stable TiO_2 layer, depicted in Figure 5.11 (a). Upon deposition of the YBCO material, it seems chemically reasonable that the very similar BaO may fill in the holes between the SrO islands (both metal ions have a nominal valence of 2+, thereby preserving the charge distribution in the layer), followed by a first full layer of CuO_2 marking the start of the YBCO structure. The result is one atomic layer where Sr and Ba are both present. In the diffraction data, this would be seen as an intermixing due to the structural averaging over large interface areas. The second option, shown in Figure 5.11 (b), is the contrary situation. The gaps between TiO_2 islands on the surface are filled with CuO_x, followed by a full BaO-layer,

---

however, although the fact that the samples are superconducting suggests that the composition is well within the superconducting range. Since the sensitivity of SXRD to oxygen is very low, we do not expect this assumption to have a significant effect on the refinement, and its consequences can in principle be studied later on in a more detailed analysis.

resulting in an apparent Cu/Ti intermixing. The number of oxygen atoms associated with each Cu atom could vary in order to preserve the nominal net layer charge, hence the notation CuO_x.

Finally, the z-positions of all symmetry-independent atoms are added as free parameters in the refinement. Initial tests have revealed that no significant movements can be observed for the lower three unit cells of STO, however. These parameters have therefore been excluded from the standard model again in order to reduce the number of free parameters as much as possible, while maintaining the necessary flexibility of the model.

Table 5.5 gives a summary of all 61 refinement parameters of this standard model.

Parameter name	Type	#	initial value(s)
General data set scale factor	scale factor	1	1.0
Substrate DW: Sr^{2+}, Ti^{4+}, O^{2-}	DW	3	1.5, 0.5, 1.0
Film DW: Y^{3+}, Ba^{2+}, Cu^{3+}, O^{2-}	DW	4	0.5, 0.5, 0.5, 1.0
(Sr:Ba) intermixing at interface	occupation	1	(1:0)
(Cu:Ti) intermixing at interface	occupation	1	(0:1)
Top YBCO layer occupation	occupation	1	0.75
Atomic z-movements	displacement	50	0
Total		**61**	

Table 5.5: Free parameters of the "standard model" and their initial values used in the refinement.

5.3.6 Traditional refinement using FIT

First refinements were carried out using the FIT program for the evaluation of SXRD data by O. Bunk [27]. It uses a simple and robust grid search algorithm which is capable of handling a large number of parameters. However, each grid search step is performed in a strict downhill manner, such that the algorithm is bound to find the nearest (and usually local) minimum to the used starting guess.

Three different starting guesses have been used in the refinement. They all contain the same initial values for the global parameters (scale factor, DW, occupations, see Table 5.5), but differ in the starting positions along the z-direction for the individual atoms, taken as (i) the bulk-like positions of YBCO on STO, (ii) the positions extracted from DCAF, and (iii) those from COBRA. The refinement has been performed in two steps. First, only the global parameters were allowed to vary, and only in a second step were the z-positions allowed to vary. Comparisons to a case where all parameters were varied at once showed that no significant differences could be detected, neither in terms of the final R-factor, nor in the parameter values themselves.

The results of the first step yielded very comparable global parameter values for all three starting points, summarized in Table 5.6. Firstly, the general scale factor for the data at approximately 0.77 is somewhat lower than unity, but given the delicate normalization procedure to obtain absolute values (detailed in Chapter C), represents a respectable agreement.

	Starting guess based on. . .		
Parameter name	bulk	DCAF	COBRA
General data set scale factor	0.80	0.77	0.74
Substrate DW: Sr^{2+}, Ti^{4+}, O^{2-}	1.84, 0.73, 1.39	1.90, 0.87, 1.20	1.83, 1.04, 1.24
Film DW: Y^{3+}, Ba^{2+}, Cu^{3+}, O^{2-}	2.61, 2.69, 2.27, 2.22	2.62, 2.67, 2.15, 2.14	2.49, 2.56, 2.05, 1.97
(Sr:Ba) intermixing at interface	(0.68:0.32)	(0.09:0.91)	(0.03:0.97)
(Cu:Ti) intermixing at interface	(0.41:0.59)	(0.87:0.13)	(0.42:0.58)
Top YBCO layer occupation	0.82	0.73	0.73
R-factor	0.147	0.150	0.153

Table 5.6: FIT results for the refinement of the "standard model" obtained from the bulk, DCAF and COBRA starting guesses (after the full refinement including the z-axis displacements).

The fitted DW factors are higher than for a bulk crystal by a factor of between 1 and 5, which seems reasonable for a thin film system. This is supported by the fact that they are lower for the substrate atoms than for the film. Also here, the reproducibility between different fits is excellent. The intermixing at the interface can unfortunately not be resolved with confidence, for which the rations seem to be widely different from one another – the DCAF- and COBRA-based results are similar for the Sr:Ba intermixing, while the bulk- and COBRA-based fits are more consistent for the Cu:Ti occupations. Finally, the top layer occupation refines stably to between 70% and 80%.

Regarding the z-displacements refined in the second step, the outcome is slightly more disappointing. As already observed in the direct methods runs, the contraction in the c-direction as a general trend is also apparent for all fits, although at a somewhat smaller level for the fit starting from a bulk-like model, as such a collective movement of so many atoms may be hard to realize in a grid-search method. The large fluctuations in the individual atomic positions, however, indicate that the solutions are far from yielding a unique answer and that

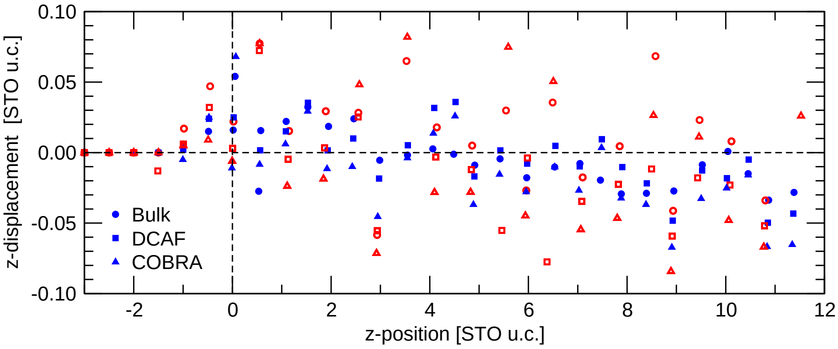

Figure 5.12: Atomic z-displacements obtained from FIT for the bulk-like (circles), DCAF (squares), and COBRA (triangles) starting guesses, showing a large scatter in the refined positions. Heavy atom positions are shown with filled blue symbols and oxygen atoms with the open red markers. The overall trend for a slight c-axis contraction remains valid, but no unambiguous statements about any detailed structural changes, especially with regard to the interface region, can be made.

the solutions represent local minima. This is also reflected in the fact that the final R-factors are considerably higher than for the direct methods results (yet, it should be kept in mind that the degrees of freedom in this atomic model are much reduced in comparison to the ED map values in the direct methods).

5.3.7 Genetic algorithms: the use of GenX

In order to alleviate the problem of getting stuck in local minima during the refinement, the fitting program GenX, which is based on a differential genetic evolution search algorithm, has been used as an alternative to FIT. A description of the working principle of genetic algorithms and a detailed account of the GenX implementation can be found in [28]. The set of refinement parameters is in principle identical, apart from two important difference. Firstly, FIT can restrict the atomic positions to comply with the *p4mm* symmetry, resulting in those atoms in equivalent positions having only one shared z-displacement parameter. This restriction is not generally applied in GenX and would have to be implemented separately for each system, which has not been done in this analysis. Therefore, the number of atomic positions to be refined is increased (all the oxygen atoms placed at the ($^1/_2$, 0, z) and (0, $^1/_2$, z) positions are now treated independently), and symmetry breaking can occur. As in the case of the DCAF analysis, which also did not include any plane group restrictions of the real-space structure, the result of symmetry breaking must still be sufficiently compatible with the *p4mm* diffraction

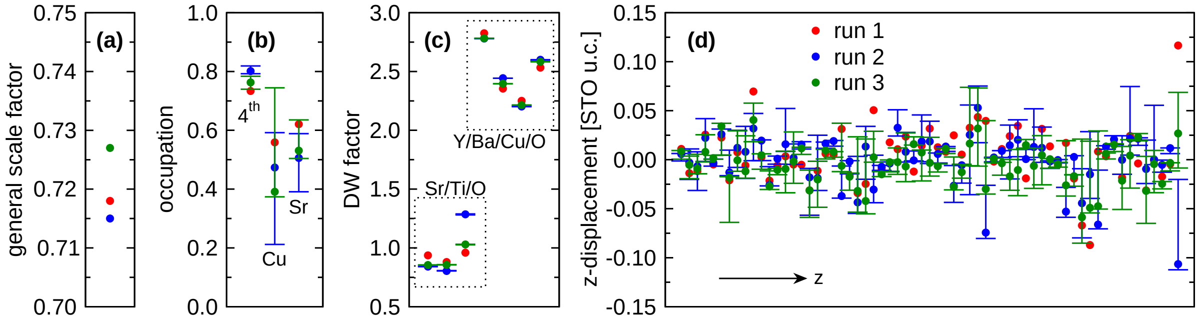

Figure 5.13: Comparison of three repeated GenX run under identical conditions using the same COBRA starting guess (run 1 = red, run 2 = blue, run 3 = green). For runs 2 and 3, also the error bars on the parameter values are shown. (a) Final value of the general scale factor. (b) The occupation parameters for the 4th YBCO layer (left), the Cu fraction of the (Cu:Ti) intermixing (middle) and the same for Sr in the (Sr:Ba) intermixing. (c) The refined DW factors for the STO atoms (three values on left) and the YBCO atoms (four values on right). (d) z-displacement values for all atom positions (plotted against their parameter indices. The z-coordinate increases from left to right).

pattern. Any deviations from this symmetry should give indications as to how reliable the data or the structure refinement result is.

The second difference concerns the general scale factor, which was not fitted independently in GenX, but rather adjusted through a minimization of the squared deviations from the measured data during the creation of each individual generation (Despite the exclusion from the parameter list, the adjusted scale factor still represents a free parameter of the optimization problem, however). With these changes, the total number of refinement parameters for the standard model increases to 73.

Through the random initialization of all the members of the algorithm's starting generation (apart from one, which contains the provided starting guess), it is possible to establish the reproducibility of a solution. Figure 5.13 shows a comparison of three GenX-runs performed under identical conditions, starting from the positions determined by the COBRA analysis. For two of the runs, the error bars determined by GenX, which are calculated as those deviations causing a 5% increase in the figure of merit, are also shown (for the last one they were not evaluated). The final R-factors were essentially identical for all three runs (0.150, 0.149, 0.150), yet the spread in parameter values suggests that also using this algorithm, only local minima could be found. These may be exceedingly close to the real solution in terms of their R-factor values, which would mean that the fluctuations are comparable to the best achievable sensitivity

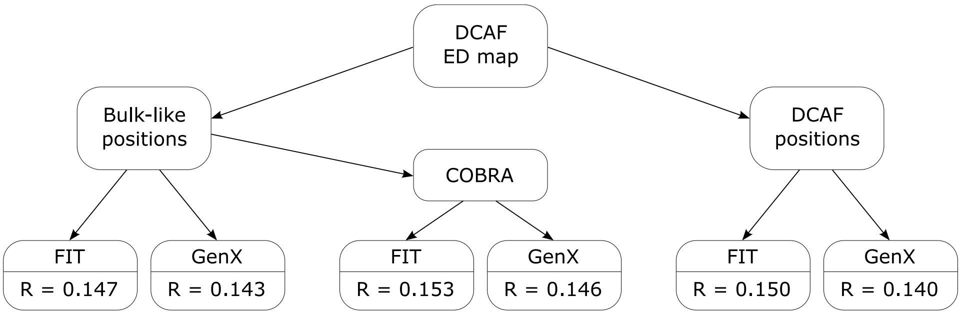

Figure 5.14: Overview of all refinement approaches for the standard model, including the best R-factors obtained.

for this system, but there is no way of knowing this for sure. So far, no better solutions could be found. The results obtained by using either the bulk-like or the DCAF starting guess exhibit a completely analogous behavior (not shown here).

5.4 Comparing the results

A number of different combinations of algorithms and techniques have been implemented to solve the structure of YBCO on STO. A direct comparison of the results is problematic, since the boundary conditions were not identical for all combinations. We have, however, tried to keep them as consistent as possible by using the previously defined standard model, which was based on the direct output of the DCAF electron density map. For this reason, an evaluation seems justified and certainly instructive for the presented case. An overview of all the tested combinations is given schematically in Figure 5.14, along with the best R-factor achieved.

Given the significant differences in the applied methods, the agreement in terms of the resulting figure of merit is astonishing. Apparently, all the solutions found by these various approaches describe the system with an equal degree of accuracy (which, however, does not necessarily imply a high level of consistency). On the other hand, through the discovered inconsistencies between equally valid analysis schemes, a realistic measure for the reliability and sensitivity of the results can be established, and possible error sources may be more accurately identified.

This is illustrated clearly in the present refinement results. There are a number of parameters yielding very stable and consistent results. The system is well described by 4 ML of YBCO,

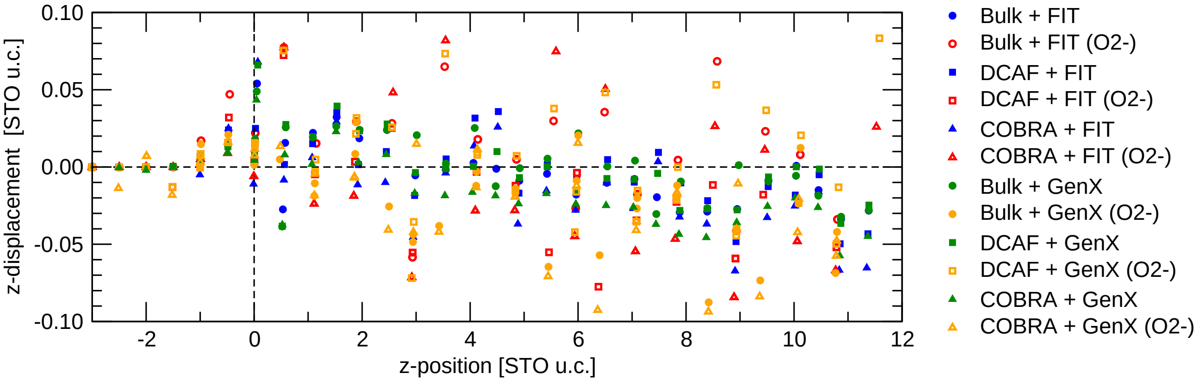

Figure 5.15: Comparison of the refined z-displacements for different combinations of structure solution algorithms.

whereby the topmost layer is only partially occupied between 70% and 80%, and no signs for the presence of a fifth layer can be found. The film terminates on BaO surface. The high crystalline quality of the film is confirmed by the very modest Debye-Waller factors of around 1.0 for the substrate atoms at the interface and approximately 2.5 for the film atoms. The refined atomic positions consistently indicate a slight compression of the YBCO film unit cell of less than 1%. Assuming the limiting case of an ideal Poisson ratio of 0.5, i.e., a constant volume of the unit cell, the compression resulting from the in-plane tensile strain would be approximately 2.5%. The observed c-axis reduction of less than 1% is in excellent agreement with the reported Poisson ration for YBCO of 0.17 [29]. Finally, the general scale factor for the data set of between 0.7 and 0.8 confirms the validity of the absolute structure factor normalization in the experimental data, but gives a lower limit of ± 25% for its accuracy.

Some other features lack this degree of consistency, however. The atomic intermixing at the interface does not give stable results in the refinement process, and does not allow one to determine the exact elemental composition. The individual atomic displacements are very small on average (less than 0.2 Å), but fluctuate considerably from fit to fit. This is shown again for all the used refinement procedures in Figure 5.15. This precludes any detailed studies on some of the physically most relevant questions to this system, like small structural distortions or changes in the oxygen content inside the conducting CuO_2 planes.

5.5 Fitting beyond the “standard model”

The standard model defined previously represents an attempt to identify a minimal set of degrees of freedom obviously present in the ED map produced by DCAF. As such, it may be still be inadequate to describe the system correctly, and any more sophisticated parameterization of the problem is likely to lead to better results. The problem simply lies in finding these superior models.

A few attempts have been made to either simplify or further extend the standard model, thereby identifying the significant parameters. By restricting all atoms to their nominal positions, but allowing the c-axis constant of the YBCO unit cell to change, the effect of the slight contraction was investigated. In addition to the compression, a further parameter describing the (unknown) bonding distance between the film and the substrate was introduced. The results confirm the contraction, to a c-axis length of 0.9958 of the nominal bulk unit cell height, and a small shift of the entire film towards the substrate by 0.045 Å, yielding a final R-factor of 0.191.

More complex models may include the fitting of individual atomic layer occupancies, site-dependent or even anisotropic DW factors, oxygen occupation, the intermixing of different film domains, either coherently or incoherently, the inclusion of more substrate layers, etc. In an attempt to estimate the potential improvement in the fits, the brute-force approach of freeing up the positions, DW-factors and occupations for each individual atom has been used. The best final R-factor was 0.098, comparable to the systematic errors in the data set, but yielded clearly unphysical results. At this stage, any further attempts were abandoned.

5.6 Conclusions and outlook

In this chapter, we have discussed a proposition towards a systematic approach to solving the structure of complex structures measured with SXRD, which may be generally applicable. The results obtained for this particular system are very encouraging, and at the same time reveal an enormous potential for further improvements.

The global structural model emerging from our analysis can be summarized as follows: Due to the very probable mixed termination of the growth substrate, there seem to be predominantly two domains of different stacking sequences at the interface, either substrate–TiO_2 | BaO–CuO_2–Y–CuO_2–. . . (B1) for the B-site terminated substrate regions, or substrate–TiO_2–SrO | CuO_2–Y–CuO_2–. . . (A3) where it is A-site terminated. The averaged structure over both domains results in an apparent SrO/BaO intermixing at the interface, observable in the ED maps as a gradual changeover from the Sr to the Ba peak heights. The same can be seen for the Ti/Cu site one layer below. Also here, the there may be a certain amount of intermixing. All other atomic layers of the structure remain in exact registry when traversing from one stacking domain to the other. The surface termination of the film was found to be predominantly on the first BaO layer following the Y-planes.

On the atomic level, the film structure remains exceedingly bulk-like. The typical detected changes in bond lengths between neighboring atoms with either COBRA or DCAF are below 0.08 Å. This value is somewhat higher after the refinement runs, but the observed fluctuations in the bond lengths between different runs are of equal magnitude as the actual changes, which must therefore be regarded as unreliable. Unfortunately, the final sensitivity to detect changes in the oxygen positions or occupations was found to be insufficient to make any conclusive statements about these aspects.

Although more detailed parameterizations of the structural model are expected to improve the fitting results, it is questionable whether a considerable increase of the achieved sensitivity is possible. In other words, one might succeed in producing a better agreement of the data with the model, but whether this would necessarily result in a more accurate determination of the individual parameters remains to be investigated. The final R-factors obtained from the refinement procedures to this point are approximately 1.5 times larger than the systematical errors within the underlying data set, which sets a final limit on the achievable accuracy.

Bibliography

[1] M. Varela, W. Grogger, D. Arias, Z. Sefrioui, C. León, C. Ballesteros, K. M. Krishnan, and J. Santamaría: "Direct Evidence for Block-by-Block Growth in High-Temperature Superconductor Ultrathin Films." *Phys. Rev. Lett.* **86**(22), 5156–5159 (2001), doi:10.1103/PhysRevLett.86.5156.

[2] T. Terashima, Y. Bando, K. Kamigaki, and H. Terauchi: "Reflection high-energy electron diffraction oscillations during epitaxial growth of high-temperature superconducting oxides." *Phys. Rev. Lett.* **65**(21), 2684–2687 (1990), doi:10.1103/PhysRevLett.65.2684.

[3] J. G. Wen, T. Morishita, N. Koshizuka, C. Traeholt, and H. W. Zandbergen: "Direct high-resolution

electron microscopy observation of nonunit-cell nucleation in the initial stage of high-T$_c$ superconducting film growth." *Appl. Phys. Lett.* **66**(14), 1830 (1995), doi:10.1063/1.113336.

[4] T. Haage, J. Zegenhagen, H.-U. Habermeier, and M. Cardona: "Nucleation Mechanism of $YBa_2Cu_3O_{7-\delta}$ on $SrTiO_3$(001)." *Phys. Rev. Lett.* **80**(19), 4225–4228 (1998), doi: 10.1103/PhysRevLett.80.4225.

[5] V. Vonk, K. J. I. Driessen, M. Huijben, G. J. H. M. Rijnders, D. H. A. Blank, H. Rogalla, S. Harkema, and H. Graafsma: "Initial Structure and Growth Dynamics of $YBa_2Cu_3O_{7-\delta}$ during Pulsed Laser Deposition." *Phys. Rev. Lett.* **99**(19), 196106 (2007), doi: 10.1103/PhysRevLett.99.196106.

[6] C. Chen and C. Tsuei: "Topography and local conductance images of $YBa_2Cu_3O_7$ crystals fractured in ultra high vacuum." *Solid State Comm.* **71**(1), 33–38 (1989), doi:10.1016/0038-1098(89)90167-1.

[7] G. Frank, C. Ziegler, and W. Göpel: "Surface composition of clean, epitaxial thin films of $YBa_2Cu_3O_{7-x}$ from quantitative x-ray photoemission spectroscopy analysis." *Phys. Rev. B* **43**(4), 2828–2834 (1991), doi:10.1103/PhysRevB.43.2828.

[8] H. L. Edwards, J. T. Markert, and A. L. D. Lozanne: "Energy gap and surface structure of $YBa_2Cu_3O_{7-x}$ probed by scanning tunneling microscopy." *Phys. Rev. Lett.* **69**(20), 2967–2970 (1992), doi:10.1103/PhysRevLett.69.2967.

[9] X. Torrelles, C. Aruta, A. Fragneto, I. Maggio-Aprile, L. Ortega, F. Ricci, J. Rius, M. Salluzzo, and U. Scotti di Uccio: "Analysis of the surface termination of $Nd_{1+x}Ba_{2x}Cu_3O_y$ thin films." *Phys. Rev. B* **70**, 104519 (2004), doi:10.1103/PhysRevB.70.104519.

[10] H. Behner, K. Rührnschopf, W. Rauch, and G. Wedler: "Structure and composition of the surfaces of sputtered $YBa_2Cu_3O_{7-\delta}$ thin films — an XPS and LEED study." *Appl. Surf. Sci.* **68**(2), 179–188 (1993), doi:10.1016/0169-4332(93)90119-V.

[11] V. C. Matijasevic, B. Ilge, B. Stäuble-Pümpin, G. Rietveld, F. Tuinstra, and J. E. Mooij: "Nucleation of a Complex Oxide during Epitaxial Film Growth: $SmBa_2Cu_3O_y$ on $SrTiO_3$." *Phys. Rev. Lett.* **76**(25), 4765–4768 (1996), doi:10.1103/PhysRevLett.76.4765.

[12] J. Rao and T. Morishita: "Determination of the surface layer of laser ablated YBCO by glancing incident–exit X-ray diffuse scattering." *Phys. C: Supercond.* **291**(3-4), 223–228 (1997), doi: 10.1016/S0921-4534(97)01624-9.

[13] T. Nakamura, S. Tanaka, and M. Iiyama: "All in situ deposition and characterization of $YBa_2Cu_3O_{7-x}$ thin films by low-energy ion scattering spectroscopy." *Appl. Phys. Lett.* **66**(24), 3362 (1995), doi:10.1063/1.113758.

[14] S. Pennycook, M. Chisholm, D. Jesson, R. Feenstra, S. Zhu, X. Zheng, and D. Lowndes: "Growth

and relaxation mechanisms of $YBa_2Cu_3O_{7-x}$ films." *Phys. C: Supercond.* **202**(1-2), 1–11 (1992), doi:10.1016/0921-4534(92)90288-N.

[15] M. Matsubara, T. Morishita, and I. Hirabayashi: "Effect of the deposition sequence on the growth of $YBa_2Cu_3O_{7-\delta}$ films by chemical vapor deposition." *Appl. Phys. Lett.* **64**(14), 1868 (1994), doi: 10.1063/1.111782.

[16] H. You, U. Welp, G. W. Crabtree, Y. Fang, X. Jiang, and S. C. Moss: "X-ray crystal-truncation-rod analysis of untwinned $YBa_2Cu_3O_{7-\delta}$ single crystals: The growth-termination plane." *Phys. Rev. B* **45**(9), 5107–5110 (1992), doi:10.1103/PhysRevB.45.5107.

[17] R. Ramesh, A. Inam, D. Hwang, T. Ravi, T. Sands, X. Xi, X. Wu, Q. Li, T. Venkatesan, and R. Kilaas: "The atomic structure of growth interfaces in Y–Ba–Cu–O thin films." *J. Mater. Res.* **6**(11), 2264–2271 (1991), doi:10.1557/JMR.1991.2264.

[18] J. Wen, C. Traeholt, and H. Zandbergen: "Stacking sequence of $YBa_2Cu_3O_7$ thin film on $SrTiO_3$ substrate." *Phys. C: Supercond.* **205**(3-4), 354–362 (1993), doi:10.1016/0921-4534(93)90402-C.

[19] J. Zegenhagen, T. Siegrist, E. Fontes, L. E. Berman, and J. R. Patel: "Epitaxy of ultrathin films of $YBa_2Cu_3O_{7-\delta}$ on $SrTiO_3(001)$ investigated with X-ray standing waves." *Solid State Comm.* **93**(9), 763–767 (1995), doi:10.1016/0038-1098(94)00866-3.

[20] S. Bals, G. J. H. M. Rijnders, D. H. A. Blank, and G. V. Tendeloo: "TEM of ultra-thin $DyBa_2Cu_3O_{7-x}$ films deposited on TiO_2 terminated $SrTiO_3$." *Phys. C: Supercond.* **355**(3-4), 225–230 (2001), doi:10.1016/S0921-4534(01)00034-X.

[21] M. Alariofranco, C. Chaillout, J. Capponi, J. Chenavas, and M. Marezio: "A family of non-stoichiometric phases based on $Ba_2YCu_3O_{7-\delta}$ $(0 \leq \delta \leq 1)$." *Phys. C: Supercond.* **156**(3), 455–460 (1988), doi:10.1016/0921-4534(88)90771-X.

[22] D. J. Werder, C. H. Chen, R. J. Cava, and B. Batlogg: "Diffraction evidence for oxygen-vacancy ordering in annealed $Ba_2YCu_3O_{7-\delta}$ $(0.3 \leq \delta \leq 0.4)$ superconductors." *Phys. Rev. B* **37**(4), 2317–2319 (1988), doi:10.1103/PhysRevB.37.2317.

[23] R. Herger, P. R. Willmott, O. Bunk, C. M. Schlepütz, B. D. Patterson, and B. Delley: "Surface of strontium titanate." *Phys. Rev. Lett.* **98**, 076102 (2007), doi:10.1103/PhysRevLett.98.076102.

[24] P. R. Willmott, S. A. Pauli, R. Herger, C. M. Schlepütz, D. Martoccia, B. D. Patterson, B. Delley, R. Clarke, D. P. Kumah, C. N. Cionca, and Y. Yacoby: "Structural basis for the conducting interface between $LaAlO_3$ and $SrTiO_3$." *Phys. Rev. Lett.* **99**, 155502 (2007), doi: 10.1103/PhysRevLett.99.155502.

[25] R. Herger, P. R. Willmott, C. M. Schlepütz, M. Björck, S. A. Pauli, D. Martoccia, B. D. Patterson, D. P. Kumah, R. Clarke, Y. Yacoby, and M. Döbeli: "Structure determination of monolayer-by-

monolayer grown $La_{1-x}Sr_xMnO_3$ thin films and the onset of magnetoresistance." *Phys. Rev. B* **77**, 085401 (2008), doi:10.1103/PhysRevB.77.085401.

[26] M. Björck, C. M. Schlepütz, S. A. Pauli, D. Martoccia, R. Herger, and P. R. Willmott: "Atomic imaging of thin films with surface x-ray diffraction: introducing DCAF." *J. Phys.: Condens. Matter* **20**(44), 445006 (2008), doi:10.1088/0953-8984/20/44/445006.

[27] O. Bunk: *Bestimmung der Struktur komplexer Halbleiter-Oberflächenrekonstruktionen mit Röntgenbeugung*. Ph.D. thesis, Universität Hamburg, Hamburg (1999).
URL `http://www.physnet.uni-hamburg.de/services/fachinfo/___Volltexte/Oliver___Bunk/Oliver___Bunk.pdf`

[28] M. Björck and G. Andersson: "GenX: an extensible X-ray reflectivity refinement program utilizing differential evolution." *J. Appl. Crystallogr.* **40**(6), 1174–1178 (2007), doi:10.1107/S0021889807045086.

[29] B. Bridge: "Anomalies arising from a comparison of the elastic constants of the high-temperature superconductor $YBa_2Cu_3O_{7-x}$ and the related perovskite structure $BaTiO_3$." *J. Mater. Sci. Lett.* **8**(6), 695–696 (1989), doi:10.1007/BF01730446.

Chapter 6

$YBa_2Cu_3O_{7\text{-}x}$ on LSAT

6.1 Introduction

The structural analysis of the $YBa_2Cu_3O_{7\text{-}x}$ on $(La_xSr_{1\text{-}x})(Al_yTa_{1\text{-}y})O_3$ sample is based on the experience gained with the YBCO-STO system. For this reason, the discussion of the individual analysis steps will be very much reduced in this chapter, and focusses mainly on the results provided by the various techniques.

The available literature on this particular system is scarce, and virtually no thin film structure determination studies have been attempted. The nature of the interface is unknown, and very little information about the surface termination and the proper preparation of LSAT has been reported [1]. The substrate used to produce this film was not prepared for a single termination, however, so the nature of its surface is, *a priori*, unknown. Further details of the film growth can be found in Chapter 4.

6.2 SXRD measurements and data reduction

The SXRD measurements were carried out under identical conditions as for the YBCO-STO samples, with an incident x-ray energy of 16.000(1) keV (λ = 0.7749 Å). The sample was kept at room temperature and moderate vacuum conditions inside a small beryllium container, and was mounted on the diffractometer with its surface normal lying in the horizontal plane. The reference lattice for the measurements has been defined as simple cubic with a lattice constant of $a = 3.866$ Å, resulting in a reciprocal lattice unit (r.l.u.) of $2\pi/a = 1.6252\text{Å}^{-1}$.

A large CTR data set, including most rods inside the first quadrant of the in-plane reciprocal space ($h, k \geqslant 0$) and many more in the remaining quadrants, has been acquired at a scan step size of 0.01 r.l.u. along the l-direction, starting from $l = 0.2$ up to the highest reachable points on the CTRs (given by the incoming x-ray angle and the wavelength) of typically around $l = 4.5$[1]. The reachable in-plane Miller indices were restricted to $h^2 + k^2 < 26$ by the requirement that the diffractometer angles for the detector should not exceed 90°. Consequently, the largest reachable in-plane momentum transfers could be measured on the $(43l)$ and $(50l)$ CTRs. The data set comprises a total of 30 CTRs with 12 184 reliable structure factors.

As mentioned in Section 4.3.1, the big unknown in this system is the accurate structure of the LSAT substrate. To begin with, we will assume a simple cubic structure with a lattice constant of $a = 3.866$ Å. The diffraction pattern shows strong Bragg peaks at all the expected positions for this structure and clean CTR signals in between. Any of the other reported structures are characterized by slight distortions of this simple cubic structure, resulting in a larger unit cell. All of the proposed models would result in measurable intensities at half-integer positions in reciprocal space, i.e., on $(\frac{n_1}{2}, \frac{n_2}{2}, \frac{n_3}{2})$ positions, where the n_i are integers. Figure 6.1 (b) shows a detector image of such a Bragg peak at $(^1\!/_2,\ ^1\!/_2,\ ^1\!/_2)$, proving that such distortions do exist and the unit cell is indeed larger. However, comparing the intensities of these superstructure peaks with the ones corresponding to the simple cubic structure, we find that the former are weaker by a factor of approximately 10^5. Their broad shape further indicates that the structure of the doubled unit cell is not well-defined. This is not surprising, considering the stoichiometry of the material. Each A and B-site of the lattice can be occupied by one of two elements, respectively, yielding 2^{15} different possible arrangements for the nearest neighbors of any oxygen octahedron, each of which might induce a slightly different distortion of the lattice. Hence, we observe an average over all of these distortions, resulting in the observed broad features. We could not observe any signal between these half-integer Bragg peaks along l, proving that they are caused by a weak bulk effect, resulting in unmeasurably weak CTRs. The YBCO film structure apparently does not contribute to any signals apart from the integer order CTRs, proving that its structure is well-described by assuming an in-plane lattice constant equal to the simple cubic LSAT approximation.

---

[1] The $(00l)$ specular rod was, unfortunately, acquired under different experimental conditions in a θ-2θ-scan and could not be reliably scaled and interpolated to match the remaining data set.

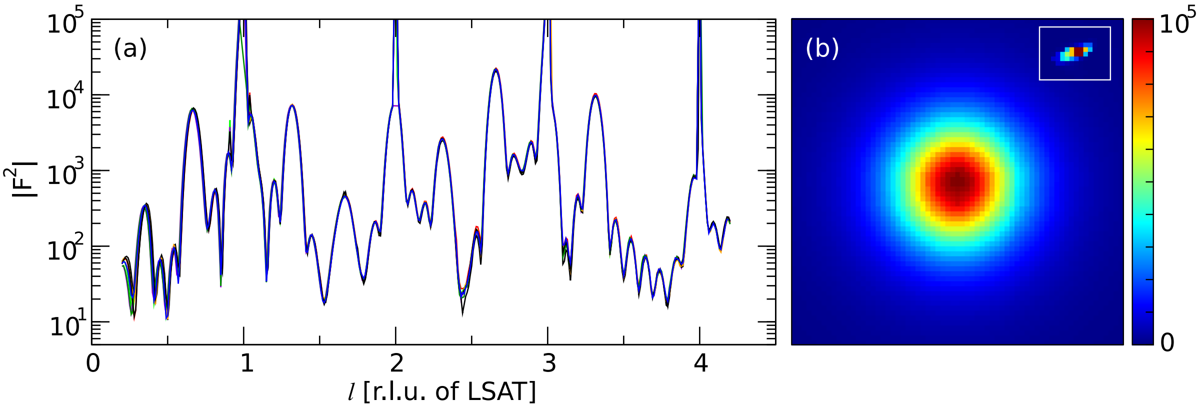

Figure 6.1: (a) Plot of all CTRs of the $(21l)$ and $(12l)$-families, demonstrating the $p4mm$ symmetry of the diffraction pattern. (b) Detector image of the $(^1/_2, ^1/_2, ^1/_2)$ Bragg peak of LSAT, taken without transmission filters. The inset shows a typical integer-order Bragg peak, recorded with a filter transmission of 8.4×10^{-6}, broadened mainly by the large beam footprint on the sample (same spatial and color scales), for comparison.

From all reported LSAT structures, the orthorhombic phase in the (001) orientation would exhibit the lowest surface symmetry of $p2mm$[2]. Comparing the eight CTRs of the $(21l)$ and $(12l)$-families, shown in Figure 6.1, it becomes apparent that the symmetry of the diffraction pattern can safely be assumed to be $p4mm$ within the accuracy of the measurements.

These findings justify the simplification of the LSAT bulk structure to a quasi-cubic unit cell with randomly occupied A- and B-sites, where the La/Sr and Al/Ta intermixing is equal to the stoichiometric ratios of the two elements, respectively. The resulting atomic coordinates and site occupations are summarized in Table 6.1.

The symmetry properties of the data set have been further investigated by applying different symmetrizations, in particular for a $p4mm$ and a $p2mm$ symmetry, and comparing the resulting systematical errors between equivalent structure factors (refer to Section C.9 for a detailed description of the procedure). As in the case of YBCO-STO, also for YBCO-LSAT, the statistical contributions ϵ_{stat} to the total error ϵ_{std} were negligible compared to the systematical deviations ϵ_{syst}. The determined values for a $p4mm$ and $p2mm$ symmetrization are summarized in Table 6.2.

Interestingly, the errors for the higher $p4mm$ symmetry are lower than for $p2mm$. This

---

[2] The symmetry at the surface could, of course be further broken and correspondingly lower.

Atom	x	y	z	occupation
La^{3+}	$1/2$	$1/2$	0	0.272
Sr^{2+}	$1/2$	$1/2$	0	0.728
Al^{3+}	0	0	$1/2$	0.648
Ta^{5+}	0	0	$1/2$	0.352
O^{2-}	$1/2$	0	$1/2$	1
O^{2-}	0	$1/2$	$1/2$	1
O^{2-}	0	0	0	1

Table 6.1: Atomic positions and occupations for the quasi-cubic $(La_{0.27}Sr_{0.73})(Al_{0.65}Ta_{0.35})O_3$ substrate unit cell with $a = 3.866$ Å.

Symmetry	ϵ_{stat}	ϵ_{syst}	ϵ_{std}
p4mm	0.007	0.070	0.070
p2mm	0.005	0.099	0.099
p4mm (1st quad.)	0.008	0.050	0.050

Table 6.2: Systematic errors between symmetry equivalent reflections, evaluated for the *p4mm* and *p2mm* symmetries from the entire data set, and for the *p4mm*, averaging only over the data from the first quadrant.

gives an important hint regarding the nature of the systematic errors. Apparently, data only within a single quadrant is much more consistent than with respect to the other quadrants. This results in a decrease of the mean systematic error for *p4mm* compared to the *p2mm* averaging. In other words, the contributions from the other quadrants must show significantly higher systematic deviations. This is confirmed by performing the *p4mm* averaging only over the data within the first quadrant, which yields a much lower average systematic error, as shown in the last line of Table 6.2.

For the calculation of the final data set, therefore, only CTRs within the first quadrant were selected. While this certainly leads to an underestimation of the systematic error, it should produce a data set with an improved internal consistency between different CTRs[3]. The averaging procedure using the *p4mm* symmetry then leads to a total of 5952 independent structure factors on 14 different CTRs in one octant of the reciprocal in-plane coordinate grid

---

[3] In the measured data set, not all CTRs have the same number of symmetry-related equivalents, nor are these equivalents from the same quadrants. The averaging over the entire data set therefore leads to a different biasing of the various CTRs and introduces a certain degree of asymmetry, which may be deleterious for further data analysis. Obviously, the overall systematic error should be calculated from the entire data set, though.

$(0 \leqslant h$ and $0 \leqslant k \leqslant h)$.

6.3 Solving the structure

Based on the experience gained with the YBCO-STO system discussed in the last chapter, we begin the structural analysis directly with DCAF, and use that result as a starting point for all further analysis.

6.3.1 DCAF analysis

Initial DCAF runs performed on the YBCO-LSAT system were somewhat more unstable than for YBCO-STO. Figure 6.2 shows the results of ten randomly initialized DCAF runs under identical conditions. Seven out of the ten solutions (marked by the thick lines) are fairly consistent with each other, while solution number 5 fails to produce an ED compatible with the expected YBCO structure. The remaining two solutions, number 6 and 3, have the same atomic stacking sequence as the other seven solutions, but are shifted by one substrate unit cell up and down, respectively. This is a consequence of the film shift constraint applied in DCAF, where the fluctuations in the height of weak ED peaks at the surface can induce a shifting operation, depending on the chosen atomicity threshold level (see Section 3.4.2 for details). By carefully selecting only those results compatible with each other, however, a reliable analysis of the features in the ED map is still possible.

Integration of the total ED in the obtained maps indicates that the measured structure factors predict a total number of electrons significantly lower than that expected for a nominal YBCO composition of the observed layer thickness, possibly caused by inaccuracies in the data correction procedure. An artificial scaling factor of 1.7 was thus applied to the measured structure factors, and the atomicity threshold slightly increased. After this optimization, the DCAF convergence was markedly improved, giving consistent results for all ten runs, and no occurrences of multiple solutions were observed. The average R-factor over all runs was $R = 10.2\%$ (lowest: 9.7%, highest: 10.7%).

The averaged ED over ten optimized DCAF runs is shown in Figure 6.3. Throughout the entire film, the atomic arrangement corresponds exactly to what would be expected for YBCO. The alternation of Ba-Y-Ba is clearly visible, and all Cu peaks have approximately the same

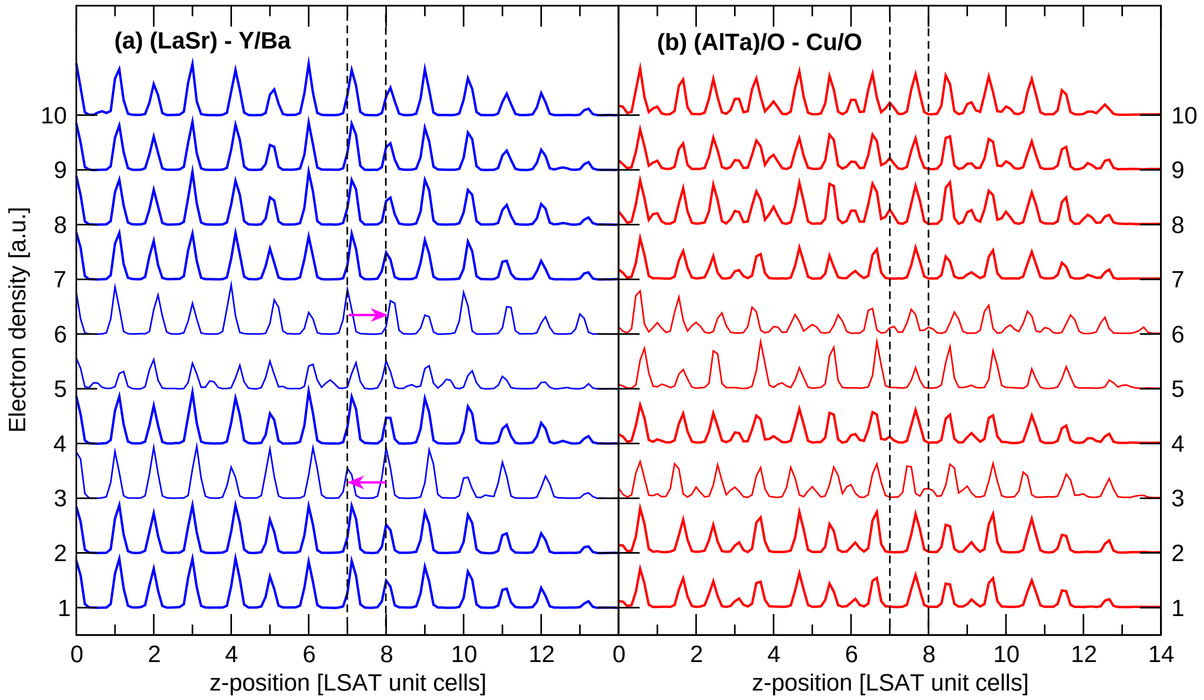

Figure 6.2: Comparison of the ED maps resulting from ten initial DCAF runs for the (LaSr)-Y/Ba and (AlTa)/O-Cu/O lines. Seven mutually consistent results are marked by thick lines. Solutions 3 and 6 are identical in terms of the atomic stacking sequences, but shifted down or up by one substrate unit cell (indicated by the arrows), while solution 5 failed to produce a sensible atomic distribution.

height and correct ratio with respect to the heavier A-site atoms. Most oxygen atoms are also present, apart from in the topmost atomic layers. This is probably an artifact, due to the decrease of the peak heights towards the surface, which is mainly a consequence of the window function applied to the experimental data rather than a real effect. This may cause the surface oxygen peaks to drop below the detection threshold of the atomicity constraint. The oxygen absences within the Y planes are correct, however, and even the fact that the Cu atoms are displaced towards neighboring Y sites can be clearly observed. The changeover from the LSAT substrate to the YBCO film is gradual, and the possibility of intermixing seems likely in at least three layers at the interface (The corresponding atom assignments in the graph are indicated by a question mark). Undoubtedly, the alternating stacking of A- and B-type layers prevails across the interface, however. The terminating layer at the surface consistently shows an additional small peak at a nominal Ba site on top of complete YBCO unit cell terminated on the CuO chain layer, suggesting the possibility of a BaO overlayer at the surface (the corresponding

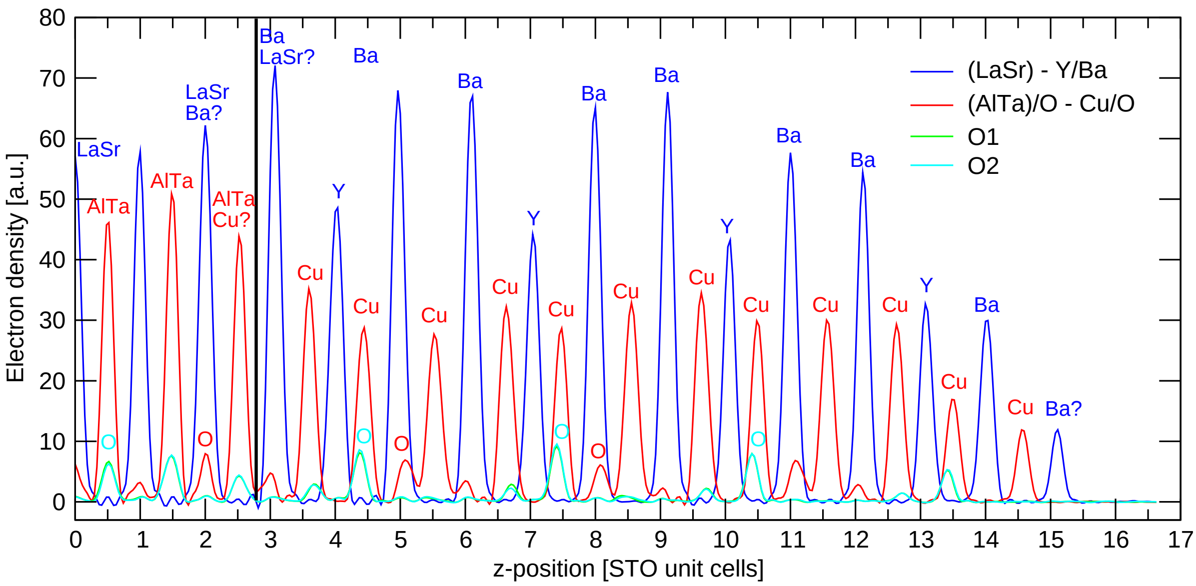

Figure 6.3: Averaged and artificially upsampled (×3) ED line-profiles from ten optimized DCAF runs. Four line-cuts through high-symmetry points of the in-plane structure are shown. The black vertical line marks the approximate position of the interface between YBCO and LSAT. Tentative assignments of the atomic species are shown above the peaks.

oxygen peaks would be too weak to be observed, due to the strong drop-off effect at the surface caused by the window-function).

The results of a quantitative analysis of the peak positions in the ED map are shown in Figure 6.4. Only those values are plotted for which the ED peak could be unambiguously identified in at least 5 out of the 10 randomly initialized runs. The z-displacements exhibit again a slight contraction with respect to a bulk-like YBCO unit cell, which was assumed to have a *c*-axis lattice constant of 11.68 Å. Otherwise, no significant atomic movements are visible. The analysis of the occupancies is somewhat undermined by the unknown effect of the window function (see above). For the bulk part, the correct stoichiometry of the intermixed cation sites was not taken into consideration here, and the integrated electron density within the peaks is simply compared to the full occupation of only one of the intermixing species, explaining the large discrepancies observed.

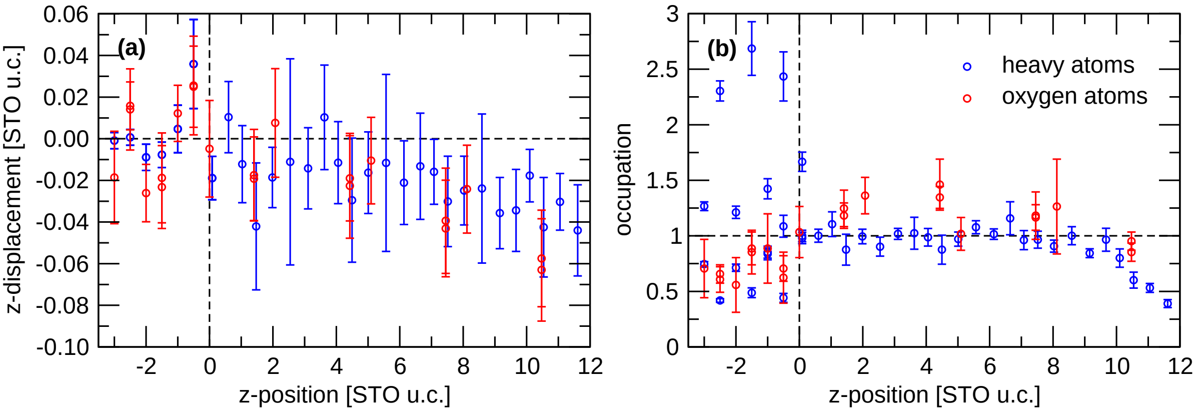

Figure 6.4: Results of a quantitative analysis of the DCAF results. The values for more stably determined heavy atom are shown in blue, and those for the much lighter oxygen atoms in red. (a) Atomic displacements in the z-direction with respect to a bulk-like YBCO reference structure, measured in fractions of the simple cubic LSAT unit cell parameters. (b) Calculated occupations of the atomic sites as a function of depth.

6.3.2 The "standard model"

The "standard model" based on the DCAF results is constructed in a manner analogous to that for the YBCO-STO case, discussed in the last chapter, and contains the following features:

- One unit cell of bulk-like LSAT, terminated on the B-type $(AlTa)O_2$ layer, as a substrate (coordinates and occupancies as given in Table 6.1).
- Four unit cells of bulk-like YBCO, starting on the A-site BaO layer and correspondingly terminating on a CuO layer (where the chain oxygens randomly occupy the two available positions).
- A single BaO overlayer at the top of the film, initialized with an occupation of 0.1.
- The occupation of the topmost YBCO unit cell is initialized with a value of 0.75, while all lower layers are assumed to be fully occupied.
- Global Debye-Waller factors for each kind of atom in the structure (oxygens within the sample are treated separately from those in the film).
- Three layers of potentially intermixed layers at the interface (two topmost substrate layers plus the first film layer).
- A general scale factor.

The number of free fit parameters and their initial values are summarized in Table 6.3. Tests where more than one unit cell of the LSAT bulk has been included have not yielded any significant improvements. In order to limit the number of free parameters, the standard model therefore includes just one LSAT unit cell.

Parameter name	Type	#	initial value(s)
General data set scale factor	scale factor	1	1.0
Substrate DW: La^{3+}, Sr^{2+}, Al^{3+}, Ta^{5+}, O^{2-}	DW	5	1.5, 0.5, 0.5, 0.5, 1.0
Film DW: Y^{3+}, Ba^{2+}, Cu^{3+}, O^{2-}	DW	4	0.5, 0.5, 0.5, 1.0
(LaSr:Ba) intermixing in top substrate layer	occupation	1	(1:0)
(AlTa:Cu) intermixing in top substrate layer	occupation	1	(1:0)
(LaSr:Ba) intermixing in bottom film layer	occupation	1	(0:1)
Top YBCO layer occupation	occupation	1	0.75
BaO overlayer occupation	occupation	1	0.10
Atomic z-movements	displacement	56	0
Total		**71**	

Table 6.3: The 71 free parameters of the YBCO-LSAT "standard model" and their initial values used in the refinement.

6.3.3 COBRA results

COBRA runs starting from the standard model have essentially confirmed the initial structure without providing further details or giving hints to necessary changes of the starting model. One interesting aspect concerns the BaO overlayer. To test the authenticity of this feature, COBRA was initialized with a reference model which did not contain the overlayer. In the course of the analysis, however, the feature reliably reappeared in the ED map, providing a very strong confirmation for its existence, as found with DCAF. The occupation of the top layer, however, remained very low at values between 10% and 25%.

A detailed analysis of the ED maps resulting from COBRA has been set aside for this system, due to the lack of new information.

6.3.4 Analysis with FIT

The classical model refinement of the standard model was again carried out using FIT. The *p4mm* symmetry of the model is strictly enforced. Furthermore, the intermixing at the interface is restricted to occur on three atomic sites, meaning that the positions of the intermixing cations had to be identical for each site. Physically, this requirement may not be sensible, as the various competing forces may well cause different displacements, depending on the atomic species. However, a relaxation of this requirement is not expected to change the nature of the solution significantly.

The solutions obtained with FIT from the standard model are, unfortunately, very unreliable. Many atoms exhibit unphysically large movements, and also the DW factors for Sr and Al consistently take on unreasonable values far above 20. Restricting the z-displacements of the atoms and the DW-factors does not help. Attempts to refine the global parameters in a first fit, followed by a second run which includes all the z-displacements did not improve the fit quality significantly, and still result in unphysical values. This behavior is observed regardless of whether the bulk-like starting positions or those provided by DCAF are used. The best achieved R-factors were 24% when starting from bulk, and 25% for the DCAF positions. Inspection of the CTRs (not shown here) shows a poor fit of the data to the final models, clearly indicating that the obtained solutions are far from optimal.

Despite the obvious problems in finding a meaningful solution, three of the model parameters were found to give very consistent results with FIT, namely the general scale factor for the data set (0.44–0.47), and the occupations of the topmost YBCO unit cell (0.59–0.70) and the BaO overlayer (0.15–0.26).

6.3.5 Analysis with GenX

In contrast to FIT, the *p4mm* symmetry was not enforced in the analysis using GenX, the reason for which was explained in Section 5.3.7. The same applies to the position of the intermixing atom at the interface. There, each atom involved in the intermixing can have a different position in the GenX refinement. Therefore, the number of free parameters in the system is increased to 83, and due to the additional degrees of freedom, a slightly better agreement with the data is to be expected than with FIT.

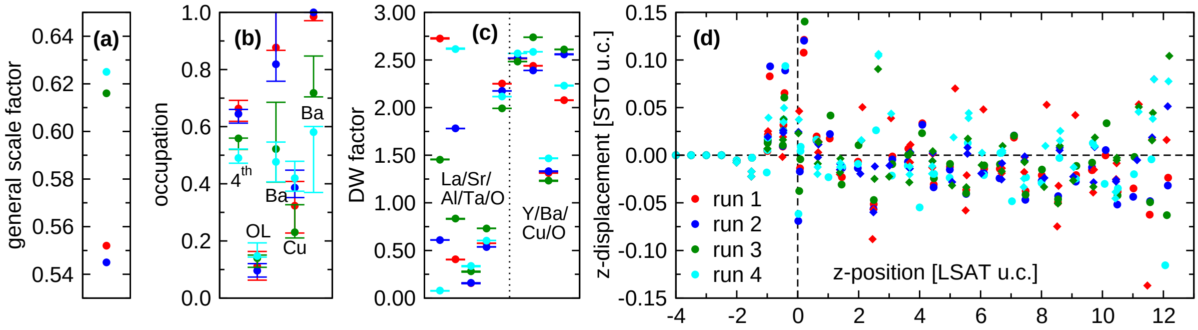

Figure 6.5: Comparison of four repeated GenX run under identical conditions using the same DCAF starting guess (run 1 = red, run 2 = blue, run 3 = green, run 4 = cyan). (a) Final value of the general scale factor. (b) The occupation parameters for the 4th YBCO layer, the BaO overlayer, the Ba fraction of the (LaSr:Ba) intermixing and the Cu fraction for the (AlTa:Cu) intermixing. (c) The refined DW factors for the LSAT atoms (five values on left) and the YBCO atoms (four values on right). (d) z-displacement values for all atom positions.

A fundamental difference between FIT and GenX concerns the use of constraints for the fitted parameters. While for the former, the application of constraints is possible in principle, but not active by default, the latter uses the chosen constraints on each parameter for the random creation of the starting population. Thereby, knowledge about the constraints is an inherent property of the members of each generation, making an uncontrolled drift virtually impossible. This is in stark contrast to the case of FIT, where each parameter is optimized separately, and, if no constraints are active, is allowed to drift far away from its starting position within a single cycle[4].

The GenX results obtained from the standard model for this system are much better than those produced by FIT, both regarding their agreement with the experimental data and their stability. The resulting R-factors are in the range of $R = 17.0\%$ when using a bulk-like starting guess, and $= 16.5\%$ for the initial positions determined with DCAF.

No unphysical movements of atoms can be observed, and virtually all atoms remain well within the given lower and upper limits of ±0.2 unit cells of STO for their deviations away from the starting positions, as seen in Figure 6.5, comparing four runs with identical starting conditions based on the DCAF analysis. The stability of the global DW-factors is also very much improved. As was the case for YBCO-STO, all substrate and film-atoms have comparable

---

[4] To prevent an exceedingly large drift within one iteration, there is, however, a parameter controlling the maximum allowed drift distance per optimization.

DW-factors, even though the spread in the substrate values is somewhat larger. This is especially true for the La/Sr atoms, and may be related to the slight distortions of the real LSAT structure compared to the ideal simple cubic structure assumed in the reference structure (see Section 7.2).

The results for the general scale factor are somewhat higher than the values found with FIT, and show a peculiar distribution with two low and two high values, the reason for which is unknown. The occupation results are fairly consistent, resulting in an approximately 60% coverage of the topmost YBCO layer, and 10-15% for the BaO overlayer. The intermixing occupations at the interface fluctuate more, and should be interpreted with care.

6.4 Comparing the results

Due to FIT's difficulties in determining a meaningful solution, a direct comparison of the results obtained from the various combinations of algorithms is difficult. When plotting the z-displacements for all methods in one graph (see Figure 6.6), however, it may be seen that the fluctuations in the final positions obtained with FIT for the standard model are not significantly larger than for those determined with GenX.

Consequently, there are hardly any signs for consistent trends in the displacements. Possibly, the interface region is slightly expanded, but this expansion does not seem to translate into the YBCO lattice on top of the substrate (which is still referenced with respect to a bulk-like model). In contrast to the YBCO-STO system, the potential c-axis compression observed with DCAF is also much less obvious after the refinement.

6.5 Conclusions

In summary, the analysis of the YBCO-LSAT data has been more ambiguous than for YBCO-STO, and has not led to an unequivocal conclusion regarding the fine details of the structure. The main reason for that may be that the chosen parameterization for the standard model is actually not an adequate description of the system. More detailed refinement studies and model optimizations would be required to investigate this point further.

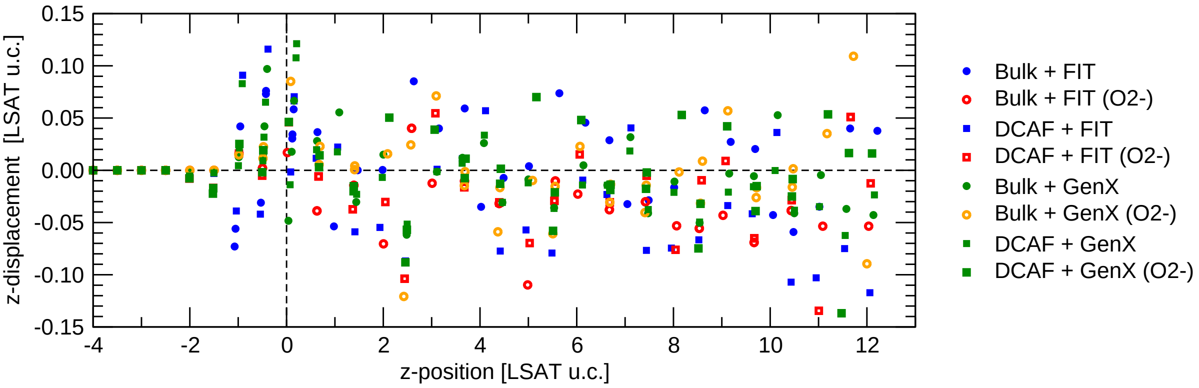

Figure 6.6: Comparison of the refined z-displacements for different combinations of structure solution algorithms. Note that some data points are cut off by the choice of the y-axis limits, which were chosen in order to highlight any potential trends seen in small displacements. Shown are only those solutions with the lowest R-factor for each of the four different approaches.

Another possibility is that the data set contains systematic errors, resulting in an inconsistent intensity distribution for which no good solution can exist. However, the good results obtained from DCAF provide strong evidence against such a scenario.

In its present state, the analysis of this system is able to provide a general picture of the global film structure with high confidence. The DCAF solution, based only on *a priori*-information and the measured structure factors, gives an excellent and model-independent confirmation for the correct atomic structure and the high quality of the heteroepitaxially grown YBCO film. The sensitivity to detect more subtle changes on the atomic level with high precision is insufficient, however, to answer many of the physically much more relevant questions regarding, for example, the exact interfacial structure, the distribution of oxygen atoms within the film, and the structural changes induced by the symmetry and strain of the substrate.

It should be stressed again, however, that the overall observed deviations from an absolutely bulk-like model are very small. The global structure of this very thin film may therefore be confidently regarded as very similar to a bulk crystal, a fact which may have a significant impact for the use in technological applications on the one hand, and the interpretation of surface-sensitive measurements performed on such films, on the other hand.

Bibliography

[1] T. Ohnishi, K. Takahashi, M. Nakamura, M. Kawasaki, M. Yoshimoto, and H. Koinuma: "A-site layer terminated perovskite substrate: $NdGaO_3$." *Appl. Phys. Lett.* **74**(17), 2531 (1999), doi: 10.1063/1.123888.

Chapter 7

Results on $NdGaO_3$ Substrates

7.1 Introduction

The third growth substrate used in this study is $NdGaO_3(110)$ (NGO), chosen for its nominal A-site termination, the slight orthorhombicity of the surface unit cell and its excellent lattice match with YBCO (see Section 4.3.1).

In a first step, the bare NGO surface after the annealing procedure was measured, in order to characterize the structure of the growth substrate before the deposition of thin films, and to independently confirm that the surface termination is on the A-site (NdO) layer. Then, the two samples with four ML of YBCO grown on top of unprepared and annealed NGO, respectively, have been investigated. Details about the growth of the films and the substrate preparation can be found in Chapter 4.

Unfortunately, no satisfactory structure determination could be obtained on these samples to date. The technical challenges involved in the use of NGO(110) as a growth substrate and the consequent problems with regard to the use of direct methods and traditional refinement procedures will be discussed briefly in this chapter. We will not go into great detail, but a short review of the experience gained with this system may help to develop an understanding for the limitations of our analysis approach, and hint at possible improvements for next experiments.

7.2 SXRD measurements and data reduction

The experimental conditions used to record the diffraction data of the bare NGO(110) substrate surface and of the four-ML-thick YBCO films on NGO are identical to those reported for YBCO-STO and YBCO-LSAT in the previous chapters.

The first obstacle when working with NGO is the definition of a useful surface unit cell for the (110) oriented crystal. Ideally, the c'^*-direction of the new unit cell should be perpendicular to the physical surface, such that the CTRs run along the l-direction. This requirement results in the real space a' and b' axes lying in the surface plane. Our particular choice of surface coordinates is illustrated schematically in Figure 7.1. The surface unit cell has a volume twice as large as the original orthorhombic bulk unit cell, and the c'-axis is no longer perpendicular to the surface planes. In reciprocal space, the situation is reversed. The c'^*-direction is normal to the surface, but the a'^*-axis is inclined with respect to the physical surface. This results in the "in-plane" Bragg peaks with $H > 0$ lying below the physical surface plane, and therefore they cannot be seen in the experiment. However, the deviation from an orthogonal coordinate system is very small ($\beta'^* = 89.27^\circ$).

Another important difference from the previously analyzed systems lies in the symmetry of the surface unit cell. The $Pbnm$ symmetry of the orthorhombic bulk structure results in the relatively low pm surface symmetry. The only mirror plane lies in the $a'c'$-plane, leading to the equivalence of (HKl) and $(H\bar{K}l)$ reflections. The irreducible part of the diffraction pattern therefore consists of all CTRs with $K \geqslant 0$. Compared to the $p4mm$ symmetry of the YBCO-LSAT and YBCO-STO systems, this means a large increase in the number of CTRs to be measured for a structure determination by approximately a factor of four. Furthermore, the unit cell parameters are approximately twice the size as for the simple cubic LSAT and STO unit cells. In order to obtain a similar resolution on the atomic level in real space, one thus has to measure twice as far in terms of the H and K indices of the CTRs. As an example, let us assume we have measured a complete data set for STO with $0 \leqslant H \leqslant 4$ and $0 \leqslant K \leqslant H$, comprising a total of 15 CTRs. A complete data set on NGO(110) having the same real space resolution consists of all CTRs with $-8 \leqslant H \leqslant 8$ and $0 \leqslant K \leqslant 8$, which amounts to 153 individual rods. One challenge for these systems is therefore simply the acquisition of sufficient amounts of data.

As a consequence of the low surface symmetry, the restrictions on the allowed atomic move-

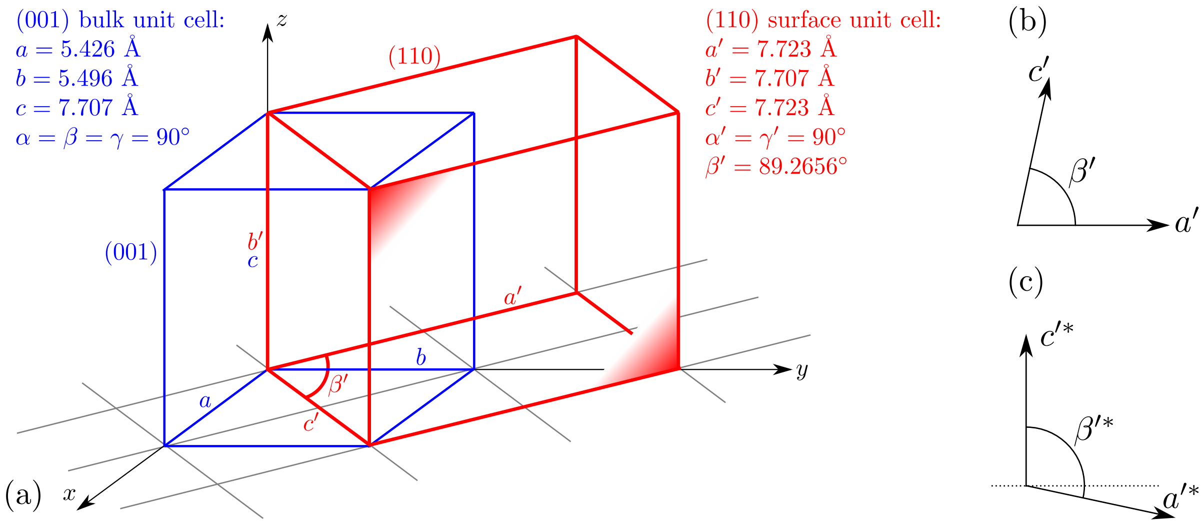

Figure 7.1: (a) Definition of the (110) surface unit cell of NGO (red) with respect to the orthorhombic (001) bulk unit cell (blue). The shaded corners highlight a plane belonging to the {110} family. Note that this definition of the coordinates results in a doubling of the unit cell volume and a c'-axis, which is not perpendicular to the physical surface, but encloses an angle of $\beta' = 89.27°$ with the surface plane, leaning into the new (100) direction, as shown in (b). The corresponding reciprocal space lattice, drawn in (c), has its c'^*-direction perpendicular to the surface (indicated by the dotted line), but the a'^*-axis is no longer in-plane. The b'^*-axis is perpendicular to the plane of the paper and still lies within the surface plane.

ments within the surface or film layers are less stringent, and the number of free parameters of any model is therefore also dramatically increased, rendering a reliable structure determination more difficult. For example, all atoms are now allowed to move within the $a'b'$-plane, as long as the movements conform to the mirror symmetry with respect to the $a'c'$-plane.

For the bare NGO(110) substrate surface, a complete data set with $-7 \leqslant H \leqslant 7$ and $0 \leqslant K \leqslant 7$ has been measured, plus 27 equivalent rods to establish the systematic error, which was found to be approximately 10%. The step-size along l was chosen to be 0.05 of a r.l.u., and the scans were started at $l = 0.4$ and continued up to the highest reachable l-values. The *pm*-symmetrized data set contains approximately 19 600 structure factors on 120 individual CTRs. Figure 7.2 shows a plot of all measured inequivalent CTRs to convey a visual impression of the sheer size of the data set.

In the case of the YBCO films on NGO(110), the step size in l had to be reduced to 0.02 r.l.u., in order to resolve the Laue oscillations between the YBCO Bragg peaks. Due to the increase

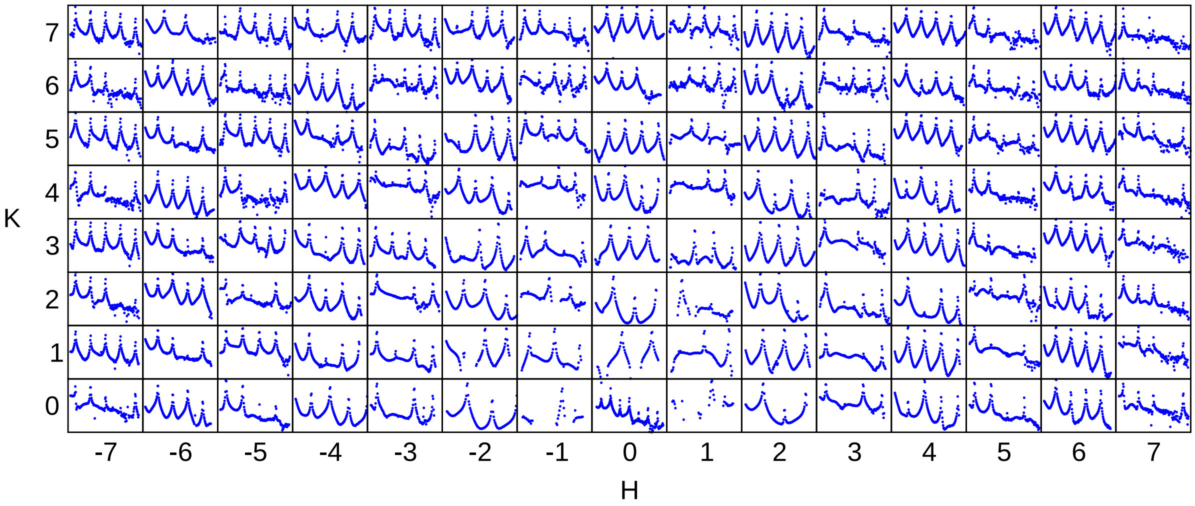

Figure 7.2: Logarithmic CTR plots of the entire acquired NGO(110) data set (no geometric correction factors applied), sorted according to their H and K indices. Each rod is scaled individually. The data set is fairly "complete", in the sense that it contains all CTRs within a certain range of H and K, with reciprocal space data only missing for the experimentally not readily accessible low l-values.

in measurement time, it was not possible to measure complete data sets with the required resolution within the available beam time. The two data sets contain 65 and 88 inequivalent CTRs for the films grown on annealed and as-received NGO substrates, respectively. To date, only the second set has been analyzed, yielding a total of close to 32 000 structure factors.

7.3 Direct methods results

Direct methods runs on the NGO surface and YBCO-NGO film system have not been able to yield any satisfactory results, neither using COBRA nor DCAF. The reasons for this failure are not known with certainty.

In case of the NGO surface, the available data set is fairly complete, apart from the low-l-data points which could not be measured reliably using the open slit geometry (see Chapter B)[1]. The diffraction data from the highly crystalline sample was very clean and easily extracted from the detector images (see Chapter C). Insufficient quality of the data therefore seems a very

---

[1] This is no different than for the YBCO-STO and YBCO-LSAT systems, however. Despite this general problem, the results obtained in those cases were far superior to those for NGO.

unlikely reason for the failure. A much more likely cause may be the somewhat complicated symmetry of the NGO(110) unit cell. So far, COBRA and DCAF have been used exclusively for the structure determination of high-symmetry systems, and it is difficult to judge whether their code can deal with sufficiently general symmetry classes. Furthermore, while being very effective for thin film systems with a well-defined layer thickness, the highly successful film shift projection used by DCAF may not be as efficient for systems which show only minor structural changes with respect to the bulk reference. Further studies would be required to investigate these effects in more detail.

For the YBCO-NGO film system, the most likely cause for failure is the incompleteness of the data set. After removing unreliable data points in the data set and accounting for all the missing CTRs and low-l-data necessary to fill up a reciprocal space volume with $-6 \leqslant H \leqslant 6$ and $0 \leqslant K \leqslant 6$ up to l-values of 9.5, the completeness of our data set was below 40%. In addition, the real space resolution resulting from this data set is so low that the application of the atomicity constraint in DCAF becomes problematic, as the individual atoms are not necessarily well enough separated from each other[2]. COBRA, on the other hand, does not use an atomicity constraint, but still failed to produce meaningful ED maps.

7.4 Refinement of the $NdGaO_3$ surface using GenX

Attempts to directly refine the structure of the bare NGO(110) surface, starting from a bulk-like NdO terminated reference structure, have also been unsuccessful. Multiple refinement runs have yielded mutually incompatible solutions without any satisfactory agreement with the data. This is not very surprising, considering the number of free parameters if the system is allowed to relax down to only one surface unit cell, comprising four atomic layers. This involves finding the x,y, and z-coordinates of 20 symmetry-independent atoms, and possibly their occupations and associated DW-factors. The refinement therefore contains more than 80 free parameters, and there is no reliable starting guess available from direct methods. A comparison of the measured data with simulations obtained for bulk-like surfaces, terminated

---

[2] Consider, for example, the voxel size along the a'-axis, which is given by $1/(2|h|_{max}+1) = 1/(2{\cdot}6+1) = 1/13$ of an NGO unit cell. We need to resolve four atom positions along that axis. Each atom occupies 3 voxels in the atomicity constraint, giving a total of 12 occupied voxels out of the 13 in total. The occupied voxels of one atom are therefore in contact with those belonging to another atom. Movements of the atoms can therefore lead to an overlap which is not compatible with the atomicity constraint.

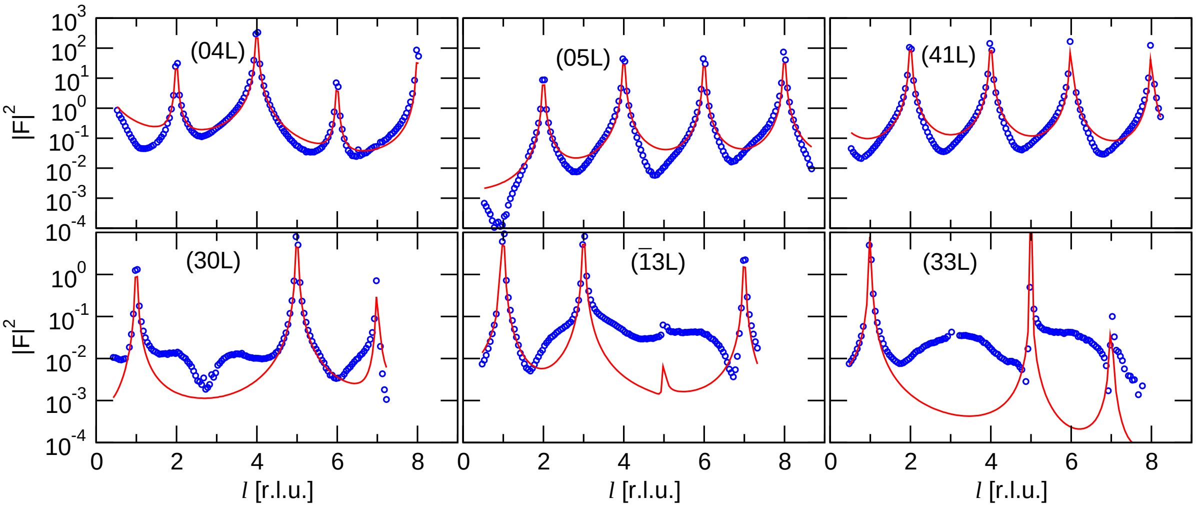

Figure 7.3: A selection of measured NGO(110) CTRs (blue circles) in comparison to the simulated CTRs (red lines) for a bulk-like surface structure, terminated either on NdO or GaO$_2$ (which give identical CTRs). Note that the upper three CTRs with even values of H have significantly higher values for $|F|^2$ than those in the lower graphs with odd values of H.

either on NdO or GaO$_2$, is show in Figure 7.3. Note that the two models, differing only in their terminating layer, have identical diffraction patterns, as long as all atoms remain on bulk-like positions. This degeneracy is lifted, however, once the atoms begin to rearrange.

The large discrepancies between the models and the experimental data suggests significant atomic rearrangements at the surface, the nature of which is unknown, however. In other words, these starting guesses are most certainly too far from the real structure to yield a successful fitting solution. Due to the lack of complementary information, the refinement runs have therefore been abandoned after several attempts.

7.5 Conclusions

In conclusion, no meaningful results could be obtained for the systems involving the NGO(110) substrates. We are confident, however, that this does not represent an intrinsic limitation of direct methods, but is rather caused by an insufficient data set, considering the size of the structure solution problem, possibly in combination with the algorithms not yet being adapted to dealing with sufficiently general symmetry definitions.

Chapter 8

Conclusions and Outlook

In Chapters 5 and 6, we have described in detail our attempts to solve the structure of an approximately four ML-thick YBCO film on top of STO and LSAT, with the aim to rely as much as possible only on the information directly obtainable from the measurements, and thus preserving the highest possible degree of objectivity, through a well-defined set of procedures, for the analysis. To date, this ambitious proposition has been to a large extent successful, although by no means as straightforward or clear-cut as initially envisaged. The reasons for this are manifold, and will be summarized in the next paragraphs.

Most importantly, it has to be stressed that in spite of all efforts, the procedures were in fact not entirely model-free or objective. Starting with the selection of adequate data sets and the extraction of the intensities from detector images, via the choice of constraints used in the direct methods, the interpretation of the resulting ED map and its particular parameterization, up to the choice of refinement parameters and the type of figure of merit, there are many decisions to be made throughout the entire analysis, for none of which there is a clear and well-defined choice. Rather, the success of the analysis still relies largely on the intuition and experience of the experimentalist.

Another critical factor for success is the quality and the amount of the available diffraction data itself. The use of the PILATUS pixel detector has led to a marked increase both in the acquisition speed and the reliability of the data, opening up the possibility to investigate systems of unprecedented complexity. At the same time, adaptation of established measurement procedures to this new technology is necessary, requiring a profound understanding of the underlying physical and experimental principles. Only then can the full potential of the detector's capabilities be exploited to extend the frontiers of surface structure determination methods. It is expected that, based on the experience gained with the PILATUS detector, further improvements of the data acquisition process will yet provide significant enhancements of the obtainable data quality, which will, in turn, allow for more precise structure determinations. Naturally, this step does not solely include the detector aspects, but the high quality and efficiency of the new detectors may call for an improved overall performance and stability of the beamline.

One particular limitation of the current SXRD setup at the Materials Science beamline of the Swiss Light Source is related to the insertion device. The large size of the focussed synchrotron beam produced by the wiggler results in a complete flooding of the sample in the beam direction at grazing incidence angles [1]. When recording data in the stationary (open slit) geometry, the entire illuminated area is visible to the detector and the diffraction data represents its average response. The sample must therefore be exceedingly homogeneous over its entire extent, up to the edges of the specimen. Additionally, the scattering from the edges themselves must be assumed to have no effect on the measured data. Finally, the exact extent and shape and the precise orientation of the sample on the diffractometer must be known to correct for the change in the illuminated area as a function of diffractometer angles. Obviously, this situation is not ideal to obtain high-quality data. The use of an undulator instead of a wiggler source would greatly improve the situation, thanks to the much smaller beam spot sizes and the higher achievable brilliance. The sample could be illuminated in a well-defined region close to the center of its surface, even at grazing angles, while the brilliance of the beam would guarantee sufficient scattering intensities. Undulator radiation at the MS beamline is planned for the end of 2010.

Finally, one should also keep in mind that direct methods for SXRD are only just becoming available, and high-quality SXRD data sets for the use with direct methods have been very difficult to obtain until recently. Experience with these methods is therefore still limited and restricted to a few groups worldwide. This pioneering work has resulted in several successful structure determinations, which convincingly corroborate the unique strengths and the usefulness of these methods. However, development is still ongoing, and the full potential is far from being exhausted. Significant improvements in the performance of direct method algorithms seem to be a realistic prospect. However, this will require many more tests and systematic studies to develop a comprehensive understanding of all elements constituting the approach, and to identify those factors crucial for the success of the method. This understanding will have to go hand in hand with the optimization of the data acquisition to fulfill the particular requirements for direct methods, which are most certainly quite different than for traditional refinement procedures.

Our attempts to achieve an absolute scaling of the structure factor amplitudes from the measured diffraction intensities have yielded very promising first results. The corrected structure factors are definitely of the right order of magnitude and certainly within a factor of two to three of the real values. A more precise estimate of their accuracy is presently difficult, due to the lack of a well-defined standard. The refined scale factors for the YBCO-STO and YBCO-LSAT systems represent only an approximation, because the true structural solution is still unknown and the accuracy of the obtained scaling parameters is therefore an open question. Secondly, the above-mentioned problems related to the flooding of the sample are expected to introduce additional experimental errors. Precise quantification can therefore only be accomplished by a direct comparison to a well-known model system of very high crystalline quality, for example using the Si(111)(7×7) reconstruction, and under ideal experimental conditions. In a second step, the tolerance of the available direct method algorithms to slight deviations away from the correct scaling factor should then be analyzed. Our results indicate, for example, that DCAF is sufficiently robust to tolerate deviations up to a factor of two and still produces meaningful ED maps. Most importantly, however, by analyzing the resulting ED maps in terms of the integrated number of electrons, a direct feedback about the scaling can be obtained and the proper corrections may be applied.

The application of DCAF to the data sets of YBCO-STO and YBCO-LSAT has led to a successful retrieval of representative ED maps, which clearly showed a distribution of atoms in close agreement with a bulk-like YBCO film on top of the corresponding substrate structure. The interpretation of these ED maps allowed us to construct a structural model that could be used as a starting point for refinement procedures.

The importance of the DCAF results cannot be overstated. Based only on the experimental data and the *a priori* knowledge that the system should be made out of atoms, have a positive electron density, and a finite film thickness, DCAF was able to retrieve the three-dimensional ED map of a structure containing approximately 70 atoms![1] The reproducibility of the struc-

---

[1] Note that this is different from "normal" bulk crystallography, in which unit cell structure far in excess of 70 atoms are routinely solved. In this latter case, the unit cell is repeated many times in all three spatial directions,

tural information can be easily ascertained by repeating the phase retrieval several times from randomly generated starting ED maps. Features which are stable between many runs may therefore be adopted with confidence as being real, while the level of the fluctuations gives an immediate feedback about the sensitivity limit. This is in absolute contrast to any model-dependent analysis, where the adequacy of a chosen model can only be evaluated with respect to other models, while the true structure may never be recovered.

The stability and accuracy of the ED maps obtained by DCAF and other direct methods depend strongly on the chosen constraints. In the case of weak constraints, the solutions may not be reproducible and fluctuate a lot between random restarts, whereas the application of very strong constraints can affect the nature of the solution (for example, the ED map will always contain a discrete set of peaks when atomicity is enforced). This has to be kept in mind when analyzing the ED maps. However, in our experience, the statistically stable features of the corresponding solutions have never been found to be mutually incompatible for different sets of constraints [2]. While they may show a different level of structural details, we have not yet found two stable solutions based on the same data set, which represent two completely distinct structures.

The observation that the choice of constraints and constraint parameters is essentially independent of the nature (but not the quality) of the results, paves the way for further developments of the algorithms and provides a large flexibility to combine different successful approaches. For example, it may be useful to initiate a given phase-retrieval run with strong constraints, designed to efficiently determine the dominant features of a structure. This rough approximation could then be used as the starting point for further runs, in which the constraints are successively relaxed in order to obtain more detailed information. For each step, the reproducibility can be easily determined, and the analysis stopped once the stability becomes insufficient.

The COBRA method provides a very efficient way to improve the quality of an electron density map further, starting from a rough approximation of the true structure. COBRA

---

giving rise to very strong diffraction features. In SXRD, we are concerned with a very thin two-dimensional layer with a structural unit repeated only in two dimensions on top of a three-dimensional crystal, which contributes strongly to the diffraction pattern. While this does not constitute a principle problem, the technical challenges for obtaining SXRD data of similar quality than for a bulk crystal are still tremendous. Structure solutions of much larger systems may therefore become routine in the future, but for the present state-of-the-art direct methods for SXRD, 70 atoms represent a large structural unit.

may therefore be ideal to optimize any model which is sufficiently well known to begin with, regarding, for example, the correct number and stacking of atomic layers, etc., which may have been determined with other direct methods or complementary techniques. Since COBRA is not bound to any strong real-space constraints, it may pick up physical effects that are precluded from other methods. One example is the overlapping of atoms in a folded (averaged) structure, which is due to the presence of domains or an incommensurate match of the film on the substrate [3], that cannot be seen when applying the atomicity constraint. On the other hand, the weakness of the constraints also allows for the appearance of artifacts. The final ED maps therefore have to be interpreted with equal care as that necessary for any other method.

Whether the structural details obtained in the retrieved ED map are sufficient for a conclusive analysis depends mainly on the physical questions asked about the system. In many cases, a quantitative or semi-qualitative picture of a two-dimensional structure may be a perfectly adequate result, while for other questions, in particular for the systematic investigation of structural changes induced by various external factors such as temperature, pressure, film thickness, etc., a parameterization of the structure in terms of an atomic model is indispensable. Naturally, the direct methods results provide invaluable indications as to how the atomic model should be built up.

There are a few different methods available to perform the subsequent model refinement. We have used both a robust grid search algorithm, as implemented in FIT [4], and a differential evolution algorithm, provided by GenX [5]. For the particular systems investigated in this thesis, the results from both methods did not differ significantly, and each has its merits and drawbacks in terms of speed and reliability. The fits obtained from the starting guesses, which were built up based on the feedback of the direct methods results, give no unique and reproducible structural solution for both methods. This is most likely due to inadequacies of the starting model to correctly describe the system, and more thorough (and correspondingly time-consuming) refinement runs will most certainly give better results. However, they require a manual and iterative optimization of the atomic model. Furthermore, it is essentially impossible to prove that the final result corresponds to the correct solution of the atomic structure. Ultimately, only reproducibility checks through random initializations or the use of different analysis methods can establish the probability of the validity of a solution. In this context, the importance of complementary techniques cannot be overstated, as only they can provide independent evidence to support or reject a model obtained with SXRD.

The structure obtained for the YBCO thin films on LSAT and STO is exceedingly bulk-like in terms of the atomic arrangement and the ratios of interatomic distances. The influence of the growth substrates seems to be essentially restricted to a heteroepitaxial straining of the YBCO film, which consequently assumes the in-plane lattice constants of the surface unit cell of the substrate. Since $a = b$ for STO and LSAT, this results in the formation of a tetragonal YBCO film unit cell. The tensile in-plane stress causes the c-axis lattice constant to contract slightly by less than 1% for YBCO on STO. This value is in excellent agreement with the contraction expected, based on the reported Poisson ratio of 0.17 [6] and the increase of the surface unit cell size with respect to the bulk structure by approximately 2.6%.

It is interesting to note that the tetragonally distorted YBCO films are superconducting with critical temperatures exceeding 60 K, even though the tetragonal bulk phase of YBCO, forming at oxygen contents below 6.5, is insulating. Apparently, there is enough oxygen incorporated in the film to allow for superconductivity, despite the substrate-induced strain.

This detailed structural information about the films is of eminent importance for other investigations. Firstly, it provides a firm structural basis for the interpretation of surface-sensitive measurements, for example of the electronic structure using angle-resolved photoelectron spectroscopy. Secondly, it may serve as a well-defined and realistic starting point for theoretical models, as for instance for band-structure calculations. Finally, the fact that the film structure is very bulk-like allows for a direct correlation between bulk properties and experimental results obtained from high-quality thin film samples, making them viable substitutes for bulk samples, where the latter are unavailable in sufficient quality.

There seems to be a small region at the interface with a thickness of two to three atomic layers where intermixing between the film and substrate atoms occurs. This could be caused by the fact that the growth substrates were not treated to have a single termination at their surface. The sensitivity of the diffraction data and the atomic model is, however, insufficient to accurately quantify the intermixing ratios. Also the surface termination could not be determined with absolute certainty, though there are strong indications that the topmost layer consists of BaO_x, where the oxygen content can, of course, be different than for a bulk BaO layer.

The phase diagrams of most complex transition metal oxides exhibit a dramatic dependence on the oxygen content of the material, resulting in a vast variety of physical properties for the same mother compound. Some of the most interesting questions therefore concern the exact distribution and concentration of oxygen atoms in these structures. As an example, for the tetragonally strained YBCO thin films, the arrangement of oxygen atoms in the nominal CuO chain layers is most certainly different from the bulk (where the oxygen preferentially occupies the lattice sites along the b-axis), since, in the pseudomorphically strained films, the a- and b-directions are degenerate.

For present state-of-the-art SXRD analyses, the accurate determination of the positions and occupations of such low-Z materials as oxygen is still very challenging. Ultimately, however, one would like to be sensitive to small movements and partial occupations of these atoms, setting stringent requirements on the accuracy of both the measurements and the employed direct methods and model refinement tools.

The future will show how far improved data acquisition and streamlined data treatment in conjunction with direct methods can establish SXRD as a standard surface and thin film characterization technique. Based on our experience, we believe there to be a large potential, at least for qualitative and semi-quantitative characterizations, providing information complementary to many other well-established surface characterization techniques. In order to obtain high-quality structure solutions, however, the input and interaction of an experienced and skillful scientist will undoubtedly always be required.

Bibliography

[1] C. M. Schlepütz, R. Herger, P. R. Willmott, B. D. Patterson, O. Bunk, Ch. Brönnimann, B. Henrich, G. Hülsen, and E. F. Eikenberry: "Improved data acquisition in grazing-incidence X-ray scattering experiments using a pixel detector." *Acta Crystallogr. A* **61**, 418–425 (2005), doi: 10.1107/S0108767305014790.

[2] M. Björck, C. M. Schlepütz, S. A. Pauli, D. Martoccia, R. Herger, and P. R. Willmott: "Atomic imaging of thin films with surface x-ray diffraction: introducing DCAF." *J. Phys.: Condens. Matter* **20**(44), 445006 (2008), doi:10.1088/0953-8984/20/44/445006.

[3] Y. Yacoby, M. Sowwan, E. A. Stern, J. O. Cross, D. Brewe, R. Pindak, J. Pitney, E. B. Dufresne, and R. Clarke: "Direct determination of epitaxial film and interface structure: Gd_2O_3 on GaAs (100)." *Phys. B: Condens. Matter.* **336**(1-2), 39–45 (2003), doi:10.1016/S0921-4526(03)00267-9.

[4] O. Bunk: *Bestimmung der Struktur komplexer Halbleiter-Oberflächenrekonstruktionen mit Röntgenbeugung.* Ph.D. thesis, Universität Hamburg, Hamburg (1999).

URL http://www.physnet.uni-hamburg.de/services/fachinfo/___Volltexte/Oliver___Bunk/Oliver___Bunk.pdf

[5] M. Björck and G. Andersson: "GenX: an extensible X-ray reflectivity refinement program utilizing differential evolution." *J. Appl. Crystallogr.* **40**(6), 1174–1178 (2007), doi: 10.1107/S0021889807045086.

[6] B. Bridge: "Anomalies arising from a comparison of the elastic constants of the high-temperature superconductor $YBa_2Cu_3O_{7-x}$ and the related perovskite structure $BaTiO_3$." *J. Mater. Sci. Lett.* **8**(6), 695–696 (1989), doi:10.1007/BF01730446.

Appendix A

Basic Elements of Scattering Theory

A.1 Introduction

The origin of scattering signals from surfaces and thin films has been illustrated in a qualitative manner based on the convolution theorem in Chapter 2. While providing an intuitive feel about the phenomena observed in SXRD, the description is clearly impractical in terms of a quantitative analysis of the diffraction patterns. In this appendix, we shall review some basics of kinematical diffraction theory, which will ultimately lead to a quantitative description of the scattering intensities we measure in an SXRD experiment.

All of the concepts collected here have been the subject of detailed description in numerous excellent textbooks and reviews. The basics of scattering theory from bulk crystals can be found in almost any introduction to solid state physics, for example[1] those by Kittel [1], or Ashcroft and Mermin [2]. More specific works about x-ray diffraction or crystallography include the books by B. E. Warren [3], M. M. Woolfson [4], P. Coppens [5], J. M. Cowley [6], J. Als-Nielsen and D. McMorrow [7], and C. Giacovazzo *et al.* [8]. The specialized area of surface x-ray diffraction is well covered in selected reviews by I. K. Robinson [9, 10], R. Feidenhans'l [11], and E. Vlieg [12], or in book chapters by I. K. Robinson [13] or J. Als-Nielsen and D. McMorrow [7]. With all these references readily at hand, there is no point trying to reinvent the wheel. Rather,

---

[1] The references given here represent only a small selection of the available literature. In no way is this selection intended to be an objective ranking in quality or relevance for the purpose at hand, but merely reflects the particular choice of books the author used as references, based mainly on availability.

the aim of the present chapter is the following: Firstly, it seems useful to provide the reader with the necessary fundamentals to follow the arguments made in this thesis without having to resort to secondary literature too frequently. The focus is kept specifically on the most relevant points for this work, while deliberately omitting everything else. Secondly, the nomenclature throughout the literature is not always consistent. Therefore, we will take special care to use a consistent notation throughout the entire derivations.

This in itself does not seem to warrant an entire chapter of such detail, however, which is common knowledge in the relevant literature. The reason why such a thorough approach is important lies in the way the experimental data is to be analyzed. On the one hand, the use of area detectors in SXRD is a recent development, and in order to exploit the potential of the "peripheral vision", it is essential to understand precisely how the signals seen on the detector arise and need to be interpreted.

On the other hand, the systems investigated are increasingly complex, and direct- or phase-retrieval methods are becoming indispensable techniques to solve their structures. Whereas virtually every SXRD experiment in the past has settled with the measurement of diffraction intensities that are merely proportional to the calculated structure factors, the use of direct methods requires the structure factors to be known on an absolute scale. Very few attempts have been made to achieve this experimentally, and the available literature is scarce [14, 15]. We have succeeded in obtaining an absolute scaling. This has only been possible by thoroughly reproducing the usual derivations, assuring that all constants and pre-factors are meticulously accounted for in each step.

A.2 Terminology

To begin, we will briefly explain some basic terminology and define a notation which will be used consistently throughout this work.

A unit cell is defined via its three unit cell vectors, which at the same time build up the real-space crystal lattice. These we will denote with

$$\mathbf{a_1}, \quad \mathbf{a_2}, \quad \mathbf{a_3}. \tag{A.1}$$

Atoms are placed inside this unit cell at positions

$$\mathbf{r} = x\,\mathbf{a_1} + y\,\mathbf{a_2} + z\,\mathbf{a_3} = (xa_1,\, ya_2,\, za_3) \qquad 0 \leqslant x,\, y,\, z < 1. \tag{A.2}$$

The lattice sites to which these unit cells are attached when building up the crystal have position vectors

$$\mathbf{r}_{uc} = j_1\,\mathbf{a_1} + j_2\,\mathbf{a_2} + j_3\,\mathbf{a_3} = (j_1 a_1,\, j_2 a_2,\, j_3 a_3) \qquad j_1,\ j_2,\ j_3 = \text{integers.} \tag{A.3}$$

The reciprocal-lattice vectors $\mathbf{a_1^*},\ \mathbf{a_2^*},\ \mathbf{a_3^*}$ are defined through the following relation to the real-space vectors $\mathbf{a_1},\ \mathbf{a_2},\ \mathbf{a_3}$:

$$\mathbf{a_1^*} = 2\pi\frac{\mathbf{a_2}\times\mathbf{a_3}}{\mathbf{a_1}\cdot\mathbf{a_2}\times\mathbf{a_3}}, \qquad \mathbf{a_2^*} = 2\pi\frac{\mathbf{a_3}\times\mathbf{a_1}}{\mathbf{a_2}\cdot\mathbf{a_3}\times\mathbf{a_1}}, \qquad \mathbf{a_3^*} = 2\pi\frac{\mathbf{a_1}\times\mathbf{a_2}}{\mathbf{a_3}\cdot\mathbf{a_1}\times\mathbf{a_2}}. \tag{A.4}$$

Finally, the incoming and scattered wavevector $\mathbf{k}$ and $\mathbf{k}'$, and the resulting scattering vector $\mathbf{q} = \mathbf{k}' - \mathbf{k}$ are given by

$$\mathbf{k} = (k_1,\, k_2,\, k_3), \quad \mathbf{k}' = (k_1',\, k_2',\, k_3'), \quad \mathbf{q} = (q_1,\, q_2,\, q_3). \tag{A.5}$$

A.3 X-ray scattering

The scattering of x-rays with matter can be described in terms of the electric component of an electromagnetic wave interacting with the electrons inside the material. Three interrelated phenomena can occur: absorption, refraction, and scattering. All of these processes can be dealt with jointly in a quantum-mechanical description, with “Fermi’s golden rule” governing the transition rates of the initial state incoming wave to the perturbed state of the system including the final exit wave. For the description of the sort of scattering processes we are interested in, this treatment is far too complex, however, and a classical picture provides a much more intuitive formalism, which leads to essentially the same results.

A.3.1 The kinematical scattering approximation

In a classical picture, the scattering of x-rays propagating through matter can be described in terms of the Huygens-Fresnel principle, which states that each point of an advancing wave front can be regarded as the source of a secondary train of waves. The advancing wave as a whole may then be described as the sum of all the secondary waves arising from all points already traversed by the wave.

X-rays are electromagnetic waves. Electrical charges interact with the electric component of this wave and can be regarded as the source of secondary waves. The amplitudes of these secondary waves depend on the interaction strength with the field. As we shall see in the following section, this is much weaker for the heavy protons than for the lighter electrons. The latter therefore represent the main contribution to the scattering of the incoming wave. The intensity distribution after the passage of the x-rays through a piece of matter can be calculated as the interference pattern of all secondary waves emitted from the electrons within the medium.

It may be instructive to briefly inspect the special case of the resulting wave scattered exactly along the propagation direction of the primary wave. Under these circumstances, no phase shift arises between the individual secondary waves, hence they all interfere constructively. The amplitude of the scattered wave must therefore be proportional to the total number of electrons participating in the scattering process - a fact which we will discuss in more detail when describing the scattering factor from an atom in Section A.3.4.

Two fundamental assumptions about the scattering process lead to the *kinematical approximation*, which simplifies the calculation of the interference terms enormously. Firstly, all scattering processes are presumed to be elastic, meaning that the scattered photon maintains the same energy as the incoming one, or alternatively, the wavelength of the secondary wave is equal to that of the primary one. Secondly, the strength of the scattering process, the so-called scattering cross section α, is assumed to be small. The probability for an x-ray to scatter twice is therefore of order α^2, which is very much smaller than for single scattering. The contributions from multiple-scattering terms to the total scattering from the system are negligible under those circumstances and justify the truncation of the corresponding series expansion after the first term, which is proportional to α. This is also called the *first Born* or *single scattering approximation*.

The kinematical approximation is, strictly speaking, not valid for either low-angle specular reflections or at Bragg peaks of highly perfect crystals, because in those cases, the scattered beams are very strong and multiple scattering can no longer be ignored. Away from the strong signals, however, the approximation is exceedingly close to reality [16]. In SXRD, we are exactly interested in those weak signals between Bragg peaks, in which case the use of single scattering theory is perfectly justified.

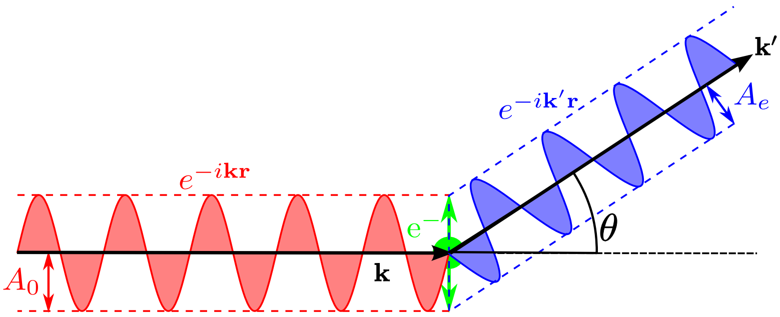

Figure A.1: Scattering of an electromagnetic wave by a free electron (only the electric components are drawn). The amplitude A_e of the scattered wave is proportional to the amplitude of the incident wave A_0 projected into the direction of $\mathbf{k}'$.

A.3.2 Scattering from a free electron

Let an electron be represented by a classical point charge. The interaction with the incoming electromagnetic wave forces this point charge to oscillate with the same frequency as the incoming wave. The plane in which the electron oscillates is given by the direction of polarization of the electric wave field. According to classical electrodynamic theory, the accelerated point-charge radiates. The resulting radiation is emitted into all directions from the electron and has the same frequency as the exciting primary wave. This process is called scattering or, more precisely, *Thomson scattering*.

Consider Figure A.1 and let A_0 be the amplitude of an incoming plane wave $A_0 \cdot e^{-i\mathbf{k}\mathbf{r}}$, with its propagation direction along the wave vector $\mathbf{k}$. The Thomson scattering (in SI-units) of this wave by a free electron situated at position $\mathbf{r}$ of the coordinate system is given by [17]:

$$A_e \cdot e^{-i\mathbf{k}'\mathbf{r}} = A_0 \cdot e^{-i\mathbf{k}\mathbf{r}} \cdot \frac{1}{4\pi\epsilon_0} \frac{e^2}{mc^2} \cdot \frac{1}{R} \cdot p, \tag{A.6}$$

where A_e is the amplitude of the scattered wave traveling into the direction of $\mathbf{k}'$ and observed at a distance R from the interaction point.

Looking at Equation A.6, which is valid not only for electrons but for any charged particle, it becomes immediately evident why the scattering of x-rays occurs predominantly on the electrons inside the material: The particle mass m in the denominator means that any scattering contributions from the atomic nucleus, the proton being approximately 2000 times heavier than the electron, are negligible[2].

---

[2] For the measured intensities, which are proportional to the squared amplitude of the wave, the proton

The emitted radiation is not isotropic in space, and its shape depends on the relative orientation of the scattered beam direction with the primary beam polarization. This has been taken into account through the additional factor p in Equation A.6. The decisive factor determining the amplitude of the scattered wave in a direction $\mathbf{k}'$ is the apparent acceleration of the electron as seen along the projection from that direction. This is illustrated in Figure A.1 for a scattering direction within the polarization plane. Obviously, the projection of the acceleration is proportional to $\cos\theta$. On the other hand, in the case in which the scattering plane, spanned by the two vectors $\mathbf{k}$ and $\mathbf{k}'$, is perpendicular to the plane of polarization, the full acceleration is visible and $p = 1$. The usual polarization factor P is defined in terms of the wave's intensity, which is proportional to the square of its amplitude, so in other words $P = p^2$. For an unpolarized incident beam, the polarization factor is given by the average of the two special cases above, and we obtain

$$\begin{aligned} P &= \cos^2\theta && \text{(scattering in polarization plane),} \\ P &= 1 && \text{(scattering perpendicular to polarization plane),} \\ P &= \tfrac{1+\cos^2\theta}{2} && \text{(unpolarized beam).} \end{aligned} \tag{A.7}$$

Substituting $\frac{1}{4\pi\epsilon_0}\frac{e^2}{mc^2} = r_e$, the classical *electron radius* or *Thomson scattering length*[3], we can solve for A_e:

$$\begin{aligned} A_e &= A_0 \cdot \frac{r_e}{R} \cdot p \cdot e^{-i\mathbf{kr}} \cdot e^{i\mathbf{k}'\mathbf{r}} = A_0 \cdot \frac{r_e}{R} \cdot p \cdot e^{i(\mathbf{k}'-\mathbf{k})\mathbf{r}} \\ &= A_0 \cdot \frac{r_e}{R} \cdot p \cdot e^{i\mathbf{qr}}, \end{aligned} \tag{A.8}$$

where $\mathbf{q} \equiv \mathbf{k}' - \mathbf{k}$ is the so-called scattering vector. The first three factors will accompany us for the remainder of the derivation, so for the sake of brevity, we will replace them by the symbol $\mathcal{K} \equiv A_0 \cdot \frac{r_e}{R} \cdot p$. It is important to remember that $\mathcal{K}$ is not a constant, but contains the polarization contribution and a factor $1/R$, which are geometry dependent. This fact, however, does not interfere with the rest of the derivation presented here and is easily and independently taken into account at the end of the calculation. So finally, we get the following simple expression for our scattered wave amplitude:

$$A_e = \mathcal{K} \cdot e^{i\mathbf{qr}}. \tag{A.9}$$

---

scattering is suppressed by a factor of $\sim (1/2000)^2$.

[3] Note that in cgs-units $r_e = \frac{e^2}{mc^2}$, a notation which is still more commonly used in the literature in this context.

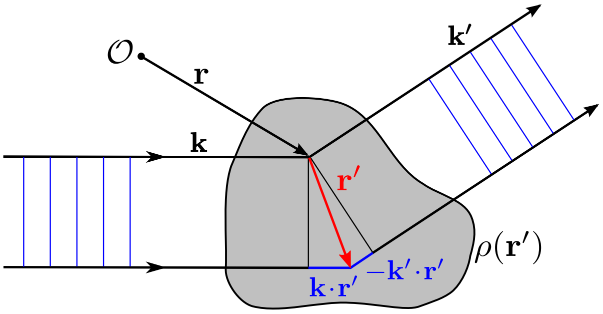

Figure A.2: Scattering from a charge distribution. The phase shift is the result of different path lengths between the two scattered waves, and is equal to $\mathbf{k} \cdot \mathbf{r} + (-\mathbf{k}' \cdot \mathbf{r}) = (\mathbf{k} - \mathbf{k}') \cdot \mathbf{r}$.

A.3.3 Scattering from a charge distribution

When considering a spatial distribution of charges rather than a single isolated point charge, the scattered wave is made up from contributions of the secondary waves emitted from each scattering center. Assuming N individual scatterers at positions $\mathbf{r}_j$ $(1 \leqslant j \leqslant N)$ from the reference point $\mathbf{r}$, the total amplitude, A_{tot}, is calculated through the coherent addition of all individual waves:

$$A_{\text{tot}} = \mathcal{K} \cdot \sum_{j=1}^{N} e^{i\mathbf{q}(\mathbf{r}+\mathbf{r}_j)} = \mathcal{K} \cdot e^{i\mathbf{q}\mathbf{r}} \cdot \sum_{j=1}^{N} e^{i\mathbf{q}\mathbf{r}_j}. \tag{A.10}$$

The sum in the last term of Equation A.10 takes into account the different path lengths between the secondary waves originating from the individual scattering centers through the resulting phase shifts. The origin of these phase factors is shown graphically in Figure A.2.

For a continuous charge distribution, represented by its charge density $\rho(\mathbf{r}')$, the summation over individual scatterers is replaced by an integration over the entire space where $\rho(\mathbf{r}')$ is nonzero:

$$A_{\rho} = \mathcal{K} \cdot \int e^{i\mathbf{q}(\mathbf{r}+\mathbf{r}')} \cdot \rho(\mathbf{r}')\, d^3\mathbf{r}' = \mathcal{K} \cdot e^{i\mathbf{q}\mathbf{r}} \cdot \int e^{i\mathbf{q}\mathbf{r}'} \cdot \rho(\mathbf{r}')\, d^3\mathbf{r}'. \tag{A.11}$$

A.3.4 Scattering from an atom

Now let us consider a single atom. The electrons are localized around the nucleus and their distribution can be described by an atomic charge density $\rho_a(\mathbf{r}')$. With the result from the previous section, we may therefore write

$$\begin{aligned} A_a &= \mathcal{K} \cdot \int_{\text{atom}} e^{i\mathbf{q}(\mathbf{r}+\mathbf{r}')} \cdot \rho_a(\mathbf{r}')\, d^3\mathbf{r}' = \mathcal{K} \cdot e^{i\mathbf{q}\mathbf{r}} \cdot \underbrace{\int_{\text{atom}} e^{i\mathbf{q}\mathbf{r}'} \cdot \rho_a(\mathbf{r}')\, d^3\mathbf{r}'}_{\equiv f_a(\mathbf{q})} \\ &= \mathcal{K} \cdot e^{i\mathbf{q}\mathbf{r}} \cdot f_a(\mathbf{q}), \end{aligned} \tag{A.12}$$

where

$$f_a(\mathbf{q}) = \int_{\text{atom}} e^{i\mathbf{q}\mathbf{r}'} \cdot \rho_a(\mathbf{r}')\, d^3\mathbf{r}' \tag{A.13}$$

is called the *atomic form factor.* It is equal to the Fourier transform of the atomic electron density. It is instructive to examine two limiting cases of the atomic form factor. Firstly, we have

$$f_a(\mathbf{q}{=}0) = \int \rho_a(\mathbf{r}')\, d^3\mathbf{r}' = Z, \tag{A.14}$$

where Z is the atomic number of the atom. The other case concerns $\mathbf{q} \to \infty$. Here, the phase factor $e^{i\mathbf{q}(\mathbf{r}')}$ begins to oscillate with a frequency approaching infinity, such that all scattering contributions cancel out on average, and therefore

$$f_a(\mathbf{q} \to \infty) = 0. \tag{A.15}$$

In the case of isolated atoms, where no bonding is present, the atomic form factor is usually expressed as

$$f_a = f_0(\theta) + f'(\omega) + if''(\omega), \tag{A.16}$$

with θ the scattering angle and $\omega/2\pi$ the frequency of the exciting wave field. f' takes into account any dispersion corrections, while absorption processes are described by f''. For x-ray energies far away from any absorption edges of the atom, the corrections are very small and can usually be ignored. In that case, $f' \approx f'' \approx 0$, leading to $f_a \approx f(\theta)$. The values of f_0, f', and f'' are available in tabulated form in the International Tables for Crystallography [18]. Although, strictly speaking, they are only valid for isolated atoms, they are still a very good approximation for most crystallographic purposes, mainly due to the fact that only the outermost electrons participate in chemical bonding, leaving the largest parts of the charge distributions sufficiently undisturbed.

It is important to note that f_a is a continuous function of the scattering vector $\mathbf{q}$, describing a wave which is scattered into all directions in space (but modulated by the angle-dependence of both $f_0(\theta)$ and the polarization correction p, as discussed in Section A.3.2).

A.4 Bulk diffraction

The work of a crystallographer starts when atoms are put together in a regular manner to form crystalline solids. Here, we shall see how these regular arrangements affect the scattered radiation to form a so-called diffraction pattern.

A.4.1 From isolated atoms to unit cells

First let us consider a unit cell at position $\mathbf{r}_{\text{uc}}$ in space containing N atoms. Each of the atoms, identified by an index j, has an atomic form factor $f_j(\mathbf{q})$ and is located at positions $\mathbf{r}_j$ inside the unit cell. Again, the scattering of the entire unit cell is the coherent addition of all the scattering contributions of the individual atoms it contains:

$$\begin{aligned} A_{uc} &= \mathcal{K} \cdot \sum_{j=1}^{N} f_j(\mathbf{q}) \cdot e^{i\mathbf{q}(\mathbf{r}+\mathbf{r}_{\text{uc}}+\mathbf{r}_j)} = \mathcal{K} \cdot e^{i\mathbf{qr}} \cdot e^{i\mathbf{qr}_{\text{uc}}} \cdot \underbrace{\sum_{j=1}^{N} f_j(\mathbf{q}) \cdot e^{i\mathbf{qr}_j}}_{\equiv F(\mathbf{q})} \\ &= \mathcal{K} \cdot e^{i\mathbf{qr}} \cdot e^{i\mathbf{qr}_{\text{uc}}} \cdot F(\mathbf{q}). \end{aligned} \tag{A.17}$$

As in the case of the atomic form factor, we can combine all the phase factors associated with the atoms of the unit cell into a single $\mathbf{q}$-dependent term, $F(\mathbf{q})$, which is called the *structure factor*. It contains all the information about the structure of that unit cell, that is, both the positions of the atoms and also their type as given by the atomic form factors. And again, it represents nothing else than the Fourier transform of the electron density inside the unit cell.

A.4.2 Scattering from an ideal bulk crystal

To make up a crystalline structure, the only thing left to do is to arrange the unit cells on their 3-dimensional crystal lattice. Once more, we add up the scattering contributions coherently to obtain an expression for the scattering from a crystal. Let us assume we have a crystal with the shape of a parallelopipedon, consisting of N_1, N_2, and N_3 unit cells along the $\mathbf{a_1}$, $\mathbf{a_2}$, and $\mathbf{a_3}$-axes, respectively. The amplitude A_c of the wave scattered by the entire crystal is then given by the amplitude A_{uc} from a single unit cell multiplied by the sum over the phase terms associated with the unit cell position $\mathbf{r}_{\text{uc}} = j_1\mathbf{a_1} + j_2\mathbf{a_2} + j_3\mathbf{a_3}$, usually referred to as the *lattice* *sum*:

$$
\begin{aligned}
A_c &= \mathcal{K} \cdot e^{i\mathbf{qr}} \cdot F(\mathbf{q}) \cdot \underbrace{\sum_{j_1=0}^{N_1-1} \sum_{j_2=0}^{N_2-1} \sum_{j_3=0}^{N_3-1} e^{i\mathbf{q}\cdot(j_1\mathbf{a_1}+j_2\mathbf{a_2}+j_3\mathbf{a_3})}}_{\text{lattice sum}} \\
&= \mathcal{K} \cdot e^{i\mathbf{qr}} \cdot F(\mathbf{q}) \cdot \sum_{j_1=0}^{N_1-1} e^{i\mathbf{q}\cdot(j_1\cdot\mathbf{a_1})} \cdot \sum_{j_2=0}^{N_2-1} e^{i\mathbf{q}\cdot(j_2\cdot\mathbf{a_2})} \cdot \sum_{j_3=0}^{N_3-1} e^{i\mathbf{q}\cdot(j_3\cdot\mathbf{a_3})}. \qquad \text{(A.18)}
\end{aligned}
$$

Each sum represents a geometric series and the amplitude can be rewritten as (see Appendix F):

$$
\begin{aligned}
A_c &= \mathcal{K} \cdot F(\mathbf{q}) \cdot e^{i\mathbf{qr}} \cdot \frac{\sin(N_1 q_1 a_1)}{\sin(q_1 a_1)} \cdot e^{iq_1 a_1\cdot(N_1-1)/2} \cdot \\
&\quad \frac{\sin(N_2 q_2 a_2)}{\sin(q_2 a_2)} \cdot e^{iq_2 a_2\cdot(N_2-1)/2} \cdot \frac{\sin(N_3 q_3 a_3)}{\sin(q_3 a_3)} \cdot e^{iq_3 a_3\cdot(N_3-1)/2}. \qquad \text{(A.19)}
\end{aligned}
$$

A.4.3 From amplitudes to intensities

In a diffraction experiment, one cannot measure the complex-valued amplitude A of the scattered wave, but only the real-valued intensity I, which is equal to the squared modulus of the amplitude or the product of the amplitude with its complex conjugate:

$$
I = |A|^2 = A \cdot A^*. \qquad \text{(A.20)}
$$

So we can calculate the scattered intensity I_c as a function of $\mathbf{q}$ from our small parallelepiped shaped crystal[4]:

$$
\begin{aligned}
I_c(\mathbf{q}) &= A_0 \cdot A_0^* \cdot \frac{r_e^2}{R^2} \cdot p^2 \cdot \underbrace{e^{i\mathbf{qr}} \cdot e^{-i\mathbf{qr}}}_{=1} \cdot |F(\mathbf{q})|^2 \cdot \\
&\quad \left(\frac{\sin(\frac{1}{2}N_1 q_1 a_1)}{\sin(\frac{1}{2}q_1 a_1)}\right)^2 \cdot \left(\frac{\sin(\frac{1}{2}N_2 q_2 a_2)}{\sin(\frac{1}{2}q_2 a_2)}\right)^2 \cdot \left(\frac{\sin(\frac{1}{2}N_3 q_3 a_3)}{\sin(\frac{1}{2}q_3 a_3)}\right)^2 \cdot \\
&\quad \underbrace{\frac{e^{iq_1 a_1(N_1-1)/2}}{e^{iq_1 a_1(N_1-1)/2}}}_{=1} \cdot \underbrace{\frac{e^{iq_2 a_2(N_2-1)/2}}{e^{iq_2 a_2(N_2-1)/2}}}_{=1} \cdot \underbrace{\frac{e^{iq_3 a_3(N_3-1)/2}}{e^{iq_3 a_3(N_3-1)/2}}}_{=1} \\
&= I_0 \cdot \frac{r_e^2}{R^2} \cdot P \cdot |F(\mathbf{q})|^2 \cdot \frac{\sin^2(\frac{1}{2}N_1 q_1 a_1)}{\sin^2(\frac{1}{2}q_1 a_1)} \cdot \frac{\sin^2(\frac{1}{2}N_2 q_2 a_2)}{\sin^2(\frac{1}{2}q_2 a_2)} \cdot \frac{\sin^2(\frac{1}{2}N_3 q_3 a_3)}{\sin^2(\frac{1}{2}q_3 a_3)}, \qquad \text{(A.21)}
\end{aligned}
$$

---

[4] Here, we have expanded $\mathcal{K} = A_0 \cdot \frac{r_e}{R} \cdot p$ again.

where $I_0 = A_0 \cdot A_0^*$ is the intensity of the incoming wave, and $P = p^2$ is the polarization factor, as discussed in Section A.3.2. Note that in this last step, also the dependence on the coordinate $\mathbf{r}$ disappears, meaning that I is independent on the arbitrarily chosen origin of the coordinate system we used, as expected.

It is interesting to see how this intensity is distributed as a function of $\mathbf{q}$. For that purpose, let us inspect Equation A.21 more closely. The first few terms are constants, so we ignore them for now. $|F(\mathbf{q})|^2$ contains the entire information about the unit cell, and we will have a look at that shortly. Finally, we have the three sine-squared terms, which are the result of a summation over the phase factors of a finite number of unit cells in the three lattice directions. These functions are strongly peaked in q_1, q_2 and q_3, respectively, whenever their denominator becomes zero, i.e. for

$$\frac{1}{2}q_1 a_1 = H\pi, \qquad \frac{1}{2}q_2 a_2 = K\pi, \qquad \frac{1}{2}q_3 a_3 = L\pi, \tag{A.22}$$

with H, K, and L integers. These are the three Laue conditions, which, when simultaneously satisfied, define a three-dimensional reciprocal lattice, spanned by the reciprocal lattice vectors $\mathbf{a_1^*}$, $\mathbf{a_2^*}$, $\mathbf{a_3^*}$:

$$\mathbf{a_1^*} = 2\pi\frac{\mathbf{a_2} \times \mathbf{a_3}}{\mathbf{a_1} \cdot \mathbf{a_2} \times \mathbf{a_3}}, \qquad \mathbf{a_2^*} = 2\pi\frac{\mathbf{a_3} \times \mathbf{a_1}}{\mathbf{a_2} \cdot \mathbf{a_3} \times \mathbf{a_1}}, \qquad \mathbf{a_3^*} = 2\pi\frac{\mathbf{a_1} \times \mathbf{a_2}}{\mathbf{a_3} \cdot \mathbf{a_1} \times \mathbf{a_2}}. \tag{A.23}$$

For the special case of orthogonal lattices, these have the magnitudes

$$a_1^* = \frac{2\pi}{a_1}, \qquad a_2^* = \frac{2\pi}{a_2}, \qquad a_3^* = \frac{2\pi}{a_3}. \tag{A.24}$$

Also note that

$$\mathbf{a_i} \cdot \mathbf{a_j^*} = 2\pi\,\delta_{ij}. \tag{A.25}$$

Now every position vector $\mathbf{r}^*$ in reciprocal space can be written in terms of the reciprocal lattice vectors and three continuous coordinates h, k, and l:

$$\mathbf{r}^* = h\mathbf{a_1^*} + k\mathbf{a_2^*} + l\mathbf{a_3^*}. \tag{A.26}$$

Figure A.3 (a) shows a plot of $s(h) = \frac{\sin^2(N_1\pi h)}{\sin^2(\pi h)}$ for $N_1 = 6$. The intensity maxima have a value of N_1^2. This is easily seen by expanding $s(h)$ around any integer value of h, which we will denote by a capital H. Since $\sin(\pi h) = \sin(\pi(H + \Delta h)) = \sin(\pi\Delta h) \approx \pi\Delta h$ for small Δh, we have

$$\frac{\sin^2(N_1\pi(H + \Delta h))}{\sin^2(\pi(H + \Delta h))} \approx \frac{(N_1\pi\Delta h)^2}{(\pi\Delta h)^2} = N_1^2. \tag{A.27}$$

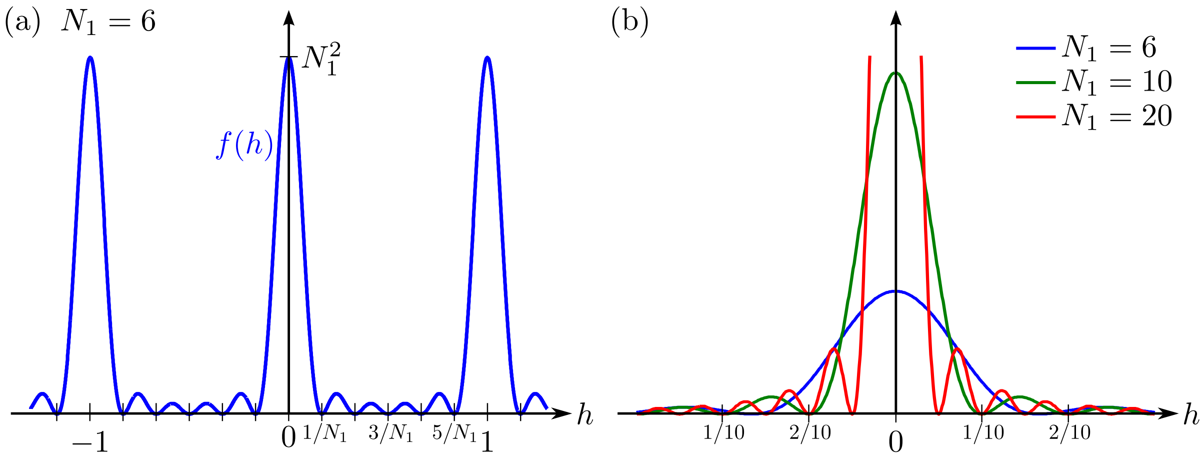

Figure A.3: Plotting the function $s(h) = \frac{\sin^2(N_1 \pi h)}{\sin^2(\pi h)}$: (a) For $N_1 = 6$ one already clearly sees the accumulation of intensity and the sharpening of peaks at integer values of h. (b) As N_1 increases, the peaks become increasingly narrow and high.

The dependence of the shape of $s(h)$ on N_1 is shown in panel (b) of the figure. With increasing N_1, the peaks become higher and narrower, the width being proportional to $1/N_1$. Also, the number of side maxima increases as $N_1 - 2$.

A.4.4 Integrated intensities

The intensity from a small crystal is given by Equation A.21. Even though we have repeatedly stated that amplitudes cannot be measured directly, but intensities can, $I_c(q)$ does not represent an observable quantity, as we shall explain here.

If all three Laue equations could be fulfilled exactly, Equation A.21 predicts an intensity maximum of

$$I_c^{max} = I_0 \cdot \frac{r_e^2}{R^2} \cdot P \cdot |F(\mathbf{q})|^2 \cdot N_1^2 N_2^2 N_3^2. \tag{A.28}$$

Experimentally, this situation cannot be achieved, however. Most crystals are slightly mosaic, meaning that different parts of the crystal are not perfectly aligned with each other, such that the Laue equations cannot be fulfilled simultaneously for all mosaic blocks. Additionally, the incoming beam will never be perfectly parallel, but has a finite divergence and spread in wavelengths. All this leads to a finite broadening of the diffraction peak and a corresponding decrease of the maximum intensity. Even in the absence of all experimental effects, the measurement of I_c^{max} would require an almost infinitely small slit size and an absolutely perfect alignment of the diffractometer. We therefore conclude, that I_c^{max} is not a readily observable quantity[5].

A measurable quantity, on the other hand, which can also be calculated easily, is the *integrated intensity* of the diffraction peak. It automatically takes any crystal imperfections and resolution effects into account and is, in the three-dimensional case, independent of all instrumental parameters, making it an *absolute* measurement [3].

Before we get started with the calculations, it may be instructive to briefly go over the units of the physical quantities we are dealing with here. The intensity, which we calculated as the squared amplitude of an electromagnetic wave in the previous sections, is defined as the time-averaged energy flux. In other words, it describes the flow of energy through a surface-element of unit area per unit time, hence the unit is J m^{-2} s^{-1}. The term *integrated intensity*, on the other hand, may be slightly misleading, because, by virtue of the integration, its units are changed. The integrated intensity therefore describes a quantity fundamentally different from the intensity itself.

As an example, consider the measurement one usually performs in a diffraction experiment. A detector with a certain size of its receiving surface A_D is placed at some distance R from the scattering source. The measurements lasts for a finite exposure time T, and all the photons reaching the detector aperture are detected. In other words, the intensity is integrated over the area of the receiving surface and over the counting time:

$$\int_T \int_{A_\mathrm{D}} I_c \,\mathrm{d}A_\mathrm{D}\,\mathrm{d}t = E. \tag{A.29}$$

Since intensity is energy per unit area per unit time, the resulting quantity E is the total *energy* striking the receiving surface of the detector during the exposure, and is therefore measured in units of Joules. So in this case, the integrated intensity is actually an energy.

In some circumstances, it may be more useful to calculate the time-averaged flow of energy through the detector area, in which case the integrated intensity has units of energy per unit

---

[5] While this statement is certainly true for those crystal systems where N_1, N_2, and N_3 tend towards very large values, and the corresponding diffraction peaks become infinitesimally narrow, it does not apply for systems where the extent along one or more spatial directions is very small. This can be seen, for example, in the finite size effects observed for the reflectivity from thin films, or the diffraction from nanostructures, which is essentially continuously modulated.

time, and therefore represents the diffracted *power* striking the detector. This ambiguity in the term *integrated intensity* may often lead to confusion, and it is important to specify clearly over which variables the integration is carried out, as this determines the units of the result.

Rather than speaking of the scattering energy E collected by the detector, we usually obtain the total number of photon counts $\mathcal{N}$ acquired in one exposure (to add to the confusion, $\mathcal{N}$ is usually also referred to as a measured intensity). For monochromatic radiation, the conversion from energy to counts is simply given by the known energy $E_{\text{xray}} = \frac{hc}{\lambda}$ per x-ray photon. The intensity I then needs to be replaced by the photon flux Φ, equal to the number of photons incident on a surface of unit area per unit time.

There are two things to do now. First, we need to understand how to calculate the integrated intensity from one diffraction peak theoretically. Then, the relationship between this calculation and the experimentally obtained intensity has to be established.

Integration in reciprocal space

Going back to the calculated intensity distribution $I_c(\mathbf{q})$ in reciprocal space (Equation A.21), we need to pick out one particular reflection and determine its intensity integrated over the reciprocal space volume it occupies, that is

$$\begin{aligned} I^*_{HKL} &= \iiint_{\text{peak}} I_c(\mathbf{q})\,\mathrm{d}^3\mathbf{q} && \text{(A.30)} \\ &= \iiint_{\text{peak}} I_0 \cdot \frac{r_e^2}{R^2} \cdot P \cdot |F(\mathbf{q})|^2 \cdot \frac{\sin^2(\frac{1}{2}N_1 q_1 a_1)}{\sin^2(\frac{1}{2}q_1 a_1)} \cdot \frac{\sin^2(\frac{1}{2}N_2 q_2 a_2)}{\sin^2(\frac{1}{2}q_2 a_2)} \cdot \frac{\sin^2(\frac{1}{2}N_3 q_3 a_3)}{\sin^2(\frac{1}{2}q_3 a_3)}\,\mathrm{d}^3\mathbf{q}. \end{aligned}$$

Referring to the discussion about the units of the integrated intensity, note that I^*_{HKL} will have the peculiar units of J s^{-1} m^{-5}. Expressing $\mathbf{q}$ in terms of h, k, and l,

$$\mathbf{q} = (q_1, q_2, q_3) = (ha_1^*, ka_2^*, la_3^*)\,, \tag{A.31}$$

leads to the following expression for the reciprocal-space volume-element:

$$\begin{aligned} \mathrm{d}V^* = \mathrm{d}^3\mathbf{q} &= \mathrm{d}\mathbf{q_1} \cdot \mathrm{d}\mathbf{q_2} \times \mathrm{d}\mathbf{q_3} = \mathrm{d}(h\mathbf{a_1^*}) \cdot \mathrm{d}(k\mathbf{a_2^*}) \times \mathrm{d}(l\mathbf{a_3^*}) = (\mathbf{a_1^*} \cdot \mathbf{a_2^*} \times \mathbf{a_3^*})\,\mathrm{d}h\,\mathrm{d}k\,\mathrm{d}l \\ &= V^*\,\mathrm{d}h\,\mathrm{d}k\,\mathrm{d}l = \frac{(2\pi)^3}{V}\,\mathrm{d}h\,\mathrm{d}k\,\mathrm{d}l, && \text{(A.32)} \end{aligned}$$

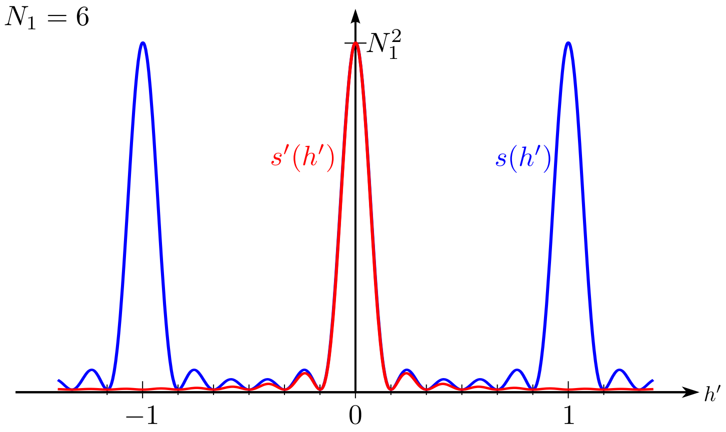

Figure A.4: The function $s(h') \equiv \frac{\sin^2(N_1\pi h')}{\sin^2(\pi h')}$ (blue line) is approximated with $s'(h') \equiv \frac{\sin^2(N_1\pi h')}{(\pi h')^2}$ (red line). This removes the periodicity in the denominator and suppresses all Bragg peaks with $h' \neq 0$. Even for very small values of N_1, the approximation of $s'(h')$ to $s(h')$ is excellent for the central peak of interest (in this example, $N_1 = 6$).

where V^* and V are the volumes of the reciprocal-space and real-space unit cells, respectively. Using the relationships in Equation A.22, Equation A.30 can then be rewritten as

$$\begin{aligned} I^*_{HKL} &= \frac{(2\pi)^3}{V} \iiint_{\text{peak}} I_c(\mathbf{q})\,\mathrm{d}h\,\mathrm{d}k\,\mathrm{d}l && \text{(A.33)} \\ &= \frac{(2\pi)^3}{V} \cdot I_0 \cdot \frac{r_e^2}{R^2} \cdot P \cdot \iiint_{\text{peak}} |F(\mathbf{q})|^2 \cdot \frac{\sin^2(N_1\pi h)}{\sin^2(\pi h)} \frac{\sin^2(N_2\pi k)}{\sin^2(\pi k)} \frac{\sin^2(N_3\pi l)}{\sin^2(\pi l)} \mathrm{d}h\,\mathrm{d}k\,\mathrm{d}l. \end{aligned}$$

Here, the question arises as to how to set the integration limits and how to calculate the resulting integrals analytically. We have seen that for any reasonably large number N_i of unit cells in each crystal direction, the intensity peaks sharply and has appreciable values only very close to a reciprocal lattice point (HKL), such that only small deviations away from the Bragg peaks are of interest. Let us focus on the first of the three fractions with the sine-squared terms and rewrite $h = H + h'$. We then obtain

$$s(h') \equiv \frac{\sin^2(N_1\pi h)}{\sin^2(\pi h)} = \frac{\sin^2(N_1\pi(H + h')}{\sin^2(\pi(H + h'))} = \frac{\sin^2(N_1\pi h')}{\sin^2(\pi h')}, \qquad \text{(A.34)}$$

since H is integral. The result of this coordinate transformation $h \rightarrow h'$ is a shift of the peak previously centered around H into the origin. Note that the shape of the function has not changed, but has only been shifted. The sine function in the numerator varies much faster than the denominator, by a factor of N_1. For small variations, it is therefore the decisive factor governing the shape of the function, and it is legitimate to approximate the slow-varying denominator with $\sin^2(\pi h') \approx (\pi h')^2$. The effect of this approximation on the intensity distribution $s(h')$ is shown in Figure A.4. By replacing the periodic function in the denominator with a rapidly decaying $1/h'^2$ term, we have effectively selected the Bragg peak at the origin of h' (which corresponds to the position H). Even for the exceedingly small value of $N_1 = 6$ shown in the figure, the approximation to the exact $s(h')$ is excellent, and improves further with increasing N_1. This now solves the problem of the integration limits, as $s(h')$ rapidly tends towards zero away from the peak, and the integration can be performed from $-\infty$ to $+\infty$. Naturally, the same considerations apply for the k and l-terms.

Another approximation concerns the scattering factor $F(\mathbf{q})$ in Equation A.30. Compared to the sine terms, this is a very slowly varying function of $\mathbf{q}$. Within the width of one particular Bragg peak (HKL), its change is therefore negligible, and we can replace it by a constant factor F_{HKL}, which we can then bring outside of the integral. Equation A.30 can thus be rewritten as

$$I^*_{HKL} = I_0 \cdot \frac{r_e^2}{R^2} \cdot P \cdot \frac{(2\pi)^3}{V} \cdot |F_{HKL}|^2 \cdot \int \frac{\sin^2(N_1 \pi h')}{(\pi h')^2} \mathrm{d}h' \int \frac{\sin^2(N_2 \pi k')}{(\pi k')^2} \mathrm{d}k' \int \frac{\sin^2(N_3 \pi l')}{(\pi l')^2} \mathrm{d}l'. \tag{A.35}$$

The values of the three integrals, which are taken from $-\infty$ to $+\infty$, can be calculated analytically and give N_1, N_2, and N_3, respectively. Letting $N = N_1 N_2 N_3$ be the total number of unit cells in the crystal, the volume-integrated intensity over the (HKL) peak in reciprocal space becomes

$$I^*_{HKL} = I_0 \cdot \frac{r_e^2}{R^2} \cdot P \cdot \frac{(2\pi)^3}{V} \cdot |F_{HKL}|^2 \cdot N. \tag{A.36}$$

Note that this expression still depends on the experimental parameters, namely the observation distance R and the angle-dependence of the polarization factor P. However, it does *not* include any details about the measurement setup, especially with regard to the employed diffractometer type, the scanned angles, slit settings, etc.

We now see that the integrated intensity distribution over the Bragg peak in reciprocal space is proportional to the number of unit cells N in the crystal. It is really this particular property that makes this measure such a useful quantity. Firstly, it relaxes our initial assumption of a crystal having a parallelopipedon shape. A small single crystal of arbitrary shape can be thought of as a composition of many small parallelopipedon blocks, for each of which Equation A.36 applies. The integrated intensities of these blocks can now be added up to yield the same value as for an exactly parallelopipedon crystal containing N unit cells. The same argument is true for the mosaic blocks in a crystal. The diffraction peaks are broadened by the slight misalignment of the blocks and by their smaller sizes, but the integrated intensity remains the same as for a perfect crystal. Similarly, it does not matter whether the scattering contributions from different parts of the crystal are added coherently or incoherently. Naturally, this principle can only be applied as long as the approximations made in the derivation of Equation A.36 hold true. Once the width of a Bragg peak becomes comparable to the rate of change in $F(\mathbf{q})$ or that of the sine term in the denominator of Equation A.35, the approximations break down. For any reasonably good crystal of sufficient size, however, the expression for the intensity integrated over reciprocal space will always be valid to a high degree of accuracy.

Integration in a measurement

The next challenge is to obtain an expression for the intensity integrated not directly in reciprocal space, but as it is collected by the detector in a real experiment. The elastic diffraction condition in reciprocal space is fulfilled only for those points lying on the Ewald sphere. For an extended signal, this means that for any fixed crystal orientation, only the intensity distribution on a spherical slice through the signal is sampled. This is illustrated schematically in Figure A.5 (a) for the projection within the scattering plane. In order to obtain the full volume integration of the peak intensity, the crystal must be rotated in a scan, such that the diffraction condition will be satisfied for each point within the signal. The figure shows the special case where the rotation axis ω lies perpendicular (pointing out of the page) to the scattering plane.

The diffracted signal from each slice is allowed to fall normally onto a detector, positioned at a distance R away from the crystal in the direction of $\mathbf{k}'$, as shown in Figure A.5 (b). In the present derivation, we will assume that the sample-to-detector collimation is sufficiently relaxed and the receiving aperture A_{D} of the detector is large enough, such that all the scattered radiation for the given slice of the reflection under consideration is received by the detector.

A surface element $\mathrm{d}A_{\mathrm{D}}$ on the detector can be characterized by an opening angle $\mathrm{d}\delta$ within the scattering plane, and $\mathrm{d}\gamma$ perpendicular to that plane, such that $\mathrm{d}A_{\mathrm{D}} = R^2\,\mathrm{d}\gamma\,\mathrm{d}\delta$. Let us assume that the crystal be fixed at a certain angle, ω, and a measurement be made. The diffracted energy collected by the entire detector aperture over the finite exposure time T is

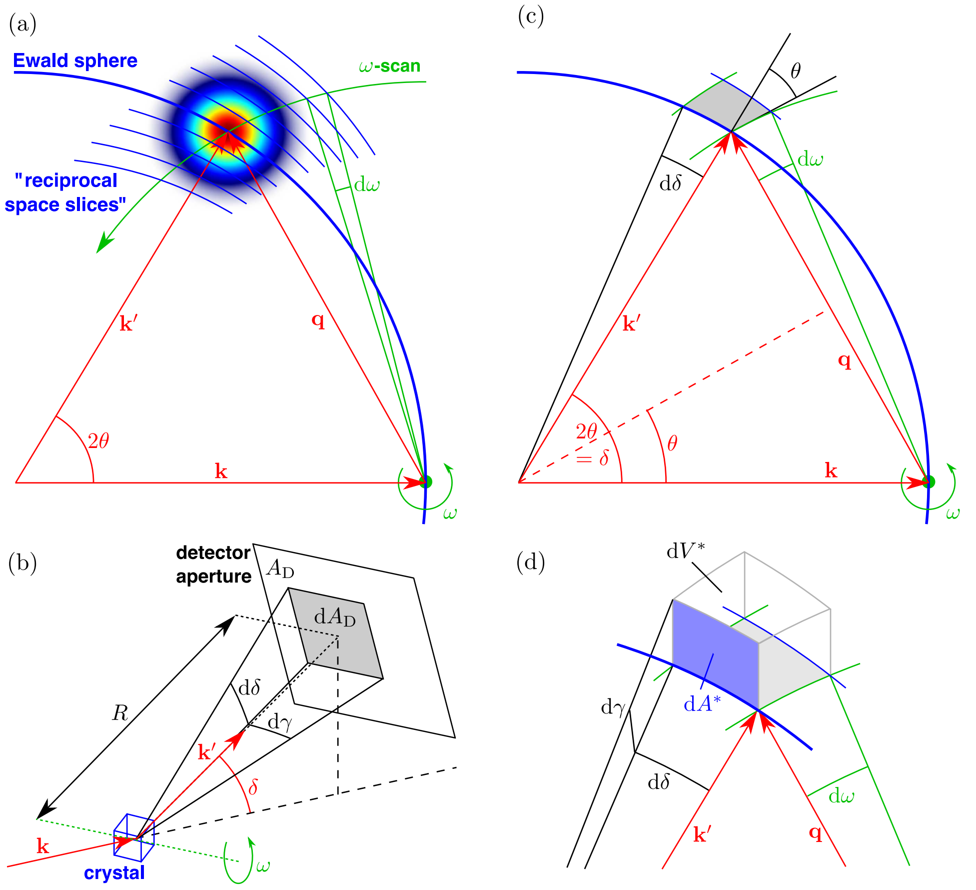

Figure A.5: Measurement and calculation of the integrated Bragg peak intensity: (a) The intersection of an extended diffraction signal in reciprocal space with the Ewald sphere results in a sampling of the signal only on a spherical slice, given by the surface of the Ewald sphere. A full sampling of the entire diffraction feature is obtained by recording the signal of several such “reciprocal space slices”. (b) The collection of the diffracted signal in real space by a detector with an aperture A_{D}, positioned at a distance R from the sample. (c) The infinitesimal line-element $|\mathbf{q}|\mathrm{d}\omega$ in an ω-scan encloses an angle of θ with respect to the $\mathbf{k}'$-direction, while $\mathrm{d}\delta$ is perpendicular to the latter. (d) Three-dimensional projection of the volume-element $\mathrm{d}V^*$ spanned by an ω-scan in reciprocal space.

then given by

$$
\begin{aligned}
E_\omega &= \int_T \int_{A_{\mathrm{D}}} I_c(\mathbf{q})\,\mathrm{d}A_{\mathrm{D}}\,\mathrm{d}t \\
&= \iiint I_c(\mathbf{q})\,R^2\,\mathrm{d}\gamma\,\mathrm{d}\delta\,\mathrm{d}t, \qquad \text{(A.37)}
\end{aligned}
$$

where the integration is performed over the exposure time T, and the entire angular range defined by the detector aperture in γ and δ. This is the diffracted energy for the current crystal orientation ω, or the reciprocal space slice currently fulfilling the diffraction condition. In order to obtain the total scattering from the entire Bragg peak, many such slices need to be recorded for slightly different crystal orientations ω, each of which samples a different part of the intensity distribution $I_c(\mathbf{q})$. For the integration, it is easier to assume that the crystal is rotated during the exposure, with a constant angular velocity $\Omega = \mathrm{d}\omega/\mathrm{d}t$. Then we can replace the integral over the exposure time in Equation A.37 with an integration over the sample rotation angle, choosing the integration limits such that the Bragg peak under consideration is fully captured. Equation A.37 can then be rewritten as

$$E = \frac{R^2}{\Omega} \iiint I_c(\mathbf{q})\, \mathrm{d}\gamma\, \mathrm{d}\delta\, \mathrm{d}\omega. \tag{A.38}$$

This angular integration cannot be calculated directly, since the intensity $I_c(\mathbf{q})$ is expressed in terms of $\mathbf{q}$. We therefore need to change the angular integration variables to the corresponding reciprocal space variables. Formally, the resulting change in integration volume can be derived by calculating the Jacobian determinant $\mathcal{J} = \left|\frac{\partial(\mathbf{q_1},\mathbf{q_2},\mathbf{q_3})}{\partial(\gamma,\delta,\omega)}\right|$. Here, we will illustrate the relationship between the angular and reciprocal space coordinates for the special situation drawn in Figure A.5, where the rotation axis ω is perpendicular to the scattering plane.

Consider panels (c) and (d) of Figure A.5. The angular changes $\mathrm{d}\gamma, \mathrm{d}\delta, \mathrm{d}\omega$ produce changes in the scattering vector $\mathbf{q}$:

$$|\mathbf{k}'|\mathrm{d}\gamma = \mathrm{d}(\mathbf{q})_\gamma, \qquad |\mathbf{k}'|\mathrm{d}\delta = \mathrm{d}(\mathbf{q})_\delta, \qquad |\mathbf{q}|\mathrm{d}\omega = \mathrm{d}(\mathbf{q})_\omega. \tag{A.39}$$

The reciprocal space volume defined through these changes is given by

$$dV^* = [\mathrm{d}(\mathbf{q})_\gamma \times \mathrm{d}(\mathbf{q})_\delta] \cdot \mathrm{d}(\mathbf{q})_\omega. \tag{A.40}$$

While $\mathrm{d}(\mathbf{q})_\gamma$ and $\mathrm{d}(\mathbf{q})_\delta$ are perpendicular to each other, panel (c) of the figure illustrates that the angle between $\mathrm{d}(\mathbf{q})_\delta$ and $\mathrm{d}(\mathbf{q})_\omega$ is equal to $90^\circ - \theta$ ($\theta = \delta/2$). In the evaluation of the dot-product in Equation A.40, we therefore obtain a factor $\sin(90 - \theta) = \cos\theta$. Using

$$|\mathbf{k}| = |\mathbf{k}'| = \frac{2\pi}{\lambda}; \qquad |\mathbf{q}| = 2|\mathbf{k}|\sin\theta = \frac{4\pi\sin\theta}{\lambda}, \tag{A.41}$$

we can now write down the conversion from angular to reciprocal space variables:

$$\begin{aligned} dV^* &= \left(\frac{2\pi}{\lambda}\right)\mathrm{d}\gamma \left(\frac{2\pi}{\lambda}\right)\mathrm{d}\delta \left(\frac{4\pi\sin\theta}{\lambda}\right)\mathrm{d}\omega\cos\theta \\ &= \left(\frac{2\pi}{\lambda}\right)^3 2\sin\theta\cos\theta\,\mathrm{d}\gamma\,\mathrm{d}\delta\,\mathrm{d}\omega \\ &= \left(\frac{2\pi}{\lambda}\right)^3 \sin 2\theta\,\mathrm{d}\gamma\,\mathrm{d}\delta\,\mathrm{d}\omega, \end{aligned} \tag{A.42}$$

where we have used the trigonometric relationship $2\sin\psi\cos\psi = \sin 2\psi$. Combining this with the variable transformation from $\mathrm{d}V^*$ to $\mathrm{d}h\,\mathrm{d}k\,\mathrm{d}l$ in Equation A.32, we finally obtain the expression for the total integration volume.

$$\begin{aligned} dV^* &= \left(\frac{2\pi}{\lambda}\right)^3 \sin 2\theta\,\mathrm{d}\gamma\,\mathrm{d}\delta\,\mathrm{d}\omega \\ &= \frac{(2\pi)^3}{V}\mathrm{d}h\,\mathrm{d}k\,\mathrm{d}l \\ \Longrightarrow &\qquad \mathrm{d}\gamma\,\mathrm{d}\delta\,\mathrm{d}\omega = \frac{\lambda^3}{V\sin 2\theta}\mathrm{d}h\,\mathrm{d}k\,\mathrm{d}l. \end{aligned} \tag{A.43}$$

$\lambda^3/(V\sin 2\theta)$ is the Jacobian determinant for the specific geometry discussed in this example. The angle-dependent part of the Jacobian is usually called the *Lorentz factor*, and we will adopt this convention. Unfortunately, other definitions are found in the literature, which can lead to confusion. For our example, the Lorentz factor is therefore $L_\omega = 1/\sin 2\theta$, where the subscript indicates that the correction applies only to an ω-scan. It should be stressed again that this Lorentz factor is only valid for the particular scattering geometry chosen in this example, where the detector is stationary (meaning that $\delta = 2\theta$ is constant), and the crystal is rotated around an axis ω perpendicular to the scattering plane. For any other configuration, the Jacobian determinant will in general take another form. A nice derivation for the calculation of a general Lorentz correction for arbitrary scan types has been published by McIntyre and Stansfield [19].

The result from Equations A.32 and A.43 can now be inserted into Equation A.38 to yield the final expression for the integrated intensity acquired in the ω-scan:

$$\begin{aligned} E &= \frac{R^2}{\Omega} \iiint I_c(\mathbf{q})\, \mathrm{d}\gamma\, \mathrm{d}\delta\, \mathrm{d}\omega \\ &= \frac{R^2}{\Omega} \frac{\lambda^3}{(2\pi)^2 \sin 2\theta} \iiint I_c(\mathbf{q})\, \mathrm{d}^3\mathbf{q} \\ &= \frac{R^2}{\Omega} \frac{(2\pi)^3}{V} \frac{\lambda^3}{(2\pi)^2 \sin 2\theta} \iiint I_c(\mathbf{q})\, \mathrm{d}h\, \mathrm{d}k\, \mathrm{d}l \\ &= I_0 \frac{r_e^2}{R^2} P \frac{R^2}{\Omega} \frac{(2\pi)^2}{V} \frac{\lambda^3}{(2\pi)^2 \sin 2\theta} |F_{HKL}|^2 N \\ &= I_0 \frac{r_e^2}{\Omega}\, P\, \frac{\lambda^3}{V \sin 2\theta}\, |F_{HKL}|^2\, N. \end{aligned} \tag{A.44}$$

Solving for the unknown structure factor $|F_{HKL}|^2$ of the reflection under consideration, we obtain:

$$|F_{HKL}|^2 = E \frac{\Omega V \sin 2\theta}{I_0 P N r_e^2 \lambda^3}. \tag{A.45}$$

Replacing the collected diffraction energy E by the usually measured total number of background-subtracted x-ray counts $\mathcal{N} = E/E_{\mathrm{xray}}$, and the incident intensity I_0 by the incident photon flux $\Phi_0 = I_0/E_{\mathrm{xray}}$, this finally leads to

$$|F_{HKL}|^2 = \mathcal{N} \frac{\Omega V \sin 2\theta}{\Phi_0 P N r_e^2 \lambda^3}. \tag{A.46}$$

All quantities on the right-hand-side of this equation are known or have been measured in the experiment, so we have successfully determined the structure factor $|F_{HKL}|^2$ in this ω-scan.

A.4.5 Towards realistic crystals: Debye-Waller factors and partial occupation

Even at the lowest possible temperatures, the atoms inside the crystal lattice are never truly stationary, but exhibit thermal fluctuations in their equilibrium positions. For measurements longer than the typical vibration frequencies (of the order of 10^{13} Hz!), one therefore obtains a scattering pattern representing the temporal average of the atomic positions. Additionally, there may be a static component of local disorder present in the system, resulting in atoms being marginally displaced from their nominal positions in a random fashion. This will then lead to a spatial averaging of the structure over the coherence volume of the x-rays. These effects can be taken into account for the calculation of the structure factor by including the so-called Debye-Waller factor, which is defined as

$$M \equiv \frac{1}{2}\, \mathbf{q}^{\dagger}\, \frac{\mathbf{B}_j}{8\pi^2}\, \mathbf{q}, \tag{A.47}$$

where $\mathbf{B}_j$ is a symmetric dispersion matrix with six independent variables and $\mathbf{q}^{\dagger}$ represents the transpose of the vector $\mathbf{q}$. Unfortunately, the terminology is not entirely unambiguous, and sometimes one also refers to $\exp(-M)$ as the Debye-Waller factor. For the special case of an isotropic Debye-Waller factor, having just one independent variable B, the root mean-square-displacement of an atom from its equilibrium position is given by

$$\sigma_j = \sqrt{\frac{B}{8\pi^2}}. \tag{A.48}$$

Generally, these positional fluctuations of atoms inside the crystal will lead to a weakening of the interference condition. This results in a lowering of the Bragg peak intensity distribution.

Another type of crystal imperfection are partially occupied atomic sites, or even missing atoms within the structure. Also, in mixed systems, some sites may be occupied randomly by one of several different species. Once more, the measured diffraction pattern is influenced by an averaging over many unit cells, so these effects need to be incorporated into the structure-factor calculation. This is most easily achieved by assigning each of the N atoms in the unit cell an occupation parameter θ_j. Including these corrections into the formula for the structure factor leads to

$$F(\mathbf{q}) = \sum_{j=1}^{N} \theta_j \exp\left(-\frac{1}{2}\, \mathbf{q}^{\dagger}\, \frac{\mathbf{B}_j}{8\pi^2}\, \mathbf{q}\right) f_j(\mathbf{q}) \cdot e^{i\mathbf{q}\mathbf{r}_j}. \tag{A.49}$$

Note that these changes only affect the calculations at the unit cell level, and all other derivations remain the same after replacing the previous expression of $F(\mathbf{q})$ (Equation A.17) with the one given here.

A.5 Surface diffraction

A.5.1 Truncation

When building up a bulk crystal, we arranged the unit cells periodically and infinitely in all three spatial directions to give the crystal structure. When dealing with a crystal surface, this is obviously not possible anymore, and somehow we have to bring the truncation of our infinite crystal into play. There is no reason to change anything about the procedure along the two directions parallel to the surface plane, but the infinite stacking of cells along the out-of-plane direction needs to be changed. The truncation effectively represents a breaking of the crystal's symmetry and a transition from an entirely periodic structure to something aperiodic in the surface normal direction. We had seen in Chapter 2 that this new aperiodicity in real-space necessarily leads to a continuous diffraction pattern along that coordinate.

To keep as much of the already developed formalism as possible, it turns out to be convenient to construct a new "unit item" to replace the standard unit cell, and which can still be stacked along those two directions maintaining their periodicity. Consequently, this "unit item" needs to describe the system along the entire out-of-plane direction, so we simply form a semi-infinite "unit slab" by the stacking of normal unit cells from $-\infty$ to 0 along the $\mathbf{a_3}$ direction. We can now calculate the scattering amplitude from such a unit slab by summing up the contributions from all unit cells in the slab:

$$A_{us} = \mathcal{K} \cdot F(\mathbf{q}) \cdot e^{i\mathbf{qr}} \cdot e^{i\mathbf{q}(j_1\mathbf{a_1}+j_2\mathbf{a_2})} \cdot \sum_{j_3=-\infty}^{0} e^{i\mathbf{q}\cdot(j_3\mathbf{a_3})}. \tag{A.50}$$

The sum in Equation A.50 can be recognized as a geometric series, $\sum_{n=0}^{\infty} b^n$, where $b = e^{i\mathbf{q}\cdot\mathbf{a_3}}$ and $n = -j_3$. This series converges only for $|b| < 1$, in which case the solution is given by (see Appendix F)

$$\sum_{n=0}^{\infty} b^n = \frac{1}{1-b}. \tag{A.51}$$

However, $|e^{i\mathbf{qa_3}}| = 1$, and thus no formal convergence can be expected. This problem can be circumvented by introducing a small damping or absorption term $e^{-\beta}$ for each unit cell layer. This is physically reasonable, as x-rays are only weakly absorbed by the material, resulting in an absorption parameter β of the order of typically 10^{-5}. As a result, the amplitude of the wave scattered from the entire unit slab then becomes

$$A_{us} = \mathcal{K} \cdot F(\mathbf{q}) \cdot e^{i\mathbf{qr}} \cdot e^{i\mathbf{q}(j_1\mathbf{a_1}+j_2\mathbf{a_2})} \cdot \sum_{j_3=-\infty}^{0} e^{i\mathbf{q}\cdot(j_3\cdot\mathbf{a_3})} \cdot e^{-j_3\beta}. \tag{A.52}$$

Now the sum converges and tends towards the $\frac{1}{1-b}$ limit for a vanishing absorption (let

$n = -j_3$):

$$\begin{aligned} \sum_{j_3=-\infty}^{0} e^{j_3 \cdot i\mathbf{q}\mathbf{a_3}} \cdot e^{-j_3\beta} &= \sum_{n=0}^{\infty} \left(e^{(i\mathbf{q}\mathbf{a_3}-\beta)}\right)^n = \frac{1}{1-e^{i\mathbf{q}\mathbf{a_3}-\beta}} \\ &\overset{\beta\to 0}{=} \frac{1}{1-e^{i\mathbf{q}\mathbf{a_3}}}. \end{aligned} \tag{A.53}$$

We can therefore write

$$A_{us} = \mathcal{K} \cdot e^{i\mathbf{q}\mathbf{r}} \cdot e^{i\mathbf{q}(j_1\mathbf{a_1}+j_2\mathbf{a_2})} \cdot F(\mathbf{q}) \cdot \underbrace{\frac{1}{1-e^{i\mathbf{q}\mathbf{a_3}-\beta}}}_{=F_{\mathrm{CTR}}(\mathbf{q})}, \tag{A.54}$$

and call $F_{\mathrm{CTR}}(\mathbf{q})$ the CTR structure factor. It is the direct consequence of the semi-infinite summation and therefore contains the information about the presence of a surface. And it describes the modification necessary to go from a unit cell structure factor to that of the unit slab:

$$F_{us}(\mathbf{q}) = F(\mathbf{q}) \cdot F_{\mathrm{CTR}}(\mathbf{q}). \tag{A.55}$$

A.5.2 From amplitudes to intensities

Now, we make up a small crystal with a surface by a stacking of the unit slabs in the two in-plane directions. Of course, we are interested in the intensity distribution resulting from such a structure, to compare to the bulk case discussed previously. For consistency, we assume again a regular shape of the crystallite, comprising N_1 and N_2 unit slabs along the $\mathbf{a_1}$ and $\mathbf{a_2}$ directions. The scattering amplitude of such a surface structure (denotes by the subscript s) will be:

$$\begin{aligned} A_s &= \mathcal{K} \cdot e^{i\mathbf{q}\mathbf{r}} \cdot F_{us}(\mathbf{q}) \cdot \sum_{j_1=0}^{N_1-1} \sum_{j_2=0}^{N_2-1} e^{i\mathbf{q}\cdot(j_1\mathbf{a_1}+j_2\mathbf{a_2})} \\ &= \mathcal{K} \cdot e^{i\mathbf{q}\mathbf{r}} \cdot F(\mathbf{q}) \cdot \sum_{j_1=0}^{N_1-1} e^{i\mathbf{q}\cdot(j_1\cdot\mathbf{a_1})} \cdot \sum_{j_2=0}^{N_2-1} e^{i\mathbf{q}\cdot(j_2\cdot\mathbf{a_2})} \cdot \sum_{j_3=-\infty}^{0} e^{j_3\cdot i\mathbf{q}\mathbf{a_3}} \cdot e^{-j_3\beta}. \end{aligned} \tag{A.56}$$

Comparing this to the bulk case in Equation A.18, we see that only the last term with the summation over j_3 has changed. Squaring this amplitude, we get the corresponding expression for the intensity.

$$I_s = A_s \cdot A_s^* = I_0 \cdot \frac{r_e^2}{R^2} \cdot P \cdot |F(\mathbf{q})|^2 \cdot \frac{\sin^2(\frac{1}{2}N_1q_1a_1)}{\sin^2(\frac{1}{2}q_1a_1)} \cdot \frac{\sin^2(\frac{1}{2}N_2q_2a_2)}{\sin^2(\frac{1}{2}q_2a_2)} \cdot \frac{1}{1-e^{i\mathbf{q}\mathbf{a_3}-\beta}} \cdot \frac{1}{1-e^{-i\mathbf{q}\mathbf{a_3}-\beta}}.$$

(A.57)

Using the trigonometric relationship $2\sin^2(\alpha) = (1 - \cos(2\alpha))$, we can rewrite the last two terms for the case of a vanishing absorption ($\beta \to 0$) to yield

$$\begin{aligned}
&\frac{1}{1 - e^{i\mathbf{qa_3} - \beta}} \cdot \frac{1}{1 - e^{-i\mathbf{qa_3} - \beta}} \\
&\quad \cong \frac{1}{1 - e^{i\mathbf{qa_3}}} \cdot \frac{1}{1 - e^{-i\mathbf{qa_3}}} = \frac{1}{1 - e^{i\mathbf{qa_3}} - e^{-i\mathbf{qa_3}} + \underbrace{e^{i(\mathbf{qa_3} - \mathbf{qa_3})}}_{=1}} \\
&\quad = \frac{1}{2 - e^{i\mathbf{qa_3}} - e^{-i\mathbf{qa_3}}} = \frac{1}{2 - \cos(\mathbf{qa_3}) + i\sin(\mathbf{qa_3}) - \cos(\mathbf{qa_3}) - i\sin(\mathbf{qa_3})} \\
&\quad = \frac{1}{2(1 - \cos(\mathbf{qa_3}))} = \frac{1}{2 \cdot 2\sin^2(\frac{1}{2}\mathbf{qa_3})} \\
&\quad = \frac{1}{4\sin^2(\frac{1}{2}\mathbf{qa_3})}.
\end{aligned} \tag{A.58}$$

For orthogonal lattices, we have $\mathbf{qa_3} = q_3 a_3 = 2\pi l$. So finally, by putting this back into Equation A.57, we end up with

$$I_s(\mathbf{q}) = I_0 \cdot \frac{r_e^2}{R^2} \cdot P \cdot |F(\mathbf{q})|^2 \cdot \frac{\sin^2(\frac{1}{2}N_1 q_1 a_1)}{\sin^2(\frac{1}{2}q_1 a_1)} \cdot \frac{\sin^2(\frac{1}{2}N_2 q_2 a_2)}{\sin^2(\frac{1}{2}q_2 a_2)} \cdot \underbrace{\frac{1}{4\sin^2(\frac{1}{2}q_3 a_3))}}_{|F_{CTR}(\mathbf{q})|^2}. \tag{A.59}$$

Of course, the same calculation can also be done for a nonzero value of the absorption, but in this case $I_s(\mathbf{q})$ does not take on such a simple algebraic expression.

Nothing has changed about the intensity distribution along the $\mathbf{q_1}$ and $\mathbf{q_2}$ directions. It is still strongly peaked around the reciprocal lattice points with negligible intensity in between for reasonably large values of N_1 and N_2. It is the last term that makes the difference, governing the intensity distribution along $\mathbf{q_3}$. Figure A.6 shows a plot of $\frac{1}{4\sin^2(\pi l))}$, along with a case where a nonzero value of the layer absorption β has been taken into account. Apart from the singularity at integer l-values, which is removed by including a finite absorption, the intensity changes continuously, just as expected. The intensity values vary by several orders of magnitude between points close to the Bragg peaks and those exactly in between, the so-called anti-Bragg points. The effect of including the absorption only becomes visible for unphysically large values of β, or very close to the Bragg peaks, where the kinematical approximation is not valid in any case. However, it effectively removes the mathematical problems associated with the singularity that arises for the case of zero absorption.

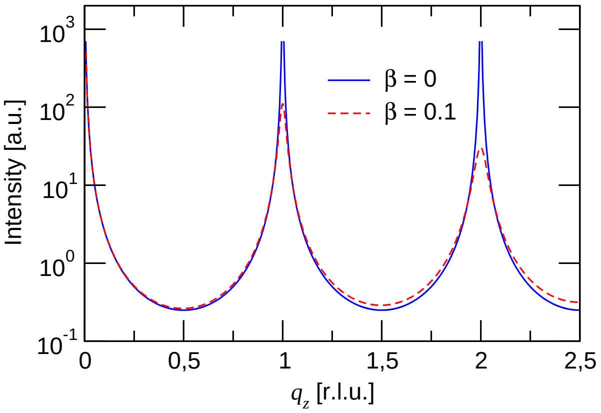

Figure A.6: The intensity distribution along a CTR for a perfectly flat and bulk-like surface is shown by the blue solid line. Including an absorption correction β results in the dashed red line. To make the effect visible, an unphysically large value of $\beta = 0.1$ had to be used, where typical values are of the order of 10^{-5}.

In summary, the intensity distribution in three dimensions is a set of rods, perpendicular to the physical surface of the crystal, and separated from each other by reciprocal lattice vectors in the in-plane direction. These streaks are called *crystal truncation rods* (CTRs) or sometimes also *Bragg rods.*

A.5.3 Adding a surface or film layer

The construction of the unit slab in Section A.5.1 assumes that all the way up to the surface, the structure of the crystal is exactly represented by atoms in their bulk-like positions. In reality, the structure of the topmost layers can be significantly different. Alternatively, one might be concerned with a film of a different material on top of a substrate. We therefore need to include an additional contribution from this top layer, which we will denote as F_{film}[6], to the bulk unit slab structure factor.

$$F_{tot} = F_{uc} \cdot F_{CTR} + F_{film}. \tag{A.60}$$

The film structure can be treated as a two dimensional crystal, periodic in the two directions parallel to the substrate surface, and one "unit cell" thick in the perpendicular direction. Again,

---

[6] Here, the film includes all parts of the structure which deviate from the bulk structure. This might be the surface region of a single-crystal or a film plus the distorted interface region of the substrate.

the thickness of this "unit cell" is equal to the depth to which the structure varies from the bulk. We calculate the structure factor for that unit cell in the usual manner (see Section A.5.2) by summing up over all the contributions of the N_f constituent atoms in the film:

$$F_{film} = \sum_{j'=1}^{N_f} f_{j'}(\mathbf{q}) \cdot e^{i\mathbf{q}\mathbf{r_{j'}}}. \tag{A.61}$$

where $f_{j'}(\mathbf{q})$ and $\mathbf{r_{j'}}$ are the atomic form factor and the position of the individual film atoms, respectively. Debye-Waller factors and occupation parameters can be included according to Section A.4.5. The expression for the scattering intensity then becomes

$$I_{tot}(\mathbf{q}) = I_0 \cdot \frac{r_e^2}{R^2} \cdot P \cdot |F_{tot}(\mathbf{q})|^2 \cdot \frac{\sin^2(\frac{1}{2}N_1 q_1 a_1)}{\sin^2(\frac{1}{2}q_1 a_1)} \cdot \frac{\sin^2(\frac{1}{2}N_2 q_2 a_2)}{\sin^2(\frac{1}{2}q_2 a_2)}. \tag{A.62}$$

Examples of how the presence of a thin film or small movements of atoms at the surface affect the shape of the CTRs have been shown in Section 2.2.3 and 2.2.4, and in Figure 2.5.

A.5.4 Integrating CTR intensities

Now that we know how to calculate the CTR profiles theoretically, we need to find out how this intensity distribution can be measured in practice. In contrast to the integrated intensities discussed for the scattering from a three-dimensional crystal in Section A.4.4, where the integration was carried out over discrete Bragg reflections in reciprocal space, we are now interested in sampling the shape of the continuously varying diffraction signal along the CTRs.

The reason why we turned to the measurement of integrated intensities for bulk crystals, rather than a direct measurement of the intensity distribution in reciprocal space, was based on the argument that it would be experimentally impossible to measure this distribution with sufficient accuracy on the one hand, and that, on the other hand, the intensity distribution calculated by assuming a perfect crystal could not be produced by real crystals with imperfections. In other words, the predicted features of the intensity distribution were too sharp to be observed in any real situation. The integrated intensity, however, was both calculable theoretically as well as observable in experiment.

This situation changes dramatically for the measurement of CTR intensities. The variations in intensity along the rod, as predicted by using the model of a perfectly truncated bulk crystal, are gradual and change slowly compared to the typical broadening effects of a sharp diffraction feature caused by instrumental effects and crystal imperfections (an exception are those points very close to the bulk Bragg peaks). This allows us to experimentally sample the intensity distribution along the direction of the rods (i.e., the l-direction). However, the width of the CTRs perpendicular to the l-direction is still determined by the broadening effects. Therefore, we need to retain the integration over the h- and k-directions.

This two-dimensional integration in reciprocal space can be directly obtained in a single detector exposure if one uses a geometry where the entire diffraction signal is captured by the detector. This requires a sufficiently large detector area, and a relaxed sample to detector collimation, such that no part of the diffraction signal is blocked, for example by slits. From here on, we will refer to this situation as the "open-slit geometry".

Consider Figure A.7 (a). Again, the diffraction condition is satisfied for all points lying on the intersection of the CTR with the Ewald sphere. The measured diffraction energy for the (HKl) reflection, where H and K are integers and l is the current position on the CTR, is given by the integration over the exposure time T and the receiving surface A_D of the detector:

$$E_{HKl} = \int_T \int_{A_\mathrm{D}} I_s(\mathbf{q})\,\mathrm{d}A_\mathrm{D}\,\mathrm{d}t = \iiint I_s(\mathbf{q})\,R^2\,\mathrm{d}\gamma\,\mathrm{d}\delta\,\mathrm{d}t. \tag{A.63}$$

Formally, the change in integration variables from angular to reciprocal-space coordinates can be achieved by including the appropriate Jacobian transformation:

$$\begin{aligned} E_{HKl} &= R^2 \int \mathrm{d}t \iint I_s(\mathbf{q})\,\mathrm{d}\gamma\,\mathrm{d}\delta \\ &= R^2 \int \mathrm{d}t \iint I_s(\mathbf{q}) \left| \frac{\partial(\gamma,\delta)}{\partial(h,k)} \right| \mathrm{d}h\,\mathrm{d}k. \end{aligned} \tag{A.64}$$

Since the integration ranges over γ and δ are small, the Jacobian is assumed to be constant over the integration range, taken outside the integral and evaluated at the nominal (HKl)-position. Substituting the expression for $I_s(\mathbf{q})$ from Equation A.62, we can now perform the

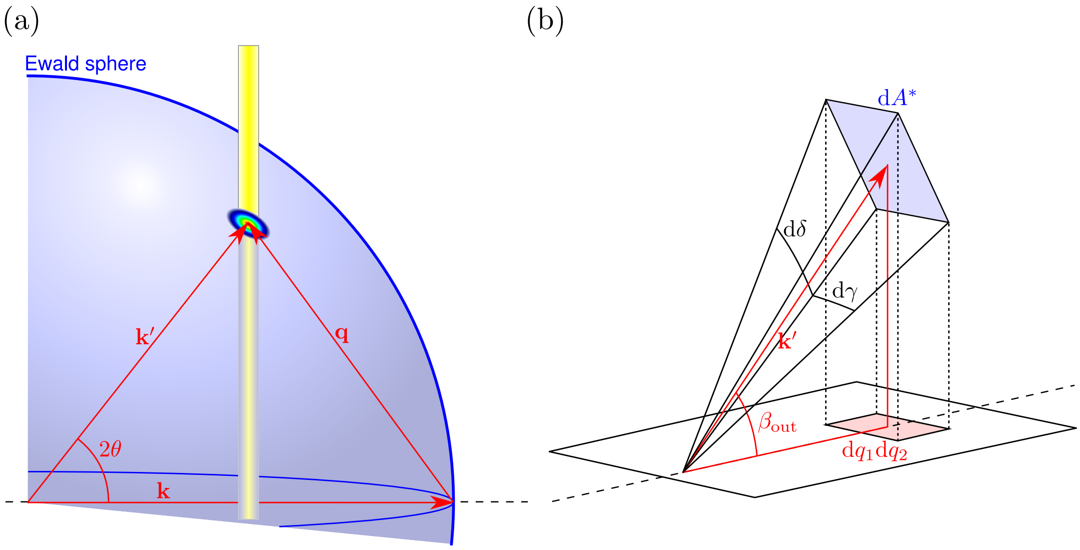

Figure A.7: (a) The elastic scattering condition is fulfilled for all points lying on the intersection of the CTR with the Ewald sphere. (b) Schematic representation of the infinitesimal integration volume when transforming from angular integration variables $\mathrm{d}\gamma, \mathrm{d}\delta$ to reciprocal space variables $\mathrm{d}\mathbf{q_1}, \mathrm{d}\mathbf{q_2}$. Here, the special case of $\mathrm{d}\mathbf{q_1}, \mathrm{d}\mathbf{q_2}$ lying within the surface plane is shown (see text for details).

integration:

$$\begin{aligned} E_{HKl} &= R^2 \left|\frac{\partial(\gamma,\delta)}{\partial(h,k)}\right| \int \mathrm{d}t \iint I_s(\mathbf{q})\,\mathrm{d}h\,\mathrm{d}k \\ &= R^2 T \left|\frac{\partial(\gamma,\delta)}{\partial(h,k)}\right| \iint I_0 \cdot \frac{r_e^2}{R^2} \cdot P \cdot |F_{tot}(\mathbf{q})|^2 \cdot \frac{\sin^2(\frac{1}{2}N_1 q_1 a_1)}{\sin^2(\frac{1}{2}q_1 a_1)} \cdot \frac{\sin^2(\frac{1}{2}N_2 q_2 a_2)}{\sin^2(\frac{1}{2}q_2 a_2)}\,\mathrm{d}h\,\mathrm{d}k \\ &= I_0 r_e^2 P T \left|\frac{\partial(\gamma,\delta)}{\partial(h,k)}\right| \iint |F_{tot}(\mathbf{q})|^2 \cdot \frac{\sin^2(N_1 \pi h)}{(\pi h)^2} \cdot \frac{\sin^2(N_2 \pi k)}{(\pi k)^2}\,\mathrm{d}h\,\mathrm{d}k. \end{aligned} \tag{A.65}$$

Note that the purely experimental parameter R^2 cancels out in this step, such that E_{HKl} is independent of the distance between the sample and the detector, as expected. As in the case of bulk diffraction (Section A.4.4), we can now make the assumption that the total structure factor varies only slowly over the sampled area in reciprocal-space. We can then replace $|F_{tot}(\mathbf{q})|^2$ by $|F_{HKl}|^2$, and take this outside the integral. Note, however, that in contrast to the bulk case, where this assumption is certainly always good enough in comparison to the very sharp diffraction features, the CTR structure factor varies much more quickly along l, especially on the steep parts close to the Bragg peaks or in the finite size fringes of thick films. For small values of β_{out}, where the intersection of the CTR with the Ewald sphere is very elongated, and thus a large region of reciprocal space is sampled, or close to the Bragg points, the approximation is therefore not valid. This has to be kept in mind when performing an experiment, and will be discussed in more detail in Appendix B. Under those conditions where the assumption is justified, we can then calculate the integral in Equation A.65:

$$\begin{aligned} E_{HKl} &= I_0 r_e^2 PT|F_{HKl}|^2 \left|\frac{\partial(\gamma,\delta)}{\partial(h,k)}\right| \int \frac{\sin^2(N_1\pi h)}{(\pi h)^2}\,\mathrm{d}h \cdot \int \frac{\sin^2(N_2\pi k)}{(\pi k)^2}\,\mathrm{d}k \\ &= I_0 r_e^2 PT|F_{HKl}|^2 \left|\frac{\partial(\gamma,\delta)}{\partial(h,k)}\right| N_1 N_2. \end{aligned} \tag{A.66}$$

The Jacobian depends on the particular measurement geometry and on the definition of the reciprocal-space coordinate through the choice of the crystal unit cell parameters. It can be evaluated easily under the assumption that the h- and k-directions are mutually perpendicular to each other and to the l-direction, and therefore lie within the physical surface plane of the sample (we have seen in Chapter 7 that this is not necessarily the case, as for example for our choice of the (110)-oriented surface unit cell of NGO). First the Jacobian is split into two parts:

$$\left|\frac{\partial(\gamma,\delta)}{\partial(h,k)}\right| = \left|\frac{\partial(\gamma,\delta)}{\partial(\mathbf{q_1},\mathbf{q_2})}\right| \left|\frac{\partial(\mathbf{q_1},\mathbf{q_2})}{\partial(h,k)}\right|. \tag{A.67}$$

The second transformation is simple:

$$\begin{aligned} &\mathbf{q_1} = h\mathbf{a}_\mathbf{1}^*, \qquad \mathbf{q_2} = k\mathbf{a}_\mathbf{1}^* \\ \Longrightarrow\ &\left|\frac{\partial(\mathbf{q_1},\mathbf{q_2})}{\partial(h,k)}\right| = \begin{vmatrix} \frac{\partial \mathbf{q_1}}{\partial h} & \frac{\partial \mathbf{q_1}}{\partial k} \\ \frac{\partial \mathbf{q_2}}{\partial h} & \frac{\partial \mathbf{q_2}}{\partial k} \end{vmatrix} = \begin{vmatrix} a_1^* & 0 \\ 0 & a_2^* \end{vmatrix} = a_1^* a_2^* = \frac{2\pi}{a_1}\frac{2\pi}{a_2} = \frac{(2\pi)^2}{A_{uc}}, \end{aligned} \tag{A.68}$$

where A_{uc} is the is the area of the surface unit cell.

The transformation of the first term in Equation A.67 is illustrated schematically in Figure A.7 (b). The reciprocal-space area-element $\mathrm{d}A^*$ on the surface of the Ewald sphere, spanned by the changes $\mathrm{d}\gamma$, $\mathrm{d}\delta$, is projected into the surface plane of the sample, which coincides with the $a_1^* a_2^*$-plane. The area $\mathrm{d}q_1\mathrm{d}q_2$ of the projection is given by the angle β_{out} enclosed by the outgoing wave-vector $\mathbf{k}'$ with respect to the surface plane:

$$\mathrm{d}q_1\mathrm{d}q_2 = \sin\beta_{\text{out}}\,\mathrm{d}A^* = \sin\beta_{\text{out}}\frac{(2\pi)^2}{\lambda^2}\mathrm{d}\gamma\,\mathrm{d}\delta, \tag{A.69}$$

and therefore

$$\left|\frac{\partial(\gamma,\delta)}{\partial(\mathbf{q_1},\mathbf{q_2})}\right| = \frac{\lambda^2}{(2\pi)^2\sin\beta_{\text{out}}}. \tag{A.70}$$

Recombining the two terms in Equations A.68 and A.70 yields the total change in integration area:

$$\left|\frac{\partial(\gamma,\delta)}{\partial(h,k)}\right| = \frac{\lambda^2}{A_{uc}}\frac{1}{\sin\beta_{\text{out}}}. \tag{A.71}$$

The angle-dependent part, $\frac{1}{\sin\beta_{\text{out}}}$, is the Lorentz factor for this particular geometry.

Re-inserting this expression in the formula for the total collected diffraction intensity from Equation A.73 for the particular point (HKl) under consideration yields

$$\begin{aligned} E_{HKl} &= I_0 r_e^2 PT|F_{HKl}|^2 \left|\frac{\partial(\gamma,\delta)}{\partial(h,k)}\right| N_1N_2 \\ &= I_0 PTN_1N_2\frac{r_e^2\lambda^2}{A_{uc}}\frac{1}{\sin\beta_{\text{out}}}|F_{HKl}|^2. \end{aligned} \tag{A.72}$$

N_1N_2 is the total number of unit slabs of the truncated crystal structure. Replacing the total energy E_{HKl} with the measured number of counts $\mathcal{N}_{HKl}$, and the incident intensity I_0 with the incident photon-flux Φ_0, we finally obtain the following expression for the CTR structure factor:

$$|F_{HKl}|^2 = \mathcal{N}_{HKl}\frac{\sin\beta_{\text{out}}}{\Phi_0 PTN_1N_2}\frac{A_{uc}}{r_e^2\lambda^2}. \tag{A.73}$$

All the quantities on the right-hand-side are either known or have been measured, so we have finally determined the CTR structure factor.

A.5.5 The incoming flux profile and the active sample area

In the derivation of the CTR structure factor in Equation A.73, we have so far assumed that the entire crystal contributes to the scattering and that the incoming flux of photons be a constant. This corresponds to the situation where a small crystal is completely bathed in a large incoming beam. In SXRD, this condition is only very seldom fulfilled, usually the samples are several square-millimeters in size and the synchrotron beam is focussed down to a few hundred microns. It is therefore never the entire crystal surface that contributes to the scattering, but only a fraction thereof, which is commonly called the *active area*. To take this fact correctly into account in the calculation of the diffracted energy, we need to know which part of the sample receives how much incoming intensity.

The transverse profile of the incoming x-ray beam at the sample location is represented by $\Phi_0(x_l, z_l)$, where x_l and z_l are the two laboratory coordinate directions normal to the incoming

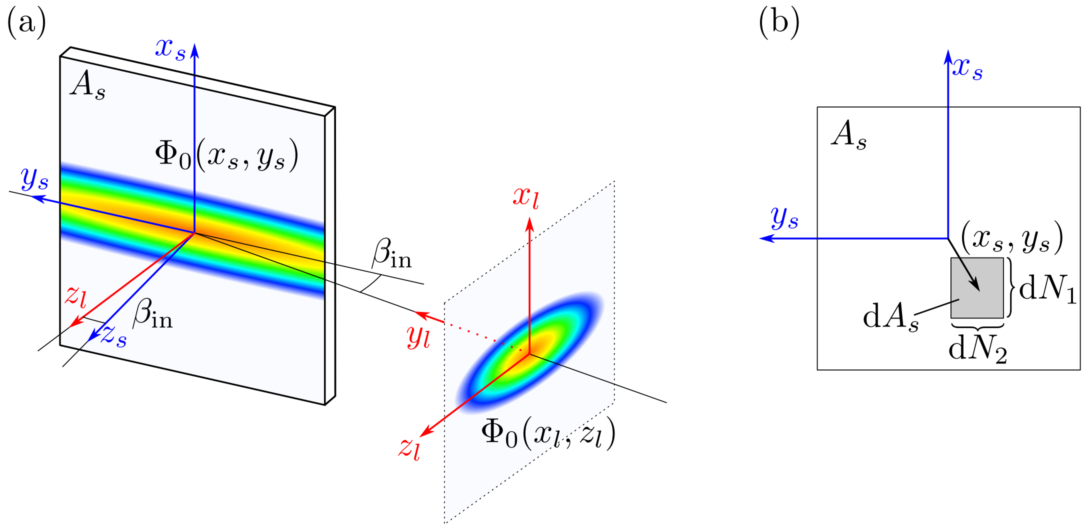

Figure A.8: (a) The incident flux $\Phi_0(x_l, z_l)$ in the laboratory frame of reference (red) produces a flux distribution $\Phi_0(x_s, z_s)$ on the sample surface (blue coordinate system). (b) Definition of the surface area element $\mathrm{d}A_s$ in the crystal surface coordinate system.

beam, which is assumed to propagate along the y_l axis[7]. At grazing incidence angles, β_{in}, with respect to the crystal surface, the z_l axis is nearly aligned with the surface normal of the crystal, and x_l lies within the crystal surface plane, as shown in Figure A.8 (a).

We have seen in Section A.4.4 that the integrated scattering intensity depends linearly on the number of unit cells involved in the scattering, and that we can decompose a crystal into many smaller sub-blocks which together will generate the same integrated intensity (but not the same intensity distribution) of a Bragg reflection as the whole crystal. We now use this fact to decompose our crystal surface into many small crystallites with surface elements $\mathrm{d}A_s$. The surface element is assumed to be rectangular in shape and contains N_1' and N_2' unit cells along each edge, respectively. This is shown schematically in Figure A.8 (b). Therefore,

$$\mathrm{d}A_s = \mathrm{d}N_1 \mathrm{d}N_2 A_{uc}, \tag{A.74}$$

where A_{uc} is the size of the surface unit cell.

Each of those surface elements is located at a position (x_s, y_s) in the crystal frame of reference, where x_s and y_s lie within the surface plane. From the transverse flux profile in the

---

[7] The orientation of the laboratory coordinate system is, of course, arbitrary and, in this case, chosen according to the setup at the Surface Diffraction station of the Materials Science beamline at the Swiss Light Source.

laboratory coordinate system, the flux distribution within the sample surface can be calculated, since the orientation of the crystal is known: $\Phi_0(x_l, z_l) \rightarrow \Phi_0(x_s, y_s)$.

The number of photons, $\mathrm{d}\mathcal{N}_{HKl}$, scattered from each surface area element is given by Equation A.73, where N_1, N_2 have been replaced by $\mathrm{d}N_1, \mathrm{d}N_2$:

$$\mathrm{d}\mathcal{N}_{HKl} = \Phi_0(x_s, y_s) r_e^2 PT |F_{HKl}|^2 \left| \frac{\partial(\gamma, \delta)}{\partial(h, k)} \right| \mathrm{d}N_1 \mathrm{d}N_2. \tag{A.75}$$

The total scattering of the sample can then be obtained by integrating the individual contributions $\mathrm{d}\mathcal{N}_{HKl}$ from all surface elements over the entire sample area A_s. Replacing $\mathrm{d}N_1 \mathrm{d}N_2 = \mathrm{d}A_s / A_{uc} = \mathrm{d}x_s \mathrm{d}y_s / A_{uc}$, we obtain

$$\mathcal{N}_{HKl} = r_e^2 PT |F_{HKl}|^2 \frac{1}{A_{uc}} \left| \frac{\partial(\gamma, \delta)}{\partial(h, k)} \right| \cdot \int_{\mathrm{A_s}} \Phi_0(x_s, y_s) \mathrm{d}x_s \mathrm{d}y_s. \tag{A.76}$$

Solving for $|F_{HKl}|^2$ and using the explicit form of the Jacobian derived previously, this yields the final result of

$$\begin{aligned} |F_{HKl}|^2 &= \mathcal{N}_{HKl} \frac{A_{uc}}{r_e^2 PT} \left| \frac{\partial(\gamma, \delta)}{\partial(h, k)} \right|^{-1} \left[\int_{\mathrm{A_s}} \Phi_0(x_s, y_s) \mathrm{d}x_s \mathrm{d}y_s \right]^{-1} \\ &= \mathcal{N}_{HKl} \frac{\sin \beta_{\mathrm{out}}}{PT} \frac{A_{uc}^2}{r_e^2 \lambda^2} \left[\int_{\mathrm{A_s}} \Phi_0(x_s, y_s) \mathrm{d}x_s \mathrm{d}y_s \right]^{-1}. \end{aligned} \tag{A.77}$$

More details on how this can be calculated in practice are given in the following two appendices, dealing with the measurement and the data treatment of SXRD data. Note that Equations A.76 and A.77 give the absolute values for the CTR structure factor as obtained from the measurement. The experimental challenge lies in determining all the ingredients of these equations with sufficient accuracy, in order to obtain reliable and correctly scaled values for the structure factors, which can then be directly compared to the calculated structure factors from an atomic model.

Bibliography

[1] C. Kittel: *Introduction to Solid State Physics*. John Wiley & Sons Inc., New York, fifth edition (1976).

[2] N. W. Ashcroft and N. D. Mermin: *Solid State Physics*. Holt, Rinehart and Winston, New York (1976).

[3] B. E. Warren: *X-ray Diffraction*. Addison-Wesley Publishing Company, Reading, Massechusetts (1969).

[4] M. M. Woolfson: *An Introduction to X-ray Crystallography*. Cambridge University Press, second edition (1997).

[5] P. Coppens, D. Cox, E. Vlieg, and I. K. Robinson: *Synchrotron Radiation Crystallography*. Academic Press, London (1992).

[6] J. M. Cowley: *Diffraction Physics*. Elsevier Science B.V., Amsterdam, The Netherlands, third edition (1995).

[7] J. Als-Nielsen and D. McMorrow: *Elements of Modern X-ray Physics*. Wiley (2000).

[8] C. Giacovazzo (Editor): *Fundamentals of Crystallography*. Oxford University Press, second edition (2002).

[9] I. K. Robinson: "Structure Factor Determination in Surface X-Ray Diffraction." *Aust. J. Phys.* **41**, 359 – 367 (1987).

[10] I. K. Robinson and D. J. Tweet: "Surface X-ray diffraction." *Rep. Progr. Phys.* **55**, 599–651 (1992), doi:10.1088/0034-4885/55/5/002.

[11] R. Feidenhans'l: "Surface structure determination by X-ray diffraction." *Surf. Sci. Rep.* **10**(3), 105–188 (1989), doi:10.1016/0167-5729(89)90002-2.

[12] E. Vlieg, J. F. van der Veen, S. J. Gurman, C. Norris, and J. E. Macdonald: "X-ray diffraction from rough, relaxed and reconstructed surfaces." *Surf. Sci.* **210**(3), 301 – 321 (1989), doi:10.1016/0039-6028(89)90598-0.

[13] I. K. Robinson: "Surface Crystallography." In *Handbook on Synchrotron Radiation*, Edited by G. Brown and D. E. Moncton, chapter 7, 221–266, Elsevier Science Publishers, third edition (1991).

[14] M. Taylor, I. Majid, P. D. Bristowe, and R. W. Balluffi: "Structures of [001] twist boundaries in gold. 1. Measurement and use of absolute boundary x-ray structure factors." *Phys. Rev. B* **40**(5), 2772–2778 (1989), doi:10.1103/PhysRevB.40.2772.

[15] E. D. Specht and F. J. Walker: "A method for the accurate determination of crystal truncation rod intensities by X-ray diffraction." *J. Appl. Crystallogr.* **26**(2), 166 – 171 (1993), doi: 10.1107/S0021889892011592.

[16] V. M. Kaganer: "Crystal truncation rods in kinematical and dynamical x-ray diffraction theories." *Phys. Rev. B* **75**, 245425 (2007), doi:10.1103/PhysRevB.75.245425.

[17] J. D. Jackson: *Classical Electrodynamics*. John Wiley & Sons Inc., New York, second edition (1975).

[18] E. Prince (Editor): *International Tables for Crystallography, Vol. C, Mathematical, physical and chemical tables*. International Union of Crystallography, Chester, first online edition (2006).

[19] G. McIntyre and R. F. D. Stansfield: "A general Lorentz correction for single-crystal diffractometers." *Acta Crystallogr. A* **44**(3), 257–262 (1988), doi:10.1107/S0108767387011656.

Appendix B

SXRD Measurements

B.1 Introduction

The kinematical diffraction theory to calculate the scattering from crystals and crystal surfaces has been discussed in depth. Now we want to turn to the question of how this can actually be measured in practice, and with the experimental setup at the Surface Diffraction station of the SLS in particular. First, we will give a brief description of the setup with regard to the important components along the x-ray beam, after which we turn to the different types of scans to be performed. The goal is to understand how we need to use the available equipment to obtain all the information required to evaluate the expression for the integrated intensity on a CTR, as given by (see Equation A.77)

$$\begin{aligned} |F_{HKl}|^2 &= \mathcal{N}_{HKl} \frac{A_{uc}}{r_e^2 PT} \left| \frac{\partial(\gamma,\delta)}{\partial(h,k)} \right|^{-1} \left[\int_{\mathrm{A_s}} \Phi_0(x_s,y_s) \mathrm{d}x_s \mathrm{d}y_s \right]^{-1} \\ &= \mathcal{N}_{HKl} \frac{\sin\beta_{\mathrm{out}}}{PT} \frac{A_{uc}^2}{r_e^2\lambda^2} \left[\int_{\mathrm{A_s}} \Phi_0(x_s,y_s) \mathrm{d}x_s \mathrm{d}y_s \right]^{-1} . \end{aligned} \tag{B.1}$$

Most factors on the right-hand-side of this expression are actually known, the only quantities to be determined are the flux profile of the incident x-ray beam at the position of the investigated crystal, $\Phi_0(x_s, z_s)$, and the measured and background-subtracted number of scattered photons, $\mathcal{N}_{HKl}$. From here on, we will adopt the usual terminology, and refer to $\mathcal{N}_{HKl}$ as the “measured intensity”, and denote this with I_{meas}, even though the quantity I_{meas} does not have the physical units of an intensity. A detailed discussion regarding the units in our measurements

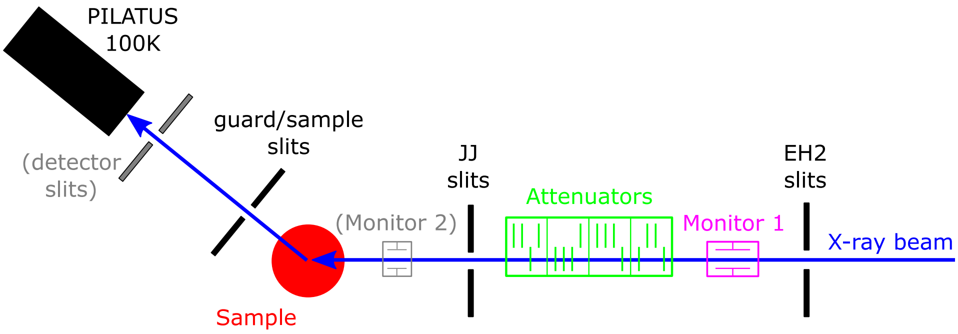

Figure B.1: Sketch of the beam shaping and monitoring components.

and clarifying the ambiguities in the nomenclature can be found in Section A.4.4.

Some of the measurements we need to perform have changed considerably through the use of an area detector in comparison to scans using point. For example, a careful detector calibration is now necessary. On the other hand, integrated intensities can often be obtained from a single detector exposure rather than having to perform a rocking scan. Despite the overall much improved, simplified and accelerated data acquisition with the pixel detector, there are also some potential pitfalls, which are also discussed.

B.2 Beam defining and monitoring components

The hardware setup at the Surface Diffraction Station of the Materials Science Beamline at the Swiss Light Source has been optimized for automatized high-quality SXRD data acquisition. A sketch of all crucial components is shown in Figure B.1, and the role of each component will be discussed briefly in the following.

X-ray beam: The collimated and monochromatic x-ray beam as it comes from the beamline optics system, consisting of a double crystal monochromator and two mirrors.

EH2 slits: Horizontal and vertical slit pairs for the surface diffraction station. Used to clean up the incoming X-ray beam for any tails and wings produced in the beamline optics.

Monitor 1: Incident beam monitor: Ionization chamber (IC) to monitor the incoming X-ray flux after all optical components. It is intentionally placed before the X-ray attenuators where only small variations in the incoming intensity are expected. Therefore, the IC operation parameters can be adjusted such that the IC works reliably within its linearity range. This point is crucial for correcting any instabilities in the incident X-ray intensity. Due to the large attenuation changes during an experiment, stable linear counting cannot be achieved when placing the IC behind the attenuator boxes.

Attenuators: A set of metal foils to attenuate the incoming X-ray beam. The thickness of all foils has been carefully calibrated, hence the attenuation for any combination of foils can be accurately calculated.

JJ slits: Horizontal and vertical beam conditioning slits. Used to define the beam size at the sample position. For glancing incidence experiments, they are usually optimized to reduce as much as possible the amount of radiation not hitting the surface under investigation (which contributes strongly to the background signal), while maintaining the intensity incident on the sample as high as possible.

Sample: The sample under investigation.

Guard/sample slits: Pairs of horizontal and vertical slits mounted on the front of the detector arm, usually as close to the sample as possible. In the open-slit configuration, these are opened up enough to capture the entire diffraction signal from the sample and used to cut out background signal which is not produced at the sample position, e.g., air scattering, scattering from container walls (Be, kapton), etc. In high-resolution or rocking scans, these slits define the visible area of the sample and the angular acceptance of the detector and thus the achievable reciprocal space resolution.

PILATUS 100k: Single photon counting pixel detector (see Section 2.3.2).

Two more components have been added in the sketch in gray color. These are not actually available presently, but would be helpful in many cases:

(Monitor 2): Ideally, one should have a second beam monitor after the beam conditioning slits in order to monitor the stability of the conditioned beam, particularly due to any changes in the attenuator and JJ-slit configuration. The IC should be optimized to work in the linear counting range for the full unattenuated X-ray beam, as those are the conditions most frequently used when recording the weak surface scattering signals. However, when looking at a heavily attenuated beam, for example when measuring signals close to Bragg peaks, the monitor will eventually stop counting due to insufficient sensitivity. Therefore, this monitor is not suitable to provide a reliable correction for the incoming X-ray beam stability, and cannot replace the first monitor. It can merely serve to identify instabilities in the setup, and provide additional corrections for those data points acquired under optimal working conditions for this IC.

(Detector slits): There are presently no slits right in front of the detector. Slitting operations can be performed electronically by selecting only appropriate pixels of the detector. However, mounting one pair of horizontal slits could prove to be advantageous when trying to protect the detector from very intense radiation close to the acquired signal. For example, when recording a reflectivity curve, it could be used to block the direct beam (rather than having to use the guard slits, where the signals are spatially not very well separated).

B.3 Measuring flat field correction data

The pixels of an area detector have different sensitivities to incoming x-rays and will have slightly different counting efficiencies with respect to each other. For high-quality measurements, the detector needs to be calibrated, in order to correct for these inhomogeneities in the pixel response. This can be achieved by illuminating the entire active area of the detector with homogeneous radiation and accumulating sufficiently large statistics to be sensitive to the required calibration level. In practice, achieving a flat illumination distribution over an extended detector area is not trivial, especially for larger detectors. In some cases, one may have to take the geometrical corrections into account separately. For the single module PILATUS 100k detector used in our experiments, positioned at about 1.15 meters from the diffractometer center with an active area of approximately 85×35 mm^2 (corresponding to subtended angles of $4.23^{o}\times1.74^{o}$), this is not so much of an issue and a sufficiently homogeneous illumination can be achieved relatively simply.

The detector calibration should always be done with an incident radiation of the same energy as that used for the experiments, since the pixel sensitivities are energy dependent. This generally rules out the use of strong fluorescence sources, as those emit x-rays at discrete energies and, in many cases, even with several different emission lines. Rather, a strong source of elastically scattered x-rays is required. Ideally, this source should be entirely amorphous, so as to avoid the occurrence of any diffraction features, and of high density (high-Z materials) to maximize the scattering efficiency. Additionally, it should contain no emission lines in the energy region of interest. For incident beam energies below 13 keV, using a disk or rod of lead glass works very well (below L_{III}-edge of Pb at 13.035 keV). For the higher energies, it has been found that a reasonably pure rod of normal glass scatters sufficiently strongly.

The scattering source needs to be positioned in the center of the diffractometer, exactly at the sample location. The detector should be moved fairly far away from the direct forward scattering direction, as this is where the scattered radiation is strongest and drops off quickly towards higher angles. At scattering angles of the order of 90°, this angular dependency is weak and a flat illumination across the entire detector can be readily achieved. The intensity can be optimized by adjusting the scattering source position (more than about 100 counts/s/pixel are desirable). Then it should be ensured again that the illumination is really flat on average[1].

The desired accuracy of the calibration is at least better than 1%, ideally close to 0.1%. This requires a statistics of between 10^4 to 10^6 integrated counts in each pixel. In order to perform a statistical analysis of the stability of each pixel, it is recommended to divide up the exposure time required to reach the total integrated intensity, acquiring between 50–200 individual exposures.

The statistical analysis performed on this data set will be discussed in depth in Section C.3.

B.4 Obtaining the incident beam flux profile

The incident x-ray beam has a certain transverse flux profile $\Phi_0(x, z)$ perpendicular to its propagation direction y, as sketched in Figure B.2 (a), which needs to be measured at the y-position of the sample, in order to evaluate the flux integral in Equation B.1. Generally, it is very difficult to measure this profile directly, as either sample chambers may prohibit direct access to the sample position, area detectors with a sufficient spatial resolution are unavailable, or raster scans using a tiny pinhole to sample the profile in two dimensions are too time-consuming.

---

[1] All slit systems between scattering source and detector need to be opened up fully to let the entire scattering signal reach the detector. The signal intensity may be increased by opening up the slit systems upstream in the incident beam as well

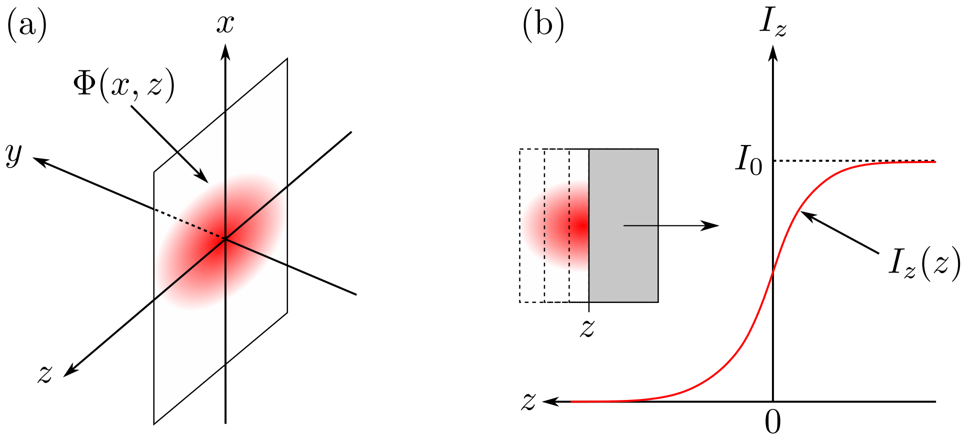

Figure B.2: (a) Sketch of the transverse flux profile $\Phi_0(x,z)$ as seen at the downstream sample position y. (b) Plot of $I_z(z)$ as it is recorded in a knife-edge scan.

Using one simple hypothesis, one can work around this problem. Let us assume the flux profile $\Phi_0(x,z)$ to be separable into two independent contributions which are each a function of only x or z. Then we can write

$$\Phi_0(x,z) = \varphi_x(x) \cdot \varphi_z(z). \tag{B.2}$$

The functions $\varphi_x(x)$ and $\varphi_z(z)$ could be easily measured by scanning a small slit across the beam in the x or z direction. However, for the same reasons as mentioned above, such a small slit may not be available at the sample position. A simple way to solve this problem is to use the sample itself (and possibly its holder) as a probe to measure the integrated flux profile instead. By scanning the sample position along the z-direction through the beam, and integrating the uneclipsed beam intensity which passes by the sample, one can record a so-called knife-edge scan of the beam. The measured intensity profile $I_z(z)$ starts with zero intensity when the sample is blocking the entire beam, then begins to rise as soon as a part of the beam is able to pass by the sample, and finally increases to the full beam intensity I_0 when the sample is completely removed from the beam. A typical scan plot is shown in Figure B.2 (b). By repeating the same procedure (using, for example, the sample holder to block the beam), one can also record the integrated beam profile $I_x(x)$ in the x-direction.

Note that we are always integrating over the entire space in the direction perpendicular to the scan (e.g., the x-direction in a $I_z(z)$-scan). Therefore, we can express the measured intensities in terms of the unknown flux profile:

$$\begin{aligned} I_x(x) &= \int_{z'=-\infty}^{\infty}\int_{x'=x}^{\infty} \Phi_0(x',z')\,dx'\,dz' \overset{(B.2)}{=} \int_{-\infty}^{\infty} \varphi_z(z')\,dz' \cdot \int_{x}^{\infty} \varphi_x(x')\,dx' \\ &= \varphi_z^{tot} \cdot \int_{x}^{\infty} \varphi_x(x')\,dx', \end{aligned} \tag{B.3}$$

where we have defined $\int_{-\infty}^{\infty} \varphi_{z'}(z')\,dz' = \varphi_z^{tot}$ and used the assumption of separability from Equation B.2. Similarly, we have

$$I_z(z) = \varphi_x^{tot} \cdot \int_{z}^{\infty} \varphi_z(z')\,dz'.$$

To obtain the total incident intensity, we integrate the flux in the entire x-z-plane:

$$I_0 = \int_{z'=-\infty}^{\infty}\int_{x'=-\infty}^{\infty} \Phi_0(x,z)\,dx\,dz = \int_{-\infty}^{\infty} \varphi_z(z)\,dz \cdot \int_{-\infty}^{\infty} \varphi_x(x)\,dx = \varphi_z^{tot} \cdot \varphi_x^{tot}. \tag{B.4}$$

Now we use the following relations for a given function $f(a)$ and its primitive function $F(a)$:

$$\begin{aligned} \int_{b}^{\infty} f(a)\,da &= [F(a)]_b^{\infty} = F(\infty) - F(b), \\ \frac{\partial F(a)}{\partial a} &= f(a), \\ \frac{\partial F(\infty)}{\partial a} &= \frac{\partial F(const)}{\partial a} = \frac{\partial\, const}{\partial a} = 0. \end{aligned}$$

Thus, the derivatives of $I_z(z)$ and $I_x(x)$, can be written as

$$\begin{aligned} \frac{\partial I_z(z)}{\partial z} &= \frac{\partial}{\partial z}\left[\varphi_x^{tot} \cdot \int_{z}^{\infty} \varphi_z(z')\,dz'\right] = \varphi_x^{tot} \cdot \frac{\partial}{\partial z}\left[F_{\varphi_z}(\infty) - F_{\varphi_z}(z)\right] \\ &= -\varphi_x^{tot} \cdot \varphi_z(z), \end{aligned} \tag{B.5}$$

$$\frac{\partial I_x(x)}{\partial x} = -\varphi_z^{tot} \cdot \varphi_x(x), \tag{B.6}$$

where F_{φ_z} denotes the (unknown) primitive function of φ_z. Multiplying (B.5) with (B.6) and solving for $\Phi_0(x,z)$ yields the desired expression for $\Phi_0(x,z)$:

$$\begin{aligned} \frac{\partial I_x(x)}{\partial x} \cdot \frac{\partial I_z(z)}{\partial z} &= \varphi_z^{tot} \cdot \varphi_x(x) \cdot \varphi_x^{tot} \cdot \varphi_z(z) = I_0 \cdot \Phi_0(x,z) \\ \Longrightarrow \quad \Phi_0(x,z) &= \frac{\frac{\partial I_x(x)}{\partial x} \cdot \frac{\partial I_z(z)}{\partial z}}{I_0}. \end{aligned} \tag{B.7}$$

$\Phi_0(x,z)$ depends only on $I_x(x)$ and $I_z(z)$, and I_0, which are all contained in the measured beam profiles.

B.5 Measuring the integrated intensity

In deriving Equation A.77, we have made one assumption which needs to be discussed in more detail, as also mentioned in Section A.5.4. The derivation was based on (a) the fact that the entire diffraction signal produced by the CTR, as it intersects the Ewald sphere, is fully captured by the detector (open slit geometry), and (b) that the structure factor $F_{\text{tot}}(\mathbf{q})$ can be approximated by a constant F_{HKl} over the full extent of the captured signal.

Figure B.3 illustrates that these assumptions cannot be fulfilled for signals with a very small outgoing angle β_{out}. This is due to the fact that the intersection angle between the rod and the Ewald sphere becomes very small, resulting in a sampling region s of the CTR over an extended range of l-values. This has consequences with respect to both assumptions: (a) may not be fulfilled anymore, because the signal becomes so large that it starts spilling over the edges of the detector aperture. Approximation (b) also fails, since the range of sampled l-values is so large that the variations in the structure factor can no longer be ignored. Which of the two requirements fails first depends on various factors related to the crystal quality of the sample and the properties of the incoming x-ray beam. Consider, for example, a substrate with a film of several monolayers thickness grown on top. The Laue oscillations produced by the finite thickness of the film need to be resolved experimentally in order to solve the structure. Hence, one period of these oscillations needs to be sampled with at least a few independent data points, for each of which the structure factor $F_{\text{tot}}(\mathbf{q})$ needs to be sufficiently constant to yield a meaningful experimental value. This sets a lower limit for the required l-resolution for the data acquisition, and therefore determines the minimum outgoing angle compatible with data collection in the open-slit geometry.

Vlieg has derived an analytical expression to estimate the minimum outgoing angle β_{out} required to achieve a given resolution Δl along the l-direction [1]. Given the full-width at half-maximum (FWHM) of the CTR in the in-plane direction, ΔQ_{FWHM}, measured in reciprocal Angstroms, the valid range of β_{out} is defined through

$$\tan\beta_{\text{out}} \geqslant \frac{2\Delta Q_{\text{FWHM}}}{a_3^*\Delta l}. \tag{B.8}$$

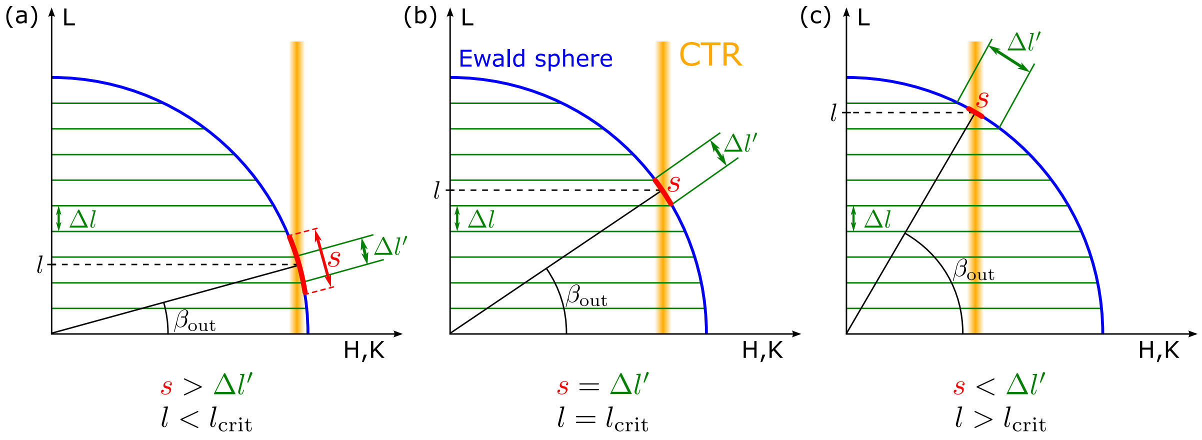

Figure B.3: The open slit geometry can only be used when the range of sampled l-values by the intersection of the CTR with the Ewald sphere, denoted by s, is smaller than the desired resolution Δl along the l-direction, determining a minimum outgoing angle β_{out} and a corresponding minimum l-value l_{crit} necessary for these measurements. The situation is shown for (a) $l < l_{\mathrm{crit}}$, (b) $l = l_{\mathrm{crit}}$, (c) $l > l_{\mathrm{crit}}$.

The open slit geometry can therefore only be successfully used above a critical l-value l_{crit}. Below this value, the CTR data has to be recorded by performing rocking scans of the sample with a fixed detector position.

B.5.1 Rod scans in the open slit geometry

Data collection in the open slit geometry is straightforward. The diffractometer controls software SPEC® calculates the motor positions for the desired (HKl) positions (see Appendix E) and for each point in the scan, a detector image is taken. During the course of this thesis, the CTR data acquisition with the PILATUS 100k pixel detector has been completely automatized, such that exposure times and filter transmission values are dynamically adjusted for each exposure, optimizing the acquisition process both for speed and for a maximization of the collected signals within the dynamic range of the detector. This allows for the routine acquisition of the large SXRD data sets necessary for direct methods structure determinations.

B.5.2 Rocking scans

For l-values below l_{crit}, the data need to be recorded by performing rocking scans of the sample at a fixed detector position, which corresponds to the nominal (HKl) position to be measured.

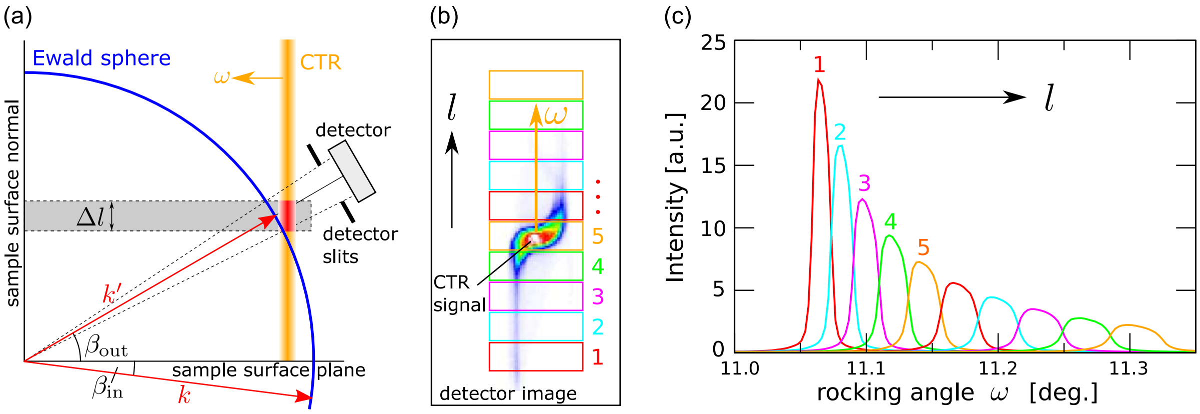

Figure B.4: Obtaining multiple rocking curves from one rocking scan using the PILATUS 100k pixel detector. (a) By using a pair of detector slits, a range of l-values visible to the stationary detector is selected (gray shaded region). While the CTR passes through the Ewald sphere in the ω-scan, the entire scattering of the CTR within the range Δl is integrated (red shaded portion of the CTR). (b) When using an area detector, the physical detector slits can be replaced by "virtual slits" by selecting only a certain region of interest (ROI) on the detector image. This is shown here for one particular image in the scan, but the same ROI must be used for all scan images. Defining several ROIs simultaneously yields multiple rocking curves from one single ω-scan, as shown by the differently colored boxes in (b) and the corresponding rocking curves in (c).

While the sample is rotated around its surface normal direction, the intersection point of the CTR with the Ewald sphere changes, moving either up or down the rod. By using a set of slits in front of the detector, a specific l-range Δl is selected[2], and the detector integrates the entire CTR signal passing through that range during the scan [1], as shown in Figure B.4 (a).

Also here, the peripheral vision of the PILATUS detector is of great advantage over a point detector. Firstly, any spurious diffraction features can be easily identified. More importantly, however, instead of using a physical slit pair, the slitting can be done digitally in the images by selecting different regions of interest on the pixel detector images. In this way, a whole series of rocking curves can be acquired in a single rocking scan, as shown in Figure B.4.

How the integrated CTR intensity from these rocking scans can be obtained and converted to a measure of the structure factor has been described in the literature [1]. Due to the

---

[2] Note that the resolution of the diffraction pattern is also affected by the size of the scattering source, which can be significantly extended in SXRD due to a large footprint of the incidence beam on the sample. To guarantee a sufficient resolution in l, it may therefore be necessary to restrict the size of the source visible to the detector by a second set of slits close to the sample.

different volume of reciprocal space sampled with respect to an image obtained in the open slit geometry, the Jacobian determinant, expressing the change in integration volume from angular to reciprocal space integration variables, will certainly be different.

Bibliography

[1] E. Vlieg: "Integrated Intensities Using a Six-Circle Surface X-ray Diffractometer." *J. Appl. Crystallogr.* **30**(5), 532 – 543 (1997), doi:10.1107/S0021889897002537.

Appendix C

SXRD Data Treatment Step-by-Step

C.1 Introduction

Some technical aspects of acquiring SXRD data, especially with regard to using a PILATUS 100k pixel detector, have been discussed in the previous appendix. Here, we shall be concerned with the question of how the acquired detector images should be interpreted, and what processing steps are required to convert the collected counts from individual pixels into a meaningful measure of diffraction intensities. The ultimate goal is to relate the measured intensities to those calculated by diffraction theory, as detailed comprehensively in Appendix A.

Many of the steps described here are generally valid for x-ray diffraction experiments, while others are quite specific to SXRD. The use of a PILATUS 100k pixel detector instead of the traditionally used point detectors has made necessary a modification of some procedures, and requires important additional analysis steps (e.g., flat-field analysis), while dispensing with others (e.g., the necessity for rocking scans). Since area detectors have so far been used only scarcely in SXRD, a comprehensive report of the necessary data processing steps is, at best, only partially available in the literature [1]. The aim of the current chapter is therefore to give an extensive account of all analysis steps applied to the data presented in this work, in the hope that it may serve as a useful reference for others working with the same experimental setup or as a conceptual starting point for applying those modifications necessary to adapt the procedures to similar experiments elsewhere.

C.2 Rate correction

For single-photon counting devices, the process of registering any one count event takes a finite amount of time. During this time span, the detector is unable to detect any further events. Physically, this is related to the electrical pulse shape created by the incoming X-ray. If two consecutive X-rays pulses overlap, the electronics are unable to discriminate them and will count them as one photon. We define the dead time τ of the detector as the minimum time delay between two impinging photons necessary to distinguish them as two separate events.

Owing to this finite dead time, the detector response becomes nonlinear as the rate of incident photons increases and their average separation in time approaches the dead time τ. The number of measured counts N_{meas} then becomes lower than the real number of incident photons N_0, as shown in Figure C.1. Using the model of a paralyzable counter, this behavior can be modeled, with only the dead time τ as a free parameter [2]:

$$N_{\text{meas}} = N_0 \cdot e^{-N_0 \tau}. \tag{C.1}$$

The dead time τ is a function of the detector's gain and trim energy settings as well as of the incident photon energy. The values for some standardized settings have been accurately determined [2] and are given in Table C.1.

Setting (see [3])	dead time τ [ns]	max. count rate N_{meas} [ph/s/pixel]	max. incident rate N_0 [ph/s/pixel]	1% nonlinearity rate [ph/s/pixel]
Low Gain	120.2 ± 3.5	$3.06 \cdot 10^6$	$8.32 \cdot 10^6$	$8.36 \cdot 10^4$
Medium Gain	202.7 ± 4.1	$1.82 \cdot 10^6$	$4.93 \cdot 10^6$	$4.96 \cdot 10^4$
High Gain	383.8 ± 1.4	$0.96 \cdot 10^6$	$2.61 \cdot 10^6$	$2.62 \cdot 10^4$

Table C.1: Dead time, maximum achievable count rate and corresponding maximum incident rate (according to Equation C.1), and calculated 1% nonlinearity rate ($N_{\text{meas}}/N_0 = 0.99$) for three standard gain settings (12.0 keV X-rays, 6.0 keV trim threshold).

Knowing τ, it is now possible to apply a dead time correction to the counts registered in each pixel. According to Equation C.1, N_0 becomes:

$$N_0 = -\tau^{-1} \cdot W(-N_{\text{meas}}\tau), \tag{C.2}$$

where W is the so-called Lambert W-function or omega function, which is the inverse function of

$$f(W) = We^W.$$

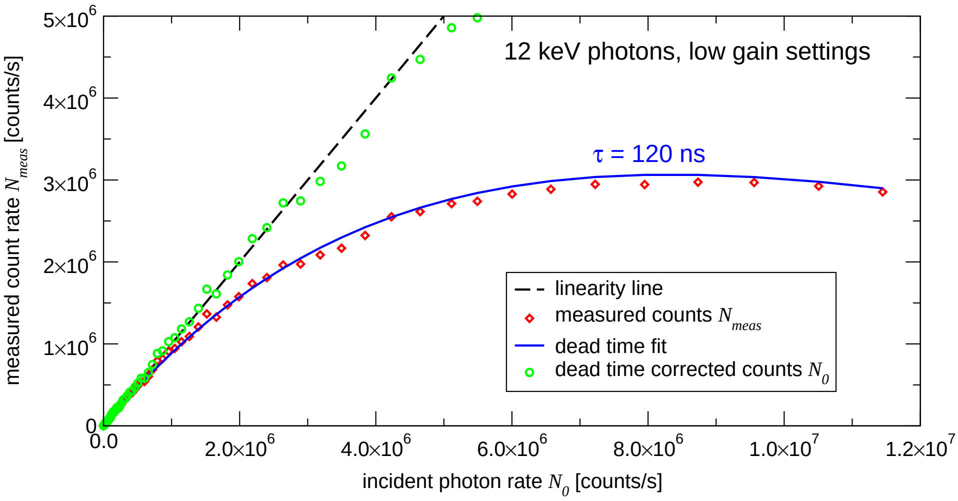

Figure C.1: Rate correction. Measured count rates N_{meas} (red diamonds) are lower than the incident photon rate N_0 (broken line) for high count rates. The blue line is the result of fitting a paralyzable counter model with a dead time of $\tau = 120$ ns to the data, and the appropriately rate-corrected data points are shown as green circles.

The dependence of the dead time on incident photon energy seems to be negligible [2] for reasonable threshold settings. We can therefore use the known values from Table C.1 for all energies without introducing any significant error. Obviously, the rate correction is only significant for high counting rates. The last column in Table C.1 gives the incident photon rate at which the total linearity correction is 1%. The effect of a slightly erroneous dead time can therefore be completely ignored for count rates below this limit.

The dead time correction for the PILATUS detectors is applied internally immediately after data readout by the controls software, and all stored images are already rate corrected. This only requires that the dead time be set up correctly at the start of an experiment.

C.3 Flat-field correction

Individual pixels of the PILATUS detector have slightly different counting efficiencies, due primarily to inhomogeneities in the sensor material, small differences of the pixels supply voltages, etc. Also, heavy irradiation can change their response, either temporarily or permanently. For accurate measurements, it is thus important to calibrate the response of each pixel and to correct the acquired image data for those variations.

A detailed description of how to acquire the data suitable for obtaining a reliable flat-field correction mask has been given in Section B.3. Here we concern ourselves with how this data should be analyzed to get a stable correction file.

There are three important criteria which each pixel must fulfill in order to yield good data:

1. Its counting efficiency should be reasonably close to the mean efficiency of all pixels. What reasonably means will be discussed shortly.
2. The counting process should be stable and reproducible over many exposures.
3. The exact value of the relative efficiency, compared to the mean efficiency of all pixels, should be well determined.

A set of approximately 50–200 flat-field exposures, taken under identical conditions, and with a mean integrated intensity of at least 1000 counts per pixel in each exposure is well suited to evaluate these criteria. The time series allows for stability checks while the integrated signal over the entire series gives good enough statistics for high-quality calibrations. With, for example, an integrated signal over the entire series of 100 000 counts/pixel, we obtain an accuracy of approximately 0.3% for the sensitivity calibration.

Since we want to determine fluctuations between the pixel responses, all potential intensity variations stemming from other sources, such as the beamline optics, the synchrotron top-up mode, or similar, should be minimized wherever possible and recorded with a beam monitor in order to properly divide out their contribution for each image in the time series. If such a monitor is not available, a viable alternative might be to use the average integrated intensity over the entire detector plane as a measure of the incident intensity. Of course, this assumes that the overall response of the detector is stable (as an average over all of the individual pixel responses). But this alternative has the added advantage of monitoring any potential instabilities between the beam monitor and the detector, for example an unstable scattering source used to generate the flat-field illumination.

Each image k in the series of N exposures can be represented as an array $\mathcal{I}_k(i,j)$ of intensities measured by each pixel with coordinates (i,j). In a first step, the mean integrated intensity over

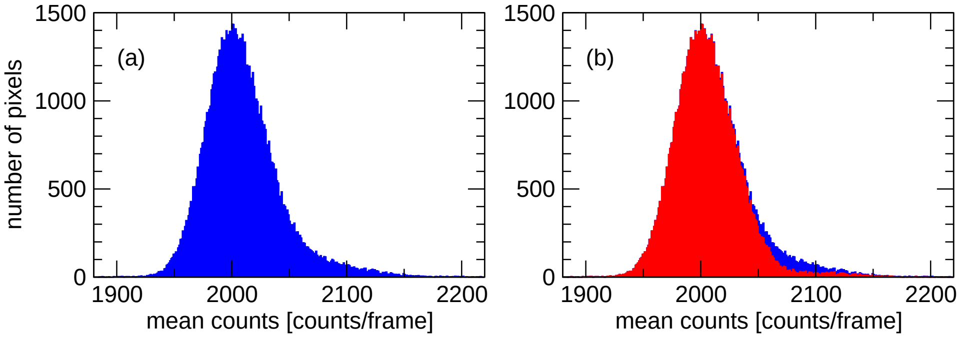

Figure C.2: Histogram of the mean number of counts $\overline{\mathcal{I}}(i,j)$ over N exposures: (a) for all pixels. (b) for normal sized pixels (red) superimposed on the one for all pixels (blue).

the N exposures, $\overline{\mathcal{I}}(i,j)$, and its corresponding standard deviation $\sigma(i,j)$ are calculated:

$$\overline{\mathcal{I}}(i,j) = \frac{1}{N}\sum_{k=0}^{N}\mathcal{I}_k(i,j), \tag{C.3}$$

$$\sigma(i,j) = \sqrt{\frac{1}{N-1}\sum_{k=0}^{N}(\mathcal{I}_k(i,j)-\overline{\mathcal{I}}(i,j))^2}. \tag{C.4}$$

The values $\overline{\mathcal{I}}(i,j)$ can be plotted as a histogram, as shown in Figure C.2 (a). It can be seen that in this example data set, most pixels have registered around 2000 counts on average per exposure. There is a slight tail towards higher count rates which can be attributed to a peculiarity of the PILATUS detectors. As explained in detail in Section D.2, there are some larger pixels on the detector, spanning the gaps between readout chips, which generally have a slightly different counting efficiency due to charge sharing effects and the choice of threshold settings. Panel (b) of Figure C.2 shows the histogram for only regular sized pixels (red) superimposed on the total histogram (blue), proving that the tail is mostly caused by the larger pixels.

Nevertheless, there seems to be a reasonable distribution of pixel sensitivities with few outliers. Analyzing the particular distribution shown here, any pixel counting less than $I_{min} =$ 1900 counts or more than $I_{max} = 2200$ counts can clearly be said to behave very differently from the rest. Generally, the pixels outside such lower and higher limits (I_{min}, I_{max}) should be deemed unreliable and added to a black list. This is done by setting the value of a binary mask array $\mathcal{M}_h(i,j)$, having the same size as $\overline{\mathcal{I}}(i,j)$, from unity to zero for all unreliable pixels (the subscript h denotes the fact that the mask is based on the histogram):

$$\mathcal{M}_h(i,j) = \begin{cases} 1 & \text{if } I_{min} \leqslant \overline{\mathcal{I}}(i,j) \leqslant I_{max} \\ 0 & \text{otherwise.} \end{cases} \tag{C.5}$$

After identifying pixels with an anomalous response in their average efficiency, we now need to find those pixels suffering from instabilities in their counting process. They can be identified by a large scatter in the number of recorded photons between different exposures when compared to the expected variations based on counting statistics, i.e., when

$$\sigma(i,j) \gg \sqrt{\overline{\mathcal{I}}(i,j)}. \tag{C.6}$$

We now need a method of filtering out pixels with a large scatter and add them to a second binary mask $\mathcal{M}_s(i,j)$. The simplest way is to require that the measured standard deviation does not exceed the theoretically expected one by more than a certain factor:

$$\mathcal{M}_s(i,j) = \begin{cases} 0 & \text{if } \sigma(i,j) > K \cdot \sqrt{\overline{\mathcal{I}}(i,j)} \\ 1 & \text{otherwise,} \end{cases} \tag{C.7}$$

where $K > 1$ is a constant which needs to be chosen carefully according to the available counting statistics. Let us define a normalized standard deviation $\sigma_n(i,j)$ in the following manner:

$$\sigma_n(i,j) = \sigma(i,j) \Big/ \sqrt{\overline{\mathcal{I}}(i,j)}\ . \tag{C.8}$$

Figure C.3 shows a histogram of $\sigma_n(i,j)$ for our sample data set. The main feature of the distribution is centered slightly above one, proving the counting process of most pixels is close to being Poisson-limited. The width of the distribution is due to the finite sampling statistics of N exposures. A second feature centered far below unity is clearly suspicious, suggesting a counting stability better than the theoretical limit. Again, this feature is related to the gap-spanning larger pixels between readout chips. As a result of their increased area, they have a better counting statistics than the normal pixels. Section D.2 describes in detail how this effect can be taken into account and gives the corrected histogram.

If we fit the main feature to a Gaussian distribution, we obtain a center position of $x_c = 1.021$ and a width of $\sigma_g = 0.103$. Given the total number of pixels of close to 100'000, no more than 7 pixels should yield values of σ_n more than $4\sigma_g$ away from the center x_c (99.994% fall within a

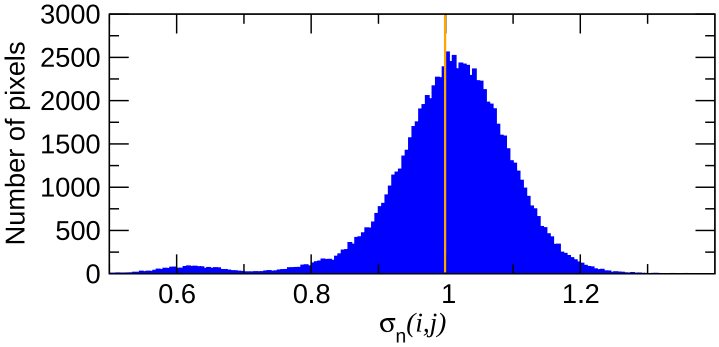

Figure C.3: Histogram of the measured flat-field's standard deviation normalized with the expectation value for a purely poisson limited counting process. The seemingly unreasonable feature at a value slightly above 0.6 is discussed in the text.

confidence interval of $4\sigma_g$). For a $3\sigma_g$ interval, this increases to 256 pixels on average (99.73% within). Therefore, a value of $K = x_c + 4\sigma_g$ in Equation C.7 should ensure that no significant number of reliable pixels are accidentally eliminated, while efficiently rejecting those pixels with anomalously high scatter.

The combined black lists from the histogram and stability checks give a binary mask identifying all unreliable pixels on the detector:

$$\mathcal{M}(i,j) = \mathcal{M}_h(i,j) \times \mathcal{M}_s(i,j). \tag{C.9}$$

Later on, when analyzing measured intensities, these black-listed pixels have to be treated specially (refer to Section C.4.4).

The true efficiency of all pixels is very difficult to determine, and we are only interested in their relative efficiencies with respect to each other in order to flatten out the measured images. These values need to be normalized to a well-defined value, which we will take as the mean integrated number of counts over all reliable pixels in the time-averaged array $\overline{\mathcal{I}}(i,j)$. Since the number of reliable pixels is equal to $\sum_{ij} \mathcal{M}(i,j)$, we obtain

$$\overline{I} = \frac{\sum_{ij} \left(\overline{\mathcal{I}}(i,j) \times \mathcal{M}(i,j)\right)}{\sum_{ij} \mathcal{M}(i,j)}. \tag{C.10}$$

The flat-field correction array can then be computed as

$$\mathcal{F}(i,j) = \frac{\overline{I}}{\overline{\mathcal{I}}(i,j)} \times \mathcal{M}(i,j). \tag{C.11}$$

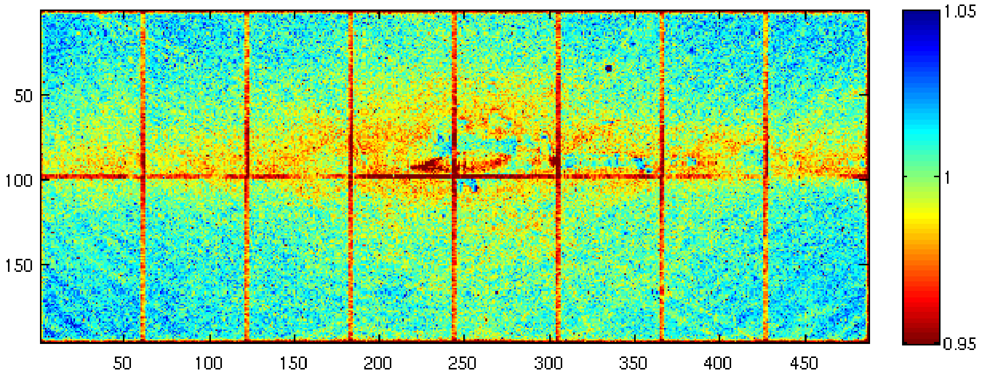

Figure C.4: False color image of a flat-field correction array. The color bar displays the corresponding flat-field correction factors. Red pixels are more sensitive than the average and their values need to be decreased while blue pixels are less sensitive and need to be amplified.

Figure C.4 shows the flat-field correction image for the above example data. Red colored pixels are more sensitive than the average and therefore have correction values smaller than one. The opposite is true for the blue-shaded pixels, which need to be corrected with factors greater than one to compensate for their sensitivities being below average. It should be mentioned that the number of unreliable pixels that need to be masked out, even when using fairly strict stability criteria, is usually below 200 (out of almost 100 000 pixels in total) for our detector.

The uncertainty $\mathcal{U}(i,j)$ of the flat-field correction factor $\mathcal{F}(i,j)$ for each pixel is calculated as the statistical error of its mean value $\overline{\mathcal{I}}(i,j)$:

$$\mathcal{U}(i,j) = \frac{\sqrt{\frac{1}{N(N-1)}\sum_{k=0}^{N}(\mathcal{I}_k(i,j) - \overline{\mathcal{I}}(i,j))^2}}{\overline{\mathcal{I}}(i,j)} = \frac{\sqrt{1/N}\cdot\sigma(i,j)}{\overline{\mathcal{I}}(i,j)}. \tag{C.12}$$

Note that $\mathcal{U}$ is the *relative* error and is therefore unaffected by the renormalization of $\mathcal{F}(i,j)$ to $\overline{I}$. For flat-field measurements where the integrated intensities summed over all frames exceed several ten thousand counts, $\mathcal{U}$ should drop well below the 1% level and therefore has a usually insignificant effect on the accuracy of a flat-field corrected measurement.

C.4 Extracting intensities from images

Extracting meaningful information from a detector image is the most critical and in many cases also the most difficult step in the data analysis. The shape, extent, position, and orientation of a diffraction signal within the image may change considerably between different measurements on the same sample, and even within a single scan. The differences observed between different types of samples are even more striking, some examples of which are shown in Figure C.5.

The main challenge lies in the correct discrimination between the real signal and the background. In many cases, the background is not flat across the image, but contains contributions from several different sources, such as scattering from Beryllium windows or sample holders, a broad thermal diffuse scattering component from the sample itself, air scattering of the scattered beam, etc., which may result in a complicated background distribution. The diffraction signals, on the other hand, may be smeared out themselves, due to crystal mosaicity of the sample, defect scattering, edge effects, a spatial inhomogeneity or large divergence in the incident beam intensity, slight sample curvatures, etc. Many of these factors can be avoided or at least reduced by a careful experimental design and thorough conditioning and alignment of the x-ray beam. Nonetheless, the data quality is intimately linked to the crystallographic perfection of the sample. It can therefore not be overstated how important good sample preparation is.

The minimum criterion for a successful background discrimination is that the entire diffraction signal must be sharper than the smallest features in the background distribution. Only under these circumstances can one hope to predict with sufficient confidence what the background contribution within the signal should be.

The analysis procedure described here relies on region-based image processing. The raw image recorded by the detector is represented by the array $\mathcal{I}_{\text{raw}}(i,j)$, where i and j are the horizontal and vertical pixel indices, respectively. The elements of $\mathcal{I}_{\text{raw}}(i,j)$ are the number of recorded counts after applying the dead-time corrections, rounded to the next integer number (performed by the PILATUS controls software as described in Section C.2).

The experimental uncertainty $m_{\text{raw}}(i,j)$ associated with each element of $\mathcal{I}_{\text{raw}}(i,j)$ is assumed to be entirely due to counting statistics, such that

$$m_{\text{raw}}(i,j) = \sqrt{\mathcal{I}_{\text{raw}}(i,j)}. \tag{C.13}$$

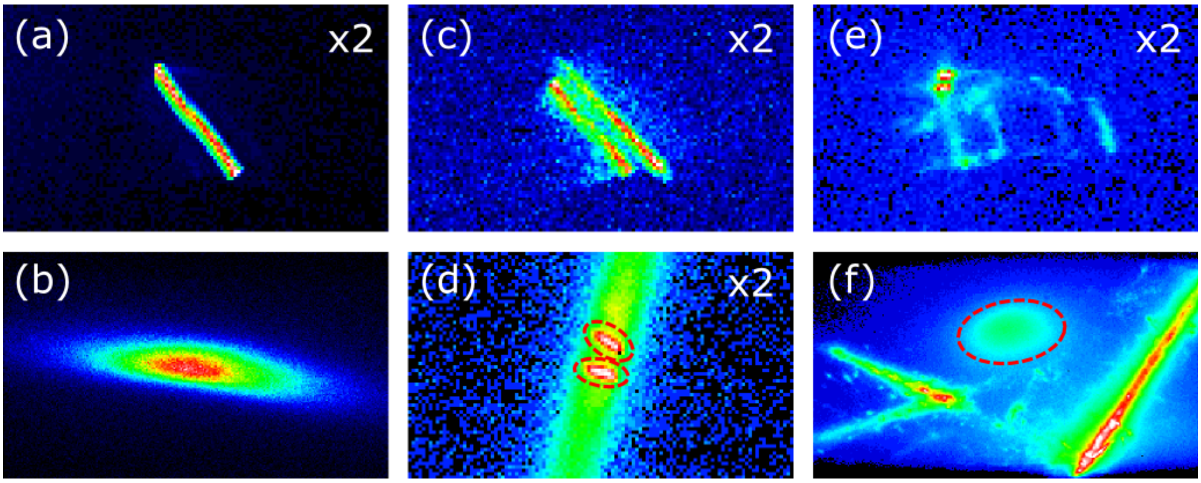

Figure C.5: Some examples of measured diffraction signals, illustrating the difficulties encountered when trying to determine reasonable signal and background ROIs. (a) the clean and sharp CTR signal from a smooth $NdGaO_3$ surface. (b) a very broad CTR of hexagonal boron-nitride (h-BN) on Rh(111); (c) split CTR of $NdGaO_3(110)$ caused by a sample miscut; (d) another split CTR of YBCO on $NdGaO_3(110)$ on top of a strongly anisotropic diffuse background; (e) strange signal shapes for a $LaAlO_3$ surface, caused by twinning and microscopic faceting; (f) spurious signals originating from the sample holder and bulk crystal, surrounding the real signal (marked by the circle) of h-BN on Ru(111). (Those images marked with "×2" are linearly magnified by a factor of two compared to the others.)

The relative uncertainty is then given by

$$r_{\mathrm{raw}}(i,j) = \frac{m_{\mathrm{raw}}(i,j)}{\mathcal{I}_{\mathrm{raw}}(i,j)}. \tag{C.14}$$

C.4.1 Applying the flat-field correction

Before analyzing any features in the image in detail, the flat-field correction should be applied to the raw image data, which is simply done by an element-wise multiplication with the flat-field correction array:

$$\mathcal{I}(i,j) = \mathcal{I}_{\mathrm{raw}}(i,j) \times \mathcal{F}(i,j). \tag{C.15}$$

The associated experimental uncertainty needs to be propagated accordingly for the scaling operation and by including the uncertainty of the flat-field correction array itself. For the relative error, we obtain

$$r(i,j) = r_{\mathrm{raw}}(i,j) + \mathcal{U}(i,j), \tag{C.16}$$

where $\mathcal{U}(i,j)$ is the relative error of the flat-field correction as defined in Equation C.12. This leads to an absolute uncertainty of

$$m(i,j) = r(i,j) \times \mathcal{I}(i,j) \tag{C.17}$$

for the flat-field corrected intensities. Remember that those pixels which have been masked out in the flat-field analysis will contain zeros both for $\mathcal{I}(i,j)$ and $m(i,j)$.

C.4.2 Selecting the regions of interest

First, a region of interest (ROI) containing the diffraction signal (hereafter referred to as "signal ROI") needs to be selected such that it encloses the signal as tightly as possible without cutting into it. This ROI is represented as a binary mask $\mathcal{R}_S(i,j)$, containing ones for all pixels belonging to the signal and zeros otherwise. The set of pixels, identified through their index-pairs (i,j), belonging to the signal ROI are defined as

$$\mathbb{S} \equiv \{(i,j) \text{ with } \mathcal{R}_S(i,j) = 1\}\,.$$

For a shorthand notation, the subset of data points belonging to $\mathbb{S}$ will be denoted by

$$\mathcal{I}_S(i,j) \equiv \mathcal{I}(i,j) \text{ with } (i,j) \in \mathbb{S}.$$

The selection of the signal ROI itself has been seen to be quite ambiguous in many cases, and as such represents one of the predominant sources for errors in the final data sets. Naturally, there is an element of subjectivity in this choice, which has to be made by the experimentalist. In most cases, this leads to systematic errors in the data sets, since the criteria employed to make the selection are likely to be consistent throughout the data set, but not necessarily correct (where the "correct" ones are, unfortunately, not known *a priori*). As to how severely these systematic errors affect the quality of the final structure solution depends on the system under investigation and the desired results. However, it is clear that this is a severe weakness of the method, and a point which one should keep in mind during the intensity extraction and later on when interpreting the data. To date, we have not succeeded in formulating an algorithm capable of reliably identifying the correct signal ROI automatically and based on a set of well-defined criteria, mainly due to the vast diversity of observed diffraction features. It is expected, though, that this may become feasible for a much improved experimental setup based on a well-focussed undulator x-ray beam, which will in any case much facilitate the data reduction.

It is worth to point out that this problem is not new in principle, and that point detector scans almost certainly suffer from the same problem much more severely. The only difference is that the peripheral vision of area detectors can often help identifying such difficulties where they may go unnoticed in other cases. In other words, with the power of advanced detectors comes a responsibility to examine the results much more carefully in order to tap the full potential for improvements.

When choosing an appropriate ROI for the determination of the scattering background, one is faced with similar problems as for the signal ROI. The background ROI should be sufficiently large to allow for a stable background determination, and ideally contain the entire signal ROI within it. Roughly speaking, at least the smallest feature sizes of the background distribution have to be captured in order to model them correctly. On the other hand, the background ROI should not be unnecessarily large, as this reduces the weight of those data points in close proximity to the signal, which are, of course, those containing the most accurate information about the locally applied interpolation. It should be stressed that we are not interested in finding a global model for the background distribution, but merely a local approximation which is accurate enough to provide a stable interpolation throughout the signal ROI. Again, the background ROI is described by a binary mask, $\mathcal{R}_B(i,j)$. Analogous to the case of the signal ROI, we define the set of pixels belonging to the background ROI as

$$\mathbb{B} \equiv \{(i,j) \text{ with } \mathcal{R}_B(i,j) = 1\}\,,$$

and those data points within $\mathbb{B}$ are denoted by $\mathcal{I}_B(i,j)$

$$\mathcal{I}_B(i,j) \equiv \mathcal{I}(i,j) \text{ with } (i,j) \in \mathbb{B}.$$

Note that those points belonging to the signal ROI cannot be part of the background ROI (meaning that their intersection set is empty: $\mathbb{S} \cap \mathbb{B} = \emptyset$).

Some examples of ROI selections are shown in Figure C.6. These represent some fairly clear-cut cases, however, much in contrast to some of the signals shown in Figure C.5.

C.4.3 Fitting a background shape

Once a background ROI has been set, the distribution of counts within needs to be modeled. In principle, any smooth function $f_B = f(i,j)$ of the two variables i and j can be used, as long as all of its parameters can be sufficiently well determined, based on the set of available data points within the background ROI. In practice, the use of a constant or linear background seems to be sufficient in many cases, whereas the combination of a Gaussian distribution on top of a constant or linear background or alternatively the use of a low-order 2-dimensional polynomial distribution nearly always provides satisfactory results for more complicated shapes. This is normally the case for those points close to the Bragg peaks, where significant thermal diffuse scattering from the bulk has to be taken into account. Using more complex functions, such as combinations of several Gaussians or higher-order polynomials, often leads to unstable fit results or produces spurious features within the signal region, which needs to be interpolated. Figure C.6 shows a few examples of successful background fits.

We have chosen to use a reduced χ^2-function to perform the fit of f_B to the set of data points within the background ROI, $\mathcal{I}_B(i,j)$, which is given by

$$\chi^2(\mathcal{I}_B) = \frac{1}{N-P} \sum_{(i,j)\in\mathbb{B}} \frac{\left(\mathcal{I}_B(i,j) - f_B(i,j)\right)^2}{\sigma'(i,j)^2}, \tag{C.18}$$

where the sum runs over all $N = \sum_{i,j} \mathcal{R}_B(i,j)$ data points[1] contained in $\mathbb{B}$, P gives the number of free parameters of f_B, and $\sigma'(i,j)$ stands for a weight factor associated with the points in $\mathcal{I}_B(i,j)$. Usually, the experimental uncertainties of the intensity measurements are used as weight factors. However, in order to avoid divisions by zero and to reduce the weight of very low-intensity points in relation to those of high intensity, we artificially increase those weight factors by adding a constant term K to the experimental errors:

$$\sigma'(i,j) = m(i,j) + K. \tag{C.19}$$

Empirically, it has been found that very modest values of K give good results, so we chose to use $K = 5$ for our analyses.

After the χ^2-optimization, the function f_B represents the best estimate to the background distribution. Evaluating f_B for all indices i and j in the measured image produces an array

---

[1] Some pixels might have been deemed unreliable in the flat-field analysis and are correspondingly masked out in the flat-field mask $\mathcal{M}_{\text{ff}}(i,j)$. These pixels are not considered to be part of $\mathbb{B}$ and do not enter the background calculation.

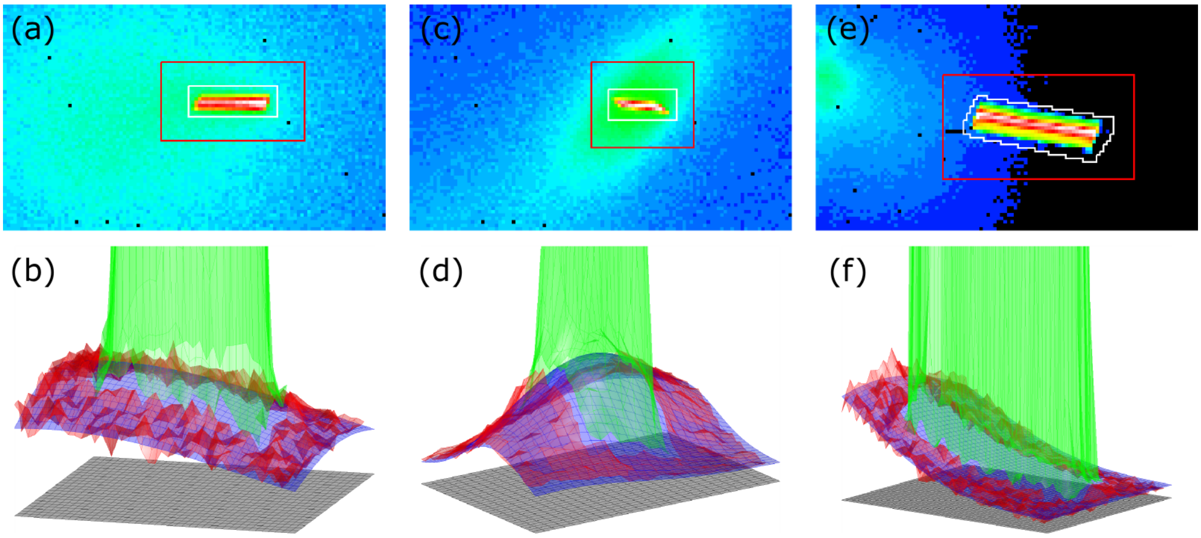

Figure C.6: Examples of ROI selections and background fitting. The top row shows the detector images with the choice of signal (white) and background (red) ROIs: (a) CTR of YBCO on LSAT far away from Bragg peaks. (c) The same CTR close to a Bragg peak of the YBCO film, giving rise to an additional diffuse component on top of the normal background. (e) Signal of an $NdGaO_3$ surface CTR on top of the diffuse scattering from a bulk Bragg peak. Some pixels appear in black since they have been masked out in the flat-field analysis.
The corresponding background fits are shown in the bottom row with signal (green), measured background (red), fitted background shape (blue) and zero-plane (black) surface plots. The fit functions used were a 2D Gauss in (b) and a 2D Gauss + constant term in (d) & (f). The vertical scale has been greatly expanded in order to show the topologies of the background signals and their fits.

$\mathcal{B}(i,j)$ of equal size, containing the estimates for each pixel. Note, however, that those values of the background array not belonging to $\mathbb{B}$ or $\mathbb{S}$ are rather meaningless and of no importance to the problem at hand. The only thing we are interested in is the subset $\mathcal{B}_S(i,j)$ of the background array, which contains the estimates for those data points lying within the signal ROI:

$$\mathcal{B}_S(i,j) \equiv \mathcal{B}(i,j) \text{ with } (i,j) \in \mathbb{S}.$$

Finding a good estimate of the error associated with the background fit turns out to be a bit trickier. For now, let us assume we had used the experimental errors as the weight factors σ' in Equation C.18, in other words used $K = 0$. The errors were assumed to follow a normal distribution, since they arise from a Poisson-limited counting process. The inclusion of the flat-field error results in somewhat larger values of σ', but does not change the nature of the normal distribution. Under these circumstances, the value of χ^2 gives the mean deviation of the fit from the data, measured in units of σ', which is therefore equal to

$$m_B(i,j) = \chi^2 \times \sigma'(i,j) = \chi^2 \times m(i,j) \qquad \forall (i,j) \in \mathbb{B}. \tag{C.20}$$

Clearly, this statement is only valid for those points within the background ROI $\mathbb{B}$. For those pixels within $\mathbb{S}$, we do not have any measured values for the background contribution – after all that is what we are trying to calculate – so we do not know the errors associated with that contribution (the only thing we do know is the total error $m(i,j)$ of the sum of the real signal with the background). Therefore, we need to estimate what those errors would be if it had been possible to measure the background directly. We have already predicted the background itself through f_B to be equal to $\mathcal{B}_S(i,j)$. Making the same assumption of pure counting statistics, we set the hypothetical counting error to

$$m'(i,j) = \sqrt{\mathcal{B}_S(i,j)} \qquad \forall (i,j) \in \mathbb{S}. \tag{C.21}$$

Including also the flat-field uncertainty yields

$$m'(i,j) = \sqrt{\mathcal{B}_S(i,j)} + \mathcal{U}(i,j) \times \mathcal{B}_S(i,j) \qquad \forall (i,j) \in \mathbb{S}. \tag{C.22}$$

Analogous to Equation C.20, the expected error for the background fit function for each pixel inside $\mathbb{S}$ is therefore

$$m_B(i,j) = \chi^2 \times m'(i,j) \qquad \forall (i,j) \in \mathbb{S}. \tag{C.23}$$

Getting back to the case of $K \neq 0$ in Equation C.19, we see that certainly the normal error distribution cannot be described through a standard deviation with the modified σ' anymore. Strictly speaking, this invalidates the assumptions that lead the above conclusions. For small values of K, however, the inaccuracies introduced are very modest. In this case, the final error estimate becomes

$$m_B(i,j) = \chi^2 \times \left(\sqrt{\mathcal{B}_S(i,j)} + \mathcal{U}(i,j) \times \mathcal{B}_S(i,j) + K\right) \qquad \forall (i,j) \in \mathbb{S}. \tag{C.24}$$

C.4.4 Handling missing pixel values

As mentioned in Section C.3, when analyzing the flat-field array, some pixels may have been deemed unreliable and masked out. Such "missing" values pose a serious problem when integrating the signal intensities, as they are effectively blind holes in the detector area, thus reducing the measured intensity value with respect to the real one. In order to obtain the correct intensities, those holes need to be filled in.

Ideally, the distribution of the measured signal surrounding the hole should be modeled as precisely as possible to perform an accurate interpolation of the missing value. In practice, this is far too complicated, time consuming, and prone to instabilities when automatized. A straightforward approach is to assume "local linearity" and set the missing value to the mean of its $n \times n$ surrounding pixels ($n = 3, 5, 7, \ldots$). A small value of n should be used to preserve this local aspect of the replacement. A slightly less accurate approach, but one which is much less sensitive to outliers than using the mean value instead, is the use of the median. In either case, this approach fails for very sharp diffraction features restricted to very few pixels, where the value in each pixel contains a "unique" piece of information.

In our measurements, the signals are typically spread out over several tens of pixels, such that using the median from a 3×3 kernel produces good results and is fast and easy to calculate. The error of that data point is taken to be the standard deviation of the eight surrounding pixels.

C.4.5 Calculating the intensity and statistical error

The next step is to calculate the background-subtracted intensity I contained in the signal ROI by summing up the contributions from all pixels:

$$I = \sum_{(i,j)\in\mathbb{S}} \mathcal{I}_S(i,j) - \mathcal{B}_S(i,j) \tag{C.25}$$

The error associated with this intensity is essentially statistical in nature, even though some of the steps described above, e.g. the determination of the background error, do not strictly follow statistical methods. Nevertheless, we will refer to this error as statistical, assume it to be normally distributed, and label it with the conventional symbol σ:

$$\sigma = \sqrt{\sum_{(i,j)\in\mathbb{S}} (m(i,j))^2 + (m_B(i,j))^2}. \tag{C.26}$$

C.5 Direct intensity corrections

The intensity value extracted from the region of interest, as given in Equation C.25, can be directly corrected for the filter transmission values C_T, and the monitor counts C_M collected during the exposure:

$$I_{\mathrm{corr}} = I \cdot \frac{1}{C_T\, C_M}. \tag{C.27}$$

Since the monitor counts are usually collected exactly at the same time as the detector exposure, they implicitly contain a measure for the exposure time. Care has to be taken when the monitor counts are expressed as counts per second, in which case one needs to correct for the actual exposure time t_E separately. The unit of I_{corr} is equal to

$$[I_{\mathrm{corr}}] = \left[\frac{\text{integrated signal counts } / \ t_E \text{ seconds}}{\text{monitor counts } / \ t_E \text{ seconds}}\right].$$

As we will see later, the monitor normalization, resulting in somewhat arbitrary values, drops out again when renormalizing the diffraction intensities to the incident beam intensity I_0, which is measured in the same units.

Naturally, the values of C_T and C_M also have an uncertainty associated with them, which we will denote by m_T and m_M. While the fluctuations in the monitor counts may be regarded as statistical in most cases, this cannot be justified anymore when considering the filter transmission values. Each filter has given thickness and hence a well-defined transmission factor, but is known only up to a certain accuracy. Therefore, each time a filter is used, it will produce the identical offset in the measurement, hence resulting in a systematic error. It is not evident how this case should be handled, and the best approach may be to actually calibrate the filters to a precision better than the expected statistical fluctuations or the desired experimental accuracy. The filter transmissions in our experimental setup have been carefully determined to an uncertainty well below 1% of their transmission values. Even if using n filters at once, the total uncertainty is expected to be of the order of $\sqrt{n}$ times the individual error. This typically amounts to well below 3% in the total error, much lower than the other typical systematic errors in our data (see section C.9).

If simply disregarding those additional sources of errors, the statistical uncertainty of the intensity needs to be scaled by the same factor as I itself:

$$\sigma_{\mathrm{corr}} = \sigma \cdot \frac{1}{C_T\, C_M}. \tag{C.28}$$

Including the supposedly statistical contribution from the monitor counts, the relative errors of I and C_M need to be added to yield

$$\sigma_{\text{corr}} = I_{\text{corr}} \cdot \left(\frac{\sigma}{I} + \frac{m_M}{C_M} \right). \tag{C.29}$$

Nevertheless, it may be useful to also include the systematical error of the filter calibration in order to get a realistic estimate of the total error to be expected from the measurements:

$$\sigma_{\text{corr}} = I_{\text{corr}} \cdot \left(\frac{\sigma}{I} + \frac{m_M}{C_M} + \frac{m_T}{C_T} \right). \tag{C.30}$$

C.6 Numerical flux integration over the sample surface

In Section B.4, we have seen how the incident beam flux profile $\Phi_0(x, z)$ can be measured through two perpendicular knife-edge scans. Now, we will demonstrate how to perform the flux integration over the sample surface S numerically; that is, we want to calculate

$$\int_S \Phi_0(x, z)\, dx\, dz. \tag{C.31}$$

In terms of the two integrated linear beam profiles along the transverse beam directions, $I_x(x)$ and $I_z(z)$, from the knife-edge scans, the flux was shown to be equal to (see Equation B.7)

$$\Phi_0(x, z) = \frac{\frac{\partial I_x(x)}{\partial x} \cdot \frac{\partial I_z(z)}{\partial z}}{I_0} = \frac{i_x(x) \cdot i_z(z)}{I_0}, \tag{C.32}$$

with I_0 being the integrated incoming flux, and where we have introduced the following notation for simplicity:

$$\frac{\partial I_x(x)}{\partial x} \equiv i_x(x), \qquad \frac{\partial I_z(z)}{\partial z} \equiv i_z(z). \tag{C.33}$$

First, we have to calculate $i_x(x)$, $i_z(z)$, and I_0, then carry out the integration. This procedure is explained step-by-step in the next few paragraphs.

C.6.1 Beam profile analysis

To start with, the intensities of the two knife-edge scans need to be extracted according to the procedure described earlier. Background subtraction should not be an issue for these scans,

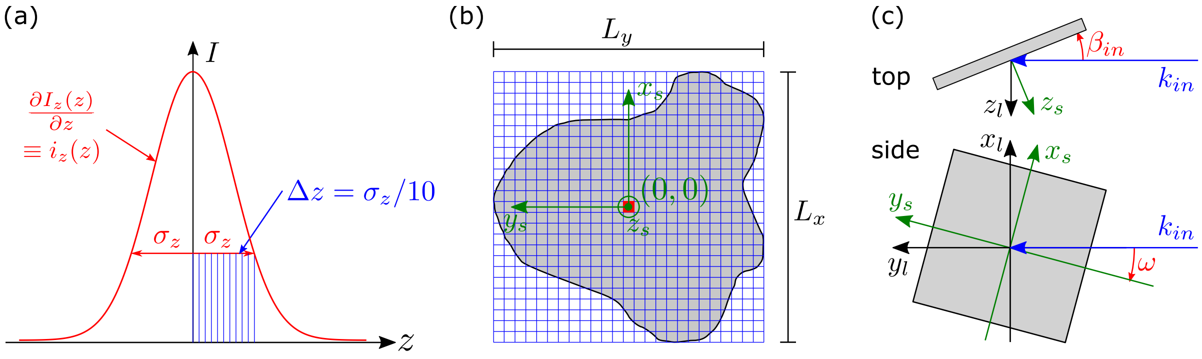

Figure C.7: (a) Determination of the sample grid spacing Δz, based on the variance σ_z of the corresponding linear flux profile $i_z(z)$. (b) Construction of a sampling grid covering an irregularly shaped sample with maximal extensions of L_x, L_y in the sample's x and y directions. (c) Definition of the sample's azimuthal (ω) and glancing (β_{in}) rotation angles with respect to the laboratory frame of reference.

since the diffuse scattering around the very intense direct beam is so weak in comparison, that its contribution to the total collected intensity is completely negligible. Rate corrections, on the other hand, can become significant if the scan was taken close to the upper limit of the dynamic detector range.

The derivatives of $I_x(x)$ and $I_z(z)$ are calculated numerically. Depending on the scan's sampling densities along the positional coordinate, a smoothing operation may be necessary to yield reasonable profiles $i_x(x)$ and $i_z(z)$.

The value of I_0 can be obtained by re-integrating $i_x(x)$ or $i_z(z)$. The two results should, of course, be consistent with each other and yield the same value as the intensity extracted from those images in the scans, where the direct beam is completely unoccluded.

C.6.2 Defining the integration grid

To begin the numerical integration, an integration grid has to be defined. Care has to be taken to make the grid fine enough to yield a sufficiently accurate result while avoiding excessive computational effort due to large arrays. Empirically, it has been found that a grid resolution Δx and Δz equal to one tenth of the variance of the narrower of the two beam profiles, as shown in Figure C.7 (a), is adequate in most cases:

$$\sigma_x = \mathrm{var}\left(\frac{\partial I_x(x)}{\partial x}\right), \quad \sigma_z = \mathrm{var}\left(\frac{\partial I_z(z)}{\partial z}\right),$$
$$\Delta x = \Delta z = \frac{\min(\sigma_x, \sigma_z)}{10}. \tag{C.34}$$

Using the resulting grid spacing, we now construct a 2-D rectangular grid which is big enough to accommodate the entire sample. In the case of non-rectangular samples, as shown in Figure C.7 (b), the grid will be as big as the enclosing box of the sample shape. How the particular shape of the sample is taken into account in the calculation will be described later on (see Section C.6.5). Each grid point P can be referenced by two linear indices i and j, along the x_s and y_s directions, respectively, and will be denoted as P_{ij}.

C.6.3 Grid point coordinate transformation

In the next step, we need to find out the coordinates (x_{ij}, z_{ij}) of each grid point relative to the measured flux profile (which is defined in the laboratory frame of reference). Starting in the sample frame of reference (denoted with a subscript s, e.g., x_s), we know that the middle point of the sample surface should be aligned with the diffractometer rotation axes, and represents the zero point of that coordinate system. Hence, we can assign the proper $x_{ij,s}$ and $y_{ij,s}$ coordinates to each grid point, since we know the grid steps and the sample dimensions. These positions now need to be transformed into the laboratory frame of reference (denoted with a subscript l, e.g. x_l). For zero azimuthal (ω) and incidence (β_{in}) angles, shown in Figure C.7 (c), the sample frame of reference coincides with with the laboratory coordinate system. For non-zero angles, the following rotation transformations need to be applied:

1. An azimuthal sample rotation by ω around the z_s axis:

$$\Omega = \begin{pmatrix} \cos\omega & \sin\omega & 0 \\ -\sin\omega & \cos\omega & 0 \\ 0 & 0 & 1 \end{pmatrix}. \tag{C.35}$$

2. A polar sample rotation around the x_l axis by β_{in}:

$$B = \begin{pmatrix} 1 & 0 & 0 \\ 0 & \cos\beta_{in} & -\sin\beta_{in} \\ 0 & \sin\beta_{in} & \cos\beta_{in} \end{pmatrix}. \tag{C.36}$$

Combining these two rotations yields the desired coordinate transformation:

$$\begin{aligned}\begin{pmatrix} x_l \\ y_l \\ z_l \end{pmatrix}_{ij} &= B \cdot \Omega \cdot \begin{pmatrix} x_s \\ y_s \\ z_s \end{pmatrix}_{ij} \\ &= B \cdot \begin{pmatrix} x_s \cos\omega + y_s \sin\omega \\ -x_s \sin\omega + y_s \cos\omega \\ z_s \end{pmatrix} \\ &= \begin{pmatrix} x_s \cos\omega + y_s \sin\omega \\ (-x_s \sin\omega + y_s \cos\omega)\cos\beta_{in} - z_s \sin\beta_{in} \\ (-x_s \sin\omega + y_s \cos\omega)\sin\beta_{in} + z_s \cos\beta_{in} \end{pmatrix}. \end{aligned} \tag{C.37}$$

Since $z_s = 0$ for all grid points (as they lie on the sample surface), this simplifies to

$$\begin{pmatrix} x_l \\ y_l \\ z_l \end{pmatrix}_{ij} = \begin{pmatrix} x_s \cos\omega + y_s \sin\omega \\ (-x_s \sin\omega + y_s \cos\omega)\cos\beta_{in} \\ (-x_s \sin\omega + y_s \cos\omega)\sin\beta_{in} \end{pmatrix}. \tag{C.38}$$

C.6.4 Interpolating the partial flux profiles

Given these coordinates (x_{ij}, z_{ij}) of each grid point P_{ij} in the laboratory frame of reference, we now need to determine the values of the partial flux profiles at these positions. Generally, however, the sampling positions of the knife-edge scans do not coincide with x_{ij} and z_{ij}, so the values of the linear flux profiles at those positions need to be interpolated to yield $i_x(x_{ij})$ and $i_z(z_{ij})$.

C.6.5 Introducing the sample shape

Introducing arbitrary sample shapes is easily achieved. The grid was constructed as a bounding box of the entire sample area. We can now simply assign a weight factor w_{ij} for each grid point, containing a value of 1 if the grid point lies on the sample surface, and 0 otherwise. In practice, these maps can be obtained, for example, by proper thresholding of an optical light microscope image of the sample, as shown in Figures C.8 (c) and (d). In principle, one could even assign fractional weights $0 < w_{ij} < 1$ for grid points at the edges of the sample which are only

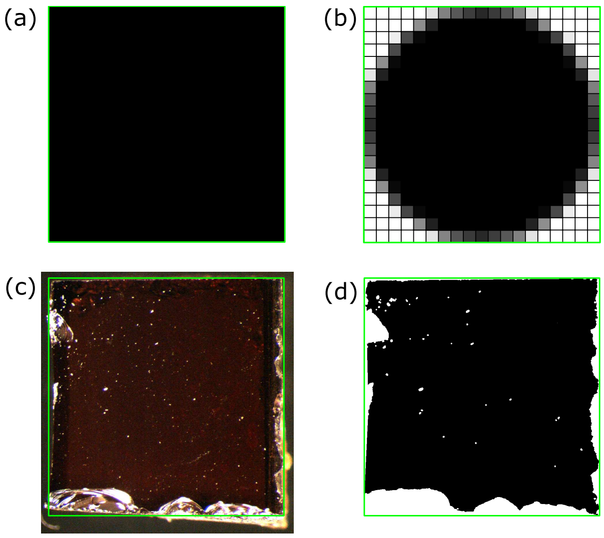

Figure C.8: Constructing a sample shape mask: Black corresponds to values of 1, white to 0. (a) rectangular sample. (b) round sample. The resolution of this mask is far too poor, but it demonstrates how fractional weights (gray color) can be applied at the edges to improve the correspondence to the real shape. (c) Optical light microscope image of an irregularly shaped sample, and (d) corresponding shape mask created by proper thresholding of the microscope image (ca. 800×800 grid points).

partly occupied [see Figure C.8 (b)], or for regions of the sample which are known to diffract non-perfectly (although, as to how this diffraction efficiency could be determined in practice remains another issue).

C.6.6 Summing up the grid points

All the ingredients to calculate the active area of the sample are now ready. The contribution a_{ij} from each grid point is

$$a_{ij} = \frac{i_x(x_{ij}) \cdot i_z(z_{ij})}{I_0} \cdot w_{ij}. \tag{C.39}$$

The sum of all individual contributions over all grid points is an approximation of the flux profile integral over the surface area:

$$\sum_{i,j} a_{ij} \cdot \Delta x \cdot \Delta z \cong \int_S \Phi_0(x,z)\, dx\, dz. \tag{C.40}$$

This is what is called the active area of the sample for a given orientation and flux profile, which we will denote with

$$A_a \equiv \sum_{i,j} a_{ij} \cdot \Delta x \cdot \Delta z. \tag{C.41}$$

C.7 CTR correction factors

To obtain the final values of the measured CTR structure factors from the background-subtracted and renormalized intensity values I_{corr} from Equation C.27, we need to apply all geometrical corrections that we have not considered so far, which include the polarization factor, the Lorentz factor, and the active area correction[2]. For the absolute scaling of the data, also the remaining constants, which we have so meticulously accounted for in each step of the theoretical derivation, have to be taken into account.

Let us look at the expression for the measured CTR structure factor from Equation A.77 once more:

$$\begin{aligned} |F_{HKl}|^2 &= I_{\text{corr}} \frac{A_{uc}}{r_e^2 P} \left| \frac{\partial(\gamma,\delta)}{\partial(h,k)} \right|^{-1} \left[\int_{\text{S}} \Phi_0(x_s, y_s) \mathrm{d}x_s \mathrm{d}y_s \right]^{-1} \\ &= I_{\text{corr}} \frac{A_{uc}^2}{r_e^2 \lambda^2} \frac{1}{P} \sin \beta_{\text{out}} \frac{1}{A_a} \\ &\equiv I_{\text{corr}}\, C_{\text{tot}} \,. \end{aligned} \tag{C.42}$$

The integration time T has been dropped here, because it is already accounted for in I_{corr}. All the remaining factors together give the total correction factor C_{tot} that still needs to be applied to I_{corr}. Naturally, the same correction factor also needs to be applied to the experimental errors σ_{corr} to obtain the uncertainty in the structure factor, σ_{HKl}:

$$\sigma_{HKl} = \sigma_{\text{corr}}\, C_{\text{tot}}. \tag{C.43}$$

All geometrical corrections are, of course, dependent on the experimental setup. Here, we will give the corresponding corrections for the vertical geometry of the Surface Diffraction setup, which has been used throughout all the measurements presented in this work (see Appendix E

---

[2] The renormalization of I_{corr} contains the monitor- and filter-corrections. Note that through the monitor-correction, the integration over the exposure time has implicitly been included, so the exposure time T does not have to be included in the remaining corrections.

for details about the setup). A generalization to other geometries should be fairly straightforward based on the derivations in Appendix A.

C.7.1 Polarization

The polarization of the MS beamline in the horizontal plane is about $p_h = 98\%$ at 12 keV photon energy. The corresponding polarization factor P depends on the detector angles parallel (γ) and perpendicular (δ) to the polarization plane. We will denote the polarization correction factor for the measured intensities for this particular configuration by C_P, in order to distinguish it from the generally valid polarization factor P:

$$C_P = \frac{1}{P} = \left[p_h(1 - \cos^2\delta\sin^2\gamma) + (1 - p_h)(1 - \sin^2\delta)\right]^{-1}. \tag{C.44}$$

C.7.2 Rod interception and Lorentz factor

The factor $\sin\beta_{\text{out}}$ in Equation C.42 has been calculated as the Lorenz factor for the special case where the h- and k-directions of reciprocal space lie within the surface plane of the sample under investigation and the entire scattering signal is acquired in a single exposure for stationary diffractometer angles (open slit geometry, see Section A.5.4). Under these circumstances, the Lorentz factor has a simple geometric interpretation: Due to the finite widths of the CTRs and the Ewald sphere (the latter of which is usually negligible, though), the extension of the reciprocal space volume probed in the l-direction at their intersection depends on the angle subtended by the surface plane and the outgoing x-ray beam, β_{out}. The situation is shown schematically in Figure C.9. The change in the sampled reciprocal-space volume gives rise to a correction factor, which is commonly called the *rod interception factor*, C_I. The integrated signal must therefore be multiplied by a factor

$$C_I = \sin(\beta_{\text{out}}), \tag{C.45}$$

in order to correct for the amount of the vertical component Δl of the CTR that is sampled.

For a more general choice of the reciprocal lattice orientation and other non-stationary types of scans, the Lorentz factor will take on a more complex form, given by the angle-dependent part of the Jacobian determinant of the appropriate variable transformation between

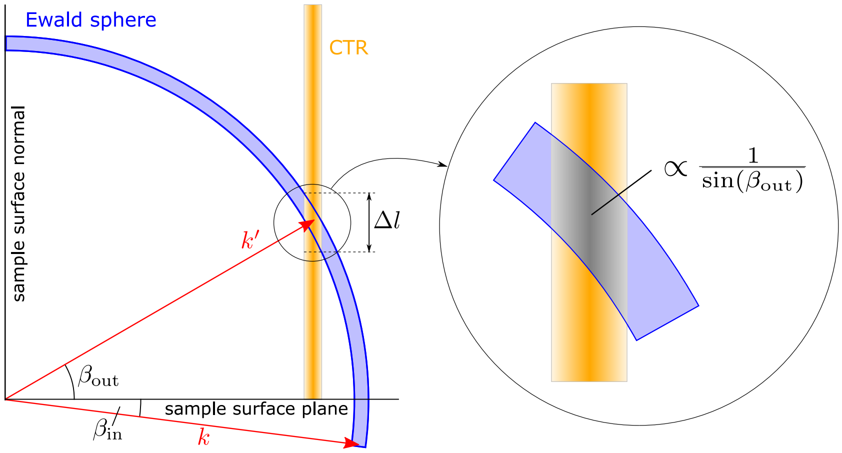

Figure C.9: Schematic k-space diagram explaining the origin of the rod interception factor (projection into a plane spanned by the surface normal direction and k'). The intersection volume between the CTR and the Ewald sphere is proportional to $1/\sin(\beta_{\mathrm{out}})$.

angular and reciprocal-space coordinates. In order to guarantee the correct scaling of the measured structure factors, also the constant factors of the Jacobian need to be included in the corrections. The effect of the rod interception will always be present as one part of these corrections, however.

C.7.3 Active area

The active area has been calculated above as the incident flux integral over the sample surface. The measured intensity values needs to be multiplied by the inverse of the integral, leading to the active area correction factor

$$C_A = \frac{1}{A_a}. \tag{C.46}$$

C.7.4 Absorption by container walls

In most experiments, the sample under investigation is kept inside a environmental chamber under UHV, atmospheric conditions, high pressure gases, etc. x-rays enter and leave the chamber through some sort of reasonably transparent material, for example beryllium, aluminum, or kapton windows. The path length traversed by the x-rays through the absorbing medium in general depends on the incident and exit angles with respect to the container wall. Two common geometries will be considered here.

Ideally, the x-rays traverse the absorbing medium of constant thickness at normal incidence for all angles. This situation can be realized when using a spherical dome of the transparent material and positioning the sample at its center. In this case, no absorption corrections are necessary, since the absorption is constant as a function of the angles. Only if the incident beam intensity is measured in the absence of the chamber, the total absorption needs to be corrected for on the measured diffraction intensities.

Another common setup is that of cylindrical windows with their cylinder axis approximately parallel to the surface normal direction of the sample, as shown schematically in Figure C.10. Now the absorption depends on the incoming (β_{in}) and outgoing (β_{out}) angles of the x-rays with respect to the surface plane. For the outgoing angle at zero, $\beta_{\text{out}} = 0$, the transmission through an exit window of thickness d_{out} is equal to

$$T_{\text{out}}(0) = e^{-\mu \cdot d_{\text{out}}}, \tag{C.47}$$

where μ is the linear absorption coefficient of the window material. For non-zero values of β_{out}, the distance x traversed inside the medium increases as $x = d/\cos\beta_{\text{out}}$, and therefore the transmission decreases to

$$T_{\text{out}} = e^{-\mu \cdot (d_{\text{out}}/\cos\beta_{\text{out}})} = (T_{\text{out}}(0))^{1/\cos\beta_{\text{out}}}. \tag{C.48}$$

The absorption correction we need to apply to the outgoing beam is therefore

$$C_{\mu,\text{out}} = \frac{1}{T_{\text{out}}} = \frac{1}{e^{-\mu \cdot (d_{\text{out}}/\cos\beta_{\text{out}})}}. \tag{C.49}$$

The correction for the incoming beam is completely analogous, resulting in a total absorption correction of

$$C_{\mu} = C_{\mu,\text{in}} \cdot C_{\mu,\text{out}}. \tag{C.50}$$

Note that the same corrections need to be applied to the measurement of the incoming beam intensity, I_0, if this is done with the sample chamber in the path of the x-rays. Usually, all angles are zero for this measurement and the sample is retracted from the direct beam, such that the correction becomes

$$C_{\mu,0} = \frac{1}{T_{\text{in}}(0) \cdot T_{\text{out}}(0)}. \tag{C.51}$$

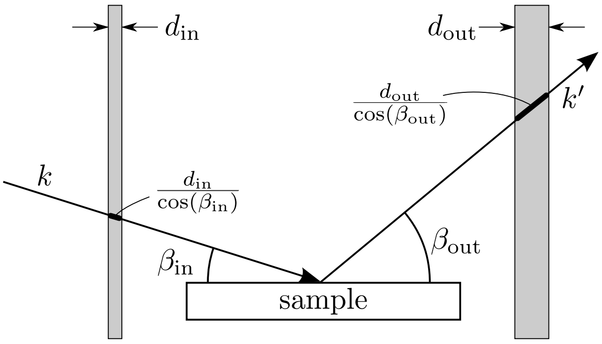

Figure C.10: Schematic diagram of the container window configuration for a cylindrical sample chamber.

C.7.5 Total correction factor

Putting all the above corrections together, we obtain the total correction factor for our particular experimental setup:

$$C_{\text{tot}} = \frac{A_{uc}^2}{r_e^2 \lambda^2} \cdot C_I \cdot C_a \cdot C_P \cdot C_\mu. \tag{C.52}$$

C.8 Symmetry averaging

In many cases, if compared to the statistical errors we have discussed in detail in the previous sections, the systematic errors inherent in a typical SXRD measurement turn out to be the dominant source of uncertainty. A simple way to quantify their magnitude is (a) to measure a set of reflections multiple times during the duration of the experiment, and (b) compare the corrected intensities of nominally symmetry equivalent reflections. This procedure can normally neither reveal the cause for the discrepancies, nor ensure that all systematical effects are detected (there may be systematics affecting all data points in an equal manner, for example wrongly calibrated filters or a slight but constant misalignment of some component). But generally, it gives a good estimate of the reliability of the data and a sensible lower limit to the accuracy achievable when fitting a model (clearly, a crystallographic R-factor of less than 5% for a data set inflicted with an average systematic error of more than 10% seems questionable).

The procedure for the data averaging has been outlined in a general manner in [4] and precisely detailed by Bunk[5], describing the exact implementation used in his SXRD model fitting program FIT. Here, we will merely reproduce his derivation as it stands, in English language.

Let I_i with $i = 1 \ldots N$ be the corrected intensities of equivalent reflections to be averaged, and σ_i their corresponding statistical errors. The weighted average of these data points is given by

$$I_\mathrm{m} = \frac{\sum_{i=1}^{N} (I_i/\sigma_i^2)}{\sum_{i=1}^{N} (1/\sigma_i^2)}, \tag{C.53}$$

and its associated statistical error is

$$\sigma_\mathrm{m:stat} = \left(\sum_{i=1} N \frac{1}{\sigma_i^2} \right)^{-1/2}. \tag{C.54}$$

The total standard deviation of the set of reflections is by definition

$$\begin{aligned} \sigma_\mathrm{m:std} &= \sqrt{\frac{N}{N-1} \left(\langle I^2 \rangle - \langle I \rangle^2 \right)} \\ &= \sqrt{\frac{N}{N-1} \left(\sum_{i=1}^{N} \left(\frac{I_i^2}{\sigma_i^2} \right) / \sum_{i=1}^{N} \left(\frac{1}{\sigma_i^2} \right) - I_\mathrm{m}^2 \right)}. \end{aligned} \tag{C.55}$$

The factor $N/(N-1)$ takes into account that the mean itself has been determined from the data set and hence represents a free parameter.

The averaged intensity I_m, its resulting statistical error $\sigma_\mathrm{m:stat}$, and standard deviation $\sigma_\mathrm{m:std}$ are now calculated for each set of equivalent reflections. Let M be the number of such equivalent sets. Their mean relative error with respect to the standard deviation

$$\epsilon_\mathrm{std} = \frac{1}{M} \sum_{j=1}^{M} \frac{\sigma_{\mathrm{m:std},j}}{I_{\mathrm{m},j}}, \tag{C.56}$$

and the statistical error

$$\epsilon_\mathrm{stat} = \frac{1}{M} \sum_{j=1}^{M} \frac{\sigma_{\mathrm{m:stat},j}}{I_{\mathrm{m},j}}, \tag{C.57}$$

can now be calculated. In order to obtain a credible approximation of the mean systematic error, it may be advantageous to include only those reflections which are sufficiently reliable regarding their statistical error, i.e., measurements with $I_\mathrm{mean} > c \cdot \sigma_\mathrm{m:stat}$, where c can be chosen freely, a typical value being $c = 3$.

We assume that for each averaged reflection, the total observed standard deviation $\sigma_{\mathrm{m:std}}$ can be described as the sum of the two independent contributions from the statistical uncertainty $\sigma_{\mathrm{m:stat}}$ and the systematic error $\sigma_{\mathrm{m:syst}}$:

$$\sigma^2_{\mathrm{m:std},j} = \sigma^2_{\mathrm{m:stat},j} + \sigma^2_{\mathrm{m:syst},j}.$$

Denoting the average systematic error by ϵ_{syst}, we can approximate this, on average, by

$$(\epsilon_{\mathrm{std}} I_{\mathrm{m},j})^2 \approx (\epsilon_{\mathrm{stat}} I_{\mathrm{m},j})^2 + (\epsilon_{\mathrm{syst}} I_{\mathrm{m},j})^2, \tag{C.58}$$

which finally leads to

$$\epsilon_{\mathrm{syst}} = \sqrt{\epsilon^2_{\mathrm{std}} - \epsilon^2_{\mathrm{stat}}}. \tag{C.59}$$

ϵ_{syst} times the intensity is an estimate for the systematic error (if the argument of the square-root is positive) and may be added as a correction to the statistical errors σ_i of all remaining non-averaged reflections:

$$\sigma_{\mathrm{corrected},i} = \sqrt{\sigma_i^2 + (\epsilon_{\mathrm{syst}} I_i)^2}. \tag{C.60}$$

It should be made very clear, however, that this procedure merely gives an indication about the uncertainty to be expected for each data point. It does not correct in any way for the error itself, that is the deviation of the measured value from its unknown true value. In other words, the *systematically* wrong data points remain *systematically* wrong. This will certainly lead to inaccuracies in the structural model refinement, regardless of the corrections applied to the error bars of the data points. For this reason, a thorough characterization and optimization of the experimental setup to identify and avoid systematical errors is indispensable to guarantee an optimal data quality.

C.9 Data treatment programs

In the course of this thesis, a set of analysis routines has been developed in MATLAB® to facilitate the extraction of integrated intensities and to apply the necessary corrections to obtain an absolute scaling of the measured structure factors. This includes all the steps described in this chapter, apart from the symmetry averaging in the last section, which is best done by using FIT [5].

Based on a library of basic functions [6] necessary to read, write, and manipulate PILATUS detector images, a large graphical user interface (GUI), called *scananalysis*, has been created to facilitate the region-based extraction of integrated intensities from the detector images including the background subtraction. Since typically several thousand to several ten thousand images have to be analyzed for each experiment, the main goal was to combine the ease-of-use of a GUI with the necessary graphical feedback to efficiently monitor the quality of the extraction process and background fitting.

The data files saved by *scananalysis* can be directly passed to a MATLAB script applying the correction factors. Additional scripts to calculate the flat-field correction array and the incident beam profile are also available.

Anyone interested in these routines should contact the surface diffraction group leader at the Swiss Light Source directly.

Bibliography

[1] C. M. Schlepütz, R. Herger, P. R. Willmott, B. D. Patterson, O. Bunk, Ch. Brönnimann, B. Henrich, G. Hülsen, and E. F. Eikenberry: "Improved data acquisition in grazing-incidence X-ray scattering experiments using a pixel detector." *Acta Crystallogr. A* **61**, 418–425 (2005), doi: 10.1107/S0108767305014790.

[2] P. Kraft, A. Bergamaschi, Ch. Brönnimann, R. Dinapoli, E. F. Eikenberry, B. Henrich, I. Johnson, M. Kobas, C. M. Schlepütz, P. R. Willmott, and B. Schmitt: "Performance of single photon counting pixel detector modules." *J. Synch. Rad.* **16**(3), 368–375 (2009), doi:10.1107/S0909049509009911.

[3] P. Kraft, A. Bergamaschi, Ch. Brönnimann, R. Dinapoli, E. F. Eikenberry, H. Graafsma, B. Henrich, I. Johnson, M. Kobas, A. Mozzanica, C. M. Schlepütz, and B. Schmitt: "Characterization and Calibration of PILATUS Detectors." *IEEE Trans Nucl Sci* (2009). Accepted.

[4] I. K. Robinson: "Surface Crystallography." In *Handbook on Synchrotron Radiation*, Edited by G. Brown and D. E. Moncton, chapter 7, 221–266, Elsevier Science Publishers, third edition (1991).

[5] O. Bunk: *Bestimmung der Struktur komplexer Halbleiter-Oberflächenrekonstruktionen mit Röntgenbeugung*. Ph.D. thesis, Universität Hamburg, Hamburg (1999).
URL `http://www.physnet.uni-hamburg.de/services/fachinfo/___Volltexte/Oliver___Bunk/Oliver___Bunk.pdf`

[6] "SD Computing and Controls: MATLAB routines for pixel image analysis." (2009).
URL `http://sls.web.psi.ch/view.php/beamlines/ms/sd/computing/index.html#matlabman`

Appendix D

PILATUS Characteristics

In this appendix, some particular characteristics of the PILATUS 100k pixel detector [1–5] used in this work will be discussed in more detail.

D.1 Charge sharing

The photons incident on the detector convert into charge clouds inside the silicon sensor. The electrical field applied across the sensor causes the created electrons and holes to travel to the collection electrodes of the pixels, where they produce an analog charge pulse. The drifting charge cloud has a certain extent which will increase with drift distance due to Coulomb repulsion and diffusion. If a photon converts close to the middle between two neighboring pixels, the collected charge will be shared among them, resulting in charge pulses of reduced amplitude in each pixel. The situation is depicted for two photons in Figure D.1. Photon 1 converts inside pixel number one, and all of the produced charge is collected there, leading to a large analog charge pulse, as shown in panel (b) of the figure. Photon 2 is absorbed in between pixels 2 and 3, causing two charge pulses of diminished amplitude in the two neighboring pixels.

If the height of the analog charge pulses exceeds the comparator threshold level, a digital signal is produced which causes the detector to register a count. When setting the threshold to exactly half of the incident photon energy, the effects of charge sharing on the counting efficiency are minimized. Since the charge is normally never split equally between the pixels,

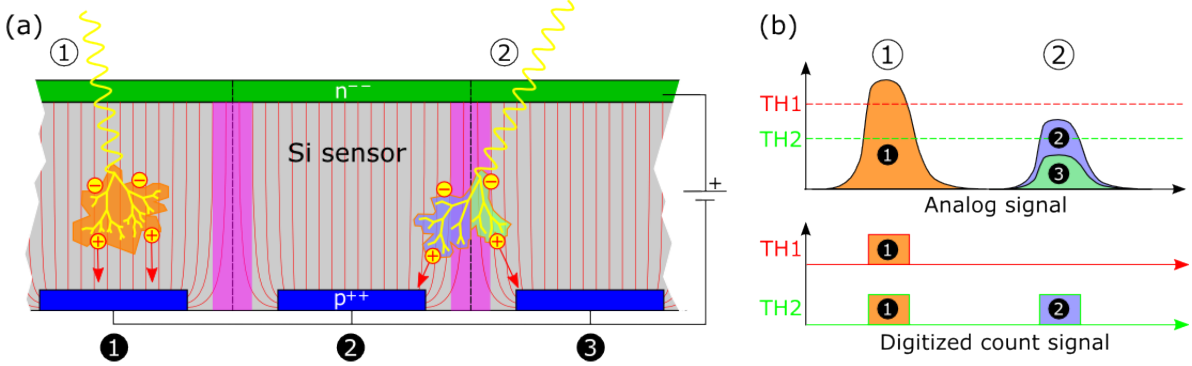

Figure D.1: Charge sharing between pixels. (a) Conversion of the incoming photons into charge clouds. Photon 1 is absorbed in the middle of pixel 1, and all of the created charge is collected there. Photon 2 converts on the border between pixels 2 and 3 (shaded area), and the created charge is shared accordingly. (b) Schematic representation of the charge pulses (top) and their conversion to digital pulses (bottom) for a high (TH1) and low (TH2) threshold level.

one of the two will see a pulse larger than the threshold while the other one remains below. In this way, each photon will be counted only once.

In certain cases, for example to suppress fluorescence background of a lower energy than that of the incident photons, it is advantageous to set the threshold level higher than at 50% of the incident energy. As a result, a "dead area" appears at the border of each pixel. If a photon is converted inside this area, the charge drained by the neighboring pixel is so large, that the pulse created in the pixel receiving the photon does not exceed the threshold limit anymore, hence the count is effectively lost. The efficiency of the detector is diminished in such a case and the decrease of efficiency is approximately linear with increasing relative threshold level as the ratio of the dead area with respect to the total pixel size increases proportionally.

D.2 Pixel geometries

A PILATUS module is built as an array of 8 × 2 PILATUS II readout chips (ROCs), each with 60 × 97 pixels, bump-bonded to a single monolithic silicon sensor. Unfortunately, a tight packing of the ROCs on the sensor is impossible due to their periphery containing the necessary leads for supply voltages and connections to address the individual pixels and a so-called seal ring. In order to avoid dead areas between adjacent readout chips, the sensor encompasses

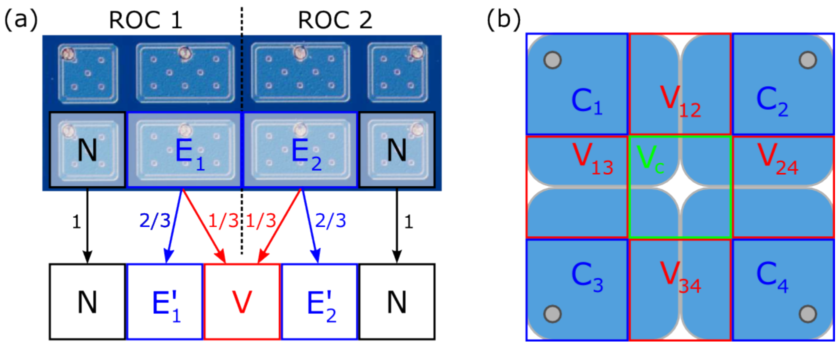

Figure D.2: Closing the gaps: (a) A light microscope image of the Si sensor back side showing the normal sized (square) and enlarged pixels (rectangular) spanning the gaps between readout chips. The superimposed diagram visualizes the redistribution of counts from two large pixels into three normal sized pixels by introducing an additional virtual pixel inside the gap. (b) Analogous redistribution at the chip corners.

pairs of rows or columns with larger pixels, having an area equal to $(1 \times \frac{3}{2})$ of a normal pixel, at the edges of each chip spanning the gaps. The registered counts of two neighboring large pixels are redistributed digitally into three normal sized pixels by introducing a virtual pixel inside the gap, as shown in Figure D.2 (a):

$$\begin{aligned} E_1' &= 2/3 \cdot E_1, \\ E_2' &= 2/3 \cdot E_2, \\ V &= 1/3 \cdot E_1 + 1/3 \cdot E_2. \end{aligned}$$

At the corners of the readout chips, the same principle is applied. The counts from four large pixels having $(\frac{3}{2} \times \frac{3}{2})$ the area of a normal pixel are digitally redistributed into four normal sized pixels and 5 virtual pixels covering the gap, as shown in Figure D.2 (b).

Since there are 1 vertical and 7 horizontal gaps in the 8×2 array, the total number of effective pixels in one module becomes $(8 \cdot 60 + 7) \times (2 \cdot 97 + 1) = 487 \times 195 = 94\,965$.

This procedure of introducing virtual pixels has two important consequences: Firstly, the larger pixels are less affected by charge sharing (see Section D.1) since their edge to area ratio is lower (more photons are converted inside the pixel compared to on its edge). This results in generally better counting efficiencies of these large pixels, and hence of their artificially derived normal sized pixels. Also, the change in efficiency as a function of the threshold level is different

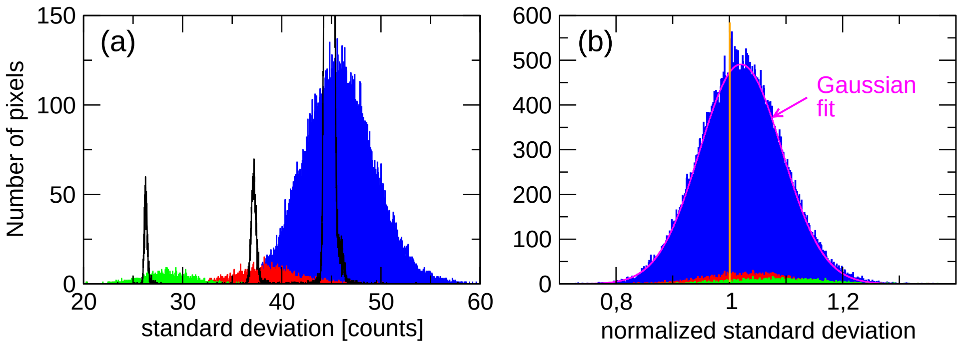

Figure D.3: (a) Histogram of measured standard deviations $\sigma(i,j)$ for normal (blue), resized edge (red) and virtual (green) pixels. Superimposed in black are the corresponding histograms for $\langle\sigma_N\rangle$, $\langle\sigma_{E'}\rangle$, and $\langle\sigma_V\rangle$. (b) Ratio of measured to expected standard deviation for the same pixels. The magenta line is a Gaussian fit to the distribution of normal sized pixels.

from normal sized pixels. This means that the pixel efficiencies need to be calibrated separately for different incident energies and threshold settings, making flat field measurements necessary for each setting.

Secondly, the artificial redistribution of counts into resized and virtual pixels results in an enhanced counting statistics with respect to normal pixels. Assuming purely Poisson-limited counting statistics, where the expectation value for the standard deviation of a measured intensity I is $\langle\sigma\rangle = \sqrt{I}$, the modified edge pixels will have the following expectation values:

$$\begin{aligned}
\langle\sigma_N\rangle &= \sqrt{I}, \\
\langle\sigma_{E_i'}\rangle &= 2/3\cdot\sqrt{E_i} \approx 2/3\cdot\sqrt{3/2\cdot I} \equiv \langle\sigma_{E'}\rangle = 0.816\cdot\langle\sigma_N\rangle, \\
\langle\sigma_V\rangle &= 1/3\cdot\sqrt{E_1+E_2} \approx 1/3\cdot\sqrt{3/2\cdot I + 3/2\cdot I)} = 1/3\cdot\sqrt{4/2\cdot I} = 0.577\cdot\langle\sigma_N\rangle.
\end{aligned}$$

where the approximation assumes that the registered counts for the pixel types N,E_i', and V are the same, as one would see from a homogeneous illumination if the pixels had the exact same efficiencies. Again, the same principle can be applied for corner pixels.

Experimental results from a flat field measurement are shown in Figure D.3. The standard deviations over 100 exposures for normal pixels (N: blue), resized edge pixels (E': red), and virtual pixels (V: green) are plotted in a histogram in panel (a). The superimposed black curves show the histograms of the corresponding expectation values for the standard deviations, $\langle\sigma_N\rangle$, $\langle\sigma_{E'}\rangle$, and $\langle\sigma_V\rangle$. Corner pixels have been omitted in this graph for clarity.

When normalizing the measured standard deviation to the appropriate expectation value, we obtain the histograms shown in panel (b) of figure D.3. We see that for all three pixel types, the distribution is centered just slightly above one, indicating that the experimentally achieved counting statistics is very close to the theoretical Poisson limit. Fitting a Gaussian to the distribution from normal sized pixels (magenta line) gives a mean value of 1.021 with a width of 0.103, the latter of which is due to the finite sampling of 100 exposures.

Bibliography

[1] C. M. Schlepütz, R. Herger, P. R. Willmott, B. D. Patterson, O. Bunk, Ch. Brönnimann, B. Henrich, G. Hülsen, and E. F. Eikenberry: "Improved data acquisition in grazing-incidence X-ray scattering experiments using a pixel detector." *Acta Crystallogr. A* **61**, 418–425 (2005), doi: 10.1107/S0108767305014790.

[2] Ch. Brönnimann, E. F. Eikenberry, B. Henrich, R. Horisberger, G. Huelsen, E. Pohl, B. Schmitt, C. Schulze-Briese, M. Suzuki, T. Tomizaki, H. Toyokawa, and A. Wagner: "The PILATUS 1M detector." *Journal of Synchrotron Radiation* **13**(2), 120–130 (2006), doi:10.1107/S0909049505038665.

[3] A. Bergamaschi, Ch. Brönnimann, E. F. Eikenberry, B. Henrich, M. Kobas, P. Kraft, and B. Schmitt: "Experience and Results from the 6 Megapixel PILATUS System." *PoS* **057**, 049 (2007).

[4] P. Kraft, A. Bergamaschi, Ch. Brönnimann, R. Dinapoli, E. F. Eikenberry, H. Graafsma, B. Henrich, I. Johnson, M. Kobas, A. Mozzanica, C. M. Schlepütz, and B. Schmitt: "Characterization and Calibration of PILATUS Detectors." *IEEE Trans Nucl Sci* (2009). Accepted.

[5] P. Kraft, A. Bergamaschi, Ch. Brönnimann, R. Dinapoli, E. F. Eikenberry, B. Henrich, I. Johnson, M. Kobas, C. M. Schlepütz, P. R. Willmott, and B. Schmitt: "Performance of single photon counting pixel detector modules." *J. Synch. Rad.* **16**(3), 368–375 (2009), doi:10.1107/S0909049509009911.

Appendix E

Angle Calculations

E.1 Introduction

In a diffraction experiment, the subject of interest is the distribution of diffraction intensities in reciprocal space. The measurement itself, however, takes place in real space, in a coordinate system given by the experimental setup. Usually, the detector and sample are positioned relative to each other and the incoming probe beam using a diffractometer which provides the adequate angular and possibly linear degrees of freedom. The instrument's position along each degree of freedom represents a physical coordinate in real space (which may not necessarily be independent of each other, however). The question is, therefore, how the diffractometer needs to be positioned in real space to reach a given point with coordinates (hkl) in reciprocal space, and vice versa, to find the (hkl) position in reciprocal space for a given set of diffractometer angles. The knowledge of these relations and correspondences is prerequisite for any diffraction experiment. Since they differ markedly depending on the construction principle and configuration of an instrument (interdependence and coupling of different rotation circles, number of degrees of freedom, etc.) there is a rich literature on angle calculations for various diffractometer types [1–6].

It is the subject of this appendix is to establish the relations between real and reciprocal space coordinates for the (2+3)-type surface diffractometer at the Materials Science beamline of the Swiss Light Source. As such, all calculations are specific to this particular setup, but wherever possible, the underlying principles are explained in a general fashion. The aim is to present all calculations in a careful and step-by-step manner, and to bring all the relevant mathematics and physics together. The derived relations have been used to create the proper angle calculation code for the diffractometer control software SPEC®. All measurement presented in this work were obtained using this code.

This appendix is based on an internal document created earlier by Willmott and Schlepütz [7]. It draws heavily from the literature, in particular the papers from Busing and Levy [1], Evans-Lutterodt and Tang [2], Vlieg [3, 4], Bunk and Nielsen [6], and Diebel [8].

E.2 Rotation matrices

Before we proceed, it may be helpful to briefly recall the mechanism of *active* right-handed rotations[1] about some angle θ around the x-, y- and z-axes in a cartesian coordinate system. These are, respectively

$$\mathcal{R}_x(\theta) = \begin{pmatrix} 1 & 0 & 0 \\ 0 & \cos\theta & -\sin\theta \\ 0 & \sin\theta & \cos\theta \end{pmatrix}; \tag{E.1}$$

$$\mathcal{R}_y(\theta) = \begin{pmatrix} \cos\theta & 0 & \sin\theta \\ 0 & 1 & 0 \\ -\sin\theta & 0 & \cos\theta \end{pmatrix}; \tag{E.2}$$

$$\mathcal{R}_z(\theta) = \begin{pmatrix} \cos\theta & -\sin\theta & 0 \\ \sin\theta & \cos\theta & 0 \\ 0 & 0 & 1 \end{pmatrix}. \tag{E.3}$$

The inverse rotation operators $\mathcal{R}^{-1}(\theta)$ of these are equal to the transposed matrices $\mathcal{R}^T(\theta)$. Because $\cos\theta = \cos(-\theta)$ and $\sin\theta = -\sin(-\theta)$, we also obtain

$$\mathcal{R}^{-1}(\theta) = \mathcal{R}(-\theta). \tag{E.4}$$

E.3 The diffractometer

The Newport 5-circle diffractometer is shown in Fig. E.1. Of particular note are the three different laboratory coordinate frames. For the calculations described here, the two lower

---

[1] An *active* rotation describes the rotation of an object within a fixed coordinate system, in contrast to a *passive* rotation, which changes the orientation of the underlying coordinate system for an object fixed in space.

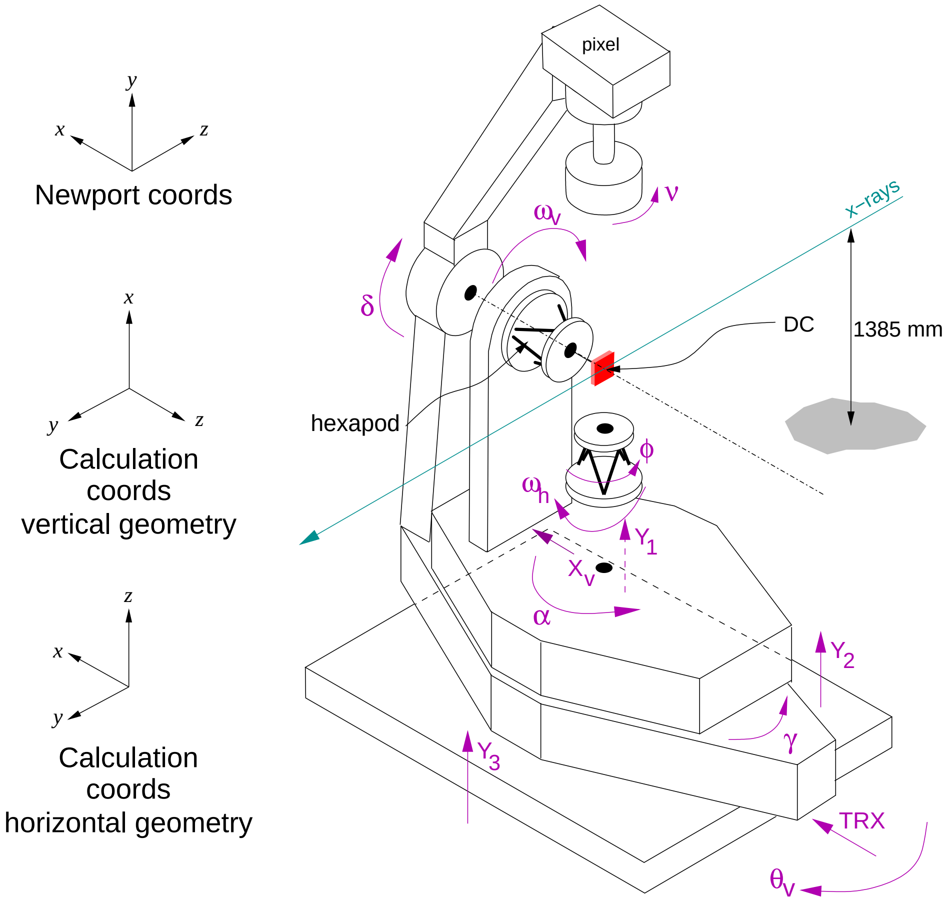

Figure E.1: Schematic figure of the 5-circle (2 sample + 3 detector) Newport diffractometer used at the Surface Diffraction station of the SLS. The sample circles are α and ω_v in the vertical geometry (hexapod axis horizontal) and ω_h and ϕ in the horizontal geometry (hexapod axis vertical), while the detector circles are γ, δ, and ν. All detector and sample motor axes cross at the diffractometer center (DC). Other important motor movements are also shown. Arrow heads point in the positive direction. Three coordinate systems are shown – the Newport Cartesian frame, which tallies with the naming convention of the motors; the calculation frame of reference in the vertical geometry (see also Fig. E.2), which is used by both Evans-Lutterodt [2] and Vlieg [3, 4]; and the calculation frame of reference in the horizontal geometry (see also Fig. E.7).

coordinate frames are relevant – they have both been chosen such that the direct beam points in the positive y-direction and the sample surface normal at 0° grazing incidence lies along the z-axis. The upper coordinate frame is also shown, as it determines the naming and positive directions of the Newport diffractometer motors (i.e., the direction of the arrows).

The diffractometer can be configured in one of two geometries: In the “vertical” mode, the surface of the sample lies in a vertical plane and the surface normal is horizontal, while in the “horizontal” geometry, the surface plane is horizontal with the surface normal pointing vertically upwards. Which geometry should be used depends on the demands of the experiment. In the vertical geometry, motors α, ω_v, γ, δ, and ν are used, while for the horizontal geometry, motors ϕ, ω_h, γ, δ, and ν are used (the naming conventions for the instrument circles follow those used by Vlieg [4] for the description of the (2+3)-type diffractometer). As a result, the angle calculations need to be performed separately for both geometries.

Six additional sample degrees of freedom (3 translations and 3 rotations) are provided by a hexapod. The 3 linear motions are used to bring the sample center into coincidence with the diffractometer center (DC). Then the sample surface normal is accurately aligned with the diffractometer's azimuthal sample rotation axis (ω_v in the vertical and ϕ in the horizontal geometry, respectively) using the hexapod rotations[2]. All angle calculations require this coincidence of sample surface normal and azimuthal rotation axis, so once the sample is accurately aligned, the hexapod positions are fixed for the rest of the experiment.

E.4 Vertical geometry

E.4.1 Geometrical setup

Consider a flat single crystal sample mounted vertically (i.e., with its flat face vertical and its surface normal horizontal), as shown in Fig. E.2.

Here, the laboratory set of coordinates (x, y, z), are fixed by y being the positive direction of the incident x-ray beam, x being the vertical direction around which both α and γ rotate, and z being the horizontal direction around which δ rotates when $\gamma = 0$, and ω_v rotates when $\alpha = 0$.[3]

Using the equations E.1 and E.3, we therefore obtain for the four circles γ, α, δ, and ω_v,

---

[2] The azimuthal rotation provided by the hexapod is of course redundant and this angle is fixed at zero.

[3] Note that ω_v and δ are left-handed rotations around the z-axis.

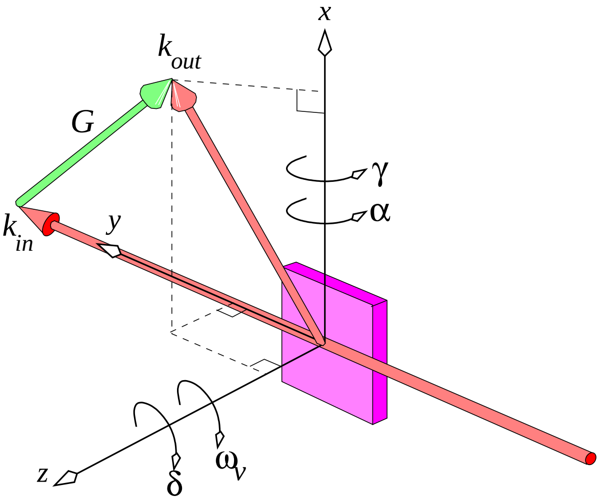

Figure E.2: Schematic figure of the laboratory coordinate system, incoming and outgoing wavevectors $\vec{k}_{in}$ and $\vec{k}_{out}$, the scattering vector $\vec{G}$, and the pertinent motor rotations in the vertical geometry setup of the surface diffractometer.

respectively, the rotation matrices Γ, A, Δ, and Ω_v, given by

$$\Gamma = \mathcal{R}_x(\gamma) = \begin{pmatrix} 1 & 0 & 0 \\ 0 & \cos\gamma & -\sin\gamma \\ 0 & \sin\gamma & \cos\gamma \end{pmatrix}; \tag{E.5}$$

$$A = \mathcal{R}_x(\alpha) = \begin{pmatrix} 1 & 0 & 0 \\ 0 & \cos\alpha & -\sin\alpha \\ 0 & \sin\alpha & \cos\alpha \end{pmatrix}; \tag{E.6}$$

$$\Delta = \mathcal{R}_z(\delta) = \begin{pmatrix} \cos\delta & \sin\delta & 0 \\ -\sin\delta & \cos\delta & 0 \\ 0 & 0 & 1 \end{pmatrix}; \tag{E.7}$$

$$\Omega_v = \mathcal{R}_z(\omega_v) = \begin{pmatrix} \cos\omega_v & \sin\omega_v & 0 \\ -\sin\omega_v & \cos\omega_v & 0 \\ 0 & 0 & 1 \end{pmatrix}, \tag{E.8}$$

where we note that Δ and Ω_v represent *positive left-handed* rotations.

The relevant rotation matrices for the horizontal geometry are handled in Section E.5, because there a different calculation coordinate frame is chosen.

E.4.2 Calculating diffractometer angles

The goal of this section is to obtain expressions for the four motor positions (angles) α, ω_v, δ, and γ in terms of the scattering vector in the frame of reference of the crystal surface and the incident and exit angles perpendicular to the crystal surface (referred to as β_{in} and β_{out}, see text below and Fig. E.3). We will derive general expressions for these angles, for which specific values will crystallize out, once we define which one of three recording modes we choose to work with, described below.

Our first task is to determine the components X, Y, and Z, of the scattering vector $\vec{G}$, which is determined by the detector position, in the laboratory frame of reference. The detector is rotated first by Δ then by Γ (the order of rotation is important, because if the γ-motion is first calculated, this moves the δ-axis out from being coaxial with the z-axis. Therefore, the δ-motion must always be performed first. This also holds for the ω_v (first) and α (second) motions of the sample). The detector is now positioned such that it is pointing back along the outgoing, elastically scattered x-ray $\vec{k}_{out}$. We use the fact that, in units of $2\pi/\lambda$ (for which the magnitude of the incident and scattered wavevectors is then equal to unity), the incoming x-ray beam can be represented by the vector

$$\vec{k}_{in} = \begin{pmatrix} 0 \\ 1 \\ 0 \end{pmatrix} \tag{E.9}$$

and express the diffraction condition

$$\vec{k}_{out} - \vec{k}_{in} = \vec{G} = \begin{pmatrix} X \\ Y \\ Z \end{pmatrix} \tag{E.10}$$

by

$$\vec{k}_{out} - \vec{k}_{in} = (\Gamma \cdot \Delta - \mathcal{I}) \begin{pmatrix} 0 \\ 1 \\ 0 \end{pmatrix}, \tag{E.11}$$

where $\mathcal{I}$ is the identity matrix. Using our rotation matrices defined above, we therefore obtain

$$\begin{pmatrix} \sin\delta \\ \cos\gamma\,\cos\delta - 1 \\ \sin\gamma\,\cos\delta \end{pmatrix} = \begin{pmatrix} X \\ Y \\ Z \end{pmatrix}. \tag{E.12}$$

We now introduce the vector $\vec{G}_\phi$ given by

$$\vec{G}_\phi = \begin{pmatrix} h_\phi \\ k_\phi \\ l_\phi \end{pmatrix}, \tag{E.13}$$

which denotes the scattering vector as viewed in the orthonormal Cartesian crystal frame of reference (x_c, y_c, z_c). This frame of reference contains x_c and y_c in the surface of the crystal and therefore z_c is normal to the surface. Note that $\vec{G}_\phi$ does *not* represent the conventional (hkl) Miller indices, because (a) we are using an orthonormal frame of reference (which is not appropriate for hexagonal, triclinic, monoclinic, or rhombohedral crystal systems), and (b) it does not take into account any miscuts of the crystal. This last aspect is dealt with later.

For the angular movements of the sample, α and ω_v, both equal to zero, (x_c, y_c, z_c) and (x, y, z) lie above one another. Let us start in this configuration. In order to satisfy the diffraction condition, we need to first rotate ω_v, then α, which will therefore reposition $\vec{G}_\phi$ into the laboratory-based diffraction condition $\vec{G}$, i.e.,

$$\begin{pmatrix} X \\ Y \\ Z \end{pmatrix} = A \cdot \Omega_v \begin{pmatrix} h_\phi \\ k_\phi \\ l_\phi \end{pmatrix} \quad \Longrightarrow \quad \begin{pmatrix} h_\phi \\ k_\phi \\ l_\phi \end{pmatrix} = \Omega_v^{-1} \cdot A^{-1} \begin{pmatrix} X \\ Y \\ Z \end{pmatrix} \tag{E.14}$$

Multiplying out, we obtain

$$\begin{pmatrix} h_\phi \\ k_\phi \\ l_\phi \end{pmatrix} = \Omega_v^{-1} \cdot \begin{pmatrix} X \\ \cos\alpha\, Y + \sin\alpha\, Z \\ -\sin\alpha\, Y + \cos\alpha\, Z \end{pmatrix} \tag{E.15}$$

$$= \begin{pmatrix} \cos\omega_v\, X - \sin\omega_v(\cos\alpha\, Y + \sin\alpha\, Z) \\ \sin\omega_v\, X + \cos\omega_v(\cos\alpha\, Y + \sin\alpha\, Z) \\ -\sin\alpha\, Y + \cos\alpha\, Z \end{pmatrix}. \tag{E.16}$$

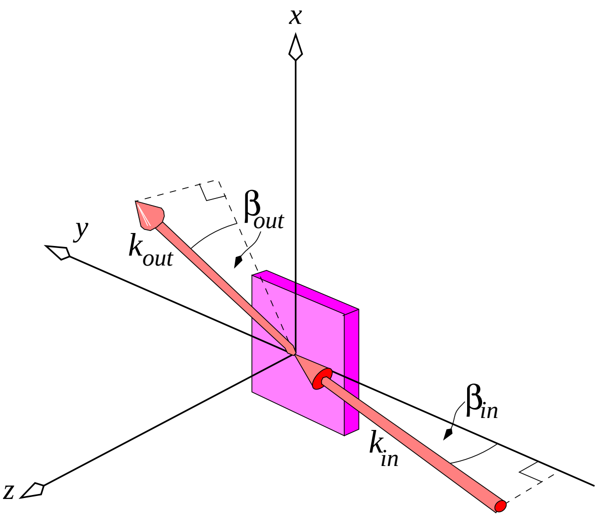

Figure E.3: Schematic of the incident and exit angles β_{in} and β_{out}. In the vertical geometry, β_{in} is equal to α. In the horizontal geometry, β_{in} is equal to ω_h.

Consider Fig. E.3. In our routines for reciprocal space navigation, three modes are offered, namely a fixed incident x-ray angle ($\beta_{in} = \alpha =$ const.); a fixed exit x-ray angle ($\beta_{out} =$ const.); or $\beta_{in} = \beta_{out}$.

The momentum transfer perpendicular to the sample surface, l_ϕ, in units of $2\pi/\lambda$, is simply

$$l_\phi = \sin\beta_{in} + \sin\beta_{out}. \tag{E.17}$$

But from Equations E.12 and E.16,

$$\begin{aligned} l_\phi &= -\sin\alpha\, Y + \cos\alpha\, Z \\ &= -\sin\alpha\,(\cos\gamma\,\cos\delta - 1) + \cos\alpha\cdot\sin\gamma\cdot\cos\delta \\ &= \cos\delta\,(\sin\gamma\,\cos\alpha - \cos\gamma\,\sin\alpha) + \sin\alpha \\ &= \underbrace{\cos\delta\,\sin(\gamma-\alpha)}_{=\sin\beta_{out}} + \underbrace{\sin\alpha}_{\sin\beta_{in}}. \end{aligned} \tag{E.18}$$

This is our first condition. We now determine the (squared) magnitude of the in-plane component of $\vec{G}_\phi$. We can predict in advance that this should be independent of ω_v, as this rotation is always normal to the crystal surface. Again, referring back to Equations E.12 and

E.16, we obtain

$$\begin{aligned} h_\phi^2 + k_\phi^2 &= [\cos\omega_v \cdot X - \sin\omega_v(\cos\alpha \cdot Y + \sin\alpha \cdot Z)]^2 \\ &+ [\sin\omega_v \cdot X + \cos\omega_v(\cos\alpha \cdot Y + \sin\alpha \cdot Z)]^2 \\ &= X^2 + (\cos\alpha \cdot Y + \sin\alpha \cdot Z)^2, \end{aligned} \tag{E.19}$$

which is indeed independent of ω_v.

The next condition we exploit is the fact that the magnitude of $\vec{G}_\phi$ is equal to that of $\vec{G}$ and that both these must also be independent of ω_v. From Equation E.12, we obtain

$$\begin{aligned} X^2 + Y^2 + Z^2 &= (\sin\delta)^2 + (\cos\gamma\,\cos\delta - 1)^2 + (\sin\gamma\,\cos\delta)^2 \\ &= \sin^2\delta + \cos^2\gamma\,\cos^2\delta - 2\cos\gamma\,\cos\delta + 1 + \sin^2\gamma\,\cos^2\delta \\ &= \underbrace{\cos^2\delta\,\underbrace{(\sin^2\gamma + \cos^2\delta)}_{=1} + \sin^2\delta}_{=1} - 2\cos\gamma\,\cos\delta + 1 \\ &= 2 - 2\cos\gamma\,\cos\delta \\ &= -2Y \;=\; h_\phi^2 + k_\phi^2 + l_\phi^2. \end{aligned} \tag{E.20}$$

From Equation E.18, we know that

$$\begin{aligned} \sin\beta_{out} &= \cos\delta \cdot \sin(\gamma - \alpha) \\ &= \cos\delta \cdot (\sin\gamma\,\cos\alpha - \cos\gamma\,\sin\alpha) \\ &= \cos\alpha \cdot \sin\gamma\,\cos\delta - \sin\alpha \cdot \cos\gamma\,\cos\delta \\ &= \cos\alpha \cdot Z - \sin\alpha \cdot (Y + 1). \end{aligned} \tag{E.21}$$

And by inserting Equation E.20, we obtain

$$\sin\beta_{out} = \cos\alpha \cdot Z - \sin\alpha \left[-\frac{1}{2}(h_\phi^2 + k_\phi^2 + l_\phi^2) + 1 \right]. \tag{E.22}$$

Remembering that $\sin\alpha = \sin\beta_{in}$, we rearrange Equation E.22 to obtain

$$Z = [\sin\beta_{out} + \sin\beta_{in}(Y + 1)] \,/\, \cos\alpha. \tag{E.23}$$

We now substitute the expressions for Y and Z (Equations E.20 and E.23) into Equation E.19:

$$\begin{aligned} h_\phi^2 + k_\phi^2 &= X^2 + (\cos\alpha \cdot Y + \sin\alpha \cdot Z)^2 \\ \Rightarrow X &= \pm\left[h_\phi^2 + k_\phi^2 - (\cos\alpha \cdot Y + \sin\alpha \cdot Z)^2\right]^{1/2} \\ &= \pm\left[h_\phi^2 + k_\phi^2 - (\cos\beta_{in} \cdot Y + \sin\beta_{in} \cdot Z)^2\right]^{1/2}. \end{aligned} \tag{E.24}$$

What have we achieved in deriving Equations E.20 to E.24? X, Y, and Z have now been expressed only in terms of h_ϕ, k_ϕ, and l_ϕ (the momentum transfer positions we want to move to in the frame of reference of the crystal surface) and β_{in} and β_{out}, which are still free variables.

We now determine the diffractometer angles α, γ, δ, and ω_v in terms of h_ϕ, k_ϕ, and l_ϕ and X, Y, and Z (which, we have just stated, can themselves be expressed in terms of h_ϕ, k_ϕ, and l_ϕ and β_{in} and β_{out}). From Equation E.12, we directly obtain

$$\sin\delta = X. \tag{E.25}$$

We perform a little mathematical trick to obtain our expression for γ:

$$\begin{aligned} \tan\gamma &= \frac{\sin\gamma}{\cos\gamma} \\ &= \frac{\sin\gamma\,\cos\delta}{\cos\gamma\cos\delta} = \frac{\sin\gamma\,\cos\delta}{(\cos\gamma\cos\delta - 1) + 1} \\ &= \frac{Z}{Y+1}. \end{aligned} \tag{E.26}$$

In order to obtain an expression for ω_v, we first redefine

$$(\cos\beta_{in} \cdot Y + \sin\beta_{in} \cdot Z) \equiv K, \tag{E.27}$$

which we substitute into Equation E.16 to obtain

$$\begin{aligned} h_\phi &= \cos\omega_v \cdot X - \sin\omega_v \cdot K \\ \Rightarrow \cos\omega_v &= \frac{h_\phi + \sin\omega_v \cdot K}{X} \end{aligned}$$

and

$$\begin{aligned} k_\phi &= \sin\omega_v \cdot X + \cos\omega_v \cdot K \\ \Rightarrow \sin\omega_v &= \frac{k_\phi - \cos\omega_v \cdot K}{X}, \end{aligned}$$

and combining these two expressions, we obtain

$$\begin{aligned}
\sin\omega_v &= \frac{k_\phi - \frac{h_\phi + \sin\omega_v \cdot K}{X}\cdot K}{X} \\
&= \frac{k_\phi}{X} - \frac{h_\phi \cdot K}{X^2} - \frac{\sin\omega_v \cdot K^2}{X^2} \\
\Rightarrow \sin\omega_v \left(1 + \frac{K^2}{X^2}\right) &= \frac{k_\phi \cdot X}{X^2} - \frac{h_\phi \cdot K}{X^2} \\
\Rightarrow \sin\omega_v &= \frac{k_\phi \cdot X - h_\phi \cdot K}{X^2 + K^2}. \qquad \text{(E.28)}
\end{aligned}$$

Because ω_v can assume values between $\pm 180^\circ$, the sine of the desired angle alone does not suffice. So, we now substitute Equation E.28 into Equation E.28, and in a similar manner obtain

$$\cos\omega_v = \frac{h_\phi \cdot X + k_\phi \cdot K}{X^2 + K^2}. \qquad \text{(E.29)}$$

From Equations E.28 and E.29, we obtain

$$\tan\omega_v = \frac{k_\phi \cdot X - h_\phi \cdot K}{h_\phi \cdot X + k_\phi \cdot K}, \qquad \text{(E.30)}$$

which, if we use the `atan2` function, unambiguously determines ω_v.

Finally, of course,

$$\sin\alpha = \sin\beta_{in}. \qquad \text{(E.31)}$$

To calculate the diffractometer angles, we need to impose one final constraint on either β_{in} or β_{out}. As we have mentioned already above, there are three available modes one can use to acquire data, namely (a) fixed β_{in}, (b) fixed β_{out}, or (c) $\beta_{in} = \beta_{out}$.

We know from Equation E.17 that

$$l_\phi = \sin\beta_{in} + \sin\beta_{out}. \qquad \text{(E.32)}$$

Therefore in case (a), $\beta_{in} = \alpha$ is fixed and hence

$$\begin{aligned}
\sin\alpha &= \sin\beta_{in}, \\
\sin\beta_{out} &= l_\phi - \sin\alpha. \qquad \text{(E.33)}
\end{aligned}$$

For fixed β_{out} [case (b)],

$$\sin\alpha = l_\phi - \sin\beta_{out}, \qquad \text{(E.34)}$$

and for $\beta_{in} = \beta_{out}$ [case (c)],

$$\sin\alpha = \frac{l_\phi}{2}. \tag{E.35}$$

Inserting the appropriate Equation E.33, E.34, or E.35 into our equations for X, Y, and Z (Equations E.24, E.20, and E.23, respectively) and then using these in Equations E.25, E.26, E.28, and E.31 we are then able to compute δ, γ, ω_v, and α, respectively.

E.4.3 Detector rotation, ν

As we can see from Fig. E.1, there is a third detector motor movement in addition to δ and γ, namely ν, the rotation of the detector and slits around their symmetry axis. In our setup, we have two active modes of ν-rotation, namely (a) a "static l-projection" (SLP) mode; and (b) a "static footprint projection" (SFP) mode.

SLP mode

The purpose of the ν rotation in the SLP mode is to keep the projection in the planes of the slits and detector of the momentum transfer perpendicular to the crystal surface $\vec{q_z} = \vec{q_\perp}$ parallel to $\vec{\Delta z}$, the opening of the slits in one direction (see Fig. E.4). In this manner, the l-direction remains along $\vec{\Delta z}$. This implies that $\vec{\Delta x}$ is always perpendicular to $\vec{q_\perp}$, i.e.,

$$\vec{q_\perp} \cdot \vec{\Delta x} = 0. \tag{E.36}$$

Let us look at the relevant geometry more closely (Fig. E.5). With all motors set to zero, the ν-axis lies along the laboratory y-axis and exhibits a right-handed rotation. The rotation matrix transform for ν, which we call N, is, according to Equation E.2, given by

$$\mathcal{R}_y(\nu) = \begin{pmatrix} \cos\nu & 0 & \sin\nu \\ 0 & 1 & 0 \\ -\sin\nu & 0 & \cos\nu \end{pmatrix} \equiv N. \tag{E.37}$$

Also, with all angles set to zero, we can express $\vec{\Delta x}$ and $\vec{q_\perp}$ as

$$\vec{\Delta x} = C_1 \cdot \begin{pmatrix} 1 \\ 0 \\ 0 \end{pmatrix}, \qquad \vec{q_\perp} = C_2 \cdot \begin{pmatrix} 0 \\ 0 \\ 1 \end{pmatrix}.$$

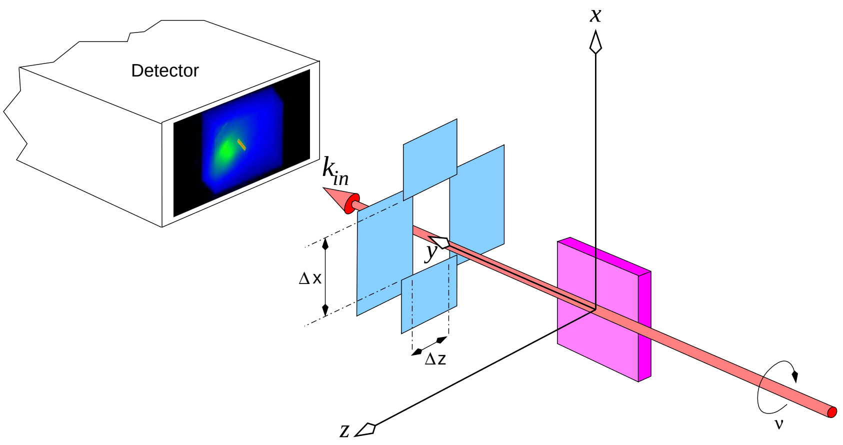

Figure E.4: Schematic figure of the detector and slit system for $\nu = \alpha = \gamma = \delta = 0$. The slit openings are Δx and Δz.

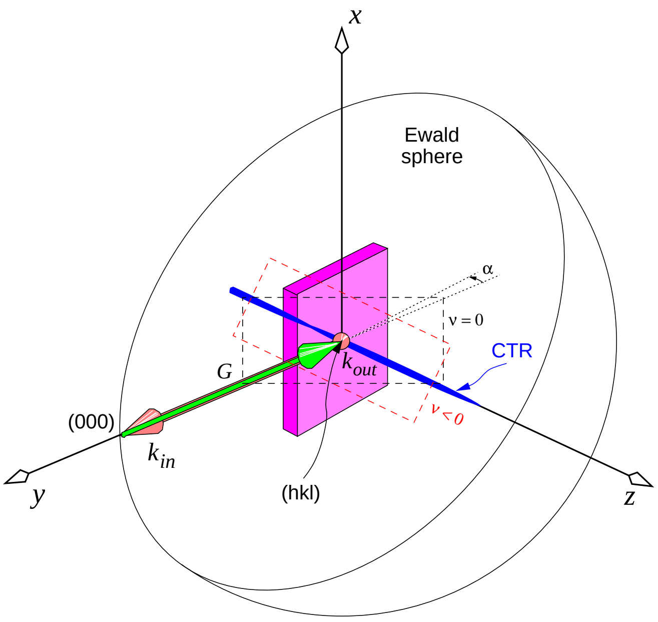

Figure E.5: Schematic figure of the vectors $\vec{k}_{in}$, $\vec{k}_{out}$, and $\vec{G}$, as viewed from the perspective of the detector, which points back along $\vec{k}_{out}$ towards the centre of the diffractometer (hence $\vec{k}_{out}$ is seen here as being "head on"). The vector $\vec{G}$ connects $\vec{k}_{in}$ [at (000)] to $\vec{k}_{out}$ [at (hkl)]. For no rotation of the detector, it is clear that the perpendicular component of $\vec{G}$ is not parallel to the detector frame, which must therefore be rotated in a negative sense to achieve this.

We now move the detector motors to some set of values (ν, δ, γ). It is immediately clear from the schematic shown in Fig. E.5 of the scattering vectors as viewed from the perspective of the detector (i.e., along the direction $-\vec{k}_{out}$) that one has to rotate ν in a negative direction to bring $q_\perp$ (the component of $\vec{G}$ perpendicular to the sample surface) parallel to $\vec{\Delta z}$. The three rotations (ν, δ, γ) cause $\vec{\Delta x}$ to become

$$\vec{\Delta x} = \Gamma\,\Delta\,N \begin{pmatrix} 1 \\ 0 \\ 0 \end{pmatrix}, \tag{E.38}$$

where we have dropped the constant C_1 (and will also drop C_2), as the magnitudes of the slit size in the x-direction or the momentum transfer perpendicular to the surface have no bearing on the condition E.36.

For non-zero values for α,

$$\vec{q}_\perp = A \begin{pmatrix} 0 \\ 0 \\ 1 \end{pmatrix}. \tag{E.39}$$

Inserting these expressions into Equation E.36, we obtain

$$\begin{aligned}
0 &= A^{-1} \cdot \Gamma\,\Delta\,N \begin{pmatrix} 1 \\ 0 \\ 0 \end{pmatrix} \begin{pmatrix} 0 \\ 0 \\ 1 \end{pmatrix} \\
&= A^{-1} \cdot \Gamma\,\Delta \begin{pmatrix} \cos\nu \\ 0 \\ -\sin\nu \end{pmatrix} \begin{pmatrix} 0 \\ 0 \\ 1 \end{pmatrix} \\
&= A^{-1} \cdot \Gamma \begin{pmatrix} \cos\delta\,\cos\nu \\ -\sin\delta\,\cos\nu \\ -\sin\nu \end{pmatrix} \begin{pmatrix} 0 \\ 0 \\ 1 \end{pmatrix} \\
&= A^{-1} \cdot \begin{pmatrix} \cos\delta\,\cos\nu \\ \cos\gamma(-\sin\delta\,\cos\nu) + \sin\gamma\,\sin\nu \\ \sin\gamma(-\sin\delta\,\cos\nu) - \cos\gamma\,\sin\nu \end{pmatrix} \begin{pmatrix} 0 \\ 0 \\ 1 \end{pmatrix} \\
&= \begin{pmatrix} \cdots \\ \cdots \\ -\sin\alpha(\cos\gamma(-\sin\delta\,\cos\nu) + \sin\gamma\,\sin\nu) + \cos\alpha(\sin\gamma(-\sin\delta\,\cos\nu) - \cos\gamma\,\sin\nu) \end{pmatrix} \begin{pmatrix} 0 \\ 0 \\ 1 \end{pmatrix}.
\end{aligned}$$

Only the bottom line is of any interest, of course, and we therefore obtain

$$\begin{aligned}
&\sin\alpha\,\cos\gamma\,\sin\delta\,\cos\nu - \sin\alpha\,\sin\gamma\,\sin\nu - \cos\alpha\,\sin\gamma\,\sin\delta\,\cos\nu - \cos\alpha\,\cos\gamma\,\sin\nu\\
&\quad = \sin\delta\,\cos\nu(\sin\alpha\,\cos\gamma - \cos\alpha\,\sin\gamma) - \sin\nu(\sin\alpha\,\sin\gamma + \cos\alpha\,\cos\gamma)\\
&\quad = \sin\delta\,\cos\nu\,\sin(\alpha-\gamma) - \sin\nu\,\cos(\alpha-\gamma) \;=\; 0\\
&\quad \Rightarrow -\sin\delta\frac{\sin(\gamma-\alpha)}{\cos(\gamma-\alpha)} \;=\; \frac{\sin\nu}{\cos\nu},
\end{aligned}$$

which then leads to

$$\Rightarrow \tan\nu \;=\; -\tan(\gamma-\alpha)\,\sin\delta. \tag{E.40}$$

SFP mode

An incoming x-ray beam incident on a surface at a glancing angle such that it floods the sample will illuminate a stripe across the sample surface. In traditional point-detector scans, a well-defined parallelogram section of this footprint is selected by two sets of slits in the detector arm. When using an area detector, the projection of the footprint is seen as a stripe [see Fig. E.6(a)]. The orientation of this stripe on the pixel image depends on the angle of the footprint on the sample, as viewed from the perspective of the detector. Hence, in Fig. E.6(b), the angle of the detector in the $\nu = 0$ position (dashed black box) is not parallel to the footprint (light purple stripe).

Hence, if either no ν-rotation or the SLP mode is chosen, the projection of the footprint is seen to rotate within the pixel frame as one moves up a CTR. For example, if there is no detector-axis rotation, the footprint stripe is seen to be parallel to the short sides of the detector frame close to the base of the CTR (low γ values), while at the maximum accessible l, for which $\delta = 0$, the footprint stripe is parallel to the long sides of the detector frame. Under such conditions, therefore, the detector slits must either be kept open at least to a square with edges equal in size to the sample footprint stripe, or else must be constantly varied from l-position to l-position in order to accommodate the apparent footprint rotation from the perspective of the detector, which is a complicated and normally impractical solution.

In the SFP mode, this problem is circumvented by rotating the ν-axis such that the long sides of the detector frame remain parallel to the footprint [the red dashed box in Fig. E.6(b)]. This therefore allows the user to close down the vertical slits (i.e., those with their edges parallel to the long sides of the detector frame) to values only marginally larger than the width of the

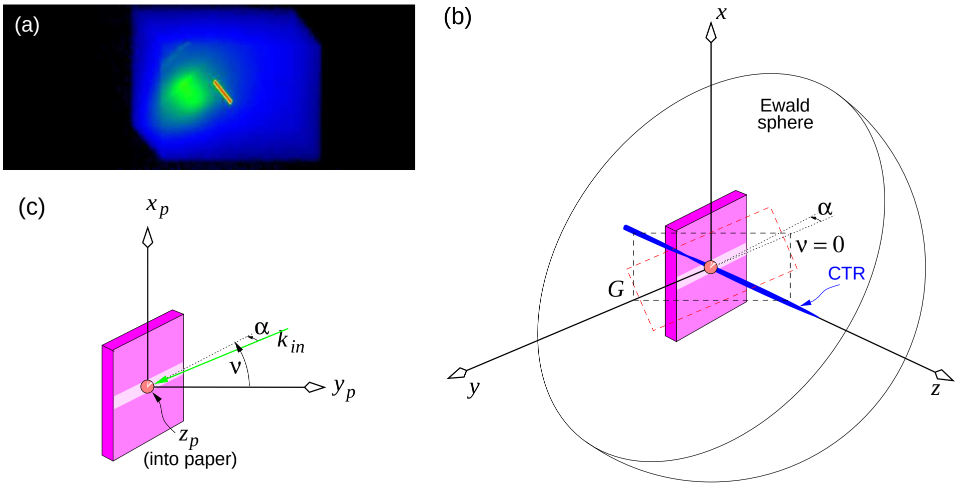

Figure E.6: (a) The footprint of the grazing-incidence beam on the sample is seen as a stripe on the area pixel detector. (b) The unrotated detector [black dashed box] sees this footprint at an angle which depends on the position of the detector and the tilt if the sample to the direct beam [i.e., the δ, γ and α angles]. The footprint can be made to be parallel to the long edge of the area detector by rotating it around ν [red dashed box]. (c) The coordinate system (x_p, y_p, z_p) used to calculate the ν-rotation for the SFP mode is defined by, and stationary with respect to, the detector.

footprint, which means stray background signal (such as that produced by the incoming beam passing through a beryllium dome) can be kept to a minimum.

We now derive the expression for the ν-rotation for any given α, δ, and γ values. We begin by assuming that $\alpha = 0$, and define a Cartesian coordinates system (x_p, y_p, z_p) that is fixed in the detector frame of reference [see Fig. E.6(c)]. In this frame of reference, it should be clear that ν is equal to the inverse tangent of the component of $-k_{in}$ in the x_p-direction divided by that in the y_p-direction, i.e.,

$$\nu \quad = \quad \tan^{-1}\left(\frac{k_{in}^{x_p}}{k_{in}^{y_p}}\right). \tag{E.41}$$

To move $-k_{in}$ into the frame of reference of the pixel detector, we imagine that we begin with the detector looking directly down the incoming beam (z_p collinear with $-k_{in}$). We now rotate γ in a negative sense around x_p, and then δ in a positive sense around y_p. This is exactly the opposite order of rotation compared to that described before in our angle calculations. This is because we are now rotating the whole diffractometer and incoming x-ray beam in the frame of reference of the detector, and *not* rotating the detector in the frame of reference of the diffractometer.

Referring back to our general expressions for rotation matrices (Equations E.1 to E.3), the relevant rotation matrices are therefore

$$\Gamma_p = \mathcal{R}_{x_p}(-\gamma) \quad = \quad \begin{pmatrix} 1 & 0 & 0 \\ 0 & \cos\gamma & \sin\gamma \\ 0 & -\sin\gamma & \cos\gamma \end{pmatrix}; \tag{E.42}$$

$$\Delta_p = \mathcal{R}_{y_p}(\delta) \quad = \quad \begin{pmatrix} \cos\delta & 0 & \sin\delta \\ 0 & 1 & 0 \\ -\sin\delta & 0 & \cos\delta \end{pmatrix}. \tag{E.43}$$

The incident beam in the detector frame of reference k'_{in} is therefore

$$\begin{aligned} k'_{in} &= \Delta_p \, \Gamma_p \, k_{in} \\ &= \Delta_p \begin{pmatrix} 1 & 0 & 0 \\ 0 & \cos\gamma & \sin\gamma \\ 0 & -\sin\gamma & \cos\gamma \end{pmatrix} \begin{pmatrix} 0 \\ 0 \\ 1 \end{pmatrix} |k| \\ &= \Delta_p \begin{pmatrix} 0 \\ \sin\gamma \\ \cos\gamma \end{pmatrix} |k| \\ &= \begin{pmatrix} \cos\delta & 0 & \sin\delta \\ 0 & 1 & 0 \\ -\sin\delta & 0 & \cos\delta \end{pmatrix} \begin{pmatrix} 0 \\ \sin\gamma \\ \cos\gamma \end{pmatrix} |k| \\ &= \begin{pmatrix} \sin\delta \, \cos\gamma \\ \sin\gamma \\ \cos\delta \, \cos\gamma \end{pmatrix} |k|. \end{aligned} \tag{E.44}$$

Using the x_p- and y_p-components of k'_{in} in Equation E.41, we obtain

$$\nu \quad = \quad \tan^{-1}\left(\frac{\sin\delta \, \cos\gamma}{\sin\gamma}\right).$$

Until now, we have assumed that $\alpha = 0$. For nonzero α, we merely need to rotate by $\gamma - \alpha$ instead of γ, and our equation becomes

$$\nu \quad = \quad \tan^{-1}\left(\frac{\sin\delta \, \cos(\gamma - \alpha)}{\sin(\gamma - \alpha)}\right). \tag{E.45}$$

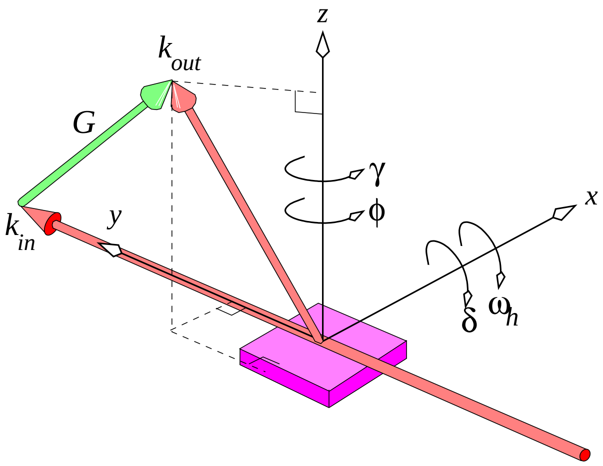

Figure E.7: Schematic figure of the laboratory coordinate system, incoming and outgoing wavevectors $\vec{k}_{in}$ and $\vec{k}_{out}$, the scattering vector $\vec{G}$, and the pertinent motor rotations in the horizontal geometry setup of the surface diffractometer.

E.5 Horizontal geometry

E.5.1 Geometrical setup

Consider a flat single crystal sample mounted horizontally (i.e., with its flat face horizontal and its surface normal vertical), as shown in Fig. E.7.

Here, the laboratory set of coordinates (x, y, z), are fixed by y being the positive direction of the incident x-ray beam, z being the vertical direction around which γ rotates and ϕ also rotates, as long as ω_h (which determines the angle of incidence of the incoming beam) is set to zero. x is the horizontal direction around which ω_h rotates and also δ rotates when $\gamma = 0$.[4]

Using the equations E.2 and E.3, we therefore obtain for the four circles γ, ϕ, δ, and ω_h,

---

[4] Note that in this geometry, all motor rotations exhibit positive right-handedness.

respectively, the rotation matrices Γ, Φ, Δ, and Ω_h, given by

$$\Gamma = \mathcal{R}_z(\gamma) = \begin{pmatrix} \cos\gamma & -\sin\gamma & 0 \\ \sin\gamma & \cos\gamma & 0 \\ 0 & 0 & 1 \end{pmatrix}; \tag{E.46}$$

$$\Phi = \mathcal{R}_z(\phi) = \begin{pmatrix} \cos\phi & -\sin\phi & 0 \\ \sin\phi & \cos\phi & 0 \\ 0 & 0 & 1 \end{pmatrix}; \tag{E.47}$$

$$\Delta = \mathcal{R}_x(\delta) = \begin{pmatrix} 1 & 0 & 0 \\ 0 & \cos\delta & -\sin\delta \\ 0 & \sin\delta & \cos\delta \end{pmatrix}; \tag{E.48}$$

$$\Omega_h = \mathcal{R}_x(\omega_h) = \begin{pmatrix} 1 & 0 & 0 \\ 0 & \cos\omega_h & -\sin\omega_h \\ 0 & \sin\omega_h & \cos\omega_h \end{pmatrix}. \tag{E.49}$$

E.5.2 Calculating diffractometer angles

The incoming x-ray beam (in units of $2\pi/\lambda$) is now represented by the vector

$$\vec{k}_{in} = \begin{pmatrix} 0 \\ 1 \\ 0 \end{pmatrix}. \tag{E.50}$$

We now essentially go through the same procedure as described above for the vertical geometry. We begin with the diffraction condition, Equation E.10

$$\vec{k}_{out} - \vec{k}_{in} = \vec{G} = \begin{pmatrix} X \\ Y \\ Z \end{pmatrix}$$

and move the detector to the required position for capturing the diffracted beam:

$$\begin{aligned}
\Rightarrow \vec{k}_{out} - \vec{k}_{in} &= (\Gamma \cdot \Delta - \mathcal{I}) \begin{pmatrix} 0 \\ 1 \\ 0 \end{pmatrix} \\
&= \Gamma \begin{pmatrix} 0 \\ \cos\delta \\ \sin\delta \end{pmatrix} - \begin{pmatrix} 0 \\ 1 \\ 0 \end{pmatrix} \\
&= \begin{pmatrix} -\cos\delta\,\sin\gamma \\ \cos\delta\,\cos\gamma - 1 \\ \sin\delta \end{pmatrix} = \begin{pmatrix} X \\ Y \\ Z \end{pmatrix}. \qquad \text{(E.51)}
\end{aligned}$$

Again, we now rotate the crystal into the diffraction condition, i.e.,

$$\begin{aligned}
\begin{pmatrix} X \\ Y \\ Z \end{pmatrix} &= \Omega_h \cdot \Phi \begin{pmatrix} h_\phi \\ k_\phi \\ l_\phi \end{pmatrix} \\
\Rightarrow \begin{pmatrix} h_\phi \\ k_\phi \\ l_\phi \end{pmatrix} &= \Phi^{-1} \cdot \Omega_h^{-1} \begin{pmatrix} X \\ Y \\ Z \end{pmatrix}. \qquad \text{(E.52)}
\end{aligned}$$

Multiplying out, we obtain

$$\begin{aligned}
\begin{pmatrix} h_\phi \\ k_\phi \\ l_\phi \end{pmatrix} &= \Phi^{-1} \cdot \begin{pmatrix} X \\ \cos\omega_h\,Y + \sin\omega_h\,Z \\ -\sin\omega_h\,Y + \cos\omega_h\,Z \end{pmatrix} \\
&= \begin{pmatrix} \sin\phi(\cos\omega_h\,Y + \sin\omega_h\,Z) + \cos\phi\,X \\ \cos\phi(\cos\omega_h\,Y + \sin\omega_h\,Z) - \sin\phi\,X \\ \cos\omega_h\,Z - \sin\omega_h\,Y \end{pmatrix}. \qquad \text{(E.53)}
\end{aligned}$$

Referring back to Fig. E.3 for the vertical geometry and remembering that the incident angle $\beta_{in} = \omega_h$, we again obtain Equation E.17

$$l_\phi = \sin\beta_{in} + \sin\beta_{out}$$

for the momentum transfer perpendicular to the substrate surface. But from Equations E.51 and E.53, we know that

$$\begin{aligned} l_\phi &= -\sin\omega_h\, Y + \cos\omega_h\, Z \\ &= -\sin\omega_h(\cos\delta\,\cos\gamma - 1) + \cos\omega_h\,\sin\delta \\ &= \underbrace{\sin\omega_h}_{\sin\beta_{in}} + \underbrace{\sin\delta\,\cos\omega_h - \cos\delta\,\sin\omega_h\,\cos\gamma}_{\sin\beta_{out}}. \end{aligned} \tag{E.54}$$

We again determine the squared magnitude of the in-plane component of $\vec{G}_\phi$, which we have argued is independent of ϕ, as this rotation is always normal to the crystal surface. Referring once more back to Equations E.51 and E.53, we obtain

$$\begin{aligned} h_\phi^2 + k_\phi^2 &= [\sin\phi(\cos\omega_h\, Y + \sin\omega_h\, Z) + \cos\phi\, X]^2 \\ &+ [\cos\phi(\cos\omega_h\, Y + \sin\omega_h\, Z) - \sin\phi\, X]^2 \\ &= X^2\cos^2\phi + \sin^2\phi(\cos\omega_h\, Y + \sin\omega_h\, Z)^2 + 2X\,\cos\phi\,\sin\phi\,(\cos\omega_h\, Y + \sin\omega_h\, Z) \\ &+ X^2\sin^2\phi + \cos^2\phi(\cos\omega_h\, Y + \sin\omega_h\, Z)^2 - 2X\,\cos\phi\,\sin\phi\,(\cos\omega_h\, Y + \sin\omega_h\, Z) \\ &= X^2 + (\cos\omega_h\, Y + \sin\omega_h\, Z)^2, \end{aligned} \tag{E.55}$$

which, as predicted, is independent of ω_h. Remembering that $\omega_h = \beta_{in}$, we rearrange Equation E.55 to obtain

$$X = \pm\left[h_\phi^2 + k_\phi^2 - (\cos\beta_{in}\cdot Y + \sin\beta_{in}\cdot Z)^2\right]^{1/2}. \tag{E.56}$$

We use the negative solution, as we will see later in Equation E.60 that this is needed in order to make the δ- and γ–circles move in a positive direction.

The next condition we exploit is the fact that the magnitude of $\vec{G}_\phi$ is equal to that of $\vec{G}$

and that both these must also be independent of ω_h. From Equation E.51, we obtain

$$\begin{aligned} X^2+Y^2+Z^2 &= \cos^2\delta\,\sin^2\gamma+\cos^2\delta\,\cos^2\gamma+1-2\cos\delta\,\cos\gamma+\sin^2\delta \\ &= \cos^2\delta+1-2\cos\delta\,\cos\gamma\;+\sin^2\delta \\ &= 2-2\cos\gamma\,\cos\delta \\ &= -2Y\;=\;h_\phi^2+k_\phi^2+l_\phi^2 \\ \Rightarrow Y &= -(h_\phi^2+k_\phi^2+l_\phi^2)/2. \qquad \text{(E.57)} \end{aligned}$$

From Equation E.51 and the far right-hand term of Equation E.54, we obtain

$$\begin{aligned} \sin\beta_{out} &= \cos\omega_h\cdot\sin\delta-\sin\omega_h\cdot\cos\delta\cdot\cos\gamma \\ &= \cos\omega_h\cdot Z-\sin\omega_h(Y+1) \\ &= \cos\omega_h\cdot Z-\sin\beta_{in}(Y+1) \\ \Rightarrow Z &= \left[\sin\beta_{out}+\sin\beta_{in}(Y+1)\right]/\cos\omega_h. \qquad \text{(E.58)} \end{aligned}$$

So, with equations E.56, E.57, and E.58, we have been able to express the three orthogonal components of the scattering vector in the laboratory frame (X, Y, and Z) in terms of the components of the same scattering vector in the crystal frame (h_ϕ, k_ϕ, and l_ϕ) and the angles β_{in} and β_{out}.

Our next step is to solve for the diffractometer angles γ, δ, ϕ, and ω_h. From Equation E.51,

$$\begin{aligned} \tan\gamma &= \frac{\sin\gamma}{\cos\gamma} \\ &= \frac{\sin\gamma\,\cos\delta}{\cos\gamma\,\cos\delta-1+1} \\ &= \frac{-X}{Y+1}. \qquad \text{(E.59)} \end{aligned}$$

Note that $\tan\gamma$ depends on the individual signs of X and $Y+1$, hence we use the quadrant-specific `atan2` function in ANSI C.

Again using Equation E.51, we immediately obtain

$$\begin{aligned}\sin\delta &= Z;\\ \cos\delta &= \frac{-X}{\sin\gamma}\end{aligned}$$

and hence

$$\tan\delta = \frac{Z\cdot\sin\gamma}{-X}. \tag{E.60}$$

For determining ϕ, we define

$$K = \cos\beta_{in}\cdot Y + \sin\beta_{in}\cdot Z. \tag{E.61}$$

Using this definition, we obtain from Equation E.53

$$\begin{aligned}h_\phi &= \sin\phi\cdot K + \cos\phi\cdot X\\ \Rightarrow \cos\phi &= \frac{h_\phi - \sin\phi\cdot K}{X}\\ k_\phi &= \cos\phi\cdot K - \sin\phi\cdot X\\ \Rightarrow \sin\phi &= \frac{-k_\phi + \cos\phi\cdot K}{X}.\end{aligned}$$

By following the same procedure as we have already detailed for the equivalent case in the vertical geometry, we obtain by inserting these two expressions into one another

$$\tan\phi = \frac{h_\phi\cdot K - k_\phi\cdot X}{h_\phi\cdot X + k_\phi\cdot K}. \tag{E.62}$$

Again, we need one additional constraint in order to solve for the four physical angles γ, δ, ω_h and ϕ, which, as before for the vertical geometry, we obtain by defining three possible recording modes, i.e., β_{in} fixed; β_{out} fixed; or $\beta_n = \beta_{out}$.

For β_{in} fixed, this implies that $\omega_h \equiv \beta_{in}$ is fixed. Therefore

$$\sin\beta_{out} = l_\phi - \sin\omega_h. \tag{E.63}$$

Similarly, for β_{out} fixed,

$$\sin\omega_h = \sin\beta_{in} = l_\phi - \sin\beta_{out}. \tag{E.64}$$

And finally for $\beta_n = \beta_{out}$,

$$\sin\beta_{in} = \sin\beta_{out} = l_\phi/2. \tag{E.65}$$

We are now able to uniquely calculate all angles by inserting Equations E.63, E.64 and E.65 into our expressions for X, Y, and Z.

E.5.3 Detector rotation, ν

There are also the same two active detector rotation modes available for the horizontal geometry. The first mode, i.e., the static l-projection (SLP) mode, produces only small adjustments of ν for modest incident angles ω_h. The second (SFP) mode invokes ν-rotations which are essentially identical to those for the same mode in the vertical geometry. Both modes are now detailed.

SLP mode

If we consider Fig. E.8, it should be clear that the detector "sees" CTRs that are almost vertical, i.e., parallel to the short edge of the detector frame, independent of the angles δ and γ. This is only approximately true, and rotation of ν is necessary for non-zero incident angles ω_h.

Using the same arguments as those for the SLP mode in the vertical geometry, we require that

$$\vec{q}_\perp \cdot \vec{\Delta x} = 0, \tag{E.66}$$

in other words, the CTR and the long edge of the detector are perpendicular to one another. As in the vertical geometry (Equation E.37), with all the motors set to zero, the ν-axis lies along the laboratory y-axis and exhibits a right-handed rotation, i.e.,

$$\mathcal{R}_y(\nu) = \begin{pmatrix} \cos\nu & 0 & \sin\nu \\ 0 & 1 & 0 \\ -\sin\nu & 0 & \cos\nu \end{pmatrix} \equiv N.$$

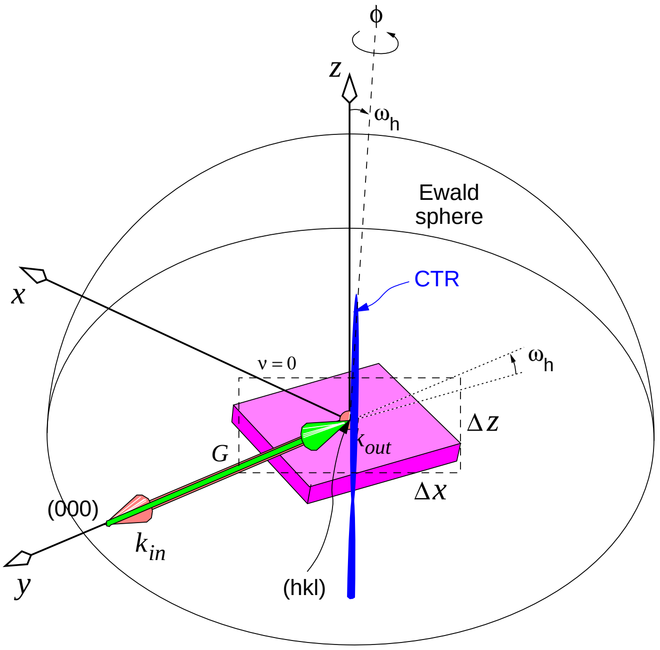

Figure E.8: Schematic figure of the vectors $\vec{k}_{in}$, $\vec{k}_{out}$, and $\vec{G}$, as viewed from the perspective of the detector, which points back along $\vec{k}_{out}$ towards the centre of the diffractometer (hence $\vec{k}_{out}$ is seen here as being "head on"). The vector $\vec{G}$ connects $\vec{k}_{in}$ [at (000)] to $\vec{k}_{out}$ [at (hkl)].

Also, with all angles set to zero, we can express $\vec{\Delta x}$ and $\vec{q_\perp}$ as

$$\begin{aligned} \vec{\Delta x} &= C_1 \cdot \begin{pmatrix} 1 \\ 0 \\ 0 \end{pmatrix}, \\ \vec{q}_\perp &= C_2 \cdot \begin{pmatrix} 0 \\ 0 \\ 1 \end{pmatrix}. \end{aligned}$$

The three detector rotations (ν, δ, γ) cause $\vec{\Delta x}$ to become

$$\vec{\Delta x} = \Gamma \, \Delta \, N \begin{pmatrix} 1 \\ 0 \\ 0 \end{pmatrix}, \tag{E.67}$$

where we will again drop the constant C_1 and C_2.

For non-zero values for ω_h,

$$\vec{q}_\perp = \Omega_h \begin{pmatrix} 0 \\ 0 \\ 1 \end{pmatrix}. \tag{E.68}$$

Inserting these expressions into Equation E.66, we obtain

$$\begin{aligned}
0 &= \Omega_h^{-1} \cdot \Gamma \, \Delta \, N \begin{pmatrix} 1 \\ 0 \\ 0 \end{pmatrix} \begin{pmatrix} 0 \\ 0 \\ 1 \end{pmatrix} = \\
&= \Omega_h^{-1} \cdot \Gamma \, \Delta \begin{pmatrix} \cos\nu \\ 0 \\ -\sin\nu \end{pmatrix} \begin{pmatrix} 0 \\ 0 \\ 1 \end{pmatrix} \\
&= \Omega_h^{-1} \cdot \Gamma \begin{pmatrix} \cos\nu \\ \sin\delta \, \sin\nu \\ -\cos\delta \, \sin\nu \end{pmatrix} \begin{pmatrix} 0 \\ 0 \\ 1 \end{pmatrix} \\
&= \Omega_h^{-1} \cdot \begin{pmatrix} \cos\gamma \, \cos\nu - \sin\gamma \, \sin\delta \, \sin\nu \\ \sin\gamma \, \cos\nu + \cos\gamma \, \sin\delta \, \sin\nu \\ -\cos\delta \, \sin\nu \end{pmatrix} \begin{pmatrix} 0 \\ 0 \\ 1 \end{pmatrix} \\
&= \begin{pmatrix} \cdots \\ \cdots \\ -\sin\omega_h \, \sin\gamma \, \cos\nu - \sin\omega_h \, \cos\gamma \, \sin\delta \, \sin\nu - \cos\omega_h \, \cos\delta \, \sin\nu \end{pmatrix} \begin{pmatrix} 0 \\ 0 \\ 1 \end{pmatrix} = 0
\end{aligned}$$

Again, only the last line is of interest here:

$$\Rightarrow \sin\nu(\sin\omega_h \, \cos\gamma \, \sin\delta) = -\sin\gamma \, \sin\omega_h \, \cos\nu,$$

yielding as a final expression for ν

$$\Rightarrow \tan\nu = \frac{-\sin\gamma \, \sin\omega_h}{\sin\omega_h \, \cos\gamma \, \sin\delta + \cos\omega_h \, \cos\delta} \tag{E.69}$$

SFP mode

The expression for the SFP mode is identical to that given by Equation E.45, except that now the correction for the incident angle to the surface is not a subtraction of α from γ, but a subtraction of ω_h from δ, i.e.,

$$\nu = \tan^{-1}\left(\frac{\sin(\delta - \omega_h)\,\cos\gamma}{\sin\gamma}\right). \tag{E.70}$$

Bibliography

[1] W. R. Busing and H. A. Levy: "Angle calculations for 3- and 4-circle X-ray and neutron diffractometers." *Acta Crystalogr.* **22**(4), 457–464 (1967), doi:10.1107/S0365110X67000970.

[2] K. Evans-Lutterodt and M. T. Tang: "Angle Calculations for a '2+2' Surface X-ray Diffractometer." *J. Appl. Crystallogr.* **28**, 318–326 (1995).

[3] E. Vlieg: "Integrated Intensities Using a Six-Circle Surface X-ray Diffractometer." *J. Appl. Crystallogr.* **30**(5), 532 – 543 (1997), doi:10.1107/S0021889897002537.

[4] E. Vlieg: "A (2+3)-Type Surface Diffractometer: Mergence of the z-Axis and (2+2)-Type Geometries." *J. Appl. Crystallogr.* **31**(2), 198–203 (1998), doi:10.1107/S0021889897009990.

[5] H. You: "Angle calculations for a '4S+2D' six-circle diffractometer." *J. Appl. Crystallogr.* **32**, 614 – 623 (1999), doi:10.1107/S0021889899001223.

[6] O. Bunk and M. M. Nielsen: "Angle calculations for a z-axis/(2S+2D) hybrid diffractometer." *J. Appl. Crystallogr.* **37**(2), 216–222 (2004), doi:10.1107/S0021889803029686.

[7] P. R. Willmott and C. M. Schlepütz: "Angle calculations for the 5-circle surface diffractometer of the Materials Science beamline at the Swiss Light Source." (2007).
URL `http://sls.web.psi.ch/view.php/beamlines/ms/sd/primer/anglecalculations.pdf`

[8] J. Diebel: "Representing Attitude: Euler Angles, Unit Quaternions, and Rotation Vectors." Technical report, Stanford University, Palo Alto, CA (2006).

Appendix F

Geometric Series

The geometric series is defined as a series with a constant ratio between two successive terms, starting from 1. The N^{th} term of the series can be written as

$$S_N = \sum_{n=0}^{N-1} b^n = \frac{1-b^N}{1-b}. \tag{F.1}$$

In the limiting case of $N \to \infty$, the series converges if and only if $|b| < 1$, otherwise it oscillates or diverges (This is also true if b is a complex number). In the converging case, its value is given by

$$S_\infty = \lim_{N\to\infty} S_N = \sum_{n=0}^{\infty} b^n = \frac{1}{1-b}. \tag{F.2}$$

When evaluating sums of phase factors, we are often faced with geometric series of the following form:

$$S_N = \sum_{n=0}^{N-1} e^{iqr\cdot n}. \tag{F.3}$$

This can be evaluated to give

$$\begin{aligned} S_N &= \sum_{n=0}^{N-1} e^{iqr\cdot n} = \frac{1-e^{iqr\cdot N}}{1-e^{iqr}} = \frac{\left(e^{-i(qr\cdot N)/2} - e^{i(qr\cdot N)/2}\right)}{e^{-i(qr)/2} - e^{i(qr)/2}} \cdot \frac{e^{i(qr\cdot N)/2}}{e^{i(qr)/2}} \\ &= \frac{\sin(\frac{1}{2}Nqr)}{\sin(\frac{1}{2}qr)} \cdot e^{iqr\cdot(N-1)/2}. \end{aligned} \tag{F.4}$$

Curriculum Vitae

CHRISTIAN M. SCHLEPÜTZ

Date of birth	March 31st, 1978
Place of birth	Zürich, Switzerland
Citizenship	German

Education	1994 – 1998	High School: Alte Kantonsschule Aarau (AG), Realgymnasium Typus C
	since 1999	Study of *Experimental Physics* at the Universität Zürich, Switzerland
	2001	1st preliminary exam (1. Vordiplom, Semester 00/01)
	2002	2nd preliminary exam (2. Vordiplom, Semester 01/02)
	2003 – 2004	Diploma thesis at the Swiss Light Source (SLS), Paul Scherrer Institut (PSI), Switzerland: *In-situ Structural Investigations of Growth of Icosahedral Ti-Ni-Zr Thin Films Deposited by Pulsed Laser Deposition*
	2005	Diploma in *Experimental Physics*, Universität Zürich, Switzerland (corresponds to M. Sc.)
	since 2005	Dissertation at the Swiss Light Source (SLS), Paul Scherrer Institut (PSI), Switzerland: *Systematic Structure Investigation of YBCO Thin Films with Direct Methods and Surface X-ray Diffraction*

International experience	1995 – 1996	Student exchange with AFS to Russel (OH), USA graduation from West Geauga High School, Chesterland (OH)
	1999	Participant of the AFS *Community Service Program* in Asunción, Paraguay. 8 months voluntary work in the social foundation *Dequení* for street children
	2002 – 2003	ERASMUS student exchange at the physics institute of the *Università degli Studi della Calabria*, Italy
Awards	2004	*Semesterpreis* of the Universität Zürich by recommendation of Prof. Dr. J. Osterwalder: *Computational Determination of Coexisting Inequivalent Orientations of a Surface-adsorbed Molecular Species from XPD Images*

Publication List

Peer-reviewed articles

[1] P. R. Willmott, R. Herger, and C. M. Schlepütz: “Multilayers, alloys, and complex profiles by pulsed laser deposition using a novel target geometry.” *Thin Solid Films* **453**, 436–439 (2004), doi:10.1016/j.tsf.2003.11.257.

[2] C. M. Schlepütz, R. Herger, P. R. Willmott, B. D. Patterson, O. Bunk, Ch. Brönnimann, B. Henrich, G. Hülsen, and E. F. Eikenberry: “Improved data acquisition in grazing-incidence X-ray scattering experiments using a pixel detector.” *Acta Crystallogr. A* **61**, 418–425 (2005), doi:10.1107/S0108767305014790.

[3] P. R. Willmott, C. M. Schlepütz, B. D. Patterson, R. Herger, A. Lange, D. Meister, D. Maden, Ch. Brönnimann, E. F. Eikenberry, G. Hülsen, and A. Al-Adwan: “In situ studies of complex PLD-grown films using hard X-ray surface diffraction.” *Appl. Surf. Sci.* **247**, 188–196 (2005), doi:10.1016/j.apsusc.2005.01.133.

[4] P. R. Willmott, C. M. Schlepütz, R. Herger, B. D. Patterson, K. Hassdenteufel, and W. Steurer: “In situ diffraction studies of the initial growth processes of textured icosahedral quasicrystalline thin films.” *Phys. Rev. B* **71**, 094203 (2005), doi:10.1103/PhysRevB.71.094203.

[5] P. R. Willmott, R. Herger, C. M. Schlepütz, D. Martoccia, and B. D. Patterson: “Energetic surface smoothing of complex metal-oxide thin films.” *Phys. Rev. Lett.* **96**, 176102 (2006), doi:10.1103/PhysRevLett.96.176102.

[6] R. Herger, P. R. Willmott, O. Bunk, C. M. Schlepütz, B. D. Patterson, and

B. Delley: "Surface of strontium titanate." *Phys. Rev. Lett.* **98**, 076102 (2007), doi: 10.1103/PhysRevLett.98.076102.

[7] P. R. Willmott, S. A. Pauli, R. Herger, C. M. Schlepütz, D. Martoccia, B. D. Patterson, B. Delley, R. Clarke, D. Kumah, C. N. Cionca, and Y. Yacoby: "Structural basis for the conducting interface between $LaAlO_3$ and $SrTiO_3$." *Phys. Rev. Lett.* **99**, 155502 (2007), doi:10.1103/PhysRevLett.99.155502.

[8] R. Herger, P. R. Willmott, O. Bunk, C. M. Schlepütz, B. D. Patterson, B. Delley, V. L. Shneerson, P. F. Lyman, and D. K. Saldin: "Surface structure of $SrTiO_3(001)$." *Phys. Rev. B* **76**, 195435 (2007), doi:10.1103/PhysRevB.76.195435.

[9] R. Herger, P. R. Willmott, C. M. Schlepütz, M. Björck, S. A. Pauli, D. Martoccia, B. D. Patterson, D. Kumah, R. Clarke, Y. Yacoby, and M. Döbeli: "Structure determination of monolayer-by-monolayer grown $La_{1-x}Sr_xMnO_3$ thin films and the onset of magnetoresistance." *Phys. Rev. B* **77**, 085401 (2008), doi:10.1103/PhysRevB.77.085401.

[10] J. W. Andreasen, S. Gevorgyan, C. M. Schlepütz, and F. Krebs: "Applicability of X-ray reflectometry to studies of polymer solar cell degradation." *Solar Energy Materials and Solar Cells* **92**(7), 793–798 (2008), doi:10.1016/j.solmat.2008.02.011.

[11] D. P. Kumah, A. Riposan, C. N. Cionca, N. S. Husseini, R. Clarke, J. Y. Lee, J. M. Millunchick, Y. Yacoby, C. M. Schlepütz, M. Björck, and P. R. Willmott: "Resonant coherent Bragg rod analysis of strained epitaxial heterostructures." *Appl. Phys. Lett.* **93**(8), 081910 (2008), doi:10.1063/1.2975835.

[12] D. Martoccia, P. R. Willmott, T. Brugger, M. Björck, S. Günther, C. M. Schlepütz, A. Cervellino, S. A. Pauli, B. D. Patterson, S. Marchini, J. Wintterlin, W. Moritz, and T. Greber: "Graphene on Ru(0001): A 25×25 Supercell." *Phys. Rev. Lett.* **101**(12), 126102 (2008), doi:10.1103/PhysRevLett.101.126102.

[13] M. Radovic, N. Lampis, F. Miletto Granozio, P. Perna, Z. Ristic, M. Salluzzo, C. M. Schlepütz, and U. Scotti di Uccio: "Growth and characterization of stable SrO-terminated $SrTiO_3$ surfaces." *Appl. Phys. Lett.* **94**(2), 022901 (2009), doi:10.1063/1.3052606.

[14] S. O. Mariager, C. M. Schlepütz, M. Aagesen, C. B. Sørensen, E. Johnson, P. R. Willmott, and R. Feidenhans'l: "High resolution three dimensional reciprocal space mapping of semiconductor nanostructures." *Phys. Status Solidi A* (2009). Accepted.

[15] P. Kraft, A. Bergamaschi, Ch. Brönnimann, R. Dinapoli, E. F. Eikenberry, H. Graafsma, B. Henrich, I. Johnson, M. Kobas, A. Mozzanica, C. M. Schlepütz, and B. Schmitt: "Characterization and Calibration of PILATUS Detectors." *IEEE Trans Nucl Sci* (2009). Accepted.

[16] S. O. Mariager, S. L. Lauridsen, A. Dohn, N. Bovet, C. B. Sørensen, C. M. Schlepütz, P. R. Willmott, and R. Feidenhans'l: "High resolution three dimensional reciprocal space mapping of InAs nanowires." *J. Appl. Crystallogr.* **42**(3), 369–375 (2009), doi: 10.1107/S0021889809009145.

[17] P. Kraft, A. Bergamaschi, Ch. Brönnimann, R. Dinapoli, E. F. Eikenberry, B. Henrich, I. Johnson, M. Kobas, C. M. Schlepütz, P. R. Willmott, and B. Schmitt: "Performance of single photon counting pixel detector modules." *J. Synch. Rad.* **16**(3), 368–375 (2009), doi:10.1107/S0909049509009911.

Non-reviewed articles

[1] P. R. Willmott, C. M. Schlepütz, R. Herger, B. D. Patterson, O. Bunk, Ch. Brönnimann, B. Henrich, G. Hülsen, and E. F. Eikenberry: "Technical Reports: A Single-photon Counting Pixel Detector for Surface Diffraction Experiments." *Synch. Rad. News* **18**(2), 16–22 (2005), doi:10.1080/08940880500457396.

[2] P. R. Willmott, R. Herger, C. M. Schlepütz, D. Martoccia, and B. D. Patterson: "Technical Reports: Pulsed Laser Deposition and in situ Surface X-ray Diffraction at the Materials Science Beamline at the Swiss Light Source." *Synch. Rad. News* **18**(4), 37–42 (2005), doi: 10.1080/08940880500457230.